TECHNISCHE UNIVERSITÄT WIEN

ATOMINSTITUT

Quantitative modeling towards continuous superradiant laser on Sr

DISSERTATION

zur Erlangung des akademischen Grades

Doktor der Technischen Wissenschaften

eingereicht von

Swadheen Dubey, M.Sc.

Matrikelnummer 12102546

ausgeführt am Atominstitut
der Fakultät für Physik der Technischen Universität Wien

Betreuung: Univ.-Prof. Dipl.-Phys. Dr. Thorsten Schumm
Zweitbetreuung: Dr. Georgy Kazakov

Wien, 5. November 2024

Swadheen Dubey	Thorsten Schumm

Technische Universität Wien
A-1040 Wien ▪ Karlsplatz 13 ▪ Tel. +43-1-58801-0 ▪ www.tuwien.at

"Every year is getting shorter, never seem to find the time. Plans that either come to naught or half a page of scribbled lines. Hanging on in quiet desperation is the English way. The time is gone, the song is over, thought I'd something more to say ."

- Roger Waters

Contents

Abstract

Optical clocks, with an accuracy of 10^{-19} level, corresponding to being off by only 1 second over the universe's age, are the most precise clocks ever built. Optical clocks promise a huge impact on the development of quantum technologies like atom interferometry and quantum metrology with applications in telecommunication, specifically in network synchronization and accuracy navigation through 5G networks instead of GPS. Other than this, if optical clocks are operated on satellites then they could be used for gravitational wave detectors, performing experiments of general relativity. Further applications are in geology, astronomy, and fundamental physics.

Current optical clocks are *passive* frequency standards. In these systems, the frequency of a highly coherent probe laser (local oscillator) is intermittently compared with the frequency of a narrow and robust *clock transition* in trapped atoms or ions. This laser is pre-stabilized by an ultrastable macroscopic cavity (flywheel), keeping the frequency in between interrogation cycles. Thermal and mechanical fluctuations in the local oscillator are among the main factors limiting the short-term stability of modern optical clocks. They entirely determine the overall clock stability on the time less than a single interrogation cycle and do not utilize the full potential of a clock transition. Finally, down-conversion of the broad-band laser frequency noise contributes to the measurement error of the frequency offset, what is known as a *Dick effect*.

To overcome this problem, one may create an *active optical clock* based on a *superradiant laser*, where the atoms with population inversion on the clock transition are coupled to a resonator mode in the *bad cavity regime*. The cavity mode of such a laser is much broader than its gain profile, and the laser frequency is inherently insensitive to cavity length fluctuations, in contrast to ordinary good-cavity lasers.

Achieving a Continuous superradiance using a narrow optical transition has the potential to improve the short-term stability of state-of-the-art optical clocks. Even though pulsed superradiant emission on a mHz linewidth clock transition has been shown, true continuous operation, without Fourier limitation, has turned out to be extremely challenging. This problem is being tackled by the FET-Flag project iqClock and European Innovative Training Network MoSaiQC, short for "Modular Systems for Advanced Integrated Quantum Clocks", and includes a wide range of academic and industrial institutions. At TU Wien, we, as a theoretical partner, have studied the ultimate

characteristics of the active optical clocks, and performed simulations to assist our experimental partners with the design of such a Laser.

We then present two different models for stimulating the generated superradiant field by taking into account position-dependent shifts, collisional decoherence, light shifts, and atom loss. Finally, we estimate a laser linewidth of less than 100 mHz, limited by atom number fluctuations, and resulting in an output power of hundreds of fW.

This thesis is divided into two main sections. The first section introduces the necessary tools for studying the superradiant laser. We begin by developing an understanding of quantum optics and open quantum systems. Then, we compare different models for simulating the superradiant laser and estimate the ultimate stability achievable using an active optical clock.

The second section of the thesis focuses on the realization of a superradiant laser. Specifically, we performed a feasibility study for the design and simulation of the continuous high-efficiency cooling, loading, and pumping to the upper lasing state inside the cavity for the superradiant mHz machine at the University of Amsterdam. The goal is to combine a high-flux continuous beam of ultra-cold strontium atoms with a bowtie cavity for the generation of superradiant lasing. This machine operates on forbidden transitions ${}^3P_0$ to ${}^1S_0$ in ultracold alkaline-earth atoms confined by a magic optical lattice.

After establishing a method for continuously injecting atoms into the upper state and ejecting ground state atoms from the bowtie cavity, We introduce two different models for stimulating the generated superradiant field by taking into account position-dependent shifts, collisional decoherence, light shifts, and atom loss. Finally, we estimate a laser linewidth of less than 100 mHz, limited by the fluctuation of the atomic flux, r, leading to an output power of several hundred fW.

Kurzfassung

Optische Uhren mit einer Genauigkeit auf dem Niveau von 10^{-19}, was einer Abweichung von nur einer Sekunde über das Alter des Universums entspricht, sind die präzisesten Uhren, die je gebaut wurden. Optische Uhren versprechen einen enormen Einfluss auf die Entwicklung von Quantentechnologien wie Atominterferometrie und Quantenmetrologie mit Anwendungen in der Telekommunikation, insbesondere bei der Netzwerksynchronisation und der präzisen Navigation durch 5G-Netze anstelle von GPS. Darüber hinaus könnten optische Uhren, die auf Satelliten betrieben werden, als Gravitationswellendetektoren genutzt werden und Experimente der Allgemeinen Relativitätstheorie ermöglichen. Weitere Anwendungen finden sich in der Geologie, Astronomie und der fundamentalen Physik.

Aktuelle optische Uhren sind *passive* Frequenzstandards. In diesen Systemen wird die Frequenz eines hochkohärenten Sondenlasers (Lokaler Oszillator) intermittierend mit der Frequenz einer schmalen und robusten *Uhrenübergangs* in gefangenen Atomen oder Ionen verglichen. Dieser Laser wird durch einen ultrastabilen makroskopischen Hohlraum (Schwungrad) vorstabilisiert, der die Frequenz zwischen den Abtastzyklen hält. Thermische und mechanische Schwankungen im lokalen Oszillator sind unter den Hauptfaktoren, die die Kurzzeitstabilität moderner optischer Uhren begrenzen. Sie bestimmen die Gesamtstabilität der Uhr vollständig in der Zeit, die kürzer ist als ein einzelner Abtastzyklus, und nutzen nicht das volle Potenzial eines Uhrenübergangs. Schließlich trägt die Abwärtskonvertierung des breitbandigen Laserfrequenzrauschens zur Messabweichung der Frequenzverschiebung bei, was als *Dick-Effekt* bekannt ist.

Um dieses Problem zu überwinden, könnte eine *aktive optische Uhr* auf Basis eines *superradianten Lasers* geschaffen werden, bei dem die Atome mit Populationsinversion auf dem Uhrenübergang an eine Resonatormode im *bad cavity regime* gekoppelt sind. Die Kavitätsmode eines solchen Lasers ist viel breiter als sein Verstärkungsprofil, und die Laserfrequenz ist von Natur aus unempfindlich gegenüber Schwankungen der Kavitätslänge, im Gegensatz zu gewöhnlichen Lasern mit guter Kavität.

Das Erreichen kontinuierlicher Superradianz unter Verwendung eines schmalen optischen Übergangs hat das Potenzial, die Kurzzeitstabilität der modernsten optischen Uhren zu verbessern. Obwohl gepulste superradiante Emissionen auf einem mHz-Linienbreiten-Uhrenübergang gezeigt wurden, hat sich der echte kontinuierliche Betrieb ohne Fourier-Beschränkung als extrem herausfordernd erwiesen. Dieses Problem wird durch das FET-

Flaggschiffprojekt iqClock und das europäische Innovative Training Network MoSaiQC, kurz für „Modular Systems for Advanced Integrated Quantum Clocks“, angegangen, an dem eine breite Palette akademischer und industrieller Einrichtungen beteiligt ist. An der TU Wien haben wir als theoretischer Partner die ultimativen Eigenschaften der aktiven optischen Uhren untersucht und Simulationen durchgeführt, um unsere experimentellen Partner bei der Entwicklung eines solchen Lasers zu unterstützen.

Wir stellen dann zwei verschiedene Modelle zur Anregung des erzeugten superradianten Feldes vor, indem wir positionsabhängige Verschiebungen, Kollisionsdekoherenz, Lichtverschiebungen und Atomverluste berücksichtigen. Schließlich schätzen wir eine Laserlinienbreite von weniger als 100 mHz, begrenzt durch Atomanzahlschwankungen, was zu einer Ausgangsleistung von mehreren hundert fW führt.

Diese Arbeit ist in zwei Hauptabschnitte unterteilt. Der erste Abschnitt führt die notwendigen Werkzeuge zum Studium des superradianten Lasers ein. Wir beginnen mit der Entwicklung eines Verständnisses der Quantenoptik und offener Quantensysteme. Anschließend vergleichen wir verschiedene Modelle zur Simulation des superradianten Lasers und schätzen die ultimative Stabilität ab, die mit einer aktiven optischen Uhr erreichbar ist.

Der zweite Abschnitt der Arbeit konzentriert sich auf die Realisierung eines superradianten Lasers. Insbesondere haben wir eine Machbarkeitsstudie für die Gestaltung und Simulation der kontinuierlichen hocheffizienten Kühlung, Beladung und Pumpen in den oberen Laserszustand innerhalb der Kavität für die superradiante mHz-Maschine an der Universität Amsterdam durchgeführt. Das Ziel ist es, einen hochflüssigen kontinuierlichen Strahl ultrakalter Strontiumatome mit einer Bowtie-Kavität für die Erzeugung von superradiantem Lasern zu kombinieren. Diese Maschine arbeitet auf verbotenen Übergängen ${}^3P_0$ zu ${}^1S_0$ in ultrakalten Alkalien-Erdatomen, die in einem magischen optischen Gitter eingeschlossen sind.

Nach der Etablierung einer Methode zur kontinuierlichen Injektion von Atomen in den oberen Zustand und dem Auswerfen von Grundzustandsatomen aus der Bowtie-Kavität stellen wir zwei verschiedene Modelle zur Anregung des erzeugten superradianten Feldes vor, indem wir positionsabhängige Verschiebungen, Kollisionsdekoherenz, Lichtverschiebungen und Atomverluste berücksichtigen. Schließlich schätzen wir eine Laserlinienbreite von weniger als 100 mHz, begrenzt durch die Schwankung des Atomflusses r, was zu einer Ausgangsleistung von mehreren hundert fW führt.

List of Figures

List of Tables

Preamble

This thesis is the culmination of research funded by the European Union's (EU) Horizon 2020 research and innovation program under Grant Agreement No. 860579 (MoSaiQc project) grant. While the collaborative efforts of the entire MoSaiQc collaboration contributed to the results presented here, my focus was primarily on the theoretical analysis associated with the realization of a superradiant laser.

I extend my gratitude to the EU Horizon grant for their financial support. This thesis stands as a testament to the collective dedication, collaboration, and exploration within the MoSaiQc community.

The plot 4.5 and the estimation of attainable stability 4.3 were provided by our collaborators from the Nicolaus Copernicus University's (Michal Zawada and Marcin Bober), as well as from PTB (Uwe Sterr). The figure C.1 was made by our collaborators at University of Amsterdam (Quantum gas group, lead by Florian Schreck). The design of the mHz machine, as described in chapter 5 and chapter 6, was the outcome of an ongoing collaborative effort with the Quantum gas group at University of Amsterdam. The experimental results in appendix C are also provided by them.

CHAPTER 1

Introduction

1.1 Background

Some of the most accurate measurements in all of physics are done by measuring frequency. It's actually a kind of unwritten rule. If you want to measure something precisely, make sure that you find a way that this quantity can be measured in a frequency measurement. Because frequencies that's what we can measure with synthesizers and clocks. So, therefore, the question, how precisely can you measure frequency, is a question that is actually relevant for all precision measurements .

- Prof. Wolfgang Ketterle

In 1945, Rabi, in a public Lecture, discussed the possibility of atomic clocks [1]. By 1955, an atomic clock based on a microwave transition in cesium was constructed, surpassing the best quartz clocks of that time in both accuracy and precision [2]. This advancement led to the redefinition of the second in 1967, based on the frequency between two atomic levels in cesium [1]. Since then, atomic clocks have significantly advanced in accuracy and precision. Currently, the optical clocks, with an accuracy of 6.6×10^{-19} level [3], corresponding to being off by only 1 second over the universe's age, are the most precise clocks.

Optical clocks promise a huge impact on the development of quantum technologies like atom interferometry and quantum metrology, with applications in telecommunication, specifically in network synchronization and accuracy navigation through 5G networks and GPS. Other than this, if optical clocks are operated on satellites, then they could be used for gravitational wave detectors [4], performing experiments of general relativity, or improving navigation systems. Further applications are in geology, astronomy, and measurement of fundamental constants [5].

Modern-day high-stability optical clocks are *passive* frequency standards, [3]. In state-of-the-art optical clock systems, the frequency of a highly coherent probe laser pre-stabilized to an ultra-stable optical cavity is intermittently compared with the frequency of a narrow and robust *clock transition* in a sample of trapped atoms (or ions). The measurement sequence includes an interrogation time, during which the phase of the laser is imprinted to the atomic sample, and a *dead time* used, for example, for preparation of atomic ensembles, when the laser pre-stabilized to an ultra-stable macroscopic cavity keeps the frequency, playing the role of a flywheel. Such a clock has demonstrated excellent stability at the level of 6.6×10^{-19} after 1 hour of averaging [3]; however, on shorter timescale, this stability is limited by thermal and mechanical fluctuations of the length of this ultra-stable cavity [6, 7]. They entirely determine the overall clock stability on time less than a single interrogation cycle, and they limit the interrogation time and inhibit exploitation of the full potential of a clock transition, given by its natural linewidth. Finally, down-conversion of the broad-band laser frequency noise contributes to the measurement error of the frequency offset, what is known as a *Dick effect* [8].

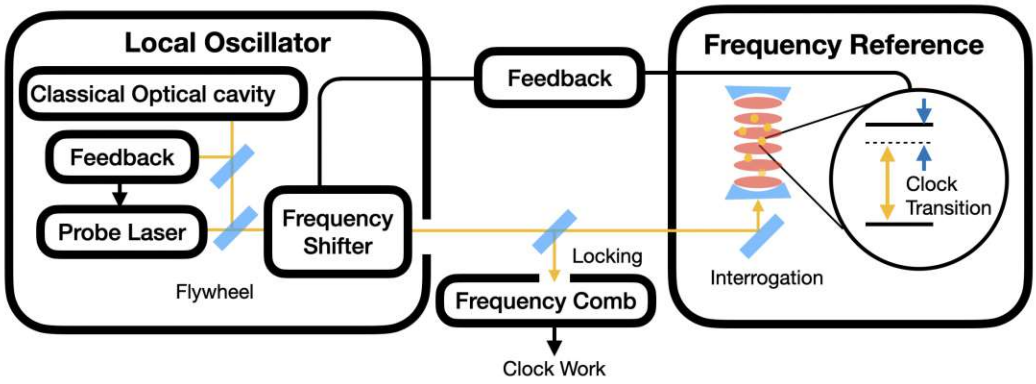

Figure 1.1: Schemetic diagram of a passive clock

This problem may be overcome with the help of an *active optical frequency standard* based on a laser operating deep in the bad-cavity regime [9, 10], where the linewidth of the cavity is much broader than the linewidth of the gain, see figure 1.3.

The gain of such a laser can be formed by forbidden transitions in alkaline-earth atoms, the same as used for passive optical lattice clocks. Similar to a hydrogen maser, the frequency of such a laser is determined by the frequency of lasing transition and is robust to fluctuations of the cavity length, which improves the stability on shorter timescales.

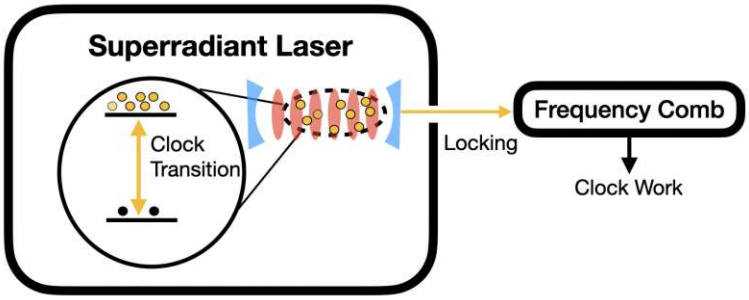

Figure 1.2: Schemetic diagram of an active optical clock

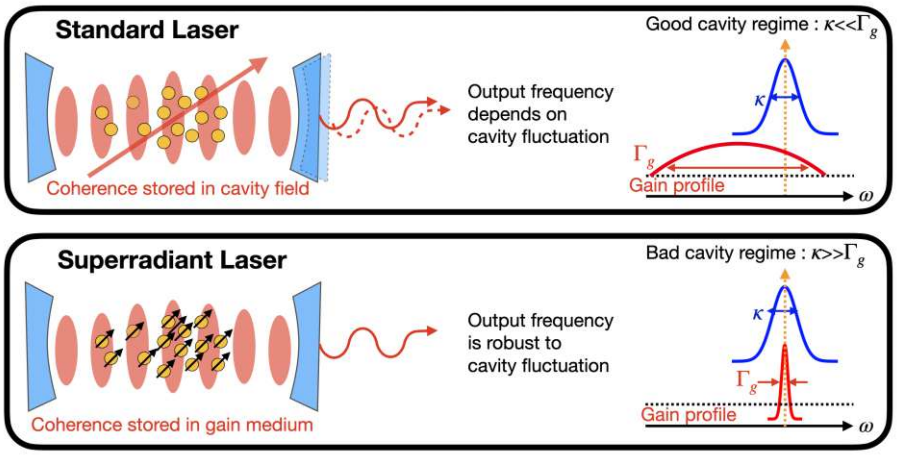

Figure 1.3: Schematic diagram comparing a good cavity and bad cavity laser

This thesis focuses on realizing such a superradiant laser and is structured in two main parts. The first part presents the tools required for studying the superradiant laser. It covers light-atom interaction and open quantum systems, compares models for simulating ultracold atom dynamics, and estimates the achievable stability of an active optical clock.

The second part addresses the superradiant laser's realization. It includes a feasibility study for continuous cooling, loading, and pumping schemes for a superradiant mHz machine operating on forbidden transitions in ultracold alkaline-earth atoms. Finally, simulations and optimizations are discussed to refine the continuous superradiant signal, with a model for the lasing process considering broadening, frequency shifts, and losses. In the next section, we provide a detailed overview of all the chapters.

1.2 Overview

Chapter 2 provides a comprehensive theoretical framework for understanding the intricate dynamics of open quantum systems. It begins with exploring classical electromagnetic fields within a cavity, setting the stage for subsequent discussions on atomic interaction

with the classical electromagnetic field and some atomic properties. Further, we describe the quantization of the electromagnetic field, specifically to understand atomic interactions with single cavity modes and collective atomic emission (*superradiance*). The chapter then delves into the theory of open quantum systems, introducing concepts such as the Lindbladian form of master equation and the quantum jump approach, employing Dyson expansion to develop tools such as Quantum Monte Carlo simulations, which is pivotal for analyzing open quantum systems. Additionally, the application of these theories is discussed in the context of Doppler cooling, showcasing a semi-classical Monte Carlo approach to efficiently simulate and understand the cooling mechanisms at play. This chapter lays a robust theoretical foundation for light-atom interaction, highlighting foundational principles and advanced computational techniques that we further use to study superradiant lasers.

In chapter 3, we study the master equation for cavity quantum electrodynamics to study the evolution of a light-atom system confined by a cavity. This approach is further extended by incorporating the Langevin equation to describe system dynamics in terms of drift and noise terms. In order to simplify complex computationally heavy quantum dynamics to manageable numerical forms, the chapter progresses to explore the c-number Langevin equation. Additionally, the chapter explores the 2nd order cumulant theory and uses two-time correlations and quantum regression theorem to calculate the linewidth. Then, we have discussed the full quantum description for a homogeneous system with and without adiabatic elimination of the cavity field. We highlight the applicability of each approach and make a comparative analysis of all the discussed methods for the simulation of a superradiant laser, offering insights into their respective advantages and limitations in practical scenarios.

In chapter 4 we investigate which short-term stability of an active optical clock can be achieved with optimized operational parameters depending on the number of active atoms and homogeneous and inhomogeneous broadening.[11]. We find that for short averaging times the stability is limited by photon shot noise from the limited emitted laser power and at long averaging times by phase diffusion of the laser output. Operational parameters for best long-term stability were identified. Using realistic numbers for an active clock based on ^{87}Sr, we find that an optimized stability of $\sigma_y(\tau) \approx 4 \times 10^{-18}/\sqrt{\tau[\mathrm{s}]}$ is achievable. As active optical frequency standards are not degraded by the Dick effect associated with dead time and noises of the local oscillator, they can outperform "traditional" passive optical frequency standards in stability or can play a role as local oscillators in future passive optical clocks. Even though their short-term stability is slightly worse than the quantum projection noise-limited stability of a passive optical clock with a comparable number of clock atoms, it can still be significantly superior to that of a high-quality cavity laser pre-stabilized to an ultra-stable cavity, which is employed in modern passive optical clocks.

Chapter 5 discusses the innovative approach and technological developments associated with the experimental setup of the superradiant laser machine at the University of Amsterdam. This chapter begins by detailing the implementation of a narrow linewidth

transition, emphasizing its significance in enhancing the precision of atomic measurements and control. Then, we proceed with an in-depth examination of the "Architecture of the Science Chamber," where the design and techniques employed for transporting, cooling, and loading atoms within the system are discussed. The chapter continues with a detailed presentation on the simulation of atom cooling processes and the loading of atoms into a moving optical lattice, highlighting the theoretical and practical considerations for achieving optimal conditions within the lattice. Lastly, pumping inside the moving optical lattice is introduced, illustrating the final steps in preparing the atomic ensemble for experiments. This section consolidates the comprehensive strategies and methodologies employed in the mHz machine to push the boundaries of what is achievable for realizing a superradiant signal.

Chapter 6 provides a detailed exploration of simulations related to superradiant signal in our mHz machine, utilizing the mean field theoretic approaches to understand and optimize the behavior of ^{88}Sr superradiant laser under various conditions. The section begins with a simulation of the superradiance signal, analyzing how the output power and the effect of cavity pulling vary as a function of the optical lattice velocity. This part of the simulation helps in understanding how the velocity of the optical lattice impacts the coherence and intensity of the superradiance observed. The chapter addresses the complexities of simulating lasing in the mHz machine, including factors such as collisional relaxation and frequency shifts due to high atomic fluxes. These simulations are crucial for predicting and mitigating potential issues in experimental setups, ensuring the stability and efficiency of the lasing process under different conditions. The "Results of Simulation" section consolidates the data obtained from the simulations, providing a detailed analysis of the outcomes and their implications for the operation of the mHz machine. This includes discussions on the optimal conditions for achieving stable lasing. Further, the chapter discusses simulations with full dephasing, where we include the losses due to collisions in an excited state, thus providing insights into the realistic, steady-state superradiant regime. Finally, the chapter presents an estimate of linewidth and the primary factors affecting it.

Finally, chapter 7 will give a conclusion of the presented material.

CHAPTER 2

Theoretical foundations

This chapter introduces the key principles of quantum optics and open quantum systems, as well as other essential theoretical concepts necessary for the simulation of superradiant lasers. In section 2.1, we consider atomic interaction with classical electromagnetic field and with quantized single-mode cavity field. Additionally, we discuss the theory of angular moment and derive expressions for atomic polarizability. section 2.2 provides a brief overview of the superradiance. In section 2.3 we study the theory of open quantum systems and derive the master equation, exploring the quantum jump approach and Dyson expansion. As an application, we calculate the force exerted on an atom by a laser, followed by a discussion of quantum Monte Carlo simulations of Doppler cooling. We then compare this approach with a more efficient semi-classical Monte Carlo simulation. Finally, we derive the Heisenberg-Langevin equations.

2.1 Atom-Light Interaction

Developing a bridge between classical electrodynamics and quantum optics is crucial for better insights. Specifically, we are interested in the interaction of atoms with light, and depending on what kind of system we are studying, which kind of interaction we are focused on, and which aspects of atom-field interaction we are interested in, we can consider the electromagnetic field either as a classical or as a quantized one, as well as some atomic degrees of freedom we treat as classical, and some as quantum ones [12].

2.1.1 Electromagnetic field in a cavity

Quantization of a field involves identifying the relevant dynamic variables, calculating the corresponding canonical momenta, and then imposing the commutation rules between

the two. We begin with Maxwell's equations in Gaussian units, without sources

$$\begin{aligned}\nabla \cdot \mathbf{E}(\mathbf{r},t) &= 0\\ \nabla \cdot \mathbf{B}(\mathbf{r},t) &= 0\\ \nabla \times \mathbf{E}(\mathbf{r},t) &= -\frac{1}{c}\frac{\partial \mathbf{B}(\mathbf{r},t)}{\partial t}\\ \nabla \times \mathbf{B}(\mathbf{r},t) &= \frac{1}{c}\frac{\partial \mathbf{E}(\mathbf{r},t)}{\partial t}\end{aligned} \tag{2.1}$$

from the equations (2.1) in Coloumb gauge ($\nabla \cdot \mathbf{A}(\mathbf{r},t) = 0$) magnetic and electric fields can be written as

$$\begin{aligned}\mathbf{B}(\mathbf{r},t) &= \nabla \times \mathbf{A}(\mathbf{r},t)\\ \mathbf{E}(\mathbf{r},t) &= -\frac{1}{c}\frac{\partial \mathbf{A}(\mathbf{r},t)}{\partial t}\end{aligned} \tag{2.2}$$

combining equations (2.2) we get the expression for vector potential

$$\nabla^2 \mathbf{A}(\mathbf{r},t) = \frac{1}{c^2}\frac{\partial^2 \mathbf{A}(\mathbf{r},t)}{\partial t^2} \tag{2.3}$$

The solution to equation (2.3) corresponding to a periodic boundary condition in a cubic quantization volume $V = L^3$ can be written as

$$\mathbf{A}(\mathbf{r},t) = \sum_{\mathbf{k},\lambda} \mathbf{e}_{\mathbf{k},\lambda}\left(A_{\mathbf{k},\lambda}e^{i(\mathbf{k}\cdot\mathbf{r}-\omega_k t)} + A^*_{\mathbf{k},\lambda}e^{i(\mathbf{k}\cdot\mathbf{r}-\omega_k t)}\right), \tag{2.4}$$

where

$$\mathbf{k} = \frac{2\pi}{L}\mathbf{n} \quad , \quad \mathbf{n} = (n_x, n_y, n_z) \quad , \quad n_i = 0, \pm 1, \pm 2, \pm 3...., \tag{2.5}$$

$\mathbf{e}_{\mathbf{k},\lambda}$ is a polarization vector of a mode $(\mathbf{k},\lambda)$, $\lambda = 1,2$ corresponds to one of 2 possible orientations of $\mathbf{e}_{\mathbf{k},\lambda}$ in the plane orthogonal to $\mathbf{k}$, ω_k is the frequency associated with the kth mode given by $\omega_k = c|\mathbf{k}|$ and c is the speed of light:

The electric and magnetic fields can be expressed from (2.4) and (2.2) as

$$\begin{aligned}\mathbf{E}(\mathbf{r},t) &= i\sum_{\mathbf{k},\lambda}\mathbf{e}_{\mathbf{k},\lambda}\omega_k\left(A_{\mathbf{k},\lambda}e^{i(\mathbf{k}\cdot\mathbf{r}-\omega_k t)} - A^*_{\mathbf{k},\lambda}e^{i(\mathbf{k}\cdot\mathbf{r}+\omega_k t)}\right),\\ \mathbf{B}(\mathbf{r},t) &= i\sum_{\mathbf{k},\lambda}(\mathbf{k}\times\mathbf{e}_{\mathbf{k},\lambda})\left(A_{\mathbf{k},\lambda}e^{i(\mathbf{k}\cdot\mathbf{r}-\omega_k t)} - A^*_{\mathbf{k},\lambda}e^{i(\mathbf{k}\cdot\mathbf{r}+\omega_k t)}\right),\end{aligned} \tag{2.6}$$

The total energy of the electromagnetic field

$$H = \frac{1}{8\pi}\int\left(|\mathbf{E}(\mathbf{r},t)|^2 + |\mathbf{B}(\mathbf{r},t)|^2\right)dV \tag{2.7}$$

using equation (2.6) we can represent this energy in terms of $A_{\mathbf{k},\lambda}$

$$H = \frac{V}{4\pi}\sum_{\mathbf{k},\lambda}\omega_k^2\frac{A_{\mathbf{k},\lambda}A^*_{\mathbf{k},\lambda} + A^*_{\mathbf{k},\lambda}A_{\mathbf{k},\lambda}}{2}, \tag{2.8}$$

redefining $A_{\mathbf{k},\lambda}$ in terms of $p_{\mathbf{k},\lambda}$ and $q_{\mathbf{k},\lambda}$ as

$$A_{\mathbf{k},\lambda} = \frac{1}{\omega_k}\sqrt{\frac{2\pi}{V}}(\omega_k q_{\mathbf{k},\lambda} + ip_{\mathbf{k},\lambda}), \quad A^*_{\mathbf{k},\lambda} = \frac{1}{\omega_k}\sqrt{\frac{2\pi}{V}}(\omega_k q_{\mathbf{k},\lambda} - ip_{\mathbf{k},\lambda}) \tag{2.9}$$

we can rewrite the total Hamiltonian as a sum of Hamiltonians of harmonic oscillators with unit masses and frequencies ω_k, described by coordinates $q_{\mathbf{k},\lambda}$ and associated canonical momenta $p_{\mathbf{k},\lambda}$.

$$H = \frac{1}{2}\sum_{\mathbf{k},\lambda}(p^2_{\mathbf{k},\lambda} + \omega_k^2 q^2_{\mathbf{k},\lambda}). \tag{2.10}$$

We have recognized the dynamical variable $q_{\mathbf{k},\lambda}$ and associated canonical momenta p_k. [13]. We can quantize the electromagnetic field by imposing the commutation relation $[\hat{\mathbf{q}}_{\mathbf{k},\lambda}, \hat{\mathbf{p}}_{\mathbf{k}',\lambda'}] = \mathbf{i}\hbar\delta_{\mathbf{k},\mathbf{k}'}\delta_{\lambda,\lambda'}$. But let us first consider atomic interaction with a classical electromagnetic field for a better understanding of the quantum nature of atoms.

2.1.2 Interaction of light with 2-level atom

Here, we consider the interaction of atoms with a classical electromagnetic field. Let's start our discussion with a simple model. Consider an atom interacting with a single monochromatic mode whose frequency ω is close to resonance with a transition between a pair of atomic states $\{|e\rangle, |g\rangle\}$. For now, we neglect all the other states. The Hamiltonian associated with such a system can be represented as

$$\begin{aligned}\hat{\mathcal{H}} &= \hat{\mathcal{H}}_A + \hat{\mathcal{H}}_{AF} \\ &= \hbar\omega_0 |e\rangle\langle e| - \hat{\mathbf{d}}\cdot\mathbf{E}(\mathbf{r},t)\end{aligned} \tag{2.11}$$

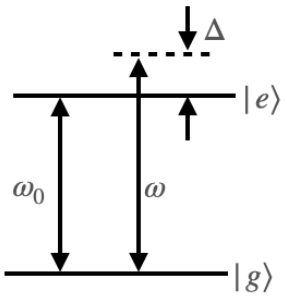

Figure 2.1: 2 level atom with energy gap ω_0 and electromagnetic field frequency ω and the difference $\Delta\omega = \omega - \omega_0$

where $\hat{\mathcal{H}}_A$ and $\hat{\mathcal{H}}_{AF}$ are free atomic Hamiltonian and the atomic-field interaction Hamiltonian, respectively, d is the atomic dipole operator, and $\mathbf{E}$ is the electric field given by (2.6).

The atomic dipole operator can be written as

$$\hat{\mathbf{d}} = \langle g| \hat{\mathbf{d}} |e\rangle (\hat{\sigma}_{ge} + \hat{\sigma}_{eg}) = \hat{\mathbf{d}}^{(+)} + \hat{\mathbf{d}}^{(-)}, \tag{2.12}$$

where operator $\hat{\sigma}_{ij} = |i\rangle \langle j|$ for $ij \in \{e, g\}$, and we used the fact that diagonal matrix elements $\langle g| \hat{\mathbf{d}} |g\rangle$ and $\langle e| \hat{\mathbf{d}} |e\rangle$ are both zero due to parity of the states $|g\rangle$ and $|e\rangle$. From equation (2.6) the electric field for a single mode can also be separated into two parts, $\mathbf{E}(\mathbf{r}, t) = E_0 \cos(\omega t)\mathbf{e} = \mathbf{E}^{(+)} e^{-i\omega t} + \mathbf{E}^{(-)} e^{i\omega t}$, and after substituting this expression and equation (2.12) into (2.11), the overall Hamiltonian can be written as

$$\begin{aligned} \hat{\mathcal{H}} &= \hbar\omega_0 \hat{\sigma}_{ee} - (\hat{\mathbf{d}}^{(+)} + \hat{\mathbf{d}}^{(-)}) \cdot (\mathbf{E}^{(+)} e^{-i\omega t} + \mathbf{E}^{(-)} e^{i\omega t}) \\ &= \hbar\omega_0 \hat{\sigma}_{ee} - \hat{\mathbf{d}}^{(+)} \mathbf{E}^{(+)} e^{-i\omega t} - \hat{\mathbf{d}}^{(+)} \mathbf{E}^{(-)} e^{i\omega t} - \hat{\mathbf{d}}^{(-)} \mathbf{E}^{(+)} e^{-i\omega t} - \hat{\mathbf{d}}^{(-)} \mathbf{E}^{(-)} e^{i\omega t} \\ &= \hbar\omega_0 \hat{\sigma}_{ee} - \hbar(\Omega_1^* e^{-i\omega t} + \Omega^* e^{i\omega t}) \hat{\sigma}_{ge} - \hbar(\Omega e^{-i\omega t} + \Omega_1 e^{i\omega t}) \hat{\sigma}_{eg} \end{aligned} \tag{2.13}$$

where $\Omega = \frac{\langle g|\mathbf{e}\cdot\hat{\mathbf{d}}|e\rangle E_0}{2\hbar}$ is the well-known Rabi frequency and $\Omega_1 = -\frac{\langle g|\mathbf{e}^*\cdot\hat{\mathbf{d}}|e\rangle E_0}{2\hbar}$ is the counter rotating frequency. In the interaction picture, our Hamiltonian looks like

$$\hat{\mathcal{H}}_I = -\hbar(\Omega_1^* e^{-i\Delta t} + \Omega^* e^{i(\omega_0+\omega)t}) \hat{\sigma}_{ge} - \hbar(\Omega e^{-i\Delta t} + \Omega_1 e^{i(\omega_0+\omega)t}) \hat{\sigma}_{eg} \tag{2.14}$$

Assuming near resonance only terms with $e^{-i\Delta t}$ will contribute this is called Rotating wave approximation, transforming back to the Schrödinger picture we get

$$\hat{\mathcal{H}} = \hbar\omega_0 \hat{\sigma}_{ee} - \hbar(\Omega^* \hat{\sigma}_{ge} e^{i\omega t} + \Omega \hat{\sigma}_{eg} e^{-i\omega t}) \tag{2.15}$$

For a a state $|\psi\rangle = c_g |g\rangle + c_e |e\rangle$ using the *Schrödinger Equation*

$$i\hbar \partial_t |\psi\rangle = \hat{\mathcal{H}} |\psi\rangle \tag{2.16}$$

we can calculate how the probability coefficients c_e and c_g associated with excited and ground state evolves in time.

$$\partial_t c_g = i\Omega^* c_e e^{i\omega t} \quad \partial_t c_e = -i\omega_0 c_e + i\Omega c_g e^{-i\omega t} \tag{2.17}$$

These are the basics of how the internal state of a simple 2-level atom changes when influenced by a classical electromagnetic field. However, in actuality, we must also account for the quantum mechanical internal state of the atom, a task we will undertake in the subsequent section.

2.1.3 Angular moment

Angular moment in quantum mechanics is not just an extension of its classical counterpart but an intrinsic property of a particle characterized by discrete quantization. angular

moment follows specific commutation relations, leading to discrete eigenvalues. The understanding of angular moment is important for description of atomic and molecular structures, the classification of subatomic particles, and for the principles governing their interactions and dynamics.

We start our discussion with orbital angular moment defined in units of $\hbar$, which has a classical counterpart and is defined by

$$\hat{\mathbf{L}} = \hbar^{-1}(\hat{\mathbf{r}} \times \hat{\mathbf{p}}) \tag{2.18}$$

Where $\hat{r}$ and $\hat{p}$ are positions and momentum operators of a particle, and they follow the commutation relation

$$[\hat{r}_i, \hat{p}_j] = i\hbar\delta_{ij} \tag{2.19}$$

Using equations (2.19) and (2.18), we get the commutation relations for the Cartesian components of the orbital angular moment operator

$$[\hat{L}_i, \hat{L}_j] = i\sum_{ij,k} \varepsilon_{i,j,k}\hat{L}_k \tag{2.20}$$

where indices $i, j, k \in \{1, 2, 3\}$ corresponding to x, y, z, and $\varepsilon_{i,j,k}$ is the Levi-Civita symbol. The square of orbital angular moment $\hat{L}^2 = \hat{L}_x^2 + \hat{L}_y^2 + \hat{L}_z^2$ commutes with each of its components, partially,

$$[\hat{L}^2, \hat{L}_z] = 0 \tag{2.21}$$

Therefore, $\hat{L}^2$ and $\hat{L}_z$ have common eigenstates, assuming it to be $|am\rangle$ such that

$$\begin{aligned} \hat{L}^2 |am\rangle &= a |am\rangle \\ \hat{L}_z |am\rangle &= m |am\rangle \end{aligned} \tag{2.22}$$

we can define the ladder operators for angular moment

$$\hat{L}_\pm = \hat{L}_x \pm i\hat{L}_y \tag{2.23}$$

the commutation relation between $\hat{L}_z$, $\hat{L}^2$ and $\hat{L}_\pm$ can be easily derived using the relation 2.20

$$\begin{aligned} [\hat{L}_z, \hat{L}_\pm] &= \pm\hat{L}_\pm \\ [\hat{L}^2, \hat{L}_\pm] &= 0 \end{aligned} \tag{2.24}$$

Using the above commutation relation one can calculate the eigenvlaues of $\hat{L}_\pm$

$$\begin{aligned} \hat{L}_z\hat{L}_\pm |am\rangle &= (\hat{L}_\pm\hat{L}_z \pm \hat{L}_\pm) |am\rangle \\ &= (\hat{L}_\pm m \pm \hat{L}_\pm) |am\rangle \\ &= (m \pm 1)\hat{L}_\pm |am\rangle \end{aligned} \tag{2.25}$$

and

$$\hat{L}^2\hat{L}_\pm |am\rangle = \hat{L}_\pm\hat{L}^2 |am\rangle = a\hat{L}_\pm |am\rangle \tag{2.26}$$

So, we can conclude that the effect of $\hat{L}_\pm$ on state $|am\rangle$ is raising or lowering the eigenvalue of $\hat{L}_z$, without affecting the eigenvalue of $\hat{L}^2$, and we can write the associated eigenvalue as a function of a and m

$$\hat{L}_\pm |am\rangle = c_\pm(a,m) |a, m\pm\rangle \tag{2.27}$$

but this suggests that given a state $|am\rangle$, there exist all the states $|a, m \pm n\rangle$ for all non negative integer values of n but there is a bound on n as $a \geq m^2$ for any value of m. for the maximum m we have $\hat{L}_+ |lm_{\max}\rangle = 0$ and using $\hat{L}_-\hat{L}_+ = \hat{L}^2 - \hat{L}_z^2 - \hat{L}_z$, we get

$$\begin{aligned} \hat{L}^2 - \hat{L}_z^2 - \hat{L}_z |lm_{\max}\rangle &= 0 \\ a - m_{\max}^2 - m_{\max} &= 0 \\ a &= m_{\max}(m_{\max}+1) \end{aligned} \tag{2.28}$$

similarly for $m_{\min}$, we get $a = m_{\min}(m_{\min}-1)$, comparing it $m_{\max}$ we get $m_{\max} = -m_{\min}$. Going from $|lm_{\min}\rangle$ to $|am_{\max}\rangle$ we have total $2l$ steps of one. We can write $a = l(l+1)$ and the eigen value associated with $\hat{L}_z$ takes values from $-l$ to l with integer step.

$$\begin{aligned} \hat{L}^2 |lm\rangle &= l(l+1) |lm\rangle \\ \hat{L}_z |lm\rangle &= m |lm\rangle \end{aligned} \tag{2.29}$$

Note that the values of l and m must be integer for orbital momentum, whereas for internal momentum of elementary particles (spin) they may accept also half-integer values. using equation (2.29), similar to 2 level atom. Now using equation (2.27) we can write

$$\begin{aligned} \langle lm| \hat{L}_-\hat{L}_+ |lm\rangle &= |c_+|^2 \\ \langle lm| (\hat{L}^2 - \hat{L}_z^2 - \hat{L}_z) |lm\rangle &= |c_+|^2 \end{aligned} \tag{2.30}$$

resulting in

$$\hat{L}_\pm |l, m\rangle = \sqrt{(l \pm m + 1)(l \mp m)}\, |l, m \pm 1\rangle \tag{2.31}$$

The common eigenfunction $Y_{l,m}$ of $\hat{L}^2$ and $\hat{L}_z$, corresponding to quantum numbers l, m are called s*pherical harmonics*. In polar coordinates they have the form

$$Y_{l,m}(\theta,\phi) = (-1)^{m+|m|} i^l \sqrt{\frac{2l+1}{4\pi}\frac{(l-|m|)!}{(l+|m|)!}} P_l^{|m|}(\cos\theta) e^{im\phi}, \tag{2.32}$$

where

$$P_l^{|m|}(\cos\theta) = \frac{1}{2^l l!} \sin^{|m|}\theta \frac{d^{|m|+l}}{(d\cos\theta)^{|m|+l}} (\cos^2\theta - 1)^l \tag{2.33}$$

is the associated Legendre polynomial. $Y_{l,m}$ forms a complete set of basis and follows the orthonormality relation given by

$$\int_0^{\pi}\int_0^{2\pi} Y^*_{l,m}(\theta,\phi)Y_{l',m'}(\theta,\phi)\,\sin\theta\,d\theta\,d\phi = \delta_{ll'}\delta_{mm'} \tag{2.34}$$

The orbital angular moment operator concerns the motional degree of freedom of particles in spherically-symmetric potential, and can be understood as quantized classical angular moment. Each of the operators defined above corresponds to its classical analog. However, spin angular moment is a purely quantum mechanical concept without any classical counterpart, representing an intrinsic form of angular moment possessed by particles. The theoretical concept of spin originates from two fundamental principles of physics depending on whether the state of the particle is symmetric or anti-symmetric and its access to the number of space-time dimensions. This is beyond the scope of our discussion, but for more details, please refer to [14]

The spin angular moment is designated by S. For spin 1/2 fermions, spin operator components are defined in terms of Pauli matrices.

$$\hat{\sigma}_x = \begin{bmatrix} 0 & 1 \\ 1 & 0 \end{bmatrix} \quad \hat{\sigma}_y = \begin{bmatrix} 0 & -i \\ i & 0 \end{bmatrix} \quad \hat{\sigma}_z = \begin{bmatrix} 1 & 0 \\ 0 & -1 \end{bmatrix} \tag{2.35}$$

as $\hat{S}_i = \frac{1}{2}\hat{\sigma}_i$. Pauli matrices also follow the similar commutational rules as orbital angular moment

$$[\hat{\sigma}_i, \hat{\sigma}_j] = 2i\hbar\hat{\sigma}_k \tag{2.36}$$

We can define a total angular moment by combining both orbital and spin angular moment.

$$\begin{aligned} \hat{\mathbf{J}} &= \hat{\mathbf{L}} + \hat{\mathbf{S}} \\ [\hat{J}_i, \hat{J}_j] &= i\hbar\hat{J}_k \end{aligned} \tag{2.37}$$

where $(i,j,k) = (x,y,z)$ and components of J follows

$$\begin{aligned} \hat{J}^2 &= \hat{J}_x^2 + \hat{J}_y^2 + \hat{J}_z^2 \\ [\hat{J}^2, \hat{J}_z] &= 0 \end{aligned} \tag{2.38}$$

Again we can define two ladder operators $\hat{J}_\pm = \hat{J}_x \pm \hat{J}_y$ which follow the commutation relation

$$\begin{aligned} [\hat{J}^2, \hat{J}_\pm] &= 0 \\ [\hat{J}_z, \hat{J}_\pm] &= \pm\hat{J}_\pm \end{aligned} \tag{2.39}$$

similar to $\hat{\mathbf{L}}$, we can define simultaneous eigenstates for $\hat{J}^2$ and $\hat{J}_z$

$$\begin{aligned} \hat{J}^2\,|j,m\rangle &= j(j+1)\,|j,m\rangle \\ \hat{J}_z\,|j,m\rangle &= m\,|j,m\rangle \end{aligned} \tag{2.40}$$

from there, we can get

$$\hat{J}_{\pm} |j, m\rangle = \sqrt{(j \pm m + 1)(j \mp m)} \, |j, m \pm 1\rangle \tag{2.41}$$

The total angular moment follows the selection rules for the transitions among quantum states due to angular moment conservation. However, as we increase the number of particles in our system, the complexity associated with total angular moment increases because of degeneracy and whatnot. To find the eigenstates of the sum of two angular momenta in terms of products of the individual angular moment eigenstates, we will use **Clebsch-Gordan Coefficients**. Consider a system which consist of 2 subsystems with angular momenta j_1 and j_2. The total angular moment of the system can

$$|j, m\rangle = \sum_{m_1, m_2} C(j_1, j_2, j; m_1, m_2, m) \, |j_1, m_1\rangle \, |j_2, m_2\rangle \tag{2.42}$$

The coefficient $C(j_1, j_2, j; m_1, m_2, m)$ are called Clebsch-Gordan Coefficients, and they follow the orthogonality condition given by

$$\sum_{m_1, m_2} C(j_1, j_2, j'; m_1, m_2, m') C(j_1, j_2, j; m_1, m_2, m) = \delta_{jj'} \delta_{mm'} \tag{2.43}$$

Some properties of Clebsch-Gordan Coefficients that we will be using for further analysis

$$\begin{aligned}
&C(j_1, j_2, j; -m_1, -m_2, -m) = (-1)^{j_1 + j_2 - j} C(j_1, j_2, j; m_1, m_2, m) \\
&C(j_1, j, j_2; m_1, -m, -m_2) = (-1)^{j_1 - m_1} \frac{2j_2 + 1}{2j + 1} C(j_1, j_2, j; m_1, m_2, m) \\
&C(j_1, j_2, j_1 + j_2; m_1, m_2, m_1 + m_2) = \\
&\sqrt{\frac{(2j_1)!(2j_2)!(j_1 + j_2 + m_1 + m_2)!(j_1 + j_2 - m_1 - m_2)!}{(2j_1 + 2j_2)!(j_2 + m_2)!(j_1 - m_1)!(j_1 + m_1)!(j_2 - m_2)!}} \\
&C(j_1, j_2, j; j_1, m - j_1, m) = \\
&\sqrt{\frac{(2j + 1)!(2j_1)!(j_2 - j_1 + j)!(j_1 + j_2 - m)!(j + m)!}{(j_1 + j_2 - j)!(j_1 - j_2 + j)!(j_1 + j_2 + j + 1)!(j_2 - j_1 + m)!(j - m)!}}
\end{aligned} \tag{2.44}$$

For more rules and properties associated with Clebsch-Gordan Coefficients, please refer to [12].

Another way of defining Clebsch-Gordan Coefficients is the **Wigner 3j Symbols**. Instead of representing the addition of two angular momenta in terms of a third, the 3-j symbols are the coefficients associated with three angular momenta, which add up to zero resultant.

$$\sum_{m_1 = -j_1}^{j_1} \sum_{m_2 = -j_2}^{j_2} \sum_{m_3 = -j_3}^{j_3} |j_1, m_1\rangle \, |j_2, m_2\rangle \, |j_3, m_3\rangle \begin{pmatrix} j_1 & j_2 & j_3 \\ m_1 & m_2 & m_3 \end{pmatrix} = |0, 0\rangle \tag{2.45}$$

The relation between Clebsch-Gordan Coefficients and the 3j symbol looks like

$$\begin{pmatrix} j_1 & j_2 & j_3 \\ m_1 & m_2 & m_3 \end{pmatrix} = \frac{(-1)^{j_1-j_2-m_3}}{\sqrt{2j_3+1}} C(j_1, j_2, j_3; m_1, m_2, -m_3) \tag{2.46}$$

For more symmetry properties, consider reference [12]. Matrix elements of irreducible tensor operators between angular moment states can be evaluated using the **Wigner-Eckart theorem**

$$\langle j_1, m_1 | \hat{T}^k_q | j_2, m_2 \rangle = (-1)^{j_1-m_1} \begin{pmatrix} j_1 & j_2 & k \\ m_1 & m_2 & q \end{pmatrix} \langle j_1 | | \hat{T}^k | | j_2 \rangle \tag{2.47}$$

where T^k_q is the irreducible tensor operator of rank k and $\langle j_1 | | \hat{T}^k | | j_2 \rangle$ is called reduced matrix element. Specifically, we are interested in the matrix elements of the irreducible operator, which will be used to calculate polarizability.

$$C^k_q = \sqrt{\frac{4\pi}{2k+1}} Y_{k,q}(\theta, \phi) \tag{2.48}$$

represented by

$$\langle l_1 | | \hat{C}^k | | l_2 \rangle = (-1)^{l_1} \sqrt{(2l_1+1)(2l_2+1)} \begin{pmatrix} l_1 & k & l_2 \\ 0 & 0 & 0 \end{pmatrix} \tag{2.49}$$

For detailed derivation, refer to [12].

2.1.4 Polarizability

In section 2.1.2, we have considered a 2-level atom interacting with a classical electromagnetic field. Now, let's consider the interaction of an N-level with the classical electromagnetic field. When an external electric field is applied, it perturbs the system's Hamiltonian, leading to shifts in the energy levels and modifications of the wave functions. These shifts can be calculated using the perturbation theory [15]. The first and the second order shift in the energy levels because of $-\hat{\mathbf{d}} \cdot \mathbf{E}$ for the i'th level looks like

$$\Delta^{(1)}_i = - \langle i | \hat{\mathbf{d}} \cdot \mathbf{E} | i \rangle = 0 \tag{2.50}$$

$$\Delta^{(2)}_i = -\frac{E_0^2}{4\hbar^2} \sum_{\mathbf{j}} \left(\frac{| \langle i | \mathbf{e} \cdot \hat{\mathbf{d}} | j \rangle |^2}{\omega_j + \omega_i} + \frac{| \langle j | \mathbf{e}^* \cdot \hat{\mathbf{d}} | j \rangle |^2}{\omega_j - \omega_i} \right) \tag{2.51}$$

$$\Delta_i = \Delta^{(1)}_i + \Delta^{(2)}_i = -\alpha_i \frac{E_0^2}{4\hbar} \tag{2.52}$$

where α being polarizability

$$\alpha_i = \frac{1}{\hbar} \sum_{\mathbf{j}} \left(\frac{| \langle i | \mathbf{e} \cdot \hat{\mathbf{d}} | j \rangle |^2}{\omega_j + \omega_i} + \frac{| \langle j | \mathbf{e}^* \cdot \hat{\mathbf{d}} | j \rangle |^2}{\omega_j - \omega_i} \right) \tag{2.53}$$

Before we proceed with calculation of polarizibility it's convenient to define cyclic coordinates which we will use to represent the electric field.

$$\mathbf{e}_1 = -\frac{\mathbf{e}_x + i\mathbf{e}_y}{\sqrt{2}}, \quad \mathbf{e}_0 = \mathbf{e}_z, \quad \mathbf{e}_{-1} = \frac{\mathbf{e}_x - i\mathbf{e}_y}{\sqrt{2}} \tag{2.54}$$

with $\mathbf{e}_0$ being the propagation direction of the electromagnetic field and $\mathbf{e}_1$ and $\mathbf{e}_{-1}$ being representing the right circularly and left circularly polarized light. The associated contra-varient vectors look like

$$\mathbf{e}^1 = -\frac{\mathbf{e}_x - i\mathbf{e}_y}{\sqrt{2}}, \quad \mathbf{e}^0 = \mathbf{e}_z, \quad \mathbf{e}^{-1} = \frac{\mathbf{e}_x + i\mathbf{e}_y}{\sqrt{2}} \tag{2.55}$$

Any unit vector in terms of these cyclic vectors will look like

$$\mathbf{e} = \sqrt{\frac{4\pi}{3}} \sum_{\mu=-1}^{1} Y^*_{1,\mu}(\theta, \phi)\mathbf{e}^\mu \tag{2.56}$$

To calculate the polarizability and shifts associated with different transitions, first we need to calculate the matrix element $|\langle i|\, \mathbf{e}\cdot\hat{\mathbf{d}}\, |k\rangle$. Lets assume states $|i\rangle = |nLSJFm\rangle$. Where $\tilde{\mathbf{n}} = n, S, J, L$, n are atomic quantum numbers, S is spin angular moment, L is orbital angular moment, J is total angular moment, I is the total momentum of the nucleus, F is total momentum and m is the projection of total momentum along quantization axis. Decay rate in terms of matrix elements

$$\begin{aligned} \gamma_{fi} &= \frac{4\omega^3}{3\hbar c^3}|\hat{d}_{fi}|^2 \\ \hat{d}_{fi} &= \sum_q e_q \langle f|\, \hat{d}^1_q\, |i\rangle \end{aligned} \tag{2.57}$$

and $|i\rangle = |n'L'S'J'F'm'\rangle$. Using the Wigner-Eckart theorem, we can write

$$\begin{aligned} \langle f|\, \hat{d}^1_q\, |i\rangle &= \langle n'L'J'I'F'm'|\, \hat{d}^1_q\, |nLJIFm\rangle \\ &= (-1)^{F'+J+I-1}\sqrt{2F'+1}C(1, F', F; q, m', m) \begin{pmatrix} J' & I & F' \\ F & I & J \end{pmatrix} \langle n'L'J'|\, |\hat{d}^1|\, |nLJ\rangle \end{aligned} \tag{2.58}$$

Now let us express $\langle n'L'J'I'F'm'|\, \hat{d}^1_q\, |nLJIFm\rangle$ via decay rate of ith state to all the hyperfine sublevels of some state with given n', J', L'.

$$\begin{aligned} \gamma_{all\{nf\}} &= \frac{4\omega^3}{3\hbar c^3}\sum_f |\hat{d}_{fi}|^2 = \frac{4\omega^3}{3\hbar c^3}\sum_{q,m,F} |\, \langle n'L'J'I'F'm'|\, \hat{d}^1_q\, |nLJIFm\rangle\, |^2 \\ &= \frac{4\omega^3}{3\hbar c^3}\sum_{q,m,F} (2F'+1)C(1, F', F; q, m', m)^2 \begin{pmatrix} J' & I & F' \\ F & I & J \end{pmatrix}^2 |\, \langle n'L'J'|\, |\hat{d}^1|\, |nLJ\rangle\, |^2 \end{aligned} \tag{2.59}$$

using the identities

$$\sum_{q,m} C(1,F',F;q,m',m)^2 = \frac{2F+1}{2F'+1} \quad , \quad \sum_F (2F+1)\begin{pmatrix} J' & I & F' \\ F & I & J \end{pmatrix}^2 = \frac{1}{2J'+1} \tag{2.60}$$

we get

$$\gamma_{all\{nf\}} = \frac{4\omega^3}{3\hbar c^3}\frac{\langle n'L'J'|\,|\hat{d}^1|\,|nLJ\rangle\,|^2}{2J'+1} \tag{2.61}$$

where

$$\langle n'L'J'|\,|\hat{d}^1|\,|nLJ\rangle\,|^2 = \sqrt{\frac{3\hbar c^3\gamma_{all\{fi\}}(2J+1)}{4|\omega_{ki}|^3}} \tag{2.62}$$

Now polarizability associated with E_1 transition for n, L, J, I, F, m hyperfine state is given by

$$\begin{aligned}\alpha_i^{E_1} = -\frac{1}{\hbar}\sum_{\mathbf{k}}\Bigg(&\frac{\sum_{F',m'}|\,\langle n'L'J'I'F'm'|\,\mathbf{e}\cdot\hat{\mathbf{d}}\,|nLJIFm\rangle\,|^2}{\omega_k+\omega_i} \\ &+\frac{\sum_{F',m'}|\,\langle n'L'J'I'F'm'|\,\mathbf{e}^*\cdot\hat{\mathbf{d}}\,|nLJIFm\rangle\,|^2}{\omega_k-\omega_i}\Bigg)\end{aligned} \tag{2.63}$$

$$\alpha_i^{E_1} = -\frac{1}{\hbar}\sum_{\mu\nu}\epsilon^\mu\epsilon^{\nu*}\sum_{\mathbf{k}}\left(\frac{\langle i|\,\hat{d}^1_\mu\,|k\rangle\,\langle k|\,\hat{d}^1_\nu\,|i\rangle}{\omega_k+\omega_i}+\frac{\langle i|\,\hat{d}^1_\nu\,|k\rangle\,\langle k|\,\hat{d}^1_\mu\,|i\rangle}{\omega_k-\omega_i}\right) \tag{2.64}$$

where states i and k are $|i\rangle = |nSLJFm\rangle = |\mathbf{n}Fm\rangle$ and $|k\rangle = |n'S'L'J'F'm'\rangle = |\mathbf{n}'F'm'\rangle$ with $\mathbf{n} = n, S, J, L$. Now we are in a position to define polarizability tensor

$$\mathbf{T}_{\mu\nu} = \sum_{m'}\langle \mathbf{n}Fm|\,\hat{d}^1_\mu\,|\mathbf{n}'F'm'\rangle\,\langle \mathbf{n}'F'm'|\,\hat{d}^1_\nu\,|\mathbf{n}Fm\rangle \tag{2.65}$$

defining $T_{Jq} = \sum_{\mu,\nu} C(1,\mu,J;1,\nu,q)\mathbf{T}_{\mu\nu}$ and $\epsilon_{Jq} = \sum_{\mu,\nu} C(1,\mu,J;1,\nu,q)\epsilon^\mu\epsilon^{\nu*}$ and using the Clebash Gordan identity $C(1,\mu,J;1,\nu,q) = (-1)^{-J}C(1,\nu,J;1,\mu,q)$ we get

$$\epsilon^\mu\epsilon^{\nu*}\mathbf{T}_{\mu\nu} = \sum_{J,q}(-1)^q T_{Jq}\epsilon_{J,-q} \tag{2.66}$$

Polarizability in terms of polarizability tensor

$$\alpha_i^{E_1} = -\frac{1}{\hbar}\sum_{\mathbf{n'F'}}\sum_{Jq}\left(\frac{\epsilon_{Jq}T_{J-q}(-1)^q}{\omega_k+\omega_i}+\frac{\epsilon_{Jq}T_{J-q}(-1)^{J-q}}{\omega_k-\omega_i}\right) \tag{2.67}$$

For electronic transition $T_{Jq} \neq 0$ and $q = 0$ we get

$$\alpha_i^{E_1} = -\frac{1}{\hbar}\sum_{\mathbf{n'F'}}\sum_{J}\epsilon_{J0}T_{J0}\left(\frac{\omega_k-\omega_i+(-1)^J(\omega_k+\omega_i)}{\omega_k^2-\omega_i^2}\right) \tag{2.68}$$

$$\epsilon_{00} = -\frac{1}{\sqrt{3}}, \quad \epsilon_{10} = -\frac{i(\epsilon^* \times \epsilon)_z}{\sqrt{2}}, \quad \epsilon_{20} = -\frac{(3\epsilon_z^* \epsilon_z - 1)}{\sqrt{6}} \tag{2.69}$$

Now, the polarizability can be written in terms of 3 tensor components

$$\alpha_i^{E_1} = \alpha_i^{(0)} + \frac{im(\epsilon^* \times \epsilon)_z}{\sqrt{F}} \cdot \alpha_i^{(1)} + \frac{(3\epsilon_z^* \epsilon_z - 1)(3m^2 - F(F+1))}{\sqrt{2F(2F-1)}} \alpha_i^{(2)} \tag{2.70}$$

where scalar, vector, and tensor polarizabilities are given by

$$\begin{aligned}
\alpha_i^{(0)} &= \beta_0 \sum_{\mathbf{n'F'}} |\langle \mathbf{n}Fm| |\hat{d}| |\mathbf{n'}F'm'\rangle|^2 \frac{2\omega_{n'F',i}}{\omega_{n'F',i}^2 - \omega^2} \\
\alpha_i^{(1)} &= \beta_1 \sum_{\mathbf{n'F'}} |\langle \mathbf{n}Fm| |\hat{d}| |\mathbf{n'}F'm'\rangle|^2 \frac{\omega}{\omega_{n'F',i}^2 - \omega^2} (-1)^{F+F'} \begin{pmatrix} 1 & 1 & 1 \\ F & F & F' \end{pmatrix} \\
\alpha_i^{(2)} &= \beta_2 \sum_{\mathbf{n'F'}} |\langle \mathbf{n}Fm| |\hat{d}^1| |\mathbf{n'}F'm'\rangle|^2 \frac{\omega_{n'F',i}}{\omega_{n'F',i}^2 - \omega^2} (-1)^{F+F'} \begin{pmatrix} 1 & 1 & 2 \\ F & F & F' \end{pmatrix}
\end{aligned} \tag{2.71}$$

with

$$\beta_0 = \frac{1}{3\hbar(2F+1)}, \quad \beta_1 = \frac{\sqrt{6F}}{\hbar\sqrt{(2F+1)(F+1)}}, \quad \beta_2 = \frac{1}{\hbar}\sqrt{\frac{40F(2F-1)}{(2F+3)(2F+1)(F+1)}} \tag{2.72}$$

when we take the sum over F', we get

$$\begin{aligned}
\alpha_i^{(0)} &= \beta_0 \sum_{n'L'J'} |\langle nLJ| |\hat{d}| |n'L'J'\rangle|^2 \frac{2\omega_{n'J',i}}{\omega_{n'J',i}^2 - \omega^2} G^{(0)}(IJ'; JF) \\
\alpha_i^{(1)} &= \beta_1 \sum_{n'L'J'} |\langle nLJ| |\hat{d}| |n'L'J'\rangle|^2 \frac{\omega}{\omega_{n'J',i}^2 - \omega^2} G^{(1)}(IJ'; JF) \\
\alpha_i^{(2)} &= \beta_2 \sum_{n'L'J'} |\langle nLJ| |\hat{d}^1| |n'L'J'\rangle|^2 \frac{\omega_{n'J',i}}{\omega_{n'J',i}^2 - \omega^2} G^{(2)}(IJ'; JF)
\end{aligned} \tag{2.73}$$

where

$$\begin{aligned}
G^{(0)}(IJ'; JF) &= (2F+1) \sum_{F'=|J'-I|}^{J'+I} (2F'+1) \begin{pmatrix} J & I & F \\ F' & 1 & J' \end{pmatrix}^2 \\
G^{(1)}(IJ'; JF) &= (2F+1) \sum_{F'=|J'-I|}^{J'+I} (2F'+1) \begin{pmatrix} J & I & F \\ F' & 1 & J' \end{pmatrix}^2 (-1)^{F+F'+1} \begin{pmatrix} 1 & 1 & 1 \\ F & F & F' \end{pmatrix} \\
G^{(2)}(IJ'; JF) &= (2F+1) \sum_{F'=|J'-I|}^{J'+I} (2F'+1) \begin{pmatrix} J & I & F \\ F' & 1 & J' \end{pmatrix}^2 (-1)^{F+F'} \begin{pmatrix} 1 & 1 & 2 \\ F & F & F' \end{pmatrix}
\end{aligned} \tag{2.74}$$

we will use the above expression in further chapters to calculate polarizability and shifts associated with different electronic transitions.

2.1.5 Quantization of Electromagnetic field

To treat light-atom interaction fully quantum mechanically, we will now quantize the electromagnetic field. We start with the canonical form of the electromagnetic field as defined in (2.11), and we will replace classical canonical variables with an analogous quantum mechanical operator as described in section 2.1.1.

The Hamiltonian for the quantum electromagnetic field will look like

$$\hat{\mathcal{H}}_F = \frac{1}{2}\sum_{\mathbf{k},\lambda}(\hat{p}^2_{\mathbf{k},\lambda} + \omega_{\mathbf{k}}, \hat{q}^2_{\mathbf{k},\lambda}) \tag{2.75}$$

These $\hat{p}_{\mathbf{k},\lambda}$ and $\hat{q}_{\mathbf{k},\lambda}$ follows commutation relation

$$[\hat{q}_{\mathbf{k},\lambda}, \hat{p}_{\mathbf{k}',\lambda'}] = i\hbar\delta_{\mathbf{k}\mathbf{k}'}\delta_{\lambda\lambda'} \tag{2.76}$$

Key to this quantization is the concept of the harmonic oscillator. It is convenient to use the creation and annihilation operator, also called the field operator

$$\hat{a}_{\mathbf{k},\lambda} = \frac{1}{\sqrt{\hbar\omega_{\mathbf{k}}}}(\omega_{\mathbf{k}}\hat{q}_{\mathbf{k},\lambda} + i\hat{p}_{\mathbf{k},\lambda}) \tag{2.77}$$

$$\hat{a}^\dagger_{\mathbf{k},\lambda} = \frac{1}{\sqrt{\hbar\omega_{\mathbf{k}}}}(\omega_{\mathbf{k}}\hat{q}_{\mathbf{k},\lambda} - i\hat{p}_{\mathbf{k},\lambda}) \tag{2.78}$$

The field operator follows the commutation relation

$$[\hat{a}_{\mathbf{k},\lambda}, \hat{a}^\dagger_{\mathbf{k},\lambda}] = \delta_{\mathbf{k}\mathbf{k}'}\delta_{\lambda\lambda'} \tag{2.79}$$

Using the commutation relation, we can write the Hamiltonian in Eq.2.20 as

$$\hat{\mathcal{H}}_F = \sum_{\mathbf{k},\lambda}\hbar\omega_{\mathbf{k}}(\hat{a}^\dagger_{\mathbf{k},\lambda}\hat{a}_{\mathbf{k},\lambda} + \frac{1}{2}) \tag{2.80}$$

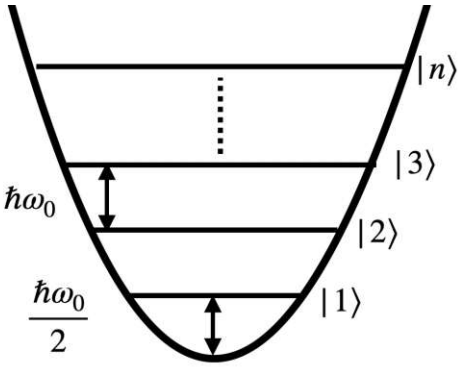

Figure 2.2: Energy description of a Harmonic oscillator.

The most convenient way to define the quantum mechanical state of an electromagnetic field is by using the eigenstate of $\hat{\mathcal{H}}_F$, also called the Fock state.

$$\hat{a}^\dagger_{\mathbf{k},\lambda}\hat{a}_{\mathbf{k},\lambda}\left|n_{\mathbf{k},\lambda}\right\rangle = n_{\mathbf{k},\lambda}\left|n_{\mathbf{k}},\lambda\right\rangle \tag{2.81}$$

and

$$\begin{aligned}\hat{a}_{\mathbf{k},\lambda}\left|n_{\mathbf{k}},\lambda\right\rangle &= \sqrt{n_{\mathbf{k}}}\left|n_{\mathbf{k},\lambda}-1\right\rangle \\ \hat{a}^\dagger_{\mathbf{k},\lambda}\left|n_{\mathbf{k}}\right\rangle &= \sqrt{n_{\mathbf{k},\lambda}+1}\left|n_{\mathbf{k},\lambda}+1\right\rangle\end{aligned} \tag{2.82}$$

where $n_{\mathbf{k},\lambda}$ represents the energy level or number of photons in $\mathbf{k},\lambda$ mode. These states form the basis for describing electromagnetic interactions in terms of quantum processes, such as the emission or absorption of photons by atoms. In the subsequent section, we will study the complete quantum mechanical description of light atom interaction.

2.1.6 2-level interaction with single cavity mode

The quantum mechanical Hamiltonian for 2-level single atom and single mode is given by

$$\hat{\mathcal{H}}_0 = \hat{\mathcal{H}}_A + \hat{\mathcal{H}}_F = \hbar\omega_0\left|e\right\rangle\left\langle e\right| + \hbar\omega\left(\hat{a}^\dagger\hat{a}+\frac{1}{2}\right) \tag{2.83}$$

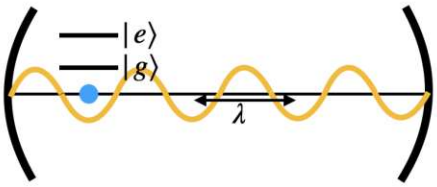

Figure 2.3: Schematic diagram of an atom-light interaction confined by a cavity.

Here we are talking about single mode so we have replaced $\hat{a}_{\mathbf{k},\lambda} \to \hat{a}$. The atom-field interaction Hamiltonian looks like

$$\hat{\mathcal{H}}_{AF} = -\hat{\mathbf{d}}\cdot\hat{\mathbf{E}} \tag{2.84}$$

and atomic dipole operator, as mentioned in section 2.1.2 is

$$\hat{\mathbf{d}} = \mathbf{d}_{ge}(\hat{\sigma}_{ge}+\hat{\sigma}_{eg}) \tag{2.85}$$

Now because we are treating electromagnetic field quantum mechanically, we define an electric field operator analogues to its classical counterpart (2.6) but only for a standing wave single mode oriented in z direction.

$$\hat{\mathbf{E}}(z,t) = \sqrt{\frac{2\pi\hbar\omega}{V}}[\mathbf{f}(z)\hat{a}e^{-i\omega t}+\mathbf{f}^*(z)\hat{a}^\dagger e^{i\omega t}] \tag{2.86}$$

where $\mathbf{f}(z) = \cos(\mathbf{k}\cdot z)\,\mathbf{e}$ Combing equation (2.84), (2.85) and (2.86) we get

$$\hat{\mathcal{H}}_{AF} = -\sqrt{\frac{2\pi\hbar\omega}{V}}(\hat{\sigma}_{ge}+\hat{\sigma}_{eg})\mathbf{d}_{ge}\cdot[\mathbf{f}(z)\hat{a}(t)+\mathbf{f}^{*}(z)\hat{a}^{\dagger}(t)] \tag{2.87}$$

Now, we can define the atom field coupling strength as

$$\hbar g(z) = -\sqrt{\frac{2\pi\hbar\omega}{V}}\mathbf{d}_{ge}\cdot\mathbf{f}(z) \tag{2.88}$$

In terms of $g(z)$ the interaction hamiltonian (2.87) looks like

$$\hat{\mathcal{H}}_{AF} = \hbar(\hat{\sigma}_{ge}+\hat{\sigma}_{eg})[g(z)\hat{a}+g^{*}(z)\hat{a}^{\dagger}] \tag{2.89}$$

if the mode is uniform over an optical cavity of volume V

$$g_0 = -\mathbf{e}\cdot\mathbf{d}_{ge}\sqrt{\frac{2\pi\omega}{\hbar V}} \tag{2.90}$$

The spatial dependence can be included as $g(z) = g_0 f(z)$

Combing equation (2.83), (2.89) , and using **Rotating wave aproximation** we get the **Jaynes-Cummings** Hamiltonian

$$\hat{\mathcal{H}}_J = \hat{\mathcal{H}}_A + \hat{\mathcal{H}}_{AF} + \hat{\mathcal{H}}_{AF} = \hbar\omega_0\hat{\sigma}_{ee} + \hbar\omega\hat{a}^{\dagger}\hat{a} + \hbar g(z)(\hat{\sigma}_{eg}\hat{a}+\hat{\sigma}_{ge}\hat{a}^{\dagger}) \tag{2.91}$$

Using the **Jaynes-Cummings** Hamiltonian, we can study how light atom interaction evolves completely quantum mechanically in a confined cavity, without including cavity decay and atomic spontaneous emission

2.1.7 Rabi flopping

The combined wave function associated with **Jaynes-Cummings** Hamiltonian looks like

$$|\psi(t)\rangle = c_{e,n}(t)\,|e\rangle\,|n\rangle + c_{g,n+1}(t)\,|g\rangle\,|n+1\rangle \tag{2.92}$$

In the interaction picture, the Jaynes-Cummings Hamiltonian looks like

$$\begin{aligned}\hat{\mathcal{H}}_I &= e^{i\hat{\mathcal{H}}_0 t/\hbar}\hat{\mathcal{H}}_{AF}e^{-i\hat{\mathcal{H}}_0 t/\hbar}\\ &= \hbar g(\hat{\sigma}_{eg}\hat{a}e^{i\Delta t}+\hat{\sigma}_{ge}\hat{a}^{\dagger}e^{-i\Delta t})\end{aligned} \tag{2.93}$$

where $\Delta = \omega_a - \omega_c$ Using the Schrödinger equation and the Interaction Hamiltonian, we get the equation of motion associated with probability coefficients of excited and ground state

$$\begin{aligned}i\frac{d}{dt}c_{e,n}(t) &= g\sqrt{n+1}c_{g,n+1}(t)\\ i\frac{d}{dt}c_{g,n+1}(t) &= g\sqrt{n+1}c_{e,n}(t)\end{aligned} \tag{2.94}$$

Similar to semiclassical treatment these equations can be solved assuming $c_{g,n+1}(0) = 0$

$$\begin{aligned} c_{e,n}(t) &= \left(c_{e,n}(0) \left(\cos\frac{\Omega t}{2} - \frac{i\Delta}{\Omega} \sin\frac{\Omega t}{2} \right) - \frac{2ig\sqrt{n+1}}{\Omega} c_{g,n+1}(0) \sin\frac{\Omega t}{2} \right) e^{i\Delta t/2} \\ c_{g,n+1}(t) &= \left(c_{g,n+1}(0) \left(\cos\frac{\Omega t}{2} + \frac{i\Delta}{\Omega} \sin\frac{\Omega t}{2} \right) - \frac{2ig\sqrt{n+1}}{\Omega} c_{e,n}(0) \sin\frac{\Omega t}{2} \right) e^{-i\Delta t/2} \end{aligned} \tag{2.95}$$

where the Rabi frequency is $\Omega^2 = \Delta^2 + 4g^2(n+1) = \Delta^2 + \Omega_0^2$, assuming $c_{g,n+1}(0) = 0$ we get

$$\begin{aligned} c_{e,n}(t) &= c_{e,n}(0) \left(\cos\frac{\Omega t}{2} - \frac{i\Delta}{\Omega} \sin\frac{\Omega t}{2} \right) e^{i\Delta t/2} \\ c_{g,n+1}(t) &= -\frac{2ig\sqrt{n+1}}{\Omega} c_{e,n}(0) \sin\frac{\Omega t}{2} e^{-i\Delta t/2} \end{aligned} \tag{2.96}$$

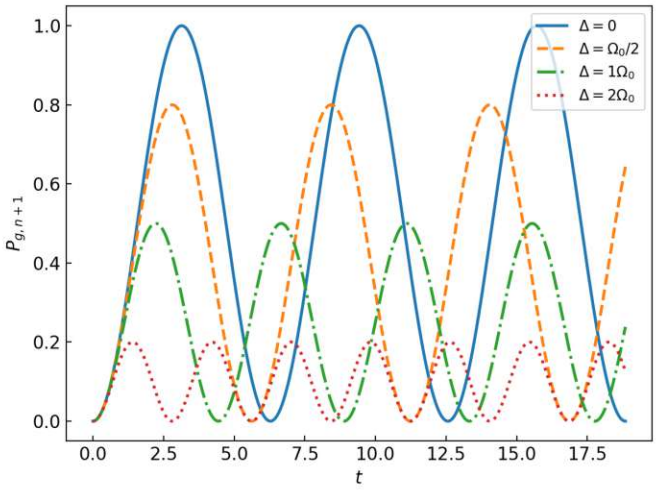

Figure 2.4: Rabi flopping for different detuning.

Now lets consider an atom in excited state and fields as a linear combination of number states.

$$|\psi(0)\rangle = \sum_{n=0}^{\infty} c_n(0) |e, n\rangle \tag{2.97}$$

Using the Schrödinger equation and the Interaction Hamiltonian (2.93), for $\Delta = 0$ we get

$$\begin{aligned} c_{e,n}(t) &= c_n(0) \cos\left(gt\sqrt{n+1}\right) \\ c_{g,n+1}(t) &= -ic_n(0) \sin\left(gt\sqrt{n+1}\right) \end{aligned} \tag{2.98}$$

which means in absence of any field the atoms will go back and forth in upper and lower state.

2.2 Spontaneous vs superradiance emmision

Instead of single mode if we include all the modesn then the interaction hamiltonian will change to

$$\hat{\mathcal{H}}_I = \hbar \sum_{\mathbf{k}} (g_{\mathbf{k}}(\mathbf{r}_0)^* \hat{\sigma}_{eg} \hat{a}_{\mathbf{k}} e^{i(\omega-\omega_{\mathbf{k}})t} + g_{\mathbf{k}}(\mathbf{r}_0) \hat{\sigma}_{ge} \hat{a}^\dagger_{\mathbf{k}} e^{-i(\omega-\omega_{\mathbf{k}})t}) \tag{2.99}$$

Where $g_{\mathbf{k}}(\mathbf{r}_0) = g_{\mathbf{k}} e^{(-i\mathbf{k}\cdot\mathbf{r}_0)}$. Here to make notation shorter we are using $\mathbf{k}$ instead of $\mathbf{k}, \lambda$ If we assume no field initially and atom in excited state, the state vector at time t will look like

$$|\psi(t)\rangle = c_{e,0}(t)\,|e,0\rangle + \sum_{\mathbf{k}} c_{g,\mathbf{k}}(t)\,|g,1_{\mathbf{k}}\rangle \tag{2.100}$$

with $c_{e,0}(0) = 1\, c_{g,\mathbf{k}}(0) = 0$ Using the Schrödinger equation and the Interaction Hamiltonian (2.99) we get

$$\dot{c}_{e,0}(t) = -\sum_{\mathbf{k}} |g_{\mathbf{k}}(\mathbf{r}_0)|^2 \int_0^t dt' e^{i(\omega-\omega_{\mathbf{k}})(t-t')} c_{e,0}(t') \tag{2.101}$$

Assuming that the modes of the field are closely spaced in frequency, we can replace the summation over $\mathbf{k}$ by an integeral and substituting the value of $g_{\mathbf{k}}(\mathbf{r}_0)$ from equation 2.90, we get

$$\dot{c}_{e,0}(t) = -\frac{4|\mathbf{d}_{ge}|^2}{(2\pi)6\hbar c^3} \int_0^\infty d\omega_{\mathbf{k}} \omega_{\mathbf{k}}^3 \int_0^t dt' e^{i(\omega-\omega_{\mathbf{k}})(t-t')} c_{e,0}(t') \tag{2.102}$$

The time derivative will only contribute significantly near $\omega_{\mathbf{k}} = \omega$ so we can replace $\omega_{\mathbf{k}}^3$ by ω^3 and using the property of delta function, we can replace

$$\int_{-\infty}^{\infty} d\omega_{\mathbf{k}} e^{i(\omega-\omega_{\mathbf{k}})(t-t')} = 2\pi\delta(t-t') \tag{2.103}$$

resulting in

$$\dot{c}_{e,0}(t) = -\frac{\gamma}{2} c_{e,0}(t) \tag{2.104}$$

where the decay coefficient $\gamma = \frac{4\omega^3|\mathbf{d}_{ge}|^2}{3\hbar c^3}$ i.e. an atom in excited state will decay exponentially in time as $|c_{e,0}(t)|^2 = e^{(-\gamma t)}$. This is called spontaneous emission.

Consider a dilute gas of atoms initially prepared in the upper state of an electronic transition in presence of a magnetic field. The atoms will spontaneously emit independently via a magnetic dipole transition, and their excited states will decay through spontaneous emission. However, when the distance between the atoms' is much smaller than the

radiation wavelength and much larger than the de Broglie wavelength, they begin to behave collectively. This results in a much faster and more intense emission of radiation. This collective behavior is known as superradiance. [16].

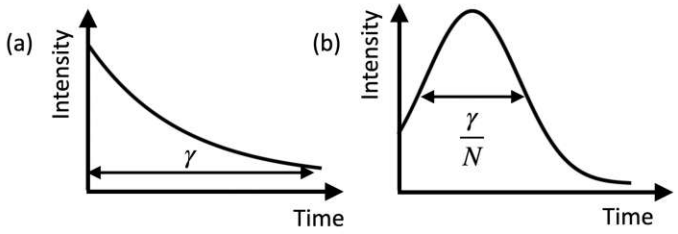

Figure 2.5: (a) Spontaneous emission with exponantially decaying intensity with decay rate (γ) while (b) Superradiant emission occurring as a brief burst of radiation ($\approx \frac{\gamma}{N}$).

To understand it better, let's assume we start with an ensemble with all atoms in the excited states. We assume the atoms are indiscernible for the photon emission or absorption process in the subsequent evolution. Therefore, the system must remain in a Hilbert subspace invariant to atomic permutations.

First, we introduce a collective operator in terms of ladder operators as defined in section 2.1.3.

$$\hat{J}^{\pm} = \sum_{j=1}^{N} \hat{s}_j^{\pm} \tag{2.105}$$

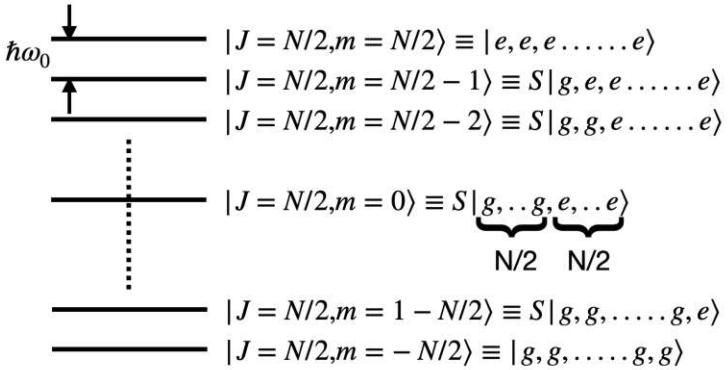

Figure 2.6: Superradiant ladder and state symmetry. S denotes symmetrization over atoms.

Under the condition of Dicke superradiance, N atoms behave as a collective dipole, resulting from the sum of all N individual dipoles.

$$\hat{D} = \sum_{j=1}^{N} \hat{D}_j = (\hat{J}^+ + \hat{J}^-) D\hat{\epsilon} \tag{2.106}$$

Rate of emission of photon is proportional to $\langle \hat{s}^+ \hat{s}^- \rangle$, similarly for collective emission $\langle \hat{J}^+ \hat{J}^- \rangle$ For the Dicke state $|J, m\rangle$ we get $(J+m)(J-m+1)$ by applying $\hat{J}^-$ on the state $|J = N/2, m = N/2\rangle$, we can see that the emission rate is maximum at m=0; that's why we see a peak in the plot.

$$\langle \hat{J}^+ \hat{J}^- \rangle = \left\langle \sum_{j=1}^{N} \hat{s}_j^+ \sum_{i=1}^{N} \hat{s}_i^- \right\rangle = N \langle \hat{s}_i^+ \hat{s}_i^- \rangle + N(N-1) \langle \hat{s}_j^+ \hat{s}_i^- \rangle \tag{2.107}$$

The term $\langle \hat{s}_j^+ \hat{s}_i^- \rangle$ represents the atomic corelation. For the superradiance to manifest, the atom-atom correlation should be nonzero.

$$\langle J, m | \, \hat{s}_j^+ \hat{s}_i^- \, | J, m \rangle = \frac{J^2 - m^2}{N(N-1)} \tag{2.108}$$

Therefore, the atomic correlation increases from 0 to a maximum of 1/4 when m goes from N/2 to 0 and decreases to 0 when the value of m goes to N/2.

Now, to study continuous superradiance, we need to study some of the fundamentals of the theory of an open quantum system.

2.3 Theory of open quantum systems

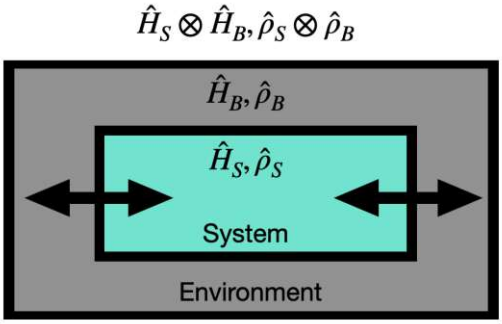

Figure 2.7: Schematic picture of an open quantum system.

In the study of nature, it can be said that there are two types of randomness, one because of lack of information and another that is intrinsic in nature. Wave function formalism

can only cater to the second one, also known as pure state; to include both, we need the *density operator formalism* that incorporates both mixed and pure states. Let us consider some combined "total" system, consisting of a quantum *system* S and a *reservoir*, or *bath* B, see Figure 2.7. We assume that the combined system is closed, and is governed by the Schrödinger equation. However, for the sake of generality, we suppose there is a lack of complete information on the state of the combined system. Instead, the total system can be found in one of the quantum pure states $|\psi_\alpha\rangle$ with probabilities P_α (in other words, we can say that we consider a *statistical ensemble* of pure states of the total system). Let us introduce the *density operator* $\hat{\rho}_{SB}$ of such a combined system as

$$\hat{\rho}_{SB}(t) = \sum_\alpha P_\alpha \left|\psi_\alpha(t)\right\rangle \left\langle\psi_\alpha(t)\right| \tag{2.109}$$

Consider first some operator $\hat{A}_{SB}$ corresponding to the total system. The expectation value of such an operator is given by

$$\begin{aligned} \langle \hat{A}_{SB} \rangle &= \sum_\alpha P_\alpha \left\langle\psi_\alpha(t)\right| \hat{A}_{SB} \left|\psi_\alpha(t)\right\rangle \\ &= \mathrm{Tr}\left[\sum_\alpha P_\alpha \left|\psi_\alpha(t)\right\rangle \left\langle\psi_\alpha(t)\right| \hat{A}_{SB}\right] = \mathrm{Tr}\left[\hat{\rho}_{SB}(t)\hat{A}_{SB}\right] \end{aligned} \tag{2.110}$$

Now consider some operator $\hat{A}_S$ associated only with the system S, but not with the bath. Then we can introduce complete sets of eigenstates $\{|s\rangle\}$ and $\{|b\rangle\}$ of the system and the bath, and write

$$\begin{aligned} \langle \hat{A}_S \rangle &= \mathrm{Tr}_{S,B}\left[\hat{\rho}_{SB} \sum_{s,b,s',b'} |b\rangle\,|s\rangle\,\langle s|\,\langle b|\,\hat{A}_S\,|b'\rangle\,|s'\rangle\,\langle b'|\,\langle s'|\right] \\ &= \mathrm{Tr}_{S,B}\left[\hat{\rho}_{SB} \sum_{b,b'} |b\rangle \underbrace{\langle b|\,|b'\rangle}_{\delta_{bb'}} \langle b'| \underbrace{\sum_{s,s'} |s\rangle\,\langle s|\,\hat{A}_S\,|s'\rangle\,\langle s'|}_{\hat{A}_S}\right] = \mathrm{Tr}_S\left[\sum_b \langle b|\,\hat{\rho}_{SB}\,|b\rangle\,\hat{A}_S\right] \end{aligned} \tag{2.111}$$

It is convenient to introduce density operator $\hat{\rho}_S$, representing the state of the system, as

$$\hat{\rho}_S(t) = \sum_b \langle b|\,\hat{\rho}_{SB}(t)\,|b\rangle = \mathrm{Tr}_B[\hat{\rho}_{SB}(t)] \tag{2.112}$$

2.3.1 Master equation

Now we derive the *quantum master equation* governing $\hat{\rho}_S$. This equation is fundamental in the study of open quantum systems, i.e., the system interacting with an external environment. This interaction leads to phenomena such as decoherence and dissipation,

which are crucial for the dynamics of open quantum systems. The most commonly used form of the quantum master equation is the Lindblad form, which is an extension of the Schrödinger equation, including dissipation. The derivation that we present here follows primarily the logic of the book [17], although we altered some notations for the sake of consistency within the thesis. We start from the Schrödinger equation for the total density operator

$$\frac{d}{dt}\hat{\rho}^0_{SB}(t) = \frac{1}{i\hbar}[\hat{\mathcal{H}}_0, \hat{\rho}^0_{SB}(t)], \tag{2.113}$$

where the index "0" indicates the Schrödinger picture. The Hamiltonian $\hat{\mathcal{H}}_0$ can be represented as

$$\hat{\mathcal{H}}_0 = \hat{\mathcal{H}}_S + \hat{\mathcal{H}}_B + \hat{\mathcal{H}}^0_{SB}, \tag{2.114}$$

Here $\hat{\mathcal{H}}_S$ is the Hamiltonian of the system, $\hat{\mathcal{H}}_B$ is the Hamiltonian of the bath, and $\hat{\mathcal{H}}^0_{SB}$ describes the interaction between the system and the bath. Hamiltonian and the density operator in the interaction picture are

$$\hat{\mathcal{H}}(t) = e^{\frac{i}{\hbar}(\hat{\mathcal{H}}_S+\hat{\mathcal{H}}_B)t}\hat{\mathcal{H}}^0_{SB}e^{-\frac{i}{\hbar}(\hat{\mathcal{H}}_S+\hat{\mathcal{H}}_B)t}, \tag{2.115}$$

$$\hat{\rho}(t) = e^{\frac{i}{\hbar}(\hat{\mathcal{H}}_S+\hat{\mathcal{H}}_B)t}\hat{\rho}^0_{SB}(t)e^{-\frac{i}{\hbar}(\hat{\mathcal{H}}_S+\hat{\mathcal{H}}_B)t}. \tag{2.116}$$

The Liouville-von Neumann equation in the interaction picture looks like

$$\frac{d}{dt}\hat{\rho}(t) = \frac{1}{i\hbar}[\hat{\mathcal{H}}(t), \hat{\rho}(t)]. \tag{2.117}$$

Substituting its formal solution $\rho(t) = \rho(0) - \frac{i}{\hbar}\int_0^t[\hat{\mathcal{H}}(t'), \hat{\rho}(t')]dt'$ again into (2.117), we obtain

$$\frac{d\hat{\rho}(t)}{dt} = -\frac{i}{\hbar}[\hat{\mathcal{H}}(t), \hat{\rho}(0)] - \frac{1}{\hbar^2}\int_0^t \left[\hat{\mathcal{H}}(t), [\hat{\mathcal{H}}(t', \hat{\rho}(t'))]\right] dt'. \tag{2.118}$$

Let us represent the system-bath interaction in the form

$$\hat{\mathcal{H}}^0_{SB} = \sum_\alpha \hat{C}^0_\alpha \hat{B}^0_\alpha, \tag{2.119}$$

where $\hat{C}^0_\alpha$ and $\hat{B}^0_\alpha$ are Hermitian operators of the system and the bath, respectively. Operator $\hat{C}^0_\alpha$ can be represented as

$$\hat{C}^0_\alpha = \sum_{n,m} |n\rangle\, C^0_{\alpha,nm}\, \langle m|\,, \tag{2.120}$$

where $|n\rangle$, $|m\rangle$ are the eigenstates of $\hat{\mathcal{H}}_S$

$$\hat{\mathcal{H}}_S\,|m\rangle = E^S_m\,|m\rangle\,, \quad \hat{\mathcal{H}}_S\,|n\rangle = E^S_n\,|n\rangle\,. \tag{2.121}$$

Then we can group elements with the same transition frequencies in expression (2.120) as

$$\hat{C}_\alpha(\omega) = \sum_{n,m|E_m^S - E_n^S = \hbar\omega} |n\rangle\, C^0_{\alpha,nm}\, \langle m|\,. \tag{2.122}$$

Note that

$$\hat{C}^0_\alpha = \sum_\omega \hat{C}_\alpha(\omega), \quad \text{and} \quad \hat{C}^\dagger_\alpha(\omega) = \hat{C}_\alpha(-\omega). \tag{2.123}$$

Now we substitute (2.122) and (2.119) into (2.115) to get

$$\hat{\mathcal{H}}(t) = \sum_{\alpha,\omega} e^{\frac{i}{\hbar}(\hat{\mathcal{H}}_S + \hat{\mathcal{H}}_B)t} \hat{C}_\alpha(\omega) \hat{B}^0_\alpha e^{-\frac{i}{\hbar}(\hat{\mathcal{H}}_S + \hat{\mathcal{H}}_B)t} = \sum_{\alpha,\omega} e^{-i\omega t} \hat{C}_\alpha(\omega) \hat{B}_\alpha(t), \tag{2.124}$$

where we have introduced

$$\hat{B}_\alpha(t) = e^{\frac{i}{\hbar}\hat{\mathcal{H}}_B t} \hat{B}^0_\alpha e^{-\frac{i}{\hbar}\hat{\mathcal{H}}_B t}. \tag{2.125}$$

Note that $\hat{B}^\dagger_\alpha(t) = \hat{B}_\alpha(t)$.

Now we should substitute (2.124) into (2.118), and take a trace over bath variables. Let us make some reasonable approximations, which significantly simplify the further analysis. The first one, the *Born approximation*, consists in the supposition that the coupling between the bath and the system is weak, and the bath has a huge amount of degrees of freedom, therefore, the influence of the system on any degree of freedom of the bath is negligibly small, and we can approximately separate the system and bath degrees of freedom as

$$\rho(t') \approx \rho_S(t') \otimes \rho_B, \tag{2.126}$$

where we assumed that the bath is in the thermal equilibrium, and its density matrix ρ_B does not depend on time. Second, we introduce the *Markov approximation*, which suggests that any temporal correlations of the bath decays much faster than the system evolves changes its internal state. It allows replacing $\rho(t')$ by $\rho_S(t) \otimes \rho_B$ in equation (2.118) and shift the lower limit of the integrals in the second term of this equation from 0 to $-\infty$. Also, we assume that

$$\mathrm{Tr}_B[\hat{\mathcal{H}}(t), \hat{\rho}(0)] = 0, \tag{2.127}$$

which is valid, for example, if the bath is thermal, and the operators $\hat{B}_\alpha$ do not have any non-zero diagonal matrix elements in the basis of eigenstates of the operator $\hat{\mathcal{H}}_B$. Finally, we use the *secular*, or the *rotating wave approximation*, where we suppose that the different frequencies ω, ω' in (2.122) are "well separated" in the sense that the typical time scale of evolution of the system S is much longer than $1/|\omega - \omega'|$.

Substituting (2.124) into (2.118), taking trace over bath variables, using the Born-Markov approximation, the assumption (2.127) and the fact that $\hat{B}_\alpha(t)$ as well as $\hat{\mathcal{H}}(t)$ are

Hermitian, we can write

$$\begin{aligned}\frac{d\hat{\rho}_S(t)}{dt} =& -\frac{1}{\hbar^2}\int_{-\infty}^{t}\sum_{\alpha,\alpha'}\sum_{\omega,\omega'} e^{i(\omega t-\omega' t')}\mathrm{Tr}_B\left[\hat{C}^\dagger_\alpha(\omega)\hat{B}_\alpha(t),[\hat{C}_{\alpha'}(\omega')\hat{B}_{\alpha'}(t'),\hat{\rho}_S(t)\otimes\hat{\rho}_B]\right]dt \\ =& -\frac{1}{\hbar^2}\sum_{\alpha,\alpha'}\sum_{\omega,\omega'} e^{i(\omega-\omega')t}\int_{-\infty}^{t} e^{i\omega'(t-t')} \\ &\times\Big\{\left[\hat{C}^\dagger_\alpha(\omega)\hat{C}_{\alpha'}(\omega')\hat{\rho}_S(t)-\hat{C}_{\alpha'}(\omega')\hat{\rho}_S(t)\hat{C}^\dagger_\alpha(\omega)\right]\langle\hat{B}_\alpha(t)\hat{B}_{\alpha'}(t')\rangle \\ &+\left[\hat{\rho}_S(t)\hat{C}_{\alpha'}(\omega')\hat{C}^\dagger_\alpha(\omega)-\hat{C}^\dagger_\alpha(\omega)\hat{\rho}_S(t)\hat{C}_{\alpha'}(\omega')\right]\langle\hat{B}_{\alpha'}(t')\hat{B}_\alpha(t)\rangle\Big\}\,dt.\end{aligned} \tag{2.128}$$

Let us introduce the one-sided Fourier transform $\Gamma_{\alpha\alpha'}(\omega)$ of the *reservoir correlation function* $\langle\hat{B}_\alpha(t)\hat{B}_{\alpha'}(t')\rangle$ as

$$\Gamma_{\alpha\alpha'}(\omega') = \int_{-\infty}^{t} e^{i\omega'(t-t')}\langle\hat{B}_\alpha(t)\hat{B}_{\alpha'}(t')\rangle dt' = \int_{0}^{\infty} e^{i\omega' s}\langle\hat{B}_\alpha(t)\hat{B}_{\alpha'}(t-s)\rangle ds, \tag{2.129}$$

which does not depend on t for stationary state of the reservoir. Also,

$$\int_{-\infty}^{t} e^{i\omega'(t-t')}\langle\hat{B}_{\alpha'}(t')\hat{B}_\alpha(t)\rangle dt' = \Gamma^*_{\alpha\alpha'}(-\omega'). \tag{2.130}$$

Now we substitute (2.129) and (2.130) into (2.128), use the rotating wave approximation (i.e., neglect all the fast oscillating terms proportional to $e^{i(\omega'-\omega)t}$ for $\omega\neq\omega'$). Also, in the last square brackets in (2.128) we replace ω by $-\omega$, switch α and α' , and use the property $\hat{C}^\dagger_\alpha(\omega)=\hat{C}_\alpha(-\omega)$. It gives

$$\begin{aligned}\frac{d\hat{\rho}_S(t)}{dt} =& \frac{1}{\hbar^2}\sum_{\alpha,\alpha',\omega}\Big\{\left[\hat{C}_{\alpha'}(\omega)\hat{\rho}_S(t)\hat{C}^\dagger_\alpha(\omega)-\hat{C}^\dagger_\alpha(\omega)\hat{C}_{\alpha'}(\omega)\hat{\rho}_S(t)\right]\Gamma_{\alpha\alpha'}(\omega) \\ &+\left[\hat{C}_{\alpha'}(\omega)\hat{\rho}_S(t)\hat{C}^\dagger_\alpha(\omega)-\hat{\rho}_S(t)\hat{C}^\dagger_\alpha(\omega)\hat{C}_{\alpha'}(\omega)\right]\Gamma^*_{\alpha'\alpha}(\omega)\Big\}.\end{aligned} \tag{2.131}$$

For further simplification we introduce matrices

$$\gamma_{\alpha\alpha'}(\omega) = \Gamma_{\alpha\alpha'}(\omega)+\Gamma^*_{\alpha'\alpha}(\omega). \tag{2.132}$$

$$S_{\alpha\alpha'}(\omega) = \frac{1}{2i}\left(\Gamma_{\alpha\alpha'}(\omega)-\Gamma^*_{\alpha'\alpha}(\omega)\right). \tag{2.133}$$

which allows us to separate the Hamiltonian contribution (often called *Lamb shift*) and the dissipative term, and rewrite the master equation as

$$\begin{aligned}\frac{d\hat{\rho}_S(t)}{dt} =& -\frac{i}{\hbar}\left[\hat{\mathcal{H}}_{LS},\hat{\rho}_S(t)\right]+\frac{1}{\hbar^2}\sum_{\alpha,\alpha',\omega}\frac{\gamma_{\alpha,\alpha'}(\omega)}{2}\Big\{2\hat{C}_{\alpha'}(\omega)\hat{\rho}_S(t)\hat{C}^\dagger_\alpha(\omega) \\ &-\hat{C}^\dagger_\alpha(\omega)\hat{C}_{\alpha'}(\omega)\hat{\rho}_S(t)-\hat{\rho}_S(t)\hat{C}^\dagger_\alpha(\omega)\hat{C}_{\alpha'}(\omega)\Big\},\end{aligned} \tag{2.134}$$

where

$$\hat{\mathcal{H}}_{LS} = \frac{1}{\hbar} \sum_{\alpha,\alpha',\omega} S_{\alpha,\alpha'}(\omega) \hat{C}^{\dagger}_{\alpha}(\omega) \hat{C}_{\alpha'}(\omega). \tag{2.135}$$

Finally, from (2.132) follows that $\gamma_{\alpha\alpha'}(\omega) = \gamma^{*}_{\alpha'\alpha}(\omega)$, i.e., $\gamma_{\alpha\alpha'}(\omega)$ can be considered as a Hermitian matrix with respect to indices α, α', and can be diagonalized. Then we can write the master equation in *Lindblad form* as

$$\frac{d\hat{\rho}_S(t)}{dt} = -\frac{i}{\hbar}\left[\hat{\mathcal{H}}_{LS}, \hat{\rho}_S(t)\right] + \sum_k \gamma_k \hat{\tilde{\mathfrak{D}}}'[\hat{J}_k]\hat{\rho}_S(t), \quad \text{where} \tag{2.136}$$

$$\hat{\tilde{\mathfrak{D}}}'[\hat{J}]\hat{\rho} = \hat{J}\hat{\rho}\hat{J}^{\dagger} - \frac{1}{2}(\hat{J}^{\dagger}\hat{J}\hat{\rho} + \hat{\rho}\hat{J}^{\dagger}\hat{J}). \tag{2.137}$$

Here the coefficients γ_k are often chosen to have a dimension of frequency and are called *rates*, $\hat{J}_k$ are called *jump operators*, and the superoperator $\hat{\tilde{\mathfrak{D}}}'[\hat{J}]\hat{\rho}$ is called *Lindbladian superoperator*.

2.3.2 Monte-Carlo wave function method

In the previous section, we derived the master equation governing the evolution of a density matrix describing a statistical ensemble of open quantum systems. If such a quantum system has N quantum states, the density matrix has N^2 complex matrix elements. Even for a moderate-size system, a direct numerical solution of the master equation may be hindered or even impossible due to the large amount of memory required to store the matrices. One efficient method to reduce the amount of required memory would be to use a wave function instead of the density matrix: such a function can be stored as a vector with only N complex elements. For closed systems, the wave function follows the Schrödinger equation, which has no direct equivalent for an open quantum system because, even being initially prepared in a pure quantum state, such a system becomes mixed due to interaction with the bath and can not be correctly described by wave functions. However, statistical ensemble of individual open quantum systems can be approximated by ensemble of individual quantum trajectories calculated with the so-called *quantum jump approach*, or the *Monte-Carlo wave function* method [18, 19], where the deterministic evolution of the wave function governed by Schrödinger-like equation is interrupted in randomly chosen instants, when the state of the system expects quantum jumps, i.e., instant change of internal state. Averaging over many of such individual stories, also called *quantum trajectores*, gives a more or less complete picture of the evolution of the statistical ensemble of quantum states.

2.3.2.1 Dyson Expansion

We start our consideration from the master equation in Lindblad form (2.136), where we also suppose the presence of some extra Hamiltonian part $\hat{\mathcal{H}}$, which is not necessarily associated only with the interaction between the system and the bath but describes some extra interaction of the system. For the sake of brevity, we consider here the situation

when we have only a single dissipation channel with rate γ and the jump operator $\hat{J}$; the generalization for the multi-channel dissipation process is straightforward. Also, we introduce new jump operator $\hat{A} = \sqrt{\gamma}\hat{J}$ incorporating the rate, and omit index S of $\hat{\rho}$. Then the master equation can be written as

$$\begin{aligned}\frac{d}{dt}\hat{\rho}(t) &= \frac{1}{i\hbar}[\hat{\mathcal{H}}, \hat{\rho}(t)] + \hat{A}\hat{\rho}(t)\hat{A}^\dagger - \frac{1}{2}(\hat{A}^\dagger\hat{A}\rho(t) + \hat{\rho}(t)\hat{A}^\dagger\hat{A}) \\ &= \frac{1}{i\hbar}\left[\hat{\mathcal{H}}_{\text{eff}}\hat{\rho}(t) - \hat{\rho}(t)\hat{\mathcal{H}}_{\text{eff}}^\dagger\right] + \hat{A}\hat{\rho}(t)\hat{A}^\dagger,\end{aligned} \tag{2.138}$$

where we introduced the effective non-Hermitian Hamiltonian $\hat{\mathcal{H}}_{\text{eff}} = \hat{\mathcal{H}} - \frac{i\hbar}{2}\hat{A}^\dagger\hat{A}$. We can rewrite this equation as

$$\frac{d}{dt}\hat{\rho}(t) = \hat{\hat{\mathcal{L}}}\hat{\rho}(t) = \hat{\hat{\mathcal{L}}}_0\hat{\rho}(t) + \hat{\hat{\mathcal{L}}}_J\hat{\rho}(t) \tag{2.139}$$

with

$$\begin{aligned}\hat{\hat{\mathcal{L}}}_0\hat{\rho}(t) &= \frac{1}{i\hbar}\left[\hat{\mathcal{H}}_{\text{eff}}\hat{\rho}(t) - \hat{\rho}(t)\hat{\mathcal{H}}_{\text{eff}}^\dagger\right], \\ \hat{\hat{\mathcal{L}}}_J\hat{\rho}(t) &= \hat{A}\hat{\rho}(t)\hat{A}^\dagger.\end{aligned} \tag{2.140}$$

Let us introduce

$$\tilde{\hat{\rho}}(t) = e^{\frac{i}{\hbar}\hat{\mathcal{H}}_{\text{eff}}t}\hat{\rho}(t)e^{-\frac{i}{\hbar}\hat{\mathcal{H}}_{\text{eff}}^\dagger t} = e^{-\hat{\hat{\mathcal{L}}}_0 t}\hat{\rho}(t), \tag{2.141}$$

which follows the equation

$$\frac{d}{dt}\tilde{\hat{\rho}}(t) = e^{-\hat{\hat{\mathcal{L}}}_0 t}\hat{\hat{\mathcal{L}}}_J e^{\hat{\hat{\mathcal{L}}}_0 t}\tilde{\hat{\rho}}(t). \tag{2.142}$$

by integrating this equation, we get the solution in the form of an integral equation

$$\tilde{\hat{\rho}}(t) = \tilde{\hat{\rho}}(0) + \int_0^t dt_1 e^{-\hat{\hat{\mathcal{L}}}_0 t_1}\hat{\hat{\mathcal{L}}}_J e^{\hat{\hat{\mathcal{L}}}_0 t_1}\tilde{\hat{\rho}}(t_1). \tag{2.143}$$

Now we can substitute $\tilde{\hat{\rho}}(t_1)$ given by (2.143) in the integral of (2.143), and repeat this process infinitely. Then we obtain the *Dyson expansion* of the solution in the form

$$\begin{aligned}\tilde{\hat{\rho}}(t) &= \tilde{\hat{\rho}}(0) + \int_0^t dt_1 e^{-\hat{\hat{\mathcal{L}}}_0 t_1}\hat{\hat{\mathcal{L}}}_J e^{\hat{\hat{\mathcal{L}}}_0 t_1}\tilde{\hat{\rho}}(0) + \int_0^t dt_2 \int_0^{t_2} dt_1 e^{-\hat{\hat{\mathcal{L}}}_0 t_2}\hat{\hat{\mathcal{L}}}_J e^{\hat{\hat{\mathcal{L}}}_0 (t_2-t_1)}\hat{\hat{\mathcal{L}}}_J e^{\hat{\hat{\mathcal{L}}}_0 t_1}\tilde{\hat{\rho}}(0) \\ &\quad + \int_0^t dt_3 \int_0^{t_3} dt_2 \int_0^{t_2} dt_1 e^{-\hat{\hat{\mathcal{L}}}_0 t_3}\hat{\hat{\mathcal{L}}}_J e^{\hat{\hat{\mathcal{L}}}_0 (t_3-t_2)}\hat{\hat{\mathcal{L}}}_J e^{\hat{\hat{\mathcal{L}}}_0 (t_2-t_1)}\hat{\hat{\mathcal{L}}}_J e^{\hat{\hat{\mathcal{L}}}_0 t_1}\tilde{\hat{\rho}}(0) + ... \\ &= \tilde{\hat{\rho}}(0) + \sum_{n=1}^{\infty}\int_0^t dt_n \int_0^{t_n} dt_{n-1} ..... \int_0^{t_3} dt_2 \int_0^{t_2} dt_1 \\ &\quad \times e^{-\hat{\hat{\mathcal{L}}}_0 t_n}\hat{\hat{\mathcal{L}}}_J e^{\hat{\hat{\mathcal{L}}}_0 (t_n-t_{n-1})}\hat{\hat{\mathcal{L}}}_J .....\hat{\hat{\mathcal{L}}}_J e^{\hat{\hat{\mathcal{L}}}_0 (t_2-t_1)}\hat{\hat{\mathcal{L}}}_J e^{\hat{\hat{\mathcal{L}}}_0 t_1}\tilde{\hat{\rho}}(0).\end{aligned} \tag{2.144}$$

Using $\tilde{\hat{\rho}}(t) = e^{\hat{\hat{\mathcal{L}}}_0 t}\hat{\rho}(t)$, we get

$$\begin{aligned}\hat{\rho}(t) = e^{\hat{\hat{\mathcal{L}}}_0 t}\hat{\rho}(0) + \sum_{n=1}^{\infty}\int_0^t dt_n \int_0^{t_n} dt_{n-1}..... \int_0^{t_3} dt_2 \int_0^{t_2} dt_1 \\ \times e^{\hat{\hat{\mathcal{L}}}_0(t-t_n)}\hat{\hat{\mathcal{L}}}_J e^{\hat{\hat{\mathcal{L}}}_0(t_n-t_{n-1})}\hat{\hat{\mathcal{L}}}_J .....e^{\hat{\hat{\mathcal{L}}}_0(t_2-t_1)}\hat{\hat{\mathcal{L}}}_J e^{\hat{\hat{\mathcal{L}}}_0 t_1}\hat{\rho}(0)\end{aligned} \tag{2.145}$$

This solution can be represented as a sum of terms which can be interpreted as individual *quantum trajectories*. Any of these trajectories consists on $(n+1)$ intervals $(0,t_1)$, (t_1,t_2),...,(t_{n-1},t_n), (t_n,t). Within each of such intervals, the system follows the von Neumann equation with a non-Hermitian Hamiltonian $\hat{\mathcal{H}}_{\text{eff}}$, and between these intervals, the system expects *quantum jumps* described by the superoperator $\hat{\hat{\mathcal{L}}}_J$. The evolution of the density matrix describing the whole statistical ensembles can be represented as a sum of integrals over possible instants $t_1,...t_n$ of quantum jumps, which sum is taken over the number n of such individual quantum jumps.

If the initial state $\hat{\rho}(0)$ is a pure quantum state, i.e., $\hat{\rho}(0) = |\psi(0)\rangle\langle\psi(0)|$, we can rewrite the Dyson expansion (2.145) as

$$\hat{\rho}(t) = \sum_{n=0}^{\infty}\int_0^t dt_n \int_0^{t_n} dt_{n-1}... \int_0^{t_3} dt_2 \int_0^{t_2} dt_1 \,|\psi(t|t_1,t_2,...,t_n)\rangle\langle\psi(t|t_1,t_2,...,t_n)|\,, \tag{2.146}$$

where

$$\begin{aligned}|\psi(t|t_1,t_2,...,t_n)\rangle =& e^{-\frac{i}{\hbar}\hat{\mathcal{H}}_{\text{eff}}(t-t_n)}\hat{A}e^{-\frac{i}{\hbar}\hat{\mathcal{H}}_{\text{eff}}(t_n-t_{n-1})}\hat{A}... \\ &...e^{-\frac{i}{\hbar}\hat{\mathcal{H}}_{\text{eff}}(t_2-t_1)}\hat{A}e^{-\frac{i}{\hbar}\hat{\mathcal{H}}_{\text{eff}}t_1}\,|\psi(0)\rangle\,.\end{aligned} \tag{2.147}$$

Note that the evolution of the wave function along a single quantum trajectory is not unitary because the effective Hamiltonian $\hat{\mathcal{H}}_{\text{eff}}$ is not Hermitian, and the jump operator $\hat{A}$ also does not preserve the norm.

Finally, let us generalise the expressions (2.146) and (2.147) on the case of multiple jump operators $\hat{A}_1,...,\hat{A}_N$. Then the master equation, instead of (2.139), can be represented as

$$\frac{d}{dt}\hat{\rho}(t) = \hat{\hat{\mathcal{L}}}_0\hat{\rho}(t) + \sum_{j=1}^{N}\hat{\hat{\mathcal{L}}}_j\hat{\rho}(t), \quad \text{where} \tag{2.148}$$

$$\hat{\hat{\mathcal{L}}}_0\hat{\rho}(t) = \frac{1}{i\hbar}\left[\hat{\mathcal{H}}_{\text{eff}}\hat{\rho}(t) - \hat{\rho}(t)\hat{\mathcal{H}}_{\text{eff}}^{\dagger}\right], \tag{2.149}$$

$$\hat{\hat{\mathcal{L}}}_j\hat{\rho}(t) = \hat{A}_j\hat{\rho}(t)\hat{A}_j^{\dagger}, \tag{2.150}$$

$$\hat{\mathcal{H}}_{\text{eff}} = \hat{\mathcal{H}} - \frac{i\hbar}{2}\sum_j \hat{A}_j^{\dagger}\hat{A}_j. \tag{2.151}$$

Then the Dyson expansion (2.146) will look like

$$\hat{\rho}(t) = \sum_{n=0}^{\infty} \sum_{j_1=1}^{N} ... \sum_{j_n=1}^{N} \int_0^t dt_n \int_0^{t_n} dt_{n-1} ... \\ ... \int_0^{t_3} dt_2 \int_0^{t_2} dt_1 \left|\psi(t|t_1, ..., t_n; j_1, ..., j_n)\right\rangle \left\langle\psi(t|t_1, ..., t_n; j_1, ..., j_n)\right| , \quad (2.152)$$

and the individual wave functions look like

$$\begin{aligned} \left|\psi(t|t_1, ..., t_n; j_1, ..., j_n)\right\rangle =& e^{-\frac{i}{\hbar}\hat{\mathcal{H}}_{\text{eff}}(t-t_n)} \hat{A}_{j_n} e^{-\frac{i}{\hbar}\hat{\mathcal{H}}_{\text{eff}}(t_n-t_{n-1})} \hat{A}_{j_{n-1}} ... \\ & ... e^{-\frac{i}{\hbar}\hat{\mathcal{H}}_{\text{eff}}(t_2-t_1)} \hat{A}_{j_1} e^{-\frac{i}{\hbar}\hat{\mathcal{H}}_{\text{eff}} t_1} \left|\psi(0)\right\rangle . \end{aligned} \quad (2.153)$$

2.3.2.2 Quantum jump algorithm

The Monte-Carlo wave function (MCWF) method consists of the simulation of the evolution of the system along individual quantum trajectories and subsequent averaging of the final result over these trajectories. Let at time t_i the system is in a state with normalized wave function $|\psi(t_i)\rangle$. The standard procedure consists of the following steps [19]:

1. We define a time step δt, much smaller than the typical relaxation time within the system. Such a time step can be either fixed for the whole simulation or be redefined for any steps if we want to avoid computational artifacts associated with periodicity (for example, when we are interested in spectral characteristics). Also we denote $t_{i+1} = t_i + \delta t$

2. calculate the wave function $|\psi'\rangle (t_{i+1}) = e^{-\frac{i}{\hbar}\hat{\mathcal{H}}_{\text{eff}}\delta t} |\psi(t_i)\rangle$. This wave function is not normalized, because $\hat{\mathcal{H}}_{\text{eff}}$ is not Hermitian, and if δt is small enough, $p_0 = \langle\psi'(t_{i+1})|\psi'(t_{i+1})\rangle \approx 1 - \delta t \langle\psi(t_i)| \sum_j \hat{A}_j^\dagger \hat{A}_j |\psi(t_i)\rangle$. This squared norm is interpreted as a probability of not performing a quantum jump on this step.

3. generate a random number r, uniformly distributed between 0 and 1, and compare it with p_0.

4. If $r < p_0$, there is no quantum jump on this step, and the wave function must be renormalized according to $|\psi(t_{i+1})\rangle = |\psi'(t_{i+1}\rangle / \sqrt{p_0}$

5. If $r > p_0$, we perform a quantum jump according to the following routine:

   - calculate conditional probabilities p_j of quantum jumps as $p_j = \delta t \langle\psi(t_i)| \hat{A}_j^\dagger \hat{A}_j |\psi(t_i)\rangle / (1 - p_0)$
   - generate a random number r uniformly distributed between 0 and 1, and select the specific jump operator $\hat{A}_j$ such that $\sum_{k=1}^{j-1} p_k < r < \sum_{k=1}^{j} p_k$
   - perform a jump: set $|\psi(t_{i+1})\rangle = \frac{\hat{A}_j|\psi(t_i)\rangle}{\sqrt{\langle\psi(t_i)|\hat{A}_j^\dagger \hat{A}_j|\psi(t_i)\rangle}}$

6. Put $i \leftarrow i+1$ and repeat

This method allows some modifications. For example, instead of generating random number r and renormalizing the wave function $|\psi\rangle$ on each step, one may generate r once just after the jump, then let $|\psi(t)\rangle$ evolve under the action of the non-Hermitian Hamiltonian $\hat{\mathcal{H}}_{\text{eff}}$ while $\langle\psi(t)|\psi(t)\rangle > r$, and when the squared norm becomes equal to r, select a jump operator $\hat{A}_j$ with probability proportional to $\langle\psi(t)|\,\hat{A}^\dagger\hat{A}\,|\psi(t)\rangle$, perform the jump and renormalize the wave function.

2.3.3 Forces on Atom

As an example, we derive a radiative force acting on a 2-level atom in the field of two counter-propagating lasers. In this analysis, we will treat the atom's internal state quantum mechanically while assuming kinematics changes to be slow relative to the change of the atoms' internal state.

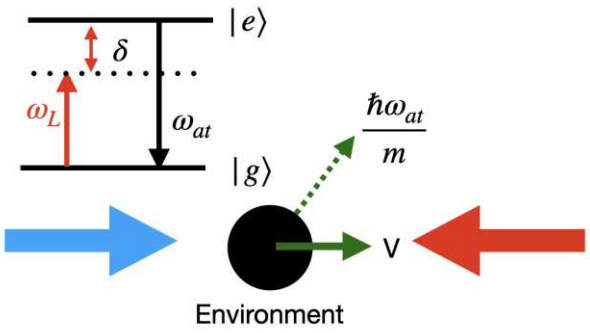

Figure 2.8: Schematics of Doppler Cooling.

We first derive the force by a single laser. The dynamics of its internal state in the electric field of the laser $\mathbf{E}(\mathbf{r}) = \frac{\mathbf{E_0}}{2}(e^{i(\mathbf{k}\cdot\mathbf{r}-\omega_L t)} + e^{-i(\mathbf{k}\cdot\mathbf{r}-\omega_L t)}) = E_0\cos(\omega_L t + \phi_L)\mathbf{r}/|\mathbf{r}|$ for a fixed position of the atom is governed by the master equation:

$$\frac{d}{dt}\hat{\rho} = \frac{1}{i\hbar}[\hat{\mathcal{H}},\hat{\rho}] + \frac{\gamma_s}{2}\hat{\hat{\mathcal{L}}}[\hat{\rho}], \tag{2.154}$$

where the Hamiltonian and the Lindbladian term are given by

$$\begin{aligned}\hat{\mathcal{H}} &= \hat{\mathcal{H}}_{at} + \hat{\mathcal{H}}_{int} = \frac{\hat{\mathbf{p}}^2}{2m} - \hbar\delta\hat{\sigma}_{ee} + \frac{\hbar}{2}(\Omega^*\hat{\sigma}_{ge} + \Omega\hat{\sigma}_{eg}),\\ \hat{\hat{\mathcal{L}}}[\hat{\sigma}_{ge}]\hat{\rho} &= (2\hat{\sigma}_{ge}\hat{\rho}\hat{\sigma}_{eg} - \hat{\sigma}_{ee}\hat{\rho} - \hat{\rho}\hat{\sigma}_{ee}).\end{aligned} \tag{2.155}$$

Where the $\hat{\mathcal{H}}_{int} = \frac{\hbar}{2}(\Omega^*\hat{\sigma}_{ge} + \Omega\hat{\sigma}_{eg})$. The complete set of equations associated with the internal state of the atom are

$$\begin{aligned}
\frac{d\rho_{gg}}{dt} &= \frac{i}{2}(\Omega\rho_{ge} - \Omega^*\rho_{eg}) + \gamma_s\rho_{ee} \\
\frac{d\rho_{ee}}{dt} &= -\frac{i}{2}(\Omega\rho_{ge} - \Omega^*\rho_{eg}) - \gamma_s\rho_{ee} \\
\frac{d\rho_{ge}}{dt} &= \frac{i}{2}\Omega^*(\rho_{gg} - \rho_{ee}) - \left(\frac{\gamma_s}{2} + i\delta\right)\rho_{ge} \\
\frac{d\rho_{eg}}{dt} &= \frac{i}{2}\Omega(\rho_{ee} - \rho_{gg}) - \left(\frac{\gamma_s}{2} - i\delta\right)\rho_{eg}
\end{aligned} \tag{2.156}$$

With ρ_{ij} representing the matrix elements $|i\rangle\langle j|$ for i, j belongs to e, g. These are called the optical Bloch equations where $\Omega = \frac{-eE_0}{\hbar}e^{i\phi_L} \propto e^{-\mathbf{k}\cdot\mathbf{r}}$ is the Rabi Frequency, and γ_s denotes the decay rate constant derived in 2.2

$$\gamma_s = \frac{4\omega^3|\mathbf{d}_{ge}|^2}{3\hbar c^3} \tag{2.157}$$

We define the population difference as $w = \rho_{gg} - \rho_{ee}$ and for steady state i.e. $\frac{dw}{dt} = 0$ we get

$$w = \frac{1}{1+s}, \quad \rho_{eg} = \frac{i\Omega}{2(\gamma_s/2 - i\delta)(1+s)}, \quad \rho_{ee} = \frac{s}{1+s} \tag{2.158}$$

with the saturation parameter s and on-resonance saturation parameter s_0 given by

$$s = \frac{s_0}{1 + (2\delta/\gamma_s)^2}, \quad s_0 = \frac{2|\Omega|^2}{\gamma_s^2} = \frac{I}{I_s}, \quad I_s = \frac{\pi\hbar\gamma_s c}{3\lambda^3}, \tag{2.159}$$

where I_s is the *saturation intensity*. The photon scattering rate is then calculated as:

$$\Gamma_p = \gamma_s\rho_{ee} = \frac{\gamma_s}{2}\left(\frac{s}{1+s}\right)\left(\frac{1}{1 + (2\delta/\gamma_s')^2}\right) \tag{2.160}$$

where $\gamma_s' = \gamma_s\sqrt{1+s_0}$ represents the power broadened linewidth.

To calculate the force on a stationary atom via a single laser beam we use the Ehrenfest theorem for the momentum operator. The kinematic part of the Hamiltonian commutes with the $\hat{\mathbf{p}}$. We assume that the expected contribution of spontaneous emission is zero because of the same likelihood in all the direction

$$\mathbf{F} = \frac{d}{dt}\langle\hat{\mathbf{p}}\rangle = -\langle\nabla\hat{\mathcal{H}}_{int}\rangle \tag{2.161}$$

In rotating frame with rotating wave approximation, defining operator $\hat{\Omega} = \Omega|e\rangle\langle g| + \Omega^*|g\rangle\langle e|$, we end up with the force expression

$$\begin{aligned}
F = \langle\nabla\hat{\Omega}\rangle &= \frac{\hbar}{2}\mathrm{Tr}\{\hat{\rho}(\nabla\hat{\Omega})\} \\
&= \frac{\hbar s}{1+s}\left(-\delta\frac{\nabla|\Omega|}{|\Omega|} + \frac{\gamma_s\nabla\phi_L}{2}\right) \\
&= \frac{\gamma_s}{2}\frac{\hbar k s}{1+s}
\end{aligned} \tag{2.162}$$

The force on a moving atom can be calculated by simply introducing the shift by the Doppler effect in the previous equation via a single laser beam. Note that the laser always accelerates the atom in the direction of the laser.

$$F = \frac{\gamma_s}{2}\frac{\hbar k s(v)}{1+s(v)}, \quad s(v) = \frac{s_0}{1+(2\delta - k_L \cdot v/\gamma_s)^2} \tag{2.163}$$

Instead of one laser, if we use two counter-propagating lasers, we can cool the atom. For low intensity, we can take $F = \frac{\gamma_s}{2}\hbar k s(v)$. For simplicity, in the case of one dimension, the force exerted on an atom via these two lasers can be expressed as.

$$F = \hbar k \frac{\gamma_s}{2}(s_+(v) - s_-(v)), \quad s_\pm(v) = \frac{s_0}{1+(2\delta \mp k_L \cdot v/\gamma_s)^2} \tag{2.164}$$

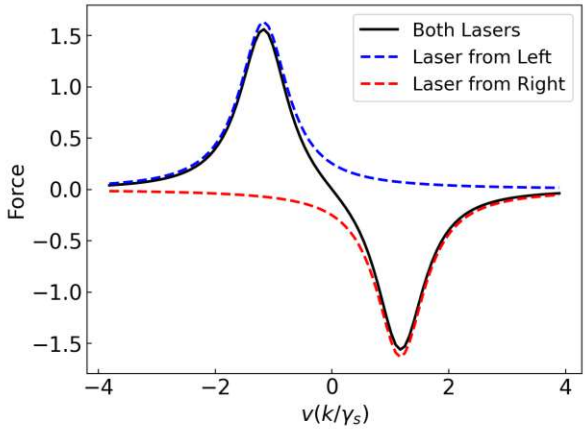

Figure 2.9: Strong damping forces for optimal detuning of $\delta = \gamma_s/2$.

This is called **Doppler cooling**, illustrated with the help of figure 2.8.

2.3.3.1 Quantum jump approach for Doppler Cooling

In the previous section, we have considered a qualitative model, but this model does not take into account recoils and can not be used for simulation of individual trajectories necessary to predict velocity distribution. For that, we need to use the Monte Carlo wave function method (MCWF) as described in section 2.3.2.2. Instead of the previous simpler description with the expected value, we will include the individual momentum kicks via spontaneous emission, and we will treat the motion of the atom classically coupled to a standing wave. We start our discussion by considering the Doppler cooling example from the documentation of [20]. The Hamiltonian of this system looks like

$$\hat{\mathcal{H}} = -\hbar\Delta\hat{\sigma}_{ee} + \hbar\cos(kx)(\hat{\sigma}_{eg} + \hat{\sigma}_{ge}) \tag{2.165}$$

Here, $\Delta = \omega_l - \omega_a$ is the detuning between the standing wave of frequency ω_L and the atomic transition frequency ω_a. The standing wave has an amplitude Ω. As mentioned in the previous section, the spontaneous emission of the atom occurs at a rate γ_s and is taken into account with

$$\hat{\hat{\mathcal{L}}}[\hat{\rho}] = \frac{\gamma_s}{2}(2\hat{\sigma}_{ge}\hat{\rho}\hat{\sigma}_{eg} - \hat{\sigma}_{ee}\hat{\rho} - \hat{\rho}\hat{\sigma}_{ee}) \tag{2.166}$$

As described in [20], the classical equations of motion for the atomic position x and its momentum p are given by

$$\begin{aligned} \frac{d}{dt}x &= \frac{p}{m} \\ \frac{d}{dt}p &= 2k\Omega\mathbf{R}\{\hat{\sigma}_{ge}\} \end{aligned} \tag{2.167}$$

In order to include the momentum kicks the atom experiences when spontaneously emitting a photon, we consider semi-classical MCWF approach where momentum kicks are added via a classical jump. The quantum mechanical states of an atom in the excited state with momentum p_0 is given by $|\psi\rangle = |e\rangle \otimes |p_0\rangle$. Now, after the spontaneous emission event a jump maps to the atomic internal state of $|g\rangle \otimes |p_0 - \hbar k\rangle$. Thus, the momentum expectation value changes when a jump occurs by

$$p = \langle\psi|\,\hat{p}\,|\psi\rangle = p_0 \to p_0 + \hbar k \tag{2.168}$$

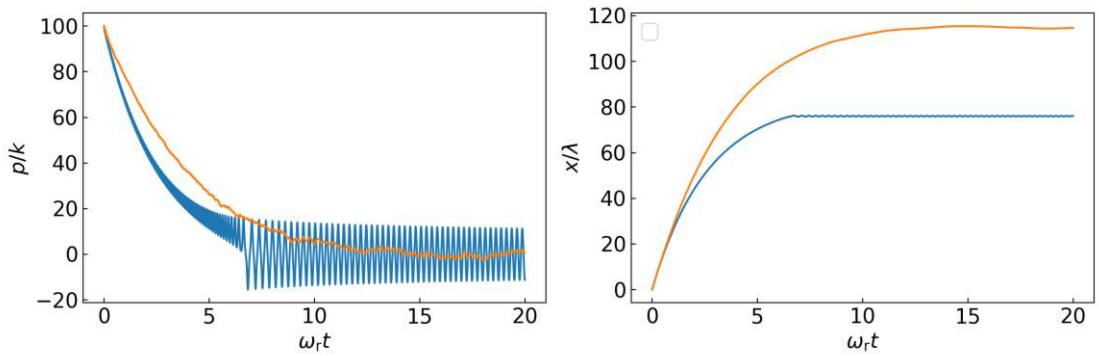

Figure 2.10: The Blue plot represents the solution of the equation of motion via the master equation (ME) without quantum jumps, and the orange plot represents an average of 100 trajectories, including the recoil from spontaneous emission. Note that the atoms are cooled until it is trapped around a field-antinode.

2.3.3.2 Semi Classical Monte Carlo

Another method to simulate individual trajectories is Semi Classical Monte Carlo (SCMC), which is the intermediate method between semi-classical force and semi-classical MCWF.

As defined in section 2.3.3.1, we use the position and velocity-dependent scattering rate Γ_p(2.160) to model jumps. For the system in consideration

$$\Gamma_p = \frac{1}{2}\frac{\gamma_s s(x,v)}{(1+s(x,v))}\left(1+4\left(\frac{\Delta - kv}{\gamma_s\sqrt{1+s(x,v)}}\right)^2\right)^{-1} \tag{2.169}$$

where

$$s(x,v) = \frac{2\Omega^2\cos(x)^2}{\gamma_s^2\left(1+\left(\frac{2(\Delta-kv)}{\gamma_s}\right)^2\right)} \tag{2.170}$$

The procedure consists of the following steps:

- Starting with an initial state (x_i, p_i) at time t_i we evolve the equation of motion (x,p) and the scattering rate $\Gamma_p(x,v)$ till $t_{i+1} = t_i + dt$.
- Generate a random number r_1 and r_2 in the interval [0,1] and [-1 or 1] respectively.
- If $r_1 > e^{-\Gamma_p(x,v)t_i}$ set $p_{i+1} = p_i - \hbar k + r_2\hbar k$ otherwise witout changing anything take another step.
- Repeat the above three steps until we reach the desired evolution time.

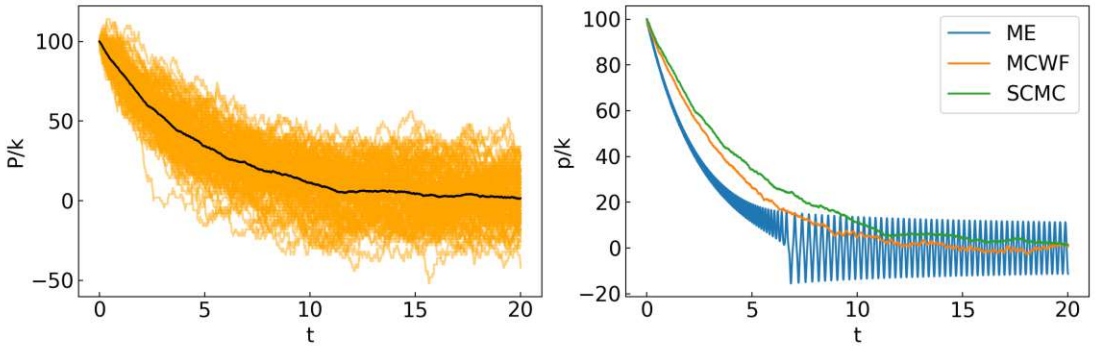

Figure 2.11: (a) shows 100 trajectories generated by SCMC and (b) presents a comparison between 3 methods ME, MCWF, SCMC with average of 100 trajectories.

In the case $\Gamma_p \ll \gamma_s$ we can assume that the instant atom absorbs a photon it spontaneously emits it. The figure 2.11 shows that the semi-classical Monte Carlo method gives more or less the same results as the semi-classical MCWF for maxima of Γ_p corresponding to $0.1\gamma_s$. However, it's more efficient in calculating multiple trajectories than semi-classical MCWF because we don't have to evolve the wave function, especially in the case of a complex system with many variables, as we will see in chapter 5.

2.3.4 Heisenberg-Langevin equations

Up to now we have considered equations for the density matrix, i.e., for the evolution of state, which corresponds to the Schrödinger picture. An alternative approach corresponds to the Heisenberg picture, where the operators are time-dependent. Equations for operators of the open quantum system are called *Heisenberg-Langevin equations*. Although these equations are operator equations and they are not convenient for direct numerical simulations, they can be used as a starting point for derivation of various approximate methods, such as c-number Langevin equations, semiclassical equations and cumulant expansion. In this section we derive the Heisenberg-Langevin equations primarily following the logic of the book [21] (ch. 9 - 11), the book [22] (ch. 9) and the paper [23].

First, let us specify the physical model. In contrast to the derivation of the master equation in section 2.3.1, we specify here a bit more details about the system and the bath; this is necessary to derive proper relations between different regular and stochastic terms in the Heisenberg-Langevin equations. As before, we consider a system (S) weakly coupled to the bath (B), and the whole Hamiltonian can be written as

$$\hat{\mathcal{H}} = \hat{\mathcal{H}}_S + \hat{\mathcal{H}}_B + \hat{\mathcal{H}}_{SB}. \tag{2.171}$$

The Hamiltonian $\hat{\mathcal{H}}_S$ of the system can be represented as

$$\hat{\mathcal{H}}_S = \hat{\mathcal{H}}_{S,0} + \hat{\mathcal{H}}_{S,1}, \tag{2.172}$$

where $\hat{\mathcal{H}}_{S,0}$ is the zero-order Hamiltonian of the system, whose eigenstates and eigenenergies are known, and $\hat{\mathcal{H}}_{S,1}$ which describes some non-trivial dynamics (like, for example, interaction with driving fields, or coupling between the atoms and the cavity mode).

The Hamiltonian $\hat{\mathcal{H}}_B$ describes the bath. Here we suppose that the bath consists of a huge amount of bosonic modes weakly coupled to the system

$$\hat{\mathcal{H}}_B = \hbar \sum_n \omega_n \hat{b}_n^\dagger \hat{b}_n, \quad [\hat{b}_n, \hat{b}_m^\dagger] = \delta_{nm}. \tag{2.173}$$

Here $\hat{b}_n^\dagger$, $\hat{b}_n$ are bosonic creation and annihilation operators.

The Hamiltonian $\hat{\mathcal{H}}_{SB}$ represents the interaction between the system and the bath. For the sake of simplicity, we consider here a case where the system has only a single channel of dissipation, i.e., the coupling of the system to the bath can be expressed as

$$\hat{\mathcal{H}}_{SB} = i\hbar \sum_n \kappa_n [\hat{b}_n^\dagger \hat{C} - \hat{C}^\dagger \hat{b}_n], \tag{2.174}$$

where $\hat{C}$ is a system operator that satisfies the commutation relation

$$[\hat{\mathcal{H}}_{S,0}, \hat{C}] = -\hbar\omega_0 \hat{C}. \tag{2.175}$$

The generalization of the derivation below to the case of several dissipative channels, where the system is coupled to the bath via several operators $\hat{C}_\alpha$, is straightforward if

these operators are well separated in frequency. The situation where these operators have close frequencies, and some of them can be coupled to the same bath modes is more cumbersome, and consideration of such systems lies beyond the scope of this thesis.

In this section, we consider the coarse-graining in time. It means that the minimal time scale Δt that we consider here is much less than the time necessary for a significant evolution of the system due to interaction with the bath and the "non-trivial" part $\hat{\mathcal{H}}_{S,1}$ of the system Hamiltonian, but is still much bigger than the typical inverse eigenfrequencies of the Hamiltonian $\hat{\mathcal{H}}_{S,0}$, particularly than $1/\omega_0$. It allows us to specify the frequency range ϑ around the transition frequency ω_0, which we call the *coupling bandwidth*. This bandwidth must fulfill two conditions. First, it should be small enough that the coupling κ_n between the bath modes and the system, as well as the density $g(\omega)$ of the bath modes, vary slightly and smoothly within this range. Second, it should be big enough, such that interaction of the system with the bath modes outside of this coupling bandwidth leads to very fast oscillations and vanishes in averaging over our coarse-grained time scale Δt. Usually, these conditions are fulfilled, if

$$\frac{1}{\Delta t} \ll \vartheta \ll \omega_0. \tag{2.176}$$

It allows us to restrict the interaction between the system and the bath only to the bath modes within the coupling bandwidth:

$$\hat{\mathcal{H}}_{SB} = i\hbar \sum_{n:|\omega_n-\omega_0|<\vartheta} \kappa(\omega_n)[\hat{b}_n^\dagger \hat{J} - \hat{J}^\dagger \hat{b}_n]. \tag{2.177}$$

Further, in this section, we consider only summation over the coupling bandwidth, and we will omit the condition $n : |\omega_n - \omega_0| < \vartheta$ for the indices of summation for the sake of brevity.

Substituting (2.177) into the Heisenberg equation for some system operator $\hat{A}$ gives

$$\frac{d\hat{A}}{dt} = \frac{i}{\hbar}[\hat{\mathcal{H}}, \hat{A}] = \frac{i}{\hbar}\left[\hat{\mathcal{H}}_S, \hat{A}\right] - \sum_n \kappa(\omega_n)[\hat{b}_n^\dagger[\hat{J}, \hat{A}] - [\hat{J}^\dagger, \hat{A}]\hat{b}_n]. \tag{2.178}$$

Similarly, the Heisenberg equations for bath operators $\hat{b}_n$, $\hat{b}_n^\dagger$ can be written as

$$\begin{aligned} \frac{d\hat{b}_n}{dt} &= -i\omega_n \hat{b}_n + \kappa(\omega_n)\hat{J}, \\ \frac{d\hat{b}_n^\dagger}{dt} &= i\omega_n \hat{b}_n^\dagger + \kappa(\omega_n)\hat{J}^\dagger, \end{aligned} \tag{2.179}$$

and their solutions can be written as

$$\begin{aligned} \hat{b}_n(t) &= e^{-i\omega_n(t-t_0)}\hat{b}_n(t_0) + \kappa(\omega_n)\int_{t_0}^{t} e^{-i\omega_n(t-t')}\hat{J}(t')dt', \\ \hat{b}_n^\dagger(t) &= e^{i\omega_n(t-t_0)}\hat{b}_n^\dagger(t_0) + \kappa(\omega_n)\int_{t_0}^{t} e^{i\omega_n(t-t')}\hat{J}^\dagger(t')dt'. \end{aligned} \tag{2.180}$$

Substituting (2.180) into (2.178), we get

$$\begin{aligned}\frac{d\hat{A}(t)}{dt} =& \frac{i}{\hbar}\left[\hat{\mathcal{H}}_S(t), \hat{A}(t)\right] + \hat{\xi}^\dagger(t)[\hat{A}(t), \hat{J}(t)] + [\hat{J}^\dagger(t), \hat{A}(t)]\hat{\xi}(t) \\ &+ \sum_n \kappa^2(\omega_n)\left(\int_{t_0}^{t} e^{i\omega_n(t-t')}\hat{J}^\dagger(t')dt'[\hat{A}(t), \hat{J}(t)]\right. \\ &\left. + [\hat{J}^\dagger(t), A(t)]\int_{t_0}^{t} e^{-i\omega_n(t-t')}\hat{J}(t')dt'\right),\end{aligned} \tag{2.181}$$

where we have introduced the *basic Langevin forces*

$$\begin{aligned}\hat{\xi}(t) =& \sum_n \kappa(\omega_n)e^{-i\omega_n(t-t_0)}\hat{b}_n(t_0), \\ \hat{\xi}^\dagger(t) =& \sum_n \kappa(\omega_n)e^{i\omega_n(t-t_0)}\hat{b}_n^\dagger(t_0).\end{aligned} \tag{2.182}$$

It is convenient to choose time t_0 such that, on the one hand, $|t-t_0|\vartheta \gg 1$ and, on the other hand, the evolution of the system on the timescale of $|t-t_0|$ is determined primarily by the operator $\hat{\mathcal{H}}_{S,0}$, therefore, in the integrands of (2.181) one may take

$$\begin{aligned}\hat{J}(t') &\approx \hat{J}(t)e^{i\omega_0(t-t')}, \\ \hat{J}^\dagger(t') &\approx \hat{J}^\dagger(t)e^{-i\omega_0(t-t')},\end{aligned} \tag{2.183}$$

that corresponds to the *Markov approximation* which we discussed in section 2.3.1. Approximation (2.183) allows to rewrite (2.181) as

$$\begin{aligned}\frac{d\hat{A}(t)}{dt} =& \frac{i}{\hbar}\left[\hat{\mathcal{H}}_S(t), \hat{A}(t)\right] + \hat{\xi}^\dagger(t)[\hat{A}(t), \hat{J}(t)] + [\hat{J}^\dagger(t), \hat{A}(t)]\hat{\xi}(t) \\ &+ \hat{J}^\dagger(t)[\hat{A}(t), \hat{J}(t)]\mathfrak{J} + [\hat{J}^\dagger(t), A(t)]\hat{J}(t)\mathfrak{J}^*,\end{aligned} \tag{2.184}$$

where

$$\mathfrak{J} = \sum_n \kappa^2(\omega_n)\int_{t_0}^{t} e^{i(\omega_n-\omega_0)(t-t')}dt'. \tag{2.185}$$

To calculate $\mathfrak{J}$, we replace summation over the bath modes by integral and put the lower limit $t_0 = t - T$ in integral over t to $-\infty$ formally. Then we can write

$$\mathfrak{J} = \lim_{T\to\infty}\int_{\omega_0-\vartheta}^{\omega_0+\vartheta}\kappa^2(\omega)g(\omega)\int_{t-T}^{t} e^{i(\omega-\omega_0)(t-t')}dt'd\omega, \tag{2.186}$$

where $g(\omega)$ is the density of states, which we suppose to be smooth and slightly varying in the interval $\omega_0 - \vartheta < \omega < \omega_0 - \vartheta$, as well as $\kappa^2(\omega)$. Then we can introduce $f(\omega) = g(\omega)\kappa^2(\omega)$ for the sake of brevity, and write

$$\begin{aligned}\mathfrak{J} &= \lim_{T\to\infty}\int_{\omega_0-\vartheta}^{\omega_0+\vartheta}\frac{1-e^{-i(\omega-\omega_0)T}}{i(\omega-\omega_0)}f(\omega)d\omega \\ &= \lim_{T\to\infty}\int_{\omega_0-\vartheta}^{\omega_0+\vartheta}\frac{1-\cos((\omega-\omega_0)T)}{i(\omega-\omega_0)}f(\omega)d\omega + \lim_{T\to\infty}\int_{\omega_0-\vartheta}^{\omega_0+\vartheta}\frac{\sin((\omega-\omega_0)T)}{\omega-\omega_0}f(\omega)d\omega.\end{aligned} \tag{2.187}$$

In the first integral in (2.187) we can omit $\cos((\omega-\omega_0)T)$, because the function $f(\omega)$ can be represented as $f(\omega) = f(\omega_0) + (f(\omega) - f(\omega_0))$, and the integral with $f(\omega_0)$ vanishes because the expression under the integral is odd with respect to the center of the interval, and the term $(f(\omega) - f(\omega_0))/(\omega - \omega_0)$ is limited; therefore, the oscillating term vanishes at $T \to \infty$ due to the Riemann-Lesbegue lemma. In the second integral, one may also represent $f(\omega) = f(\omega_0) + (f(\omega) - f(\omega_0))$, and again, the integral with $f(\omega) - f(\omega_0)$ vanishes due to the Riemann-Lesbegue lemma, whereas the integral with $f(\omega_0))$ becomes the (doubled) Dirichlet integral. Therefore, one can write

$$\mathfrak{J} = \pi\kappa^2(\omega_0)g(\omega_0) - i\,\text{v.p.}\int\limits_{\omega_0-\vartheta}^{\omega_0+\vartheta}\frac{\kappa^2(\omega)g(\omega)}{\omega-\omega_0}d\omega, \tag{2.188}$$

where v.p. stands for Cauchy principal value. Substituting (2.188) into (2.184), we get to

$$\begin{aligned}\frac{d\hat{A}}{dt} =& \frac{i}{\hbar}\left[\hat{\mathcal{H}}_S + \hat{\mathcal{H}}_{LS}, \hat{A}\right] + \hat{\xi}^\dagger[\hat{A},\hat{J}] + [\hat{J}^\dagger,\hat{A}]\hat{\xi} \\ &+ \frac{\gamma}{2}\left(2\hat{J}^\dagger\hat{A}\hat{J} - \hat{A}\hat{J}^\dagger\hat{J} - \hat{J}^\dagger\hat{J}\hat{A}\right),\end{aligned} \tag{2.189}$$

where all the operators are taken at t, and we introduced the *relaxation rate* γ as

$$\gamma = 2\pi\kappa^2(\omega_0)g(\omega_0) \tag{2.190}$$

Lamb shift Hamiltonian $\hat{\mathcal{H}}_{LS}$ as

$$\hat{\mathcal{H}}_{LS} = \hbar\hat{J}^\dagger\hat{J}\,\text{v.p.}\int\limits_{\omega_0-\vartheta}^{\omega_0+\vartheta}\frac{\kappa^2(\omega)g(\omega)}{\omega-\omega_0}d\omega. \tag{2.191}$$

One may show that the Hamiltonian (2.191) corresponds to the Hamiltonian (2.135), if the interaction between the bath and the system is specified as here. Further, we are not interested in $\hat{\mathcal{H}}_{SL}$, supposing that it is added into $\hat{\mathcal{H}}_S$.

Let us consider basic Langevin forces (2.182). Using the same approach as in the derivation (2.186) – (2.188), we can show that

$$\begin{aligned}[\hat{\xi}(t), \hat{\xi}^\dagger(t')] &= \gamma\delta(t-t'), \\ \langle\hat{\xi}(t)\hat{\xi}^\dagger(t')\rangle &= (N_T+1)\gamma\delta(t-t'), \\ \langle\hat{\xi}^\dagger(t)\hat{\xi}(t')\rangle &= N_T\gamma\delta(t-t'),\end{aligned} \tag{2.192}$$

where N_T is the average occupation number of the bath mode with frequency ω_0 (we suppose the thermal bath), and the time t is considered as coarse-grained, i.e., if $t \neq t'$, then $|t-t'|\vartheta \gg 1$.

Now we consider the commutation relation between the system operator $\hat{A}(t)$ and the basic Langevin force $\xi(t')$. Using (2.182), and expressing $\hat{b}_n(t_0)$ via $\hat{b}_n(t)$ with the help of

(2.180) and bosonic commutation relations (2.173), we can write

$$\begin{aligned}[\hat{A}(t),\hat{\xi}(t')] =& \sum_n \kappa(\omega_n) e^{-i\omega_n(t'-t_0)} [\hat{A}(t),\hat{b}_n(t_0)] = \sum_n \kappa(\omega_n) e^{-i\omega_n(t'-t_0)} \\ =& \left[\hat{A}(t), \left(\hat{b}_n(t) - \kappa(\omega_n)\int_{t_0}^{t} e^{-i\omega_n(t-t'')}\hat{J}(t'')dt''\right) e^{i\omega_n(t'-t_0)}\right].\end{aligned} \tag{2.193}$$

Using the Markov approximation $\hat{J}(t'') \approx \hat{J}(t')e^{i\omega_0(t'-t'')}$ and replacing summation over modes by integration, we get

$$\begin{aligned}[\hat{A}(t),\hat{\xi}(t')] =& -[\hat{A}(t),\hat{J}(t')]\int_{\omega_0-\vartheta}^{\omega_0+\vartheta} f(\omega)\int_{t_0}^{t} e^{i(\omega_0-\omega)(t'-t'')}dt''d\omega \\ =& -[\hat{A}(t),\hat{J}(t')]\int_{-\vartheta}^{\vartheta} f(\omega_0+\vartheta)\frac{e^{i\Omega(t-t')} - e^{-i\Omega(t'-t_0)}}{i\Omega}d\Omega,\end{aligned} \tag{2.194}$$

where, as before, $f(\omega) = \kappa^2(\omega) + g(\omega)$. Neglecting the variation of $f(\omega)$ on the interval $\omega_0 - \vartheta < \omega < \omega_0 + \vartheta$, we replace $f(\omega)$ by $f(\omega_0) = \gamma/(2\pi)$. Then, using the symmetry properties of the integrand in (2.194), we can write

$$\begin{aligned}[\hat{A}(t),\hat{\xi}(t')] = -[\hat{A}(t),\hat{J}(t')]\frac{\gamma}{2\pi} \\ \times\left[\int_{-\vartheta}^{\vartheta}\frac{\sin(\Omega(t-t'))}{\Omega}d\Omega + \int_{-\vartheta}^{\vartheta}\frac{\sin(\Omega(t'-t_0))}{\Omega}d\Omega\right].\end{aligned} \tag{2.195}$$

In the coarse-grained time resolution, we can replace the limits of the integration from $[-\theta,\theta]$ to $(-\infty,\infty)$. Then the integrals in the square brackets become doubled Dirichlet integrals, and we can write

$$\begin{aligned}[\hat{A}(t),\hat{\xi}(t')] =& -\pi[\hat{A}(t),\hat{J}(t')]\frac{\gamma}{2\pi}(\mathrm{sign}(t-t') + \mathrm{sign}(t'-t_0)). \\ =& -\gamma[\hat{A}(t),\hat{J}(t')]u(t-t'),\end{aligned} \tag{2.196}$$

where

$$u(\tau) = \begin{cases} 1, & \tau > 0 \\ \frac{1}{2}, & \tau = 0 \\ 0, & \tau < 0 \end{cases} \tag{2.197}$$

This result may be interpreted as the causality, i.e., the influence of the quantum noise terms in preceding instants of time on the system in the subsequent instants of time. However, there is a non-zero commutator at $t = t'$. This is because the equation (2.189) are the quantum stochastic equations in Stratonovich form. It is more convenient to go from the Stratonovich to the Itô form, where the noise terms $\hat{\xi}(t)$, $\hat{\xi}^\dagger(t)$ should be taken not "simultaneously", but "a little bit after" the instant t, then the commutator $[\hat{A}(t),\hat{\xi}(t)] = 0$. One may show [23], that such a transition leads to modification of the regular part in the equation (2.189), and it transforms to

$$\begin{aligned}\mathrm{I}\,\frac{d\hat{A}}{dt} =& \frac{i}{\hbar}\left[\hat{\mathcal{H}}_S,\hat{A}\right] + \hat{\xi}^\dagger[\hat{A},\hat{J}] + [\hat{J}^\dagger,\hat{A}]\hat{\xi} + \frac{\gamma}{2}\left[N_T\left(2\hat{J}\hat{A}\hat{J}^\dagger - \hat{A}\hat{J}\hat{J}^\dagger - \hat{J}\hat{J}^\dagger\hat{A}\right)\right. \\ &\left.+(N_T+1)\left(2\hat{J}^\dagger\hat{A}\hat{J} - \hat{A}\hat{J}^\dagger\hat{J} - \hat{J}^\dagger\hat{J}\hat{A}\right)\right],\end{aligned} \tag{2.198}$$

where I stands for Itô form, $[\hat{A}(t), \hat{\xi}(t)] = [\hat{A}(t), \hat{\xi}^\dagger(t)] = 0$, and we have included $\hat{\mathcal{H}}_{LS}$ in $\hat{\mathcal{H}}_S$. Interestingly, at $N_T = 0$ both the Stratonovic (2.189) and the Itô (2.198) forms of the Langevin equation coincide.

Finally, we should note that moving from the Heisenberg to the Schrödinger picture and performing averaging over the bath degrees of freedom (which are independent of the system operators), we can obtain the master equation corresponding to (2.198) in the form

$$\begin{aligned}\frac{d\hat{\rho}}{dt} = &-\frac{i}{\hbar}\left[\hat{\mathcal{H}}_S, \hat{\rho}\right] + \frac{\gamma}{2}\Big[N_T\left(2\hat{J}^\dagger\hat{\rho}\hat{J} - \hat{\rho}\hat{J}\hat{J}^\dagger - \hat{J}\hat{J}^\dagger\hat{\rho}\right)\\ &+(N_T+1)\left(2\hat{J}\hat{\rho}\hat{J}^\dagger - \hat{\rho}\hat{J}^\dagger\hat{J} - \hat{J}^\dagger\hat{J}\hat{\rho}\right)\Big].\end{aligned} \tag{2.199}$$

If $k_B T \ll \hbar\omega_0$, we can put $N_T = 0$, and obtain the master equation similar to (2.138). This is the most relevant case for the thesis, and further, we put $N_T = 0$.

Generalizing the equation (2.198) to the case of multiple independent dissipation processes with jump operators $\hat{J}_k$ and rates γ_k, we get the Heisenberg-Langevin equations in the form

$$\frac{d\hat{A}}{dt} = \frac{i}{\hbar}\left[\hat{\mathcal{H}}_S, \hat{A}\right] + \hat{F}_A + \sum_k \gamma_k \hat{\hat{\mathfrak{D}}}[\hat{J}_k]\hat{A}, \tag{2.200}$$

where the *Langevin force* $\hat{F}_A$ corresponding to operator $\hat{A}$ is expressed via the basic Langevin forces $\hat{\xi}$, $\hat{\xi}^\dagger$ as

$$\hat{F}_A = \sum_k \left(\hat{\xi}_k^\dagger[\hat{A}, \hat{J}_k] + [\hat{J}_k^\dagger, \hat{A}]\hat{\xi}_k\right), \tag{2.201}$$

the superoperator $\hat{\hat{\mathfrak{D}}}$ and the commutation relations are

$$\hat{\hat{\mathfrak{D}}}[\hat{J}]\hat{A} = \hat{J}^\dagger\hat{A}\hat{J} - \frac{1}{2}(\hat{J}^\dagger\hat{J}\hat{A} + \hat{A}\hat{J}^\dagger\hat{J}), \tag{2.202}$$

$$[\hat{\xi}_k(t), \hat{\xi}_j^\dagger(t')] = \gamma_k\delta_{kj}\delta(t-t'), \quad [\hat{\xi}_k, \hat{\xi}_j] = [\hat{\xi}_k^\dagger, \hat{\xi}_j^\dagger] = [\hat{\xi}_k^\dagger, \hat{\xi}_j] = 0, \tag{2.203}$$

and $[\hat{A}(t), \hat{\xi}_k(t)] = 0$. Now, consider another operator $\hat{B}$. The associated *Langevin force* will look like

$$\hat{F}_B = \sum_k \left(\hat{\xi}_k^\dagger[\hat{B}, \hat{J}_k] + [\hat{J}_k^\dagger, \hat{B}]\hat{\xi}_k\right), \tag{2.204}$$

Using the commutation relations given in (2.192) and (2.203) and taking occupation numbers of the respective cavity modes $N_{T,k} = 0$, one can calculate the correlation between these two forces as

$$\langle\hat{F}_B(t)\hat{F}_A(t')\rangle = \sum_k \gamma_k\langle[\hat{J}_k^\dagger, \hat{B}][\hat{A}, \hat{J}_k]\rangle\delta(t-t') = 2\mathcal{D}_{AB}\delta(t-t') \tag{2.205}$$

Where $\mathcal{D}_{AB} = \sum_k \gamma_k \langle [\hat{J}_k^\dagger, \hat{B}][\hat{A}, \hat{J}_k] \rangle / 2$ is the diffusion matrix.

Similarly, the master equation (2.199) can be generalized to the case of multiple dissipation processes at $N_T = 0$ as

$$\frac{d\hat{\rho}}{dt} = -\frac{i}{\hbar}\left[\hat{\mathcal{H}}_S, \hat{\rho}\right] + \sum_k \gamma_k \hat{\hat{\mathfrak{D}}}'[\hat{J}_k]\hat{\rho}, \tag{2.206}$$

where the superoperator $\hat{\hat{\mathfrak{D}}}'$ is defined in (2.137).

Finally, we should note that the relaxation terms are invariant to unitary transformations. This concludes all the basic tools we need to perform quantitative modeling of a continuous superradiant laser. In the next chapter we will discuss different methods to perform simulation for a superradiant signal.

CHAPTER 3

Methods of simulation of superradiant lasers

Active optical clocks are based on a bad-cavity laser operating in the bad-cavity regime, often called also *superradiant laser*. Development of such clocks requires an understanding of different processes in the laser, simulation of its parameters, and optimization of physical parameters of the laser in order to achieve the best characteristics of the output radiation, such as satisfactory output power, minimal linewidth, robustness to fluctuations of environmental parameters, etc. However, a direct solution of the master equation for a laser containing about 10^4 – 10^8 atoms interacting with the cavity mode seems to be impossible because of the exponential growth of the respective Hilbert space. Therefore, one has to use approximate methods.

In this chapter, we consider and compare various approximate methods for the simulation of the output field of the superradiant lasers. The simplest and probably the most straightforward method is the *semiclassical*, or the *mean-field* approach, where the correlations between individual atoms are neglected, and the density matrix is supposed to be separable, i.e., representable as a product of density matrices of individual atoms and the field. This method allows us to calculate the number of intracavity photons, the intensity of the output field, the sensitivity of this field to variation of different environmental parameters, and the cavity pulling coefficient. However, this method does not allow the calculation of the linewidth of the output radiation and, therefore, the stability of the active optical clock. Another method is based on the *c-number Langevin equations*. Here, the mean-field equations are modified by adding of stochastic components, the so-called *Langevin forces*, to account for the quantum noise. The third method that we consider here is the *second-order cumulant expansion* approach, where pair correlations between individual atoms are also taken into account. Finally, we describe a method of explicit solution of the master equation for a homogeneous ensemble of a relatively small (several tens) number of 2-level atoms interacting with the cavity

mode. In this case, due to the symmetry of the system, the size of the Hilbert space grows not exponentially but polynomially with the number N of the atoms.

This chapter consists of 7 sections. In section 3.1, we introduce the quantum master equation for a homogeneous ensemble of N 2-level atoms interacting with a single-mode cavity field, a system that will be used to test different simulation methods. In section 3.2, we discuss how to calculate the linewidth of the output radiation of the superradiance laser. In section 3.3, we derive the quantum Langevin equations. In sections 3.4 and 3.5, we utilize these equations to derive the c-number Langevin equations and the mean-field equations, respectively. In section 3.6, we introduce the second-order Cumulant theory. section 3.7 covers the complete quantum description of a homogeneous system, and finally, in section 3.8, we compare these different methods.

3.1 Master equation of a bad-cavity Laser

We start our discussion from the Master equation for an ensemble of N two-level atoms confined in space and homogeneously coupled to a single cavity mode:

$$\frac{d}{dt}\hat{\rho} = \frac{1}{i\hbar}[\hat{\mathcal{H}}, \hat{\rho}] + \hat{\hat{\mathcal{L}}}[\hat{\rho}]. \tag{3.1}$$

The Hamiltonian $\hat{\mathcal{H}}$ of our system in the rotating frame is given by

$$\hat{\mathcal{H}} = \hbar\Delta_a \sum_{j=1}^{N} \hat{\sigma}_{ee}^{j} + \hbar\delta_c \hat{a}^\dagger \hat{a} + \hbar g \sum_{j=1}^{N} \left(\hat{a}^\dagger \hat{\sigma}_{ge}^{j} + \hat{a}\hat{\sigma}_{eg}^{j} \right), \tag{3.2}$$

where $\hat{a}^\dagger$ and $\hat{a}$ are the cavity field creation and annihilation operators, index j runs over the atoms, $\hat{\sigma}_{\alpha\beta}^{j} = |\alpha^j\rangle\langle\beta^j| \bigotimes_{k\neq j} \hat{I}^k$ are single-atom transition (for $\alpha \neq \beta$) or projection (for $\alpha = \beta$) operators, $|\alpha^j\rangle$ and $|\beta^j\rangle$ run over ground ($|g^j\rangle$) and excited ($|e^j\rangle$) states of jth atom, g is the coupling strength between the atoms and the field, $\Delta_a = \omega_a - \omega$ is the shift of the atomic transition frequency ω_a from the frequency ω of our rotating frame, and $\delta_c = \omega_c - \omega$ is the respective shift of the cavity resonance frequency ω_c from ω.

The dissipative processes are described by the Liouvillian term

$$\hat{\hat{\mathcal{L}}}\hat{\rho} = \kappa\hat{\hat{\mathfrak{D}}}'[\hat{a}]\hat{\rho} + \sum_{j=1}^{N} \left(\gamma_s \hat{\hat{\mathfrak{D}}}'[\hat{\sigma}_{ge}^{j}]\hat{\rho} + \nu\hat{\hat{\mathfrak{D}}}'[\hat{\sigma}_{ee}^{j}]\hat{\rho} + R\hat{\hat{\mathfrak{D}}}'[\hat{\sigma}_{eg}^{j}]\hat{\rho} \right), \tag{3.3}$$

where $\hat{\hat{\mathfrak{D}}}'[\hat{O}]\hat{\rho} = \hat{O}\hat{\rho}\hat{O}^\dagger - \frac{1}{2}(\hat{O}^\dagger\hat{O}\hat{\rho} + \hat{\rho}\hat{O}^\dagger\hat{O})$ is the Lindbladian superoperator (2.137), κ is the decay rate of the energy of the cavity field, γ_s is the spontaneous emission rate, R is the rate of incoherent repumping of the atoms from the ground into the excited state (modeled by an "inverse spontaneous decay decay"), ν is the rate of additional dephasing process of the atomic dipole.

3.2 Spectrum and linewidth

3.2.1 Filter cavity and power spectral density

One of the most important properties of laser radiation is its spectrum. Following [24], the spectrum of some field $\hat{a}$ can be determined with the help of an additional *filter cavity* weakly coupled to this field. The resonant frequency of the filter cavity can be scanned near the central frequency of the field, and the number of photons in the filter cavity will represent the spectrum of the field.

The Hamiltonian of the filter cavity coupled to the field of the "main" laser cavity (in frame co-rotating with the rotating frame of the superradiant laser output, or some other rotating frame) is

$$\hat{\mathcal{H}}_f = \hbar(\delta_f \hat{b}^\dagger \hat{b} + G(\hat{a}^+ \hat{b} + \hat{a}\hat{b}^\dagger)), \tag{3.4}$$

where $\delta_f = \omega_f - \omega$ is the detuning of the filter cavity, and G is the coupling strength between the filter cavity and the main cavity. There is also an additional relaxation term

$$\hat{\hat{\mathcal{L}}}_f[\hat{\rho}] = -\frac{\beta}{2}\left(\hat{b}^\dagger \hat{b}\hat{\rho} + \hat{\rho}\hat{b}^\dagger \hat{b} - 2\hat{b}\hat{\rho}\hat{b}^\dagger\right). \tag{3.5}$$

The coupling strength G and the decay rate β are supposed to be extremely small. Then the equations for the operators $\hat{b}$ and $\hat{b}^\dagger$ are:

$$\begin{aligned}\frac{d\hat{b}}{dt} =& \frac{i}{\hbar}[\hat{\mathcal{H}}_f, \hat{b}] - \frac{\beta}{2}\left(\hat{b}^\dagger \hat{b}\hat{b} + \hat{b}\hat{b}^\dagger \hat{b} - 2\hat{b}^\dagger \hat{b}\hat{b}\right) + \hat{F}_f \\ =& -i\delta_f \hat{b} - iG\hat{a} - \frac{\beta}{2}\hat{b} + \hat{F}_f, \end{aligned} \tag{3.6}$$

$$\frac{d\hat{b}^\dagger}{dt} = i\delta_f \hat{b}^\dagger + iG\hat{a}^+ - \frac{\beta}{2}\hat{b}^\dagger + \hat{F}_{f^+}. \tag{3.7}$$

We can write the solutions of these equations as

$$\hat{b}(t) = \int_{-\infty}^{t} e^{-(\frac{\beta}{2}+i\delta_f)(t-t')}\left(-iG\hat{a}(t') + \hat{F}_f(t')\right)dt' \tag{3.8}$$

$$\hat{b}^\dagger(t) = \int_{-\infty}^{t} e^{-(\frac{\beta}{2}-i\delta_f)(t-t'')}\left(iG\hat{a}^+(t'') + \hat{F}_{f^+}(t'')\right)dt'' \tag{3.9}$$

therefore, the average number of photons in the filter cavity is

$$\langle \hat{b}^\dagger(t)\hat{b}(t)\rangle = \int_{-\infty}^{t}\int_{-\infty}^{t} e^{-\frac{\beta}{2}(2t-t'-t'')}e^{i\delta_f(t'-t'')}\left(G^2\langle \hat{a}^+(t'')\hat{a}(t')\rangle + \langle \hat{F}_{f^+}(t'')\hat{F}_f(t')\rangle\right)dt'dt'' \tag{3.10}$$

Note that in low temperature limit $\langle \hat{F}_{f^+}(t'')\hat{F}_f(t')\rangle = 0$. In a stationary regime one may take $t = 0$, and introduce

$$R(\tau) = \langle \hat{a}^+(t+\tau)\hat{a}(t)\rangle \qquad \tau = t'' - t' \qquad T = -\frac{t'+t''}{2} \tag{3.11}$$

Using the following transformation of a double integral

$$\begin{aligned}\int_{-\infty}^{0}\int_{-\infty}^{0} f(t',t'')dt'dt'' &= \int_{0}^{\infty}\int_{-2T}^{2T} f\left(-T+\frac{\tau}{2},-T-\frac{\tau}{2}\right)d\tau\, dT \\ &= \int_{-\infty}^{\infty}\int_{|\tau|/2}^{\infty} f\left(-T+\frac{\tau}{2},-T-\frac{\tau}{2}\right)dT\, d\tau,\end{aligned} \tag{3.12}$$

the fact that β is small (in comparison with the decay rate of 2-time correlation function $R(\tau)$), and using $R(\tau) = R^*(-\tau)$, we can rewrite (3.10) as

$$\begin{aligned}\langle \hat{b}^\dagger(0)\hat{b}(0)\rangle &= \int_{-\infty}^{\infty}\int_{|\tau|/2}^{\infty} e^{-\beta T}dT e^{-i\delta_f\tau}G^2R(\tau)d\tau = \int_{-\infty}^{\infty}\frac{\exp[-\beta|\tau|/2]}{\beta}e^{-i\delta_f\tau}G^2R(\tau)d\tau \\ &\approx \frac{G^2}{\beta}\int_{-\infty}^{\infty} e^{-i\delta_f\tau}R(\tau)d\tau = \frac{G^2}{\beta}\int_0^\infty R(\tau)e^{-i\delta_f\tau}d\tau + \frac{G^2}{\beta}\int_0^\infty R^*(\tau)e^{i\delta_f\tau}d\tau \\ &= \frac{2G^2}{\beta}\mathrm{Re}\left\{\int_0^\infty R(\tau)e^{-i\delta_f\tau}d\tau\right\}\end{aligned} \tag{3.13}$$

This expression coincides, up to a constant factor, with the 2-sided the power spectral density $S_E(f + \delta_f/(2\pi))$, (where $f = \omega/(2\pi)$) expressed via the 2-times correlation function according to the Wiener-Khintchine theorem (see, for example, [25], section 3.1):

$$\begin{aligned}S_E(f+\delta_f/(2\pi)) &= \int_{-\infty}^{\infty} R(\tau)e^{-i\delta_f\tau}d\tau = \int_{-\infty}^{0} R(\tau)e^{-i\delta_f\tau}d\tau + \int_0^\infty R(\tau)e^{-i\delta_f\tau}d\tau \\ &= \int_0^\infty R(-\tau)e^{i\delta_f\tau}d\tau + \int_0^\infty R(\tau)e^{-i\delta_f\tau}d\tau = 2\mathrm{Re}\int_0^\infty R(\tau)e^{-i\delta_f\tau}d\tau,\end{aligned} \tag{3.14}$$

(note that in our case $R(\tau)$ is calculated in the rotating frame, in contrast to [25]).

Consider a simple but very important case of exponentially decaying 2-time correlation function in the form

$$R(\tau) = R_0 e^{-(\lambda - i\delta_0)\tau} \tag{3.15}$$

Then the number of photons in the filter cavity is proportional to

$$S_E(f+\delta_f/(2\pi)) \propto \mathrm{Re}\int_0^\infty e^{-(\lambda+i(\delta_f-\delta_0))\tau}d\tau = \frac{\lambda}{\lambda^2+(\delta_f-\delta_0)^2}. \tag{3.16}$$

This corresponds to the Lorentzian spectrum with full-width half-maximum (FWHM) equal to 2λ and the center of the line shifted to δ_0 from the frequency ω of our rotating frame. In other words, in a laser with Lorentzian spectrum, the 2-times correlation function $R(\tau)$ decays as

$$|R(\tau)| = R(0)e^{-\frac{\text{FWHM}}{2}\tau}. \tag{3.17}$$

3.2.2 Quantum regression theorem

Here we will state a useful theorem named the *Onsager-Lax*, or *Quantum Regression Theorem*. Consider, for the sake of simplicity, some closed quantum system without dissipations. Then the two-time correlation function between two operators, say $\hat{A}_1$ and $\hat{A}_2$, can be calculated as

$$\begin{aligned}\langle \hat{A}_1(t+\tau)\hat{A}_2(t)\rangle &= \text{Tr}\{e^{\frac{i}{\hbar}\hat{\mathcal{H}}\tau}\hat{A}_1(t)e^{-\frac{i}{\hbar}\hat{\mathcal{H}}\tau}\hat{A}_2(t)\hat{\rho}\}\\ &= \text{Tr}\{e^{-\frac{i}{\hbar}\hat{\mathcal{H}}\tau}\hat{A}_2(t)\hat{\rho}e^{\frac{i}{\hbar}\hat{\mathcal{H}}\tau}\hat{A}_1(t)\}\\ &= \text{Tr}\{\hat{S}(\tau)\hat{A}_1(t)\},\end{aligned} \tag{3.18}$$

Where we introduced a "fictional" density matrix

$$\hat{S}(\tau) = e^{-\frac{i}{\hbar}\hat{\mathcal{H}}\tau}\hat{A}_2(t)\hat{\rho}e^{\frac{i}{\hbar}\hat{\mathcal{H}}\tau}. \tag{3.19}$$

Then the evolution of 2-time correlation function $\langle \hat{A}_1(t+\tau)\hat{A}_2(t)\rangle$ is equivalent to evolution of the mean value of operator $\hat{A}_1$ in fictional "ensemble of systems" described by the "fictional" density matrix $\hat{S}(t)$ such that

$$\hat{S}(0) = \hat{A}_2(t)\rho(t), \tag{3.20}$$

and governed by the same master equation, as the "true" density matrix ρ:

$$\frac{d}{d\tau}\langle \hat{A}_1(t+\tau)\hat{A}_2(t)\rangle = \text{Tr}\left\{\left(\frac{d}{d\tau}\hat{S}(\tau)\right)\hat{A}_1(t)\right\}. \tag{3.21}$$

It is easy to see that the consideration presented above remains valid if the master equation governing the system also contains dissipative terms.

3.3 Quantum Langevin equations

The quantum Langevin equations are the equations for operators of the system in the Heisenberg picture. The overview of these equations was given in the section 2.3.4. Now we are interested in the following operators describing the ensemble of N 2-levels atoms coupled to the cavity: cavity field annihilation and creation operators $\hat{a}$ and $\hat{a}^\dagger$, atomic polarizations $J^- = \frac{1}{N}\sum_{j=1}^N \hat{\sigma}_{ge}^j$, $J^+ = \frac{1}{N}\sum_{j=1}^N \hat{\sigma}_{eg}^j$ and inversion $J^z = \frac{1}{N}\sum_{j=1}^N \hat{\sigma}_z^j$, where

$\hat{\sigma}_z^j = \hat{\sigma}_{ee}^j - \hat{\sigma}_{gg}^j$. The Heisenberg-Langevin equations for these operators are given by

$$\frac{d}{dt}\hat{a} = -\frac{1}{2}(\kappa + 2i\delta_c)\hat{a} - iNg\hat{J}^- + \hat{F}_a, \tag{3.22}$$

$$\frac{d}{dt}\hat{a}^\dagger = -\frac{1}{2}(\kappa - 2i\delta_c)\hat{a}^\dagger + iNg\hat{J}^+ + \hat{F}_{a\dagger}, \tag{3.23}$$

$$\frac{d}{dt}\hat{J}^- = -\frac{1}{2}(\Gamma + 2i\Delta_a)\hat{J}^- + ig\hat{a}\hat{J}^z + \hat{F}_-, \tag{3.24}$$

$$\frac{d}{dt}\hat{J}^+ = -\frac{1}{2}(\Gamma - 2i\Delta_a)\hat{J}^+ - ig\hat{a}^\dagger\hat{J}^z + \hat{F}_+, \tag{3.25}$$

$$\frac{d}{dt}\hat{J}^z = -(R + \gamma_s)(\hat{J}^z - d_0) + i2g(\hat{a}^\dagger\hat{J}^- - \hat{a}\hat{J}^+) + \hat{F}_z. \tag{3.26}$$

Where $d_0 = \frac{R-\gamma_s}{R+\gamma_s}$ and $\Gamma = R + \gamma_s + \nu$. Here we also introduced *Langevin forces* which can be expressed via the *basic Langevin forces* $\hat{\xi}_\alpha$ as (2.200) For our system, the non-zero elements of the diffusion matrix can be easily calculated using (2.205):

$$\begin{aligned}
&2\mathcal{D}_{\hat{a}\hat{a}^\dagger} = \kappa, \quad 2\mathcal{D}_{+-} = \frac{1}{N}\left(R + \frac{\nu}{2}(1 + \langle\hat{J}^z\rangle)\right), \quad 2\mathcal{D}_{-+} = \frac{1}{N}\left(\gamma_s + \frac{\nu}{2}(1 - \langle\hat{J}^z\rangle)\right),\\
&2\mathcal{D}_{+z} = -\frac{2R}{N}\langle\hat{J}^+\rangle, \quad 2\mathcal{D}_{z-} = -\frac{2R}{N}\langle\hat{J}^-\rangle, \quad 2\mathcal{D}_{-z} = \frac{2\gamma_s}{N}\langle\hat{J}^-\rangle, \quad 2\mathcal{D}_{z+} = \frac{2\gamma_s}{N}\langle\hat{J}^+\rangle,\\
&2\mathcal{D}_{zz} = \frac{2\gamma_s}{N}(1 + \langle\hat{J}^z\rangle) + \frac{2R}{N}(1 - \langle\hat{J}^z\rangle).
\end{aligned} \tag{3.27}$$

3.3.1 Adiabatic elimination of the cavity field

We are interested in the "deep bad cavity regime", where the cavity decay rate κ is much bigger than any other rates associated with different processes involved. In this case the cavity mode follows adiabatically the state of the atoms, and equations for this mode can be eliminated.

By integrating the cavity field variable from equation (3.22) we get

$$\hat{a}(t) = -iNg\int_{-\infty}^{t} e^{-\frac{(\kappa+2i\delta_c)(t-t')}{2}}\hat{J}^-(t')dt' + \mathrm{I}\int_{-\infty}^{t} e^{-\frac{(\kappa+2i\delta_c)(t-t')}{2}}\hat{F}_a(t')dt'. \tag{3.28}$$

Using partial integration, we can expand the integral in the first term of (3.28) as

$$\int_0^t e^{-\frac{(\kappa+2i\delta_c)(t-t')}{2}}\hat{J}^-(t')dt' = \frac{2}{\kappa + 2i\delta_c}\hat{J}^-(t) - \left(\frac{2}{\kappa + 2i\delta_c}\right)^2\frac{d}{dt}\hat{J}^-(t) + ... \tag{3.29}$$

If the condition

$$|\hat{J}^-| \gg \left|\frac{2}{(\kappa + 2i\delta_c)}\frac{d}{dt}\hat{J}^-\right| \tag{3.30}$$

is satisfied, we can keep only the first term in this expansion, and approximate the first term in (3.28) by $\frac{-2iNg}{(\kappa+2i\delta_c)}\hat{J}^-$. Substituting the equation of motion for $\hat{J}^-$(3.23) to condition (3.30) and estimating $|\hat{J}^z| \approx 1$, we get our adiabatic condition to be

$$\kappa \gg \frac{4Ng^2}{\kappa} = NC\gamma_s, \tag{3.31}$$

where $C = \frac{4g^2}{\kappa\gamma_s}$ is a single atom coperativity. So if the adiabatic conditions (3.31) are satisfied we can set $\hat{a}$ as

$$\hat{a} = -\frac{2iNg}{(\kappa + 2i\delta_c)}\hat{J}^- + \hat{G}(t) \tag{3.32}$$

where

$$\hat{G}(t) = \mathrm{I}\int_{-\infty}^{t} dt' e^{-\frac{(\kappa+2i\delta_c)(t-t')}{2}}\hat{F}_a(t')$$

Therefore, the Heisenberg equation for some arbitrary atomic operator $\hat{C}$ can be written as

$$\begin{aligned}
\frac{d\hat{C}}{dt} =& \frac{i}{\hbar}[\hat{\mathcal{H}}_{\mathrm{at}}, \hat{C}] + \sum_{j=1}^{N}\left(\gamma_s\hat{\mathfrak{D}}[\hat{\sigma}^j_{ge}]\hat{C} + \nu\hat{\mathfrak{D}}[\hat{\sigma}^j_{ee}]\hat{C} + R\hat{\mathfrak{D}}[\hat{\sigma}^j_{eg}]\hat{C}\right) \\
&+ igN\left[\hat{a}^\dagger[\hat{J}^-, \hat{C}] + [\hat{J}^+, \hat{C}]\hat{a}\right] + \hat{F}_c \\
=& \frac{i}{\hbar}[\hat{\mathcal{H}}_{at}, \hat{C}] + \sum_{j=1}^{N}\left(\gamma_s\hat{\mathfrak{D}}[\hat{\sigma}^j_{ge}]\hat{C} + \nu\hat{\mathfrak{D}}[\hat{\sigma}^j_{ee}]\hat{C} + R\hat{\mathfrak{D}}[\hat{\sigma}^j_{eg}]\hat{C}\right) \\
&- gN\left[\frac{2gN\hat{J}^+}{\kappa - 2i\delta_c}[\hat{J}^-, \hat{C}] + [\hat{J}^+, \hat{C}]\frac{-2gN\hat{J}^-}{\kappa + 2i\delta_c}\right] \\
&+ \hat{F}_c + igN\left[\hat{G}^\dagger(t)[\hat{J}^-, \hat{C}] + [\hat{J}^+, \hat{C}]\hat{G}(t)\right],
\end{aligned} \tag{3.33}$$

where $\hat{\mathcal{H}}_{\mathrm{at}}$ is the atomic part of the Hamiltonian. The last line in this expression represents the corrected Langevin force (we denote it $\hat{F}'$). The previous line can be represented as a sum of dissipative and Hamiltonian parts:

$$-gN\left[\frac{2gN\hat{J}^+}{\kappa - 2i\delta_c}[\hat{J}^-, \hat{C}] + [\hat{J}^+, \hat{C}]\frac{-2gN\hat{J}^-}{\kappa + 2i\delta_c}\right] = \frac{4g^2N^2\kappa}{\kappa^2 + 4\delta_c^2}\hat{\mathfrak{D}}[\hat{J}^-]\hat{C} + \frac{i}{\hbar}[\hat{\mathcal{H}}_{\mathrm{eff}}, \hat{C}], \tag{3.34}$$

where the Hamiltonian term is equal to

$$\hat{\mathcal{H}}_{\mathrm{eff}} = -\frac{4\hbar g^2N^2\delta_c}{\kappa^2 + 4C^2}\hat{J}^+\hat{J}^-. \tag{3.35}$$

Therefore, the equation for some atomic operator $\hat{C}$ can be written as

$$\begin{aligned}
\frac{d\hat{C}}{dt} =& \frac{i}{\hbar}[\hat{\mathcal{H}}_{\mathrm{at}} + \hat{\mathcal{H}}_{\mathrm{eff}}, \hat{C}] + \sum_{j=1}^{N}\left(\gamma_s\hat{\mathfrak{D}}[\hat{\sigma}^j_{ge}]\hat{C} + \nu\hat{\mathfrak{D}}[\hat{\sigma}^j_{ee}]\hat{C} + R\hat{\mathfrak{D}}[\hat{\sigma}^j_{eg}]\hat{C}\right) \\
&+ \frac{4g^2N^2\kappa}{\kappa^2 + 4\delta_c^2}\hat{\mathfrak{D}}[\hat{J}^-]\hat{C} + \hat{F}',
\end{aligned} \tag{3.36}$$

and the respective master equation can be written as

$$\begin{aligned}\frac{d}{dt}\hat{\rho} = &-\frac{i}{\hbar}\left[\hat{\mathcal{H}}_{\text{at}} + \hat{\mathcal{H}}_{\text{eff}}, \hat{\rho}\right] + \frac{4N^2g^2\kappa}{\kappa^2 + 4\delta_c^2}\hat{\hat{\mathfrak{D}}}'[\hat{J}^-]\hat{\rho} \\ &+ \sum_{j=1}^{N}\left(\gamma_s\hat{\hat{\mathfrak{D}}}'[\hat{\sigma}_{ge}^j]\hat{\rho} + \nu\hat{\hat{\mathfrak{D}}}'[\hat{\sigma}_z^j]\hat{\rho} + R\hat{\hat{\mathfrak{D}}}'[\hat{\sigma}_{eg}^j]\hat{\rho}\right).\end{aligned} \tag{3.37}$$

Such an equation has a term corresponding to a dissipation via the collective atomic operator $N\hat{J}^- = \sum_{j=1}^{N}\hat{\sigma}_{ge}^j$. A similar situation arises in the case of the Dicke superradiance, where different atoms are collectively coupled to the same bath modes. In our situation, the atoms are coupled collectively only to one mode, the cavity mode, which can be eliminated from the master equation, like the modes of the bath, see section 2.3.1. Therefore, the regime of operation of the bad-cavity laser where the condition (3.31) is fulfilled, and such an adiabatic elimination becomes possible, can be called *superradiant regime*.

Adiabatic elimination of the cavity field is useful for numerical calculation because it allows not only to reduce the number of equations but also to increase the integration time step because of the elimination of fast variables.

3.4 C-number Langevin equations

The quantum Langevin equations are operator-valued stochastic differential equations. As such, they are not suited for practical computations. To obtain practical equations, we use the by *c*-numbers Langevin equations, where the operator-valued (q-number) variables are replaced by respective equivalent classical (*c*-number) variables [22]. To establish a correspondence between the operators and the *c*-number variables, we need to choose some specific ordering of operators such that the product of *c*-number variables should correspond to the product of operators taken in this order, and the equations for the first and second moments of *c*-number variables should be identical to corresponding equations of properly ordered operator variables. In [26] the *"normal ordering"* $(\hat{a}^\dagger, \hat{J}^+, \hat{J}^z, \hat{J}^-, \hat{a})$ of operators was chosen. However, this can lead to certain difficulties for numerical simulation, particularly, the diffusion matrix of classical Langevin forces calculated for respective real *c*-number variables may have negative eigenvalues, which would lead to imaginary noises [27]. Instead, we use a *symmetric ordering* of the operators, following [28], where the products of *c*-number variables should correspond to the symmetrized product of the respective operators. Then the set of *c*-number Langevin equations looks like:

$$\begin{aligned}\frac{d}{dt}a &= -\frac{1}{2}(\kappa + 2i\delta_c)a - iNgJ^- + F_a, \\ \frac{d}{dt}J^- &= -\frac{1}{2}(\Gamma + 2i\Delta_a)J^- + igaJ^z + F_-, \\ \frac{d}{dt}J^z &= -(R + \gamma_s)(J^z - d_0) + 2ig(a^\dagger J^- - aJ^+) + F_z.\end{aligned} \tag{3.38}$$

For the sake of simplicity, we, following [28], introduce real-valued c-number variables as

$$\begin{aligned} \hat{q} &= \frac{1}{2}(\hat{a}^\dagger + \hat{a}), \quad \hat{p} = \frac{1}{2i}(\hat{a}^\dagger - \hat{a}), \\ \hat{J}^x &= \frac{1}{2}(\hat{J}^+ + \hat{J}^-), \quad \hat{J}^y = \frac{1}{2i}(\hat{J}^+ - \hat{J}^-). \end{aligned} \tag{3.39}$$

The associated c-number equations are

$$\begin{aligned} \frac{d}{dt}q &= -\frac{1}{2}\kappa q + \delta_c p - NgJ^y + F_q, \\ \frac{d}{dt}p &= -\frac{1}{2}\kappa p - \delta_c q + NgJ^x + F_q, \\ \frac{d}{dt}J^x &= -\frac{1}{2}\Gamma J^x - \Delta_a J^y + gpJ^z + F_x, \\ \frac{d}{dt}J^y &= -\frac{1}{2}\Gamma J^y + \Delta_a J^x - gqJ^z + F_x, \\ \frac{d}{dt}J^z &= -(R+\gamma_s)(J^z - d_0) + 2g(qJ^y - pJ^x) + F_z. \end{aligned} \tag{3.40}$$

Similarly, the corresponding noise operators are

$$\begin{aligned} \hat{F}_q &= \frac{1}{2}(\hat{F}_{\hat{a}^\dagger} + \hat{F}_{\hat{a}}), \quad \hat{F}_p = \frac{1}{2i}(\hat{F}_{\hat{a}^\dagger} - \hat{F}_{\hat{a}}). \\ \hat{F}_x &= \frac{1}{2}(\hat{F}_+ + \hat{F}_-), \quad \hat{F}_y = \frac{1}{2i}(\hat{F}_+ - \hat{F}_-). \end{aligned} \tag{3.41}$$

The diffusion matrix in this real space will look like

$$\begin{aligned} &2\mathcal{D}_{qq} = \kappa/2, \quad 2\mathcal{D}_{pp} = \kappa/2, \quad 2\mathcal{D}_{xx} = \frac{\Gamma}{2N}, \quad 2\mathcal{D}_{yy} = \frac{\Gamma}{2N}, \\ &2\mathcal{D}_{xz} = 2\mathcal{D}_{zx} = \frac{2(-R+\gamma_s)}{N}\langle\hat{J}^x\rangle, \quad 2\mathcal{D}_{yz} = 2\mathcal{D}_{yx} = \frac{2(-R+\gamma_s)}{N}\langle\hat{J}^y\rangle, \\ &2\mathcal{D}_{zz} = \frac{2}{N}((R+\gamma_s) + (-R+\gamma_s)\langle\hat{J}^z\rangle) \end{aligned} \tag{3.42}$$

For the simulation, the noises F_μ can be calculated using the diffusion matrix

$$F_\mu = \sum_\nu \sqrt{\lambda_\nu}\mathcal{M}^T_{\mu\nu}F_\nu \tag{3.43}$$

where the $\mathcal{M}_{\mu\nu}$ is the transformation matrix which digonalizes the diffusion matrix, λ_ν are the associated eigenvalues and F_ν are independent Wiener processes as described in [29]. For a good set of parameters in bad cavity regime we can adiabatically eliminate c-number a as

$$a = -\frac{i2Ng}{(\kappa + 2i\delta_c)}J^- \tag{3.44}$$

resulting in elimination of p and q

$$\begin{aligned} q &= \frac{4\delta_c N g J^x - 2Ng\kappa J^y}{(\kappa^2 + 4\delta_c^2)}. \\ p &= \frac{-8\delta_c^2 N g J^x + 4\delta_c N g \kappa J^y + 2Ng\kappa(\kappa^2 + 4\delta_c^2)J^x}{\kappa(\kappa^2 + 4\delta_c^2)}. \end{aligned} \tag{3.45}$$

3.5 Mean field equations

In the mean-field approximations we neglect the correlations between the dynamical variables. By taking the expectation of equations (3.22) – (3.26), we get the set of mean-field equations for this system

$$\frac{d}{dt}\langle\hat{a}\rangle = -\frac{1}{2}(\kappa + 2i\delta_c)\langle\hat{a}\rangle - iNg\langle\hat{J}^-\rangle, \tag{3.46}$$

$$\frac{d}{dt}\langle\hat{a}^\dagger\rangle = -\frac{1}{2}(\kappa - 2i\delta_c)\langle\hat{a}^\dagger\rangle + iNg\langle\hat{J}^+\rangle, \tag{3.47}$$

$$\frac{d}{dt}\langle\hat{J}^-\rangle = -\frac{1}{2}(\Gamma + 2i\Delta_a)\langle\hat{J}^-\rangle + ig\langle\hat{a}\rangle\langle\hat{J}^z\rangle, \tag{3.48}$$

$$\frac{d}{dt}\langle\hat{J}^+\rangle = -\frac{1}{2}(\Gamma - 2i\Delta_a)\langle\hat{J}^+\rangle - ig\langle\hat{a}^\dagger\rangle\langle\hat{J}^z\rangle, \tag{3.49}$$

$$\frac{d}{dt}\langle\hat{J}^z\rangle = -(R + \gamma_s)(\langle\hat{J}^z\rangle - d_0) + 2ig(\langle\hat{a}^\dagger\rangle\langle\hat{J}^-\rangle - \langle\hat{a}\rangle\langle\hat{J}^+\rangle). \tag{3.50}$$

The noise terms drop out because they have zero mean. The mean field equations capture many of the most important features of the physical system because the noise terms scale as $\sqrt{N}$ while expectation values scale as N. However, the information about the linewidth is lost.

Using the mean-field equations, one can calculate the steady-state population inversion and the cavity photon number as

$$\begin{aligned} \langle\hat{J}^z\rangle &= \frac{d_0}{1 + \frac{4g^2\langle\hat{a}^\dagger\hat{a}\rangle}{R+\gamma_s}\frac{2\Gamma}{\Gamma^2+4(\Delta_a)^2}}, \\ \langle\hat{a}^\dagger\hat{a}\rangle = \langle\hat{a}^\dagger\rangle\langle\hat{a}\rangle &= \frac{R+\gamma_s}{4g^2}\frac{\Gamma^2 + 4(\Delta_a)^2}{2\Gamma}\left(\frac{d_0 N 4g^2}{(\kappa + 2i(\delta_c))(\Gamma + 2i(\Delta_a))} - 1\right). \end{aligned} \tag{3.51}$$

Note that we need to have $\kappa\Delta_a + \Gamma\delta_c = 0$ for $\langle\hat{a}^\dagger\hat{a}\rangle$ to be real. In other words, a rotating frame where the steady-state solution becomes possible should rotate with a frequency

$$\omega = \frac{\kappa\omega_a + \Gamma\omega_c}{\kappa + \Gamma}, \tag{3.52}$$

which is also the frequency of the output radiation. If $\kappa \gg \gamma$, the frequency ω will be determined primarily by the frequency ω_a of the atoms, and just slightly shifted towards the detuned cavity frequency (this effect is called *cavity pulling*), being robust to fluctuations of the frequency of the cavity mode.

3.6 Second-order cumulant theory

To include the higher order effect, one can use the cumulant expansion [9] of the correlators between different operator variables and truncate cumulants higher than some specific order. As Theorem 1 in Ref [30] states, the joint cumulant of a set of operators is zero, if some subset of them is statistically independent of the others. Neglecting higher-order cumulants is equivalent to neglecting higher-order correlations between different operators.

The mean-field equations considered above correspond to "first-order cumulant theory", where even the second-order cumulants were not kept, and the second-order correlators were approximated by $\langle \hat{A}\hat{B}\rangle \approx \langle \hat{A}\rangle\langle \hat{B}\rangle$. In 2nd-order cumulant theory, the second-order correlators are kept, whereas the third-order correlators are approximated by

$$\langle \hat{A}\hat{B}\hat{C}\rangle \approx \langle \hat{A}\rangle\langle \hat{B}\hat{C}\rangle + \langle \hat{B}\rangle\langle \hat{A}\hat{C}\rangle + \langle \hat{C}\rangle\langle \hat{A}\hat{B}\rangle - 2\langle \hat{A}\rangle\langle \hat{B}\rangle\langle \hat{C}\rangle. \tag{3.53}$$

Also, for the second-order cumulant theory, one may suppose that the phase invariance is not broken, i.e., we consider an ensemble of identical systems initially prepared in states with different phases of the cavity field and the atomic ensemble. Then $\langle \hat{a}\rangle = \langle \hat{\sigma}_{ge}\rangle = 0$, what significantly simplifies the task.

Let us construct the set of equations describing the bad-cavity laser in the second-order cumulant approximation. From equation (3.26), we get the equation for a single atomic inversion

$$\frac{d}{dt}\langle \hat{\sigma}_z^1\rangle = -(R+\gamma_s)(\langle \hat{\sigma}_z^1\rangle - d_0) + 2ig(\langle \hat{a}^\dagger \hat{\sigma}_{ge}^1\rangle - \langle \hat{a}\hat{\sigma}_{eg}^1\rangle). \tag{3.54}$$

Since $\langle \hat{a}^\dagger\hat{\sigma}_{ge}^1\rangle$ couples into (3.54), its evolution equation must also be calculated:

$$\begin{aligned}\frac{d}{dt}\langle \hat{a}^\dagger\hat{\sigma}_{ge}^1\rangle = &-\frac{1}{2}(\kappa + R + \gamma_s + \nu - 2i\delta)\langle \hat{a}^\dagger\hat{\sigma}_{ge}^1\rangle \\ &+ ig(\langle \hat{a}^\dagger\hat{a}\hat{\sigma}_z^1\rangle + \frac{1}{2}(1+\langle \hat{\sigma}_z^1\rangle) + ig(N-1)\langle \hat{\sigma}_{eg}^1\hat{\sigma}_{ge}^2\rangle,\end{aligned} \tag{3.55}$$

where $\delta = \omega_c - \omega_a$ Here we have a third-order correlation, which we can expand using (3.53) as

$$\begin{aligned}\langle \hat{a}^\dagger\hat{a}\hat{\sigma}_z^1\rangle &= \langle \hat{a}^\dagger\hat{a}\rangle\langle \hat{\sigma}_z^1\rangle + \langle \hat{a}^\dagger\hat{\sigma}_z^1\rangle\langle \hat{a}\rangle + \langle \hat{a}\hat{\sigma}_z^1\rangle\langle \hat{a}^\dagger\rangle - 2\langle \hat{a}^\dagger\rangle\langle \hat{a}\rangle\langle \hat{\sigma}_z^1\rangle \\ &= \langle \hat{a}^\dagger\hat{a}\rangle\langle \hat{\sigma}_z^1\rangle,\end{aligned} \tag{3.56}$$

where we have taken $\langle \hat{a}\rangle = \langle \hat{a}^\dagger\rangle = 0$ because of the phase invariance. Then the equation (3.55) can be written as

$$\begin{aligned}\frac{d}{dt}\langle \hat{a}^\dagger\hat{\sigma}_{ge}^1\rangle = &-\frac{1}{2}(\kappa + R + \gamma_s + \nu - 2i\delta)\langle \hat{a}^\dagger\hat{\sigma}_{ge}^1\rangle \\ &+ ig(\langle \hat{a}^\dagger\hat{a}\rangle\langle \hat{\sigma}_z^1\rangle + \frac{1}{2}(1+\langle \hat{\sigma}_z^1\rangle) + ig(N-1)\langle \hat{\sigma}_{eg}^1\hat{\sigma}_2^-\rangle.\end{aligned} \tag{3.57}$$

To get a complete set, we need also equations for $\langle\hat{\sigma}^1_{eg}\hat{\sigma}^2_{ge}\rangle$ and $\langle\hat{a}^\dagger\hat{a}\rangle$:

$$\begin{aligned}\frac{d}{dt}\langle\hat{\sigma}^1_{eg}\hat{\sigma}^2_{ge}\rangle &= -\left(R+\gamma_s+\nu\right)\langle\hat{\sigma}^1_{eg}\hat{\sigma}^2_{ge}\rangle - ig\langle\hat{\sigma}^z_1\rangle(\langle\hat{a}^\dagger\hat{\sigma}^1_{ge}\rangle - \langle\hat{a}\hat{\sigma}^1_{eg}\rangle),\\ \frac{d}{dt}\langle\hat{a}^\dagger\hat{a}\rangle &= -\kappa\langle\hat{a}^\dagger\hat{a}\rangle - iNg(\langle\hat{a}^\dagger\hat{\sigma}^1_{ge}\rangle - \langle\hat{a}\hat{\sigma}^1_{eg}\rangle).\end{aligned} \tag{3.58}$$

In chapter 4, we will get second-order cumulant equations for an inhomogeneous system. Also, the higher-order cumulant equations can be calculated using the package QuantumCumulants.jl [31].

3.6.1 Linewidth

Now, using the two-time expectation value of the cavity operator, cumulant expansion, and the quantum regression theorem, we can calculate the spectral linewidth of the emitted cavity field. As it was shown in section 3.2.1, the spectrum is related to the 2-time correlation function $\langle\hat{a}^\dagger(t+\tau)\hat{a}(t)\rangle$. To get the equation for this function, one can fix t, multiply the equation for $d\hat{a}^\dagger(t+\tau)/d\tau$ (3.23) by $\hat{a}(t)$ from right, and perform ensemble averaging keeping in mind that quantum noise terms taken after do not correlate with system operators taken before (causality). We get

$$\frac{d}{d\tau}\langle\hat{a}^\dagger(t+\tau)\hat{a}(t)\rangle = \left(i\delta_c - \frac{\kappa}{2}\right)\langle\hat{a}^\dagger(t+\tau)\hat{a}(t)\rangle + iNg\langle\hat{\sigma}^1_{eg}(t+\tau)\hat{a}(t)\rangle. \tag{3.59}$$

Similarly, from the equation (3.25) we derive

$$\frac{d}{dt}\langle\hat{\sigma}^1_{eg}(t+\tau)\hat{a}(t)\rangle = \left(i\Delta_a - \frac{\Gamma}{2}\right)\langle\hat{\sigma}^1_{eg}(t+\tau)\hat{a}(t)\rangle - ig\langle\hat{a}^\dagger(t+\tau)\hat{\sigma}^1_z(t+\tau)\hat{a}(t)\rangle, \tag{3.60}$$

where $\Gamma = R+\gamma_s+\nu$, and $\langle\hat{a}^\dagger(t+\tau)\hat{\sigma}^1_z(t+\tau)\hat{a}(t)\rangle$ can be decomposed to $\langle\hat{\sigma}^1_z(t+\tau)\rangle\langle\hat{a}^\dagger(t+\tau)\hat{a}(t)\rangle$ using cumulant expansion. In the steady-state regime we can also replace $\langle\hat{\sigma}^1_z(t+\tau)\rangle$ by its steady-state value $\langle\hat{\sigma}_z\rangle$.

Consider the resonant case $\delta_c = \Delta_a = 0$. We have

$$\begin{aligned}\frac{d}{dt}\langle\hat{a}^\dagger(t+\tau)\hat{a}(t)\rangle &= -\frac{\kappa}{2}\langle\hat{a}^\dagger(t+\tau)\hat{a}(t)\rangle + iNg\langle\hat{\sigma}^1_{eg}(t+\tau)\hat{a}(t)\rangle,\\ \frac{d}{dt}\langle\hat{\sigma}^1_{eg}(t+\tau)\hat{a}(t)\rangle &= -ig\langle\hat{\sigma}_z\rangle\langle\hat{a}^\dagger(t+\tau)\hat{a}(t)\rangle - \frac{\Gamma}{2}\langle\hat{\sigma}^1_{eg}(t+\tau)\hat{a}(t)\rangle.\end{aligned} \tag{3.61}$$

This is a set of linear differential equations for $\langle\hat{a}^\dagger(t+\tau)\hat{a}(t)\rangle = \mathcal{C}(\tau)$ and $\langle\hat{\sigma}^1_{eg}(t+\tau)\hat{a}(t)\rangle = \mathcal{A}(\tau)$, which has a form

$$\begin{aligned}\frac{d}{d\tau}\mathcal{C}(\tau) &= c_1\mathcal{C}(\tau) + c_2\mathcal{A}(\tau),\\ \frac{d}{d\tau}\mathcal{A}(\tau) &= c_3\mathcal{C}(\tau) + c_4\mathcal{A}(\tau).\end{aligned} \tag{3.62}$$

Applying Laplace transformation to both sides, one can write

$$\begin{aligned} -\mathcal{C}(0) + s\mathcal{C}(s) &= c_1\mathcal{C}(s) + c_2\mathcal{A}(s), \\ -\mathcal{A}(0) + s\mathcal{A}(s) &= c_3\mathcal{C}(s) + c_4\mathcal{A}(s), \end{aligned} \tag{3.63}$$

where

$$\begin{aligned} \mathcal{C}(s) &= \int_0^\infty e^{-s\tau}\mathcal{C}(\tau)d\tau, \\ \mathcal{A}(s) &= \int_0^\infty e^{-s\tau}\mathcal{A}(\tau)d\tau. \end{aligned} \tag{3.64}$$

from equation (3.63), we can write

$$\begin{aligned} \mathcal{C}(s) &= \frac{(s-c_4)\mathcal{C}(0) + c_2\mathcal{A}(0)}{(s-c_1)(s-c_4) - c_2c_3} \\ &= \frac{\mathcal{X}}{(s - \frac{\Delta\nu_+}{2})} + \frac{\mathcal{Y}}{(s - \frac{\Delta\nu_-}{2})} \end{aligned} \tag{3.65}$$

where

$$\begin{aligned} \Delta\nu_\pm &= -(c_1+c_4) \mp \sqrt{(c_1+c_4)^2 - 4(c_1c_4 - c_2c_3)} \\ &= \frac{\kappa+\Gamma}{2} \mp \frac{1}{2}\sqrt{(\kappa-\Gamma)^2 + 4Ng^2\langle\hat{\sigma}_z^1\rangle} \end{aligned} \tag{3.66}$$

Using inverse Laplace transformation, we get

$$\langle\hat{a}^\dagger(\tau+t)\hat{a}(t)\rangle = \mathcal{C}(\tau) = \mathcal{X}e^{-\frac{\delta\nu_+\tau}{2}} + \mathcal{Y}e^{-\frac{\delta\nu_-\tau}{2}} \tag{3.67}$$

Since $\Delta\nu_+ \ll \Delta\nu_-$, the second term (which corresponds to fast relaxation of the cavity field towards the quasi-equilibrium with "slow" atomic variables) decays fast to zero, so the first term dominates. Then, since the Fourier transform of an exponential with decay rate $\Delta\nu$ is a Lorentzian with a full-width half-maximum linewidth $\Delta\nu$, the steady state linewidth $\Delta\nu$ of our system is described by (see equations (3.15) and (3.16))

$$\Delta\nu = \frac{\kappa+\Gamma}{2} - \frac{1}{2}\sqrt{(\kappa-\Gamma)^2 + 4Ng^2\langle\hat{\sigma}_z^1\rangle} \tag{3.68}$$

This is an example of a simple homogeneous system, where the linewidth can be found analytically. For more complex systems, such as inhomogeneous systems considered in chapter 4, or solvable homogenous system, as we will see in chapter 4 and chapter 6 for a relatively more complex set of equations, including inhomogeneity, to find the linewidth, we use other methods based on the Wiener-Khintchine theorem (3.14).

3.7 Full quantum description for homogeneous system

The bulk of this section has been presented as part of [32]

As we mentioned above, the density matrix describing a system of N 2-level atoms has 4^N elements. This makes the full quantum description of even relatively small systems, with few tens of atoms, computationally intractable. However, for homogeneous systems of identical atoms, not all the elements of the density matrix are independent. In [33] evolution operators such as (3.1) – (3.3) were shown to be invariant under $SU(4)$ transformations, and the master equation can be solved for intermediate-size systems with up to a few hundred atoms [28]. In the present section, we describe the method of calculation of the master equation for a bad cavity laser with a homogeneous ensemble of 2-level atoms, based on the symmetry between the atoms. However, instead of expressing the superoperators via the elements of the respective representations of the $SU(4)$ group, as in [33], we build the respective matrix elements explicitly. The method described in this section has been presented in the results of the EU project FET-Flag No. 820404 "iqClock", Deliverable D6.2 [32]

We consider N 2-level atoms homogeneously coupled to the bath and (optionally) to another part of the system. If the atoms were initially prepared in some symmetric state, then, in the absence of relaxations, their state remains symmetric in all the subsequent instants of time. So, in the absence of relaxations the system of such atoms can be described as an effective "particle" with total pseudospin equal to $N/2$ (for composite system consisting of such atoms plus some other quantum system, the state Ψ of the whole system may be decomposed into $|\Psi\rangle = \sum_{m,k} c_{mk}|\psi_m\rangle \otimes |\phi_k\rangle$, where $\{|\psi_m\rangle\}$ are symmetric pure states of the atoms (say, m is a z-projection of the pseudospin), and $\{|\phi_m\rangle\}$ are some basis states describing another part of the system). For our analysis, we will consider a system consisting of atoms only, because generalization to the composite system is straightforward, and, on top of that, we are interested in that parameter regime of bad-cavity laser where we can adiabatically eliminate cavity field that is condition (3.31) is satisfied.

In the presence of dissipation, the density matrix describing these atoms cannot be decomposed into $\sum_{m,k} |\psi_m\rangle\langle\psi_k|$ [33]. However, the density matrix itself keeps the permutation symmetry.

Let us introduce a short notation for single-atom operators

$$\hat{u}_i = \hat{\sigma}^i_{ee}, \quad \hat{d}_i = \hat{\sigma}^i_{gg}, \quad \hat{s}_i = \hat{\sigma}^i_{eg}, \quad \hat{c}_i = \hat{\sigma}^i_{ge}. \tag{3.69}$$

We suppose that the atoms are initially in the fully symmetric state, which will later lead to a fully symmetric density matrix which can be represented as

$$\hat{\rho} = \sum_{\alpha\beta\gamma\delta} \rho_{\alpha\beta\gamma\delta} \hat{P}_{\alpha\beta\gamma\delta}, \tag{3.70}$$

where

$$\hat{P}_{\alpha\beta\gamma\delta} = S(\hat{u}^\alpha \hat{d}^\beta \hat{s}^\gamma \hat{c}^\delta) \equiv \frac{1}{C_{\alpha\beta\gamma\delta}} \sum_p \hat{O}^1_{p_1} \otimes ... \otimes \hat{O}^N_{p_N}. \tag{3.71}$$

Here S means symmetrization, $p = \{p_1, ..., p_N\}$ is an ordered set of indices $1, 2, 3$ and 4 such that each of indices 1, 2, 3 and 4 appears α, β, γ and δ times respectively; $\hat{O}^i_{p_i} = \hat{u}_i, \hat{d}_i, \hat{s}_i$ or $\hat{c}_i$ at $p_i = 1, 2, 3$ or 4 respectively (here $\hat{O}^i$ acts on the state of ith atom), and

$$C_{\alpha\beta\gamma\delta} = \frac{(\alpha+\beta+\gamma+\delta)!}{\alpha!\cdot\beta!\cdot\gamma!\cdot\delta!} \tag{3.72}$$

is a number of the summands (this is a straightforward generalization of the binomial coefficient).

3.7.1 Master equation with adiabatic elimination

We start from the master equation (3.37) for the bad-cavity laser with N identical 2-level atoms with incoherent pumping, where we performed adiabatic elimination of the cavity field. For the sake of simplicity, we take the frequency ω of our rotating frame equal to the resonant frequency ω_c of the cavity mode. Then, introducing operators

$$\hat{E} = \sum_{j=1}^{N} \hat{\sigma}^j_{ee}, \quad \hat{G} = \sum_{j=1}^{N} \hat{\sigma}^j_{gg}, \quad \hat{X} = \sum_{j=1}^{N} \hat{\sigma}^j_{ge} \tag{3.73}$$

we can write the master equation as

$$\frac{d\hat{\rho}}{dt} = -i\Delta_a \left[\hat{E}\hat{\rho} - \hat{\rho}\hat{E}\right] + \sum_j \left[\gamma_s \hat{\hat{\mathfrak{D}}}[\hat{\sigma}^j_{ge}]\hat{\rho} + R\hat{\hat{\mathfrak{D}}}[\hat{\sigma}^j_{eg}]\hat{\rho} + \nu\hat{\hat{\mathfrak{D}}}[\hat{\sigma}^j_{ee}]\hat{\rho}\right] + \frac{4g^2}{\kappa}\hat{\hat{\mathfrak{D}}}[\hat{X}]\hat{\rho}. \tag{3.74}$$

where Δ_a is the detuning of the atomic transition from the cavity resonant frequency.

It is convenient to introduce superoperators

$$\begin{aligned}
&\hat{\hat{E}}_L\hat{\rho} = \hat{E}\hat{\rho}, \quad \hat{\hat{E}}_R\hat{\rho} = \hat{\rho}\hat{E}, \quad \hat{\hat{E}}_{LR}\hat{\rho} = \sum_{j=1}^{N} \hat{\sigma}^j_{ee}\hat{\rho}\hat{\sigma}^j_{ee} \\
&\hat{\hat{G}}_L\hat{\rho} = \hat{G}\hat{\rho}, \quad \hat{\hat{G}}_R\hat{\rho} = \hat{\rho}\hat{G}, \quad \hat{B}\hat{\rho} = \sum_{j=1}^{N} \hat{\sigma}^j_{ge}\hat{\rho}\hat{\sigma}^j_{eg}, \\
&\hat{\hat{X}}_L\hat{\rho} = \hat{X}\hat{\rho}, \quad \hat{\hat{X}}^+_L\hat{\rho} = \hat{X}^+\hat{\rho} \quad \hat{T}\hat{\rho} = \sum_{j=1}^{N} \hat{\sigma}^j_{eg}\hat{\rho}\hat{\sigma}^j_{ge}, \\
&\hat{\hat{X}}_R\hat{\rho} = \hat{\rho}\hat{X}, \quad \hat{\hat{X}}^+_R\hat{\rho} = \hat{\rho}\hat{X}^+.
\end{aligned} \tag{3.75}$$

Using these superoperators, one can rewrite the master equation (3.74) as

$$\frac{d\hat{\rho}}{dt} = \hat{\hat{A}}\hat{\rho}, \tag{3.76}$$

where

$$\begin{aligned}
\hat{\hat{A}} = &-i\Delta_a\left[\hat{\hat{E}}_L - \hat{\hat{E}}_R\right] - \frac{\gamma_s}{2}\left[\hat{\hat{E}}_L + \hat{\hat{E}}_R - 2\hat{B}\right] - \frac{R}{2}\left[\hat{\hat{G}}_L + \hat{\hat{G}}_R - 2\hat{\hat{T}}\right] \\
&- \frac{\nu}{2}\left[\hat{\hat{E}}_L + \hat{\hat{E}}_R - 2\hat{\hat{E}}_{LR}\right] - \frac{2g^2}{\kappa}\left[\hat{\hat{X}}^+_L\hat{\hat{X}}_L + \hat{\hat{X}}_R\hat{\hat{X}}^+_R - 2\hat{\hat{X}}^+_R\hat{\hat{X}}_L\right].
\end{aligned} \tag{3.77}$$

3.7.2 Matrix elements of superoperators

The density matrix $\hat{\rho}$ is expanded into elementary matrices $\hat{P}_{\alpha\beta\gamma\delta}$ with coefficients $\rho_{\alpha\beta\gamma\delta}$. To calculate matrix elements of superoperators (3.75), one has to find how these superoperators act on $\hat{P}_{\alpha\beta\gamma\delta}$. Consider, for example, $\hat{\hat{X}}_L\hat{P}_{\alpha\beta\gamma\delta}$:

$$\begin{aligned}\hat{\hat{X}}_L\hat{P}_{\alpha\beta\gamma\delta} = \hat{X}\hat{P}_{\alpha\beta\gamma\delta} &= \sum_{j=1}^{N}\hat{\sigma}_{ge}^{j}\hat{P}_{\alpha\beta\gamma\delta} \\ &= \sum_{j=1}^{N}\hat{1}^1\otimes....\otimes\hat{c}^j\otimes\hat{1}^{j+1}\otimes....\otimes\hat{1}^{j+1}\cdot\frac{1}{C_{\alpha\beta\gamma\delta}}\sum_p\left(...\hat{O}_p^j...\right).\end{aligned} \tag{3.78}$$

The specific term in this double sum corresponding to jth atom and some ordered set p of indices $1, 2, 3$ and 4 appearing α, β, γ and δ times respectively contains $\hat{c}_j\cdot\hat{O}_p^j$, where $\hat{O}_p^j\in\{\hat{u}^j, \hat{d}^j, \hat{c}^j, \hat{s}^j\}$.

Using $\hat{c}\hat{u}=\hat{c}$, $\hat{c}\hat{d}=0$, $\hat{c}\hat{s}=\hat{d}$ and $\hat{c}\hat{c}=0$, we can write

$$\hat{\hat{X}}_L\hat{P}_{\alpha\beta\gamma\delta} = C_1\hat{P}_{\alpha-1,\beta,\gamma,\delta+1} + C_2\hat{P}_{\alpha,\beta+1,\gamma-1,\delta},$$

where the coefficients C_1 and C_2 are the number of terms with $\hat{O}=\hat{u}$ and $\hat{O}=\hat{s}$ respectively divided by $\hat{C}_{\alpha\beta\gamma\delta}$.

Another important result is $C_1 = C_{\alpha-1,\beta,\gamma,\delta}\times N/C_{\alpha\beta\gamma\delta}$, where $C_{\alpha-1,\beta,\gamma,\delta}$ is a number of sets p with $\hat{O}_p^j=\hat{u}$, and N comes from summation over j. such terms at any fixed j, and summation over j gives another factor N. Therefore, $C_1=\alpha$. Similarly, $C_2=\gamma$, and

$$\hat{\hat{X}}_L\hat{P}_{\alpha\beta\gamma\delta} = \alpha\cdot\hat{P}_{\alpha-1,\beta,\gamma,\delta+1} + \gamma\cdot\hat{P}_{\alpha,\beta+1,\gamma-1,\delta}. \tag{3.79}$$

The action of other superoperators (3.75) on $\hat{P}_{\alpha\beta\gamma\delta}$ can be found in the same manner. It gives

$$\begin{aligned}
\hat{\hat{E}}_L\hat{P}_{\alpha\beta\gamma\delta} &= (\alpha+\gamma)\hat{P}_{\alpha\beta\gamma\delta}, \quad \hat{\hat{G}}_L\hat{P}_{\alpha\beta\gamma\delta} = (\beta+\delta)\hat{P}_{\alpha\beta\gamma\delta}, \\
\hat{\hat{T}}\hat{P}_{\alpha\beta\gamma\delta} &= \beta\hat{P}_{\alpha+1,\beta-1,\gamma,\delta}, \quad \hat{\hat{E}}_R\hat{P}_{\alpha\beta\gamma\delta} = (\alpha+\delta)\hat{P}_{\alpha\beta\gamma\delta}, \\
\hat{\hat{G}}_R\hat{P}_{\alpha\beta\gamma\delta} &= (\beta+\gamma)\hat{P}_{\alpha\beta\gamma\delta}, \quad \hat{B}\hat{P}_{\alpha\beta\gamma\delta} = \alpha\hat{P}_{\alpha-1,\beta+1,\gamma,\delta} \\
\hat{\hat{X}}_L\hat{P}_{\alpha\beta\gamma\delta} &= \alpha\hat{P}_{\alpha-1,\beta,\gamma,\delta+1} + \gamma\hat{P}_{\alpha,\beta+1,\gamma-1,\delta} \\
\hat{\hat{X}}_R\hat{P}_{\alpha\beta\gamma\delta} &= \beta\hat{P}_{\alpha,\beta-1,\gamma,\delta+1} + \gamma\hat{P}_{\alpha+1,\beta,\gamma-1,\delta} \\
\hat{\hat{X}}_L^+\hat{P}_{\alpha\beta\gamma\delta} &= \beta\hat{P}_{\alpha,\beta-1,\gamma+1,\delta} + \delta\hat{P}_{\alpha+1,\beta,\gamma,\delta-1}, \\
\hat{\hat{X}}_R^+\hat{P}_{\alpha\beta\gamma\delta} &= \alpha\hat{P}_{\alpha-1,\beta,\gamma+1,\delta} + \delta\hat{P}_{\alpha,\beta+1,\gamma,\delta-1}, \\
\hat{\hat{E}}_{LR}\hat{P}_{\alpha\beta\gamma\delta} &= \alpha\hat{P}_{\alpha\beta\gamma\delta}.
\end{aligned} \tag{3.80}$$

From (3.80) one can easily get matrix elements of all the superoperators necessary to generate the evolution matrix of superoperator $\hat{\hat{A}}$ (3.77). The spectrum of the bad-cavity

laser can be found using the Fourier transform of real part of the two-time correlation function $\langle \hat{a}^\dagger(t)\hat{a}(0)\rangle$, where

$$\hat{a} = -\frac{2ig}{\kappa}\hat{X}. \tag{3.81}$$

what, in turn, can be calculated with the help of the quantum regression theorem, see section 3.2.2. For $\Delta_a = 0$, one can approximate $\langle \hat{a}^\dagger(t)\hat{a}(0)\rangle$ by $n\exp(-\lambda t)$, and estimate the spectral linewidth $\Delta\omega$ as $\Delta\omega \approx 2\lambda$, according to (3.17) .

We should note that the set of equations for non-zero elements $\rho_{\alpha\beta\gamma\delta}$ of the density matrix is linear, which allows us to use the methods of linear algebra to find the steady-state density matrix.

3.7.3 Model without adiabatic elimination of the cavity field

In this thesis, we consider bad-cavity lasers operating in a superradiant regime, where the condition (3.31) is fulfilled, and adiabatic elimination of the cavity field is allowed. However, for the sake of completeness, we also present equations without adiabatic elimination. In this case, one can use a truncated Fock state to describe cavity degrees of freedom. Then the density matrix can be represented as

$$\hat{\rho} = \sum_{m,n}\sum_{\alpha\beta\gamma\delta} \rho_{\alpha\beta\gamma\delta,nm}\hat{P}_{\alpha\beta\gamma\delta} \otimes |n\rangle\langle m|, \tag{3.82}$$

where $|m\rangle$ and $|n\rangle$ are the Fock states of the cavity field. The master equation has the form (3.76) with

$$\begin{aligned}\hat{\hat{A}} = &-i\Delta_a\left[\hat{\hat{E}}_L - \hat{\hat{E}}_R\right] - ig\left(\hat{a}_L^\dagger\hat{\hat{X}}_L - \hat{\hat{X}}_R\hat{a}_R^\dagger + \hat{\hat{X}}_L^+\hat{a}_L - \hat{a}_R\hat{\hat{X}}_R^+\right)\\ &- \frac{\gamma_s}{2}\left[\hat{\hat{E}}_L + \hat{\hat{E}}_R - 2\hat{\hat{B}}\right] - \frac{R}{2}\left[\hat{\hat{G}}_L + \hat{\hat{G}}_R - 2\hat{\hat{T}}\right]\\ &- \frac{\nu}{2}\left[\hat{\hat{E}}_L + \hat{\hat{E}}_R - 2\hat{\hat{E}}_{LR}\right] - \frac{\kappa}{2}\left(\hat{a}_L^\dagger\hat{a}_L + \hat{a}_R\hat{a}_R^\dagger - 2\hat{a}_L\hat{a}_R^\dagger\right),\end{aligned} \tag{3.83}$$

where $\hat{\hat{a}}_L\hat{\rho} = \hat{a}\hat{\rho}$, $\hat{\hat{a}}_R\hat{\rho} = \hat{\rho}\hat{a}$, $\hat{\hat{a}}_L^\dagger\hat{\rho} = \hat{a}^\dagger\hat{\rho}$, $\hat{\hat{a}}_R^\dagger\hat{\rho} = \hat{\rho}\hat{a}^\dagger$, and other superoperators are defined using (3.80).

3.8 Comparison of different methods of simulation

As the Hilbert space describing such a system grows exponentially with the number of atoms N, it is necessary to apply approximations to reduce the problem's complexity. We can't use the full quantum solution for an arbitrarily large number of atoms, so we need to choose the approximate method for the treatment of our system.

In this section, we compare different methods of calculation of parameters of the superradiant laser on a homogeneous ensemble of 2-level atoms with incoherent pumping, namely, the steady-state intracavity photon number n, the inversion J^z of the atoms,

and the linewidth $\Delta\nu$ of the output radiation. The methods we exploited here are the mean-field approximation (only for n and J^z), the second-order cumulant theory, the simulation of stochastic c-number Langevin equations (averaging over 1000 trajectories), and the full quantum approach. We perform calculations for a relatively small ensemble of atoms ($N = 40$ or $N = 100$).

To find the linewidth within the full quantum approach, we first found the steady-state density matrix using the methods of linear algebra, and then we performed numerical simulation of 2-time correlation function $R(\tau) = \langle \hat{a}^\dagger(t+\tau)\hat{a}(t)\rangle$ using the quantum regression theorem, see equations (3.20) - (3.21). Then we approximated $R(\tau)$ by an exponentially decaying function and found the linewidth using (3.17). To check this method, we also employed another method based on Laplace transform (similar to the one described in section (4.1.1.1) for the inhomogeneous system in the second-order cumulant approximation) for several selected points. The results match at least in the first 2 digits.

While the analysis closely follows that of [29], we investigate the set of parameters more relevant for the bad-cavity lasers in the superradiant regime, where the condition (3.31) is satisfied, and we can perform adiabatic elimination of the cavity field. Namely, we set $\kappa = 1$ and $\gamma_s = 10^{-6}\kappa$, assuming no dephasing ($\nu = 0$) and no shift ($\Delta_a = \delta_c = 0$). We performed our simulation for different values of $CN = \frac{4Ng^2}{\kappa\gamma}$, and for different pumping rates R between $R_{\min}$ and $R_{\max}$, calculated according to expressions (4.19), chapter 4).

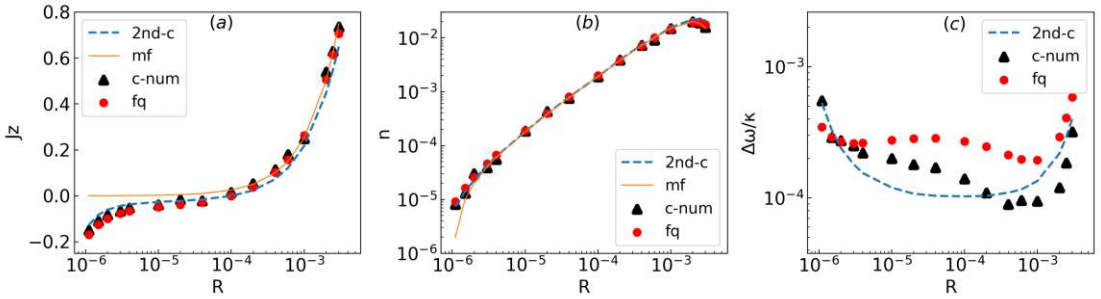

Figure 3.1: Characteristics of superradiant laser for $N = 40$ atoms, $CN = 4000$, (a): inversion, (b): number of intracavity photons, (c): linewidth (right) calculated using different methods: mean-field theory (orange solid curve), second-order cumulant theory (blue dashed curve), c-number Langevin equations (black triangles) and full quantum approach (red circles).

In figure 3.1, we present the results of the calculation for $N = 40$ atoms, $CN = 4000$. We can see that all the methods give quite similar results for the photon number and inversion, but different methods predict different linewidths, and the positions of the minimum also differs up to a factor of about 3. The stochastic c-number method predicts the dependence of the linewidth on the pumping rate slightly better, at least qualitatively.

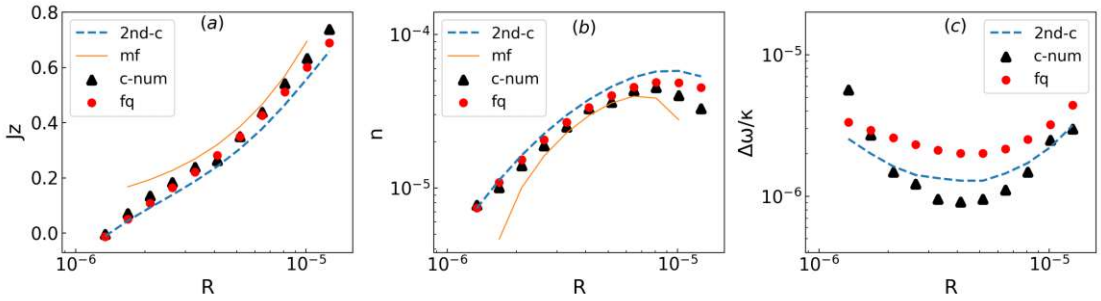

Figure 3.2: Characteristics of superradiant laser for $N = 40$ atoms at $CN = 16$: (a): inversion, (b): number of intracavity photons, (c): linewidth (right) calculated using different methods (same style-color encoding as in figure 3.1).

Next, we consider a deeper bad cavity regime with $CN = 16$, while keeping all other parameters unchanged. This regime, as will be shown in the next chapter, is more relevant to attaining the ultimately small linewidth of the bad cavity laser. Then the simulation of c-number Langevin equations matches the full quantum solution for both inversion and photon number, but the mean-field and the second-order cumulant methods underestimate and overestimate these quantities, respectively, see Figure 3.2. The linewidth minimized with respect to the pumping rate R occurs to be underestimated when using the Langevin c-number and the second-order cumulant expansion methods, in comparison to the full quantum solution, however, the second-order cumulant performs better.

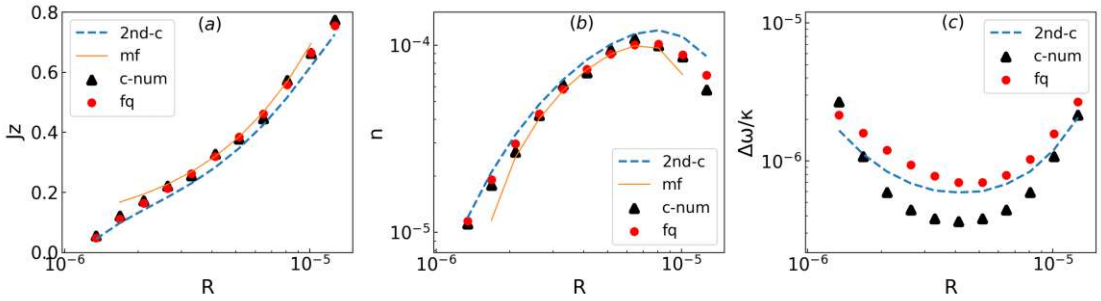

Figure 3.3: Characteristics of superradiant laser for $N = 100$ atoms at $CN = 16$: (a): inversion, (b): number of intracavity photons, (c): linewidth (right) calculated using different methods (same style-color encoding as in figure 3.1).

In Figure 3.3, we present the results for $N = 100$ atoms and $CN = 16$. We see that the agreement of the inversion and the intracavity photon number between all the

methods becomes much better than for 40 atoms (although the mean-field approach still underestimates the intracavity photon number near the lower lasing threshold). It is remarkable, that the results for the linewidth calculated with the help of the second-order cumulant approach get significantly closer to the prediction of the full quantum theory.

Now, let us summarize the results. First, the *mean-field* approach allows us to calculate the inversion and the intracavity photon number with a precision of about a few tens percent or below, which makes this method suitable for such calculations, where we are not interested in the linewidth. The *second-order cumulant expansion* method seems to be well-suitable for situations where we need to calculate the linewidth, and we can expect that the accuracy of this method increases with the number of atoms in the system. We should note that for an inhomogeneously broadened ensemble, the atoms should be divided into M clusters, and the number of equations in the mean-field approach scales as M, whereas in the second-order cumulant approach as M^2, what makes this method more computationally expensive. The c-number Langevin approach seems to be not so promising. First, it is quite expensive computationally (despite the linear scaling of the number of equation with number M of clusters), because it requires simulation of many trajectories and averaging over them. Second, we haven't observed any significant improvement in its precision for the calculation of the linewidth with an increase in the number of atoms, in contrast to the second-order cumulant approach.

So, we can conclude that the most relevant methods are the mean-field approximation or, if we are interested in the linewidth, the second-order cumulant approach. These methods will be used in the subsequent chapters.

CHAPTER 4

Ultimate stability of active optical frequency standards

The bulk of this chapter is published in Physical Review A [11]

In this chapter, we study the ultimate stability that can be attained with a superradiant laser and compare it with that of a passive optical clock based on an atomic ensemble with similar characteristics. For the sake of definiteness, we consider the model of two-level laser with continuous incoherent repumping [9], similar to the one considered in chapter 3, but here we consider not only homogeneous but also inhomogeneous atomic ensembles. Bad-cavity lasers based on other schemes, such as atomic beam lasers [10], optical conveyor lasers [34], and lasers with sequential coupling of atomic ensembles [27] should have similar ultimate characteristics, up to some numerical factors. Such a two-level model can correctly represent the dynamic of a real multilevel superradiant laser with continuous repumping and single lasing transition, if the lifetimes of the intermediate levels are much shorter than any other timescale in the system except, may be, the decay rate of the cavity field [35]. In this chapter, following [9] and [36], we will use second-order cumulant theory which allows calculating both output power and spectrum of the superradiant laser.

In section 4.1 we begin by providing an overview of the model and highlighting the key aspects of the calculations. We then consider the case of a homogeneous system, in this simplified scenario, we derive analytical expressions for the output power and linewidth and analyze their dependencies qualitatively. Finally, we study the linewidth quantitatively, both for the simple homogeneous model and for a more realistic model with inhomogeneous coupling of the atoms to the cavity field and inhomogeneous broadening of the lasing transition. We optimize the cooperativity as well as the rate of incoherent pumping to attain a minimum linewidth at a given atomic number and cavity finesse. We express these optimized parameters as well as the linewidth and the respective number

of intracavity photons via characteristic properties of the atomic ensemble. In section 4.2 we present general expressions for the short-term stability of a secondary laser phase locked to a low-power narrow-line continuous-wave bad-cavity laser. In section 4.3 we estimate the achievable performance for ensembles of atoms trapped in an optical lattice potential and compare the respective frequency stabilities that can be obtained with the help of active and passive frequency standards based on such ensembles.

In the following section, we present a generic model of a two-level bad cavity laser (superradiant laser) with incoherent pumping and derive general expressions for the minimum linewidth $\Delta\omega$ and the necessary set of optimized parameters.

4.1 Linewidth of a bad cavity laser

In this section, we provide an overview of how the linewidth is influenced by the characteristics of a bad-cavity superradiant laser operating with continuous incoherent repumping, and we estimate the minimum achievable linewidth for such a laser. We begin by considering a two-level bad-cavity laser model with incoherent pumping, as analyzed in [9]. This type of laser operates between two lasing thresholds, R_{min} and R_{max}. If the pumping rate is below R_{min}, the population inversion required for lasing is not achieved. Conversely, if the pumping rate exceeds R_{max}, the coherence is destroyed, preventing coherent light emission.

For a homogeneous system (see section 3.1), where each atom contributing to the gain has identical parameters such as coupling strength with the cavity field, transition frequency, and dephasing rate, and assuming the laser operates well within the range of the lower and upper lasing thresholds, the minimum linewidth $\Delta\omega_{\mathrm{min}}$ of this laser can be approximated as described in [9].

$$\Delta\omega_{\mathrm{min}} \approx C\gamma_s = 4g^2/\kappa. \tag{4.1}$$

It may initially appear that reducing the cooperativity C as much as possible would minimize the linewidth. However, the expression (4.1) is only valid when the pumping rate R is much greater than the lower lasing threshold R_{min} and much smaller than the upper lasing threshold R_{max}. Accurate expressions for these thresholds in the homogeneous case will be derived in section 4.1.2. From expressions (4.19) and (4.20), it can be seen that both lasing thresholds approach each other as cooperativity C decreases for a given number N of atoms. As a result, the minimum linewidth is reached in a parameter range where the condition $R_{\mathrm{min}} \ll R \ll R_{\mathrm{max}}$ is no longer satisfied, and the estimate (4.1) becomes invalid. Therefore, a more accurate estimate for $\Delta\omega_{\mathrm{min}}$ is required.

As discussed in section 3.2.2, the spectral properties of a continuous-wave laser can be derived from the two-time correlation function of its output field, $\langle\hat{a}^\dagger(t_0+\tau)\hat{a}(t_0)\rangle$. In the bad-cavity regime, this correlation is directly proportional to the atomic coherence correlation [9], since the cavity field can be adiabatically eliminated (3.31).

4.1.1 Inhomogeneous system: description of the model and equations

We consider an ensemble of N two-level atoms confined in space (for instance, using an optical lattice potential) and interacting with a single cavity mode. Dipole-dipole interactions between atoms and the collective coupling of the atoms to the bath are neglected. The master equation governing this system can be written as

$$\frac{d\hat{\rho}}{dt} = \frac{i}{\hbar}[\hat{\mathcal{H}}, \hat{\rho}] + \kappa\hat{\mathfrak{D}}'[\hat{a}]\hat{\rho} + \xi\hat{\mathfrak{D}}'[\hat{a}^\dagger\hat{a}]\hat{\rho} + \sum_{j=1}^{N}\left[\gamma_s\hat{\mathfrak{D}}'[\hat{\sigma}^j_{ge}]\hat{\rho} + w_j\hat{\mathfrak{D}}'[\hat{\sigma}^j_{eg}]\hat{\rho} + \nu_j\hat{\mathfrak{D}}'[\hat{\sigma}^j_{ee}]\hat{\rho}\right] \quad (4.2)$$

The Hamiltonian $\hat{\mathcal{H}}$ in the rotating frame can be written as

$$\hat{\mathcal{H}} = \hbar\left[\delta_c\hat{a}^\dagger\hat{a} + \sum_{j=1}^{N} g_j(\hat{\sigma}^j_{eg}\hat{a} + \hat{a}^\dagger\hat{\sigma}^j_{ge}) + \sum_j \Delta_j\hat{\sigma}^j_{ee}\right], \quad (4.3)$$

Here, γ_s represents the spontaneous decay rate of the upper lasing state, ξ is the dephasing rate of the cavity field, and R_j and ν_j denote the incoherent pumping and dephasing rates of the jth atom, respectively. A closed set of differential equations for the stochastic means of the system operators can be derived using a second-order cumulant expansion and the phase invariance, as described in section 3.6.

$$\begin{aligned}
\frac{d}{dt}\langle\hat{a}^\dagger\hat{a}\rangle &= -\kappa\langle\hat{a}^\dagger\hat{a}\rangle + i\sum_{j=1}^{N} g_j(\langle\hat{\sigma}^j_{eg}\hat{a}\rangle - \langle\hat{a}^\dagger\hat{\sigma}^j_{ge}\rangle)\\
\frac{d}{dt}\langle\hat{\sigma}^k_{eg}\hat{a}\rangle &= -\left[\frac{\kappa'_k}{2} + i\delta'_k\right]\hat{\sigma}^k_{eg} + ig_k\left[\langle\hat{a}^\dagger\hat{a}\rangle(1 - 2\langle\hat{\sigma}^k_{ee}\rangle) - \langle\hat{\sigma}^k_{ee}\rangle\right] - i\sum_{j\neq k} g_j\langle\hat{\sigma}^k_{eg}\hat{\sigma}^j_{ge}\rangle\\
\frac{d}{dt}\langle\hat{\sigma}^k_{ee}\rangle &= ig_k\left[\langle\hat{a}^\dagger\hat{\sigma}^k_{ge}\rangle - \langle\hat{\sigma}^k_{eg}\hat{a}\rangle\right] - (\gamma_s + R_k)\langle\hat{\sigma}^k_{ee}\rangle + R_k\\
\frac{d}{dt}\langle\hat{\sigma}^k_{eg}\hat{\sigma}^l_{ge}\rangle &= -\left[\Gamma'_{kl} + i\Delta_{lk}\right]\langle\hat{\sigma}^k_{eg}\hat{\sigma}^l_{ge}\rangle - ig_k\langle\hat{a}^\dagger\hat{\sigma}^l_{ge}\rangle(2\langle\hat{\sigma}^k_{ee}\rangle - 1) + ig_l\langle\hat{\sigma}^k_{eg}\hat{a}\rangle(2\langle\hat{\sigma}^l_{ee}\rangle - 1)
\end{aligned} \quad (4.4)$$

Here, $\kappa'_k = \kappa + \xi + R_k + \nu_k + \gamma_s$, $\delta'_k = \delta_c - \Delta_k$, $\Gamma'_{kl} = \gamma_s + (R_k + R_l + \nu_k + \nu_l)/2$, and $\Delta_{lk} = \Delta_l - \Delta_k$. As can be observed from equations (4.4), the number of equations scales quadratically with the number of atoms. For practical simulations involving ensembles of tens of thousands of atoms, it is necessary to group the atoms into M clusters, where all N_k atoms in the kth cluster are treated as identical. This clustering approach will be utilized in chapter 6 for modeling our mHz laser, discussed in chapter 5.

If the condition (3.31) is satisfied then it is advantageous to perform an **adiabatic**

elimination of the fast variables $\langle\hat{a}^\dagger\hat{a}\rangle$, $\langle\hat{a}^\dagger\hat{\sigma}_{ge}\rangle$, and $\langle\hat{\sigma}_{eg}\hat{a}\rangle$. Then, one can express

$$\begin{aligned}\langle\hat{a}^\dagger\hat{a}\rangle = &\left[\kappa - \sum_k \frac{4N_k g_k^2 \kappa'_k}{\kappa_k'^2 + 4\delta_k'^2}[2\langle\hat{\sigma}^k_{ee}\rangle - 1]\right]^{-1} \\ &\times \sum_k \frac{4g_k N_k}{\kappa_k'^2 + 4\delta_k'^2}\left[\kappa'_k\left(g_k\langle\hat{\sigma}^k_{ee}\rangle + \sum_j N'_{j,k} g_j Re(\langle\hat{\sigma}^k_{eg}\hat{\sigma}^j_{ge}\rangle)\right)\right. \\ &\left. + 2\delta'_k\left(\sum_j N'_{j,k} g_j Im(\langle\hat{\sigma}^k_{eg}\hat{\sigma}^j_{ge}\rangle)\right)\right]\end{aligned} \tag{4.5}$$

and

$$\langle\hat{\sigma}^k_{eg}\hat{a}\rangle = \frac{2}{\kappa'_k + 2i\delta'_k}\left\{ig_k\left[\langle\hat{a}^\dagger\hat{a}\rangle(1 - 2\langle\hat{\sigma}^k_{ee}\rangle) - \langle\hat{\sigma}^k_{ee}\rangle\right] - i\sum_j N'_{j,k} g_j \langle\hat{\sigma}^k_{eg}\hat{\sigma}^j_{ge}\rangle\right\}. \tag{4.6}$$

Here, the sums are taken over clusters instead of atoms, N_k is the number of atoms in the kth cluster, and

$$N'_{j,k} = \begin{cases} N_j, & j \neq k \\ \max(0, N_k - 1), & j = k \end{cases} \tag{4.7}$$

Substituting expressions (4.5) and (4.6) into equations (4.4), and resolving them, one can find the steady-state values of $\langle\hat{\sigma}^j_{eg}\hat{a}\rangle$ and $\langle\hat{\sigma}^j_{ee}\rangle$, assuming the atomic dipoles get synchronized. Then one can express the steady-state values of $\langle\hat{a}^\dagger\hat{a}\rangle$, $\langle\hat{\sigma}^j_{eg}\hat{a}\rangle$ and $\langle\hat{a}^\dagger\hat{\sigma}^j_{ge}\rangle$ with the help of equations (4.5) and (4.6). The output power P of the laser is equal to

$$P = \eta\hbar\omega\kappa\langle\hat{a}^\dagger\hat{a}\rangle, \tag{4.8}$$

where η is the efficiency of the outcoupling mirror, and ω is the frequency of the laser radiation.

4.1.1.1 Spectrum of the superradiant laser

Similar to section 3.2, using the Wiener-Khintchine theorem (3.14), the spectral density $S_E(\omega)$ of the signal can be obtained as a real part of the Fourier transform of the 2-time correlation function :

$$S_E(\omega) \propto \mathrm{Re}\int_0^\infty \langle\hat{a}^\dagger(t_0 + \tau)\hat{a}(t_0)\rangle e^{-i\omega\tau} d\tau. \tag{4.9}$$

In established steady-state regime $\langle\hat{a}^\dagger(t_0 + \tau)\hat{a}(t_0)\rangle = \langle\hat{a}^\dagger(\tau)\hat{a}(0)\rangle \equiv \langle\hat{a}^\dagger\hat{a}_0\rangle$, where $\hat{a}^\dagger = \hat{a}^\dagger(t)$, and $\hat{a}_0 = \hat{a}(0)$. To find this function, one needs to solve the set of equations obtained with the help of the quantum regression theorem, see section 3.2.2:

$$\frac{d}{dt}\langle\hat{a}^\dagger\hat{a}_0\rangle = -\left[\frac{\kappa + \xi}{2} - i\delta_c\right]\langle\hat{a}^\dagger\hat{a}_0\rangle + i\sum_k N_k g_k \left\langle\hat{\sigma}^k_{eg}\hat{a}_0\right\rangle, \tag{4.10}$$

$$\frac{d}{dt}\langle\hat{\sigma}^k_{eg}\hat{a}_0\rangle = -\left[\frac{\gamma_s + R_k + \nu_k}{2} - i\Delta_k\right]\langle\hat{\sigma}^k_{eg}\hat{a}_0\rangle - ig_k\left\langle\hat{\sigma}^k_z\right\rangle\langle\hat{a}^\dagger\hat{a}_0\rangle. \tag{4.11}$$

where $\left\langle\hat{\sigma}^k_z\right\rangle = \left\langle\hat{\sigma}^k_{ee}\right\rangle - \left\langle\hat{\sigma}^k_{gg}\right\rangle$. Substituting here the steady state values of $\langle\hat{\sigma}^k_z\rangle$ into (4.11) and (4.10) and performing Laplace transform, one gets the set of linear equations of the form $(\mathbb{A} + \mathbb{I}\,s)\cdot\mathbb{X} = \hat{B}$, where $\mathbb{I}$ is identity matrix,

$$\begin{gathered}\mathbb{A} = \begin{bmatrix} \frac{\kappa+\xi}{2} - i\delta_c & -iN_1g_1 & \cdots\ \cdots & -iN_Mg_M \\ ig_1\langle\sigma^1_z\rangle & \frac{\gamma_s+R_1+\nu_1}{2} - i\Delta_1 & \cdots 0 \cdots & 0 \\ \vdots & \vdots & \ddots & \vdots \\ ig_M\left\langle\sigma^M_z\right\rangle & 0 & \cdots 0 \cdots & \frac{\gamma_s+R_M+\nu_M}{2} - i\Delta_M \end{bmatrix}, \\ \hat{B} = \begin{bmatrix} \langle\hat{a}^\dagger\hat{a}\rangle_s \\ \langle\hat{\sigma}^1_{eg}\hat{a}\rangle_s \\ \vdots \\ \langle\hat{\sigma}^1_{eg}\hat{a}\rangle_s \end{bmatrix}, \quad \mathbb{X} = \begin{bmatrix} \mathfrak{L}\{\langle\hat{a}^\dagger\hat{a}\rangle\}(s) \\ \mathfrak{L}\{\langle\hat{\sigma}^1_{eg}\hat{a}\rangle\}(s) \\ \vdots \\ \mathfrak{L}\{\langle\hat{\sigma}^1_{eg}\hat{a}\rangle\}(s) \end{bmatrix}\end{gathered} \tag{4.12}$$

$\mathfrak{L}\{f\}(s) = \int_0^\infty f(t)e^{-st}dt$ is a Laplace transform, and index s denotes "steady-state". Using the connection between the Laplace and Fourier transforms, the spectral density

$$S(\omega) \propto \mathrm{Re}\left[\mathfrak{L}\{\langle\hat{a}^\dagger\hat{a}\rangle\}(i\omega)\right]. \tag{4.13}$$

can be found with the help of (4.12) and (4.13), and one can calculate its full linewidth at half maximum $\Delta\omega$.

4.1.2 Homogeneous case: analytic expressions and qualitative considerations

In this section, we examine the simplest case of a bad-cavity laser with homogeneous gain, where all atoms have identical transition frequencies ω_a, pumping and dephasing rates R and ν, and coupling strengths g to the cavity field. The steady-state solution and linewidth for this simplified system, within the second-order cumulant approximation, can be determined analytically or semi-analytically. This analysis has been partially conducted in [9], and here we provide an overview of the main results and derive a few additional useful relations.

First, from equations (4.4) one can easily describe the homogeneous case

$$\begin{aligned}\langle\hat{a}^\dagger\hat{a}\rangle_s &= \frac{N(\gamma_s + R)}{2\kappa}\left(\frac{R-\gamma_s}{R+\gamma_s} - \langle\hat{\sigma}_z\rangle_s\right) \\ \langle\hat{\sigma}^1_{eg}\hat{\sigma}^2_{ge}\rangle_s &= \frac{\langle\hat{\sigma}_z\rangle_s(\gamma_s + R)}{2\Gamma'}\left(\frac{R-\gamma_s}{R+\gamma_s} - \langle\hat{\sigma}_z\rangle_z\right)\end{aligned} \tag{4.14}$$

where $\Gamma' = \gamma_s + R + \nu$, $\kappa' = \kappa + \xi + \Gamma'$. Substituting these expressions into equation (4.4), one can obtain, after simplification, the following quadratic equation for $\langle\hat{\sigma}_z\rangle_s$:

$$\langle\hat{\sigma}_z\rangle_s^2\left(\frac{N(\gamma_s+R)}{2\kappa}+\frac{(N-1)(\gamma_s+R)}{2\Gamma'}\right)+\frac{(R-\gamma_s)(\kappa'^2+4(\delta_c-\Delta)^2)}{8g^2\kappa'}-\frac{1}{2}$$
$$-\langle\hat{\sigma}_z\rangle_s\left[\frac{(R+\gamma_s)(\kappa'^2+4(\delta_c-\Delta)^2)}{8g^2\kappa'}+\frac{1}{2}+\frac{(R-\gamma_s)}{2}\left(\frac{N}{\kappa}+\frac{N-1}{\Gamma'}\right)\right]=0 \quad (4.15)$$

Solving this equation, one can get the steady-state values $\langle\hat{\sigma}_z\rangle_s$, as well as $\langle\hat{a}^\dagger\hat{a}\rangle_s$ and $\langle\hat{\sigma}_{eg}^1\hat{\sigma}_{ge}^2\rangle_s$ with the help of (4.5) and (4.6).

For the sake of simplicity, we assume that all the atoms are in resonance with the cavity ($\delta_c = \Delta = 0$), and the cavity dephasing ξ is negligible ($\xi = 0$). Then the equation (4.15) simplifies to

$$\langle\hat{\sigma}_z\rangle_s^2\left(\frac{N(\gamma_s+R)}{2\kappa}+\frac{(N-1)(\gamma_s+R)}{2\Gamma'}\right)+\frac{(R-\gamma_s)\kappa'}{8g^2}-\frac{1}{2}$$
$$-\langle\hat{\sigma}_z\rangle_s\left[\frac{(R+\gamma_s)\kappa'}{8g^2}+\frac{1}{2}+\frac{(R-\gamma_s)}{2}\left(\frac{N}{\kappa}+\frac{N-1}{\Gamma'}\right)\right]=0. \quad (4.16)$$

Consider the equation (4.16), taking first $N-1 \approx N$ and neglecting γ_s, R and g in comparison with κ, one can find the approximate solutions as

$$\langle\hat{\sigma}_z\rangle_{s,1} \approx \frac{\kappa\Gamma'}{4g^2N}. \quad \langle\hat{\sigma}_z\rangle_{s,2} \approx \frac{R-\gamma_s}{R+\gamma_s}, \quad (4.17)$$

From the above solution, it is evident that only the first solution yields $\langle\hat{a}^\dagger\hat{a}\rangle_s \neq 0$. This solution enables us to estimate the lasing thresholds. By substituting (4.17) into (4.14), we can determine that lasing is possible, i.e., $\langle\hat{a}^\dagger\hat{a}\rangle_s > 0$, only if

$$\frac{R-\gamma_s}{R+\gamma_s} > \frac{\kappa(\gamma_s+R+\nu)}{4g^2N} = \frac{\gamma_s+R+\nu}{NC\gamma_s}, \quad (4.18)$$

is satisfied, resulting in the limits of the pumping rate R:

$$\begin{aligned} R_{min} &= \frac{NC\gamma_s-\nu-\sqrt{(NC\gamma_s-\nu)^2-8\gamma_s^2NC}}{2}-\gamma_s, \\ R_{max} &= \frac{NC\gamma_s-\nu+\sqrt{(NC\gamma_s-\nu)^2-8\gamma_s^2NC}}{2}-\gamma_s. \end{aligned} \quad (4.19)$$

With $\gamma_s, \nu \ll NC\gamma_s$ it gives

$$\begin{aligned} R_{min} &\approx \gamma_s\frac{NC\gamma_s+\nu}{NC\gamma_s-\nu}, \\ R_{max} &\approx NC\gamma_s-\nu, \end{aligned} \quad (4.20)$$

In accordance with [37], the spectrum for the homogeneous system can be obtained from the set of linear equations derived from (4.13) and (4.12). Instead of performing a Laplace

transform, we can calculate the full width at half maximum (FWHM) $\Delta\omega$ as $\Delta\omega = 2|\lambda|$, where λ is the smallest in absolute value eigenvalue of the matrix for this system. This can be demonstrated by performing a Fourier transform of the exponentially decaying term in $\langle \hat{a}^\dagger \hat{a}_0 \rangle$. Assuming $\kappa \gg |\lambda|$, the linewidth can be expressed as

$$\Delta\omega = \Gamma' - \frac{4g^2 N \langle \hat{\sigma}_z \rangle_s}{\kappa}. \tag{4.21}$$

In fact, substituting $\langle \hat{\sigma}_z \rangle_s$ from (4.17) into (4.21) results in $\Delta\omega = 0$, so to calculate the linewidth we need to go beyond the approximation that we have used to derive (4.17). A direct approach to determine $\Delta\omega$ would involve solving the quadratic equation (4.16) exactly; however, the resulting expression is too complex for a straightforward qualitative analysis. Instead, we can calculate a correction to the approximate solution (4.17) by expanding the coefficients of the equation (4.21) into a Fourier series.

$$\Delta\omega \approx \frac{\Gamma'(\Gamma' + NC\gamma_s)}{2\langle \hat{a}^\dagger \hat{a} \rangle_s} - \frac{\Gamma'}{N}. \tag{4.22}$$

In the limit where $\gamma_s, \nu \ll R \ll NC\gamma_s$, the linewidth approximates to $\Delta\omega \approx C\gamma_s$. This result, reported in [9], represents the minimum attainable linewidth for a given cooperativity C. However, C cannot be arbitrarily small, as this would lead to a situation where $R_{\min} > R_{\max}$, making lasing impossible. The minimum value of C, above which lasing remains feasible, can be determined by setting $R_{\min}$ equal to $R_{\max}$ in (4.19), which yields

$$(NC_{\min}\gamma_s - \nu)^2 = 8NC_{\min}\gamma_s^2. \tag{4.23}$$

For $\nu = 0$, the minimum value of C is $C_{\min} = 8/N$. Furthermore, at very small C, the condition $\gamma_s, \nu \ll R \ll NC\gamma_s$ cannot be satisfied, and thus the optimal value of C, where the minimum linewidth is achieved, is larger than but proportional to $C_{\min}$.

We can conclude that the minimum attainable linewidth $\Delta\omega_{\min}$ is proportional to γ_s/N. Therefore, it is convenient to express $\Delta\omega$ in units of γ_s/N as a function of CN. Additionally, from expressions (4.14) and (4.17), we observe that the dimensionless value $\langle \hat{a}^\dagger \hat{a} \rangle \kappa/(N\gamma_s)$ is independent of κ and N for given values of CN, R/γ_s, and ν/γ_s.

4.1.3 Minimized Linewidth

In this subsection, we investigate in more detail the dependence of the optimized spectral linewidth $\Delta\omega$ on various parameters of the superradiance laser. First, we consider the homogeneous case. In Figure 4.1, we present the linewidth $\Delta\omega$ for different values of CN as a function of incoherent repumping rate R, calculated according to the method described in subsection 4.1.2. One can see that, being expressed in units of γ_s/N, all the linewidths show quite similar behavior, except near the lower and the upper lasing thresholds.

For each curve, similar to those shown in Figure 4.2, we can determine the minimum linewidth $\Delta\omega_{\min}$, which is achieved at some optimal repumping rate R_{opt}. Figure 4.2

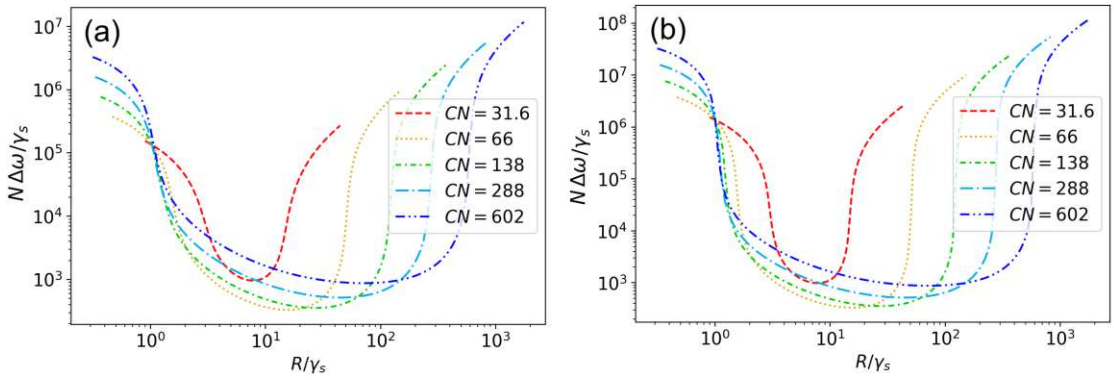

Figure 4.1: Dependency of linewidth $\Delta\omega$ on repumping rate R for a homogeneous system at different values of CN for different values of number N of atoms and finesse $\mathcal{F}$ of the cavity. (a): $N = 10^4$, $\mathcal{F} = 10^4$. (b): $N = 10^5$, $\mathcal{F} = 10^5$. In both cases the atomic dephasing rate is $\nu = 0.1$ s^{-1} and the cavity length is $l_{\mathrm{cav}} = 10$ cm, which corresponds to $\kappa = \pi c/(\mathcal{F} l_{\mathrm{cav}}) \approx 9.4 \times 10^5$ s^{-1} and $\kappa \approx 9.4 \times 10^4$ s^{-1} respectively.

presents the dependence of these minimized linewidths on CN for different values of the atomic dephasing rate ν, the number of atoms N, and the cavity finesse $\mathcal{F}$. It is noteworthy that the value of $\Delta\omega_{\mathrm{min}}$, when expressed in units of γ_s/N, as well as the optimal repumping rate R_{opt}, do not depend on N (i.e., the optimized linewidth $\Delta\omega_{\mathrm{min}}$ is inversely proportional to N at a given value of CN). Similarly, the ratio of $\langle \hat{a}^\dagger \hat{a} \rangle \cdot \kappa$ to $N\gamma_s$ corresponding to the minimized linewidth, as well as the optimal repumping rate R_{opt}, depending on the atomic dephasing rate ν but not on $\mathcal{F}$ or N. In this example, the cavity length l_{cav} is set to $l_{\mathrm{cav}} = 10$ cm; however, the results are not sensitive to variations in the cavity length as long as the laser operates in the bad-cavity regime, as discussed in section 4.3.

It is also important to note that the quantity $\langle \hat{a}^\dagger \hat{a} \rangle \cdot \kappa/(N\gamma_s)$ has a straightforward physical interpretation: it represents the ratio of the number of photons emitted from the cavity mode (assuming perfect outcoupling with $\eta = 1$) to the single-atom spontaneous emission rate γ_s multiplied by the number of atoms. Near the maximum of the output power, this ratio is proportional to N. However, near the minimum of the linewidth, it is independent of N. In the absence of atomic dephasing, the minimum attainable linewidth (optimized by both the repumping rate R and the cooperativity C) is approximately $\Delta_{\mathrm{opt}} \approx 64\gamma_s/N$.

Up to now, we calculated the line widths for a fully homogeneous model. However, in real systems, different atoms may experience varying level shifts, dephasing rates due to interactions with the environment, and pumping rates. Furthermore, atoms may be coupled differently to the superradiant cavity field. This is particularly evident when atoms trapped within a magic optical lattice inside the superradiant cavity are coupled to the standing-wave mode of the cavity. This coupling discrepancy arises due to the mismatch between the magic wavelength that traps the atoms and the wavelength of the superradiant mode, as detailed in expression 4.38 in section 4.3. The spectral linewidth

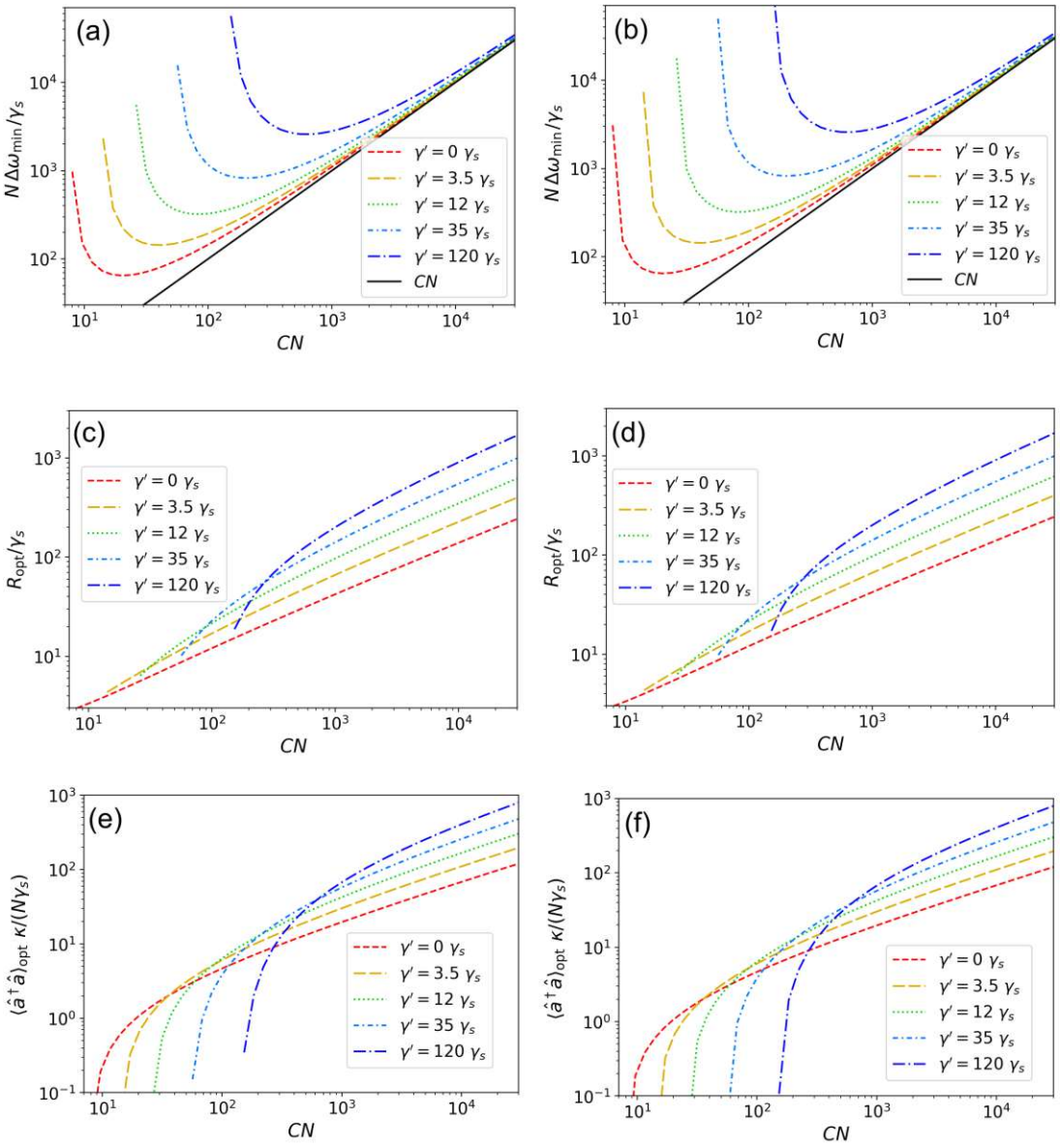

Figure 4.2: Dependency of minimum attainable linewidth $\Delta\omega_{\min}$, the optimal repumping rate R_{opt} in units of γ_s ((c),(d)), and the respective intracavity photon number $\langle\hat{a}^\dagger\hat{a}\rangle_{\text{opt}}$ multiplied by $\kappa/(N\gamma_s)$ ((e),(f))) on the parameter CN for different values of atomic dephasing ν. The graphs are for different values of number N of atoms and finesse $\mathcal{F}$ of the cavity: (a, c, e): $N = 10^4$, $\mathcal{F} = 10^4$. (b, d, f): $N = 10^5$, $\mathcal{F} = 10^5$. In (a) and (b), the asymptotic CN behavior is indicated by a black line.

of the output radiation can be computed using the method outlined in subsection 4.1.1. In Figure 4.3, we present the dependencies of the minimum attainable linewidth $\Delta\omega_{\min}$ and the intracavity photon number $\langle\hat{a}^\dagger\hat{a}\rangle$ on cooperativity CN, calculated for repumping

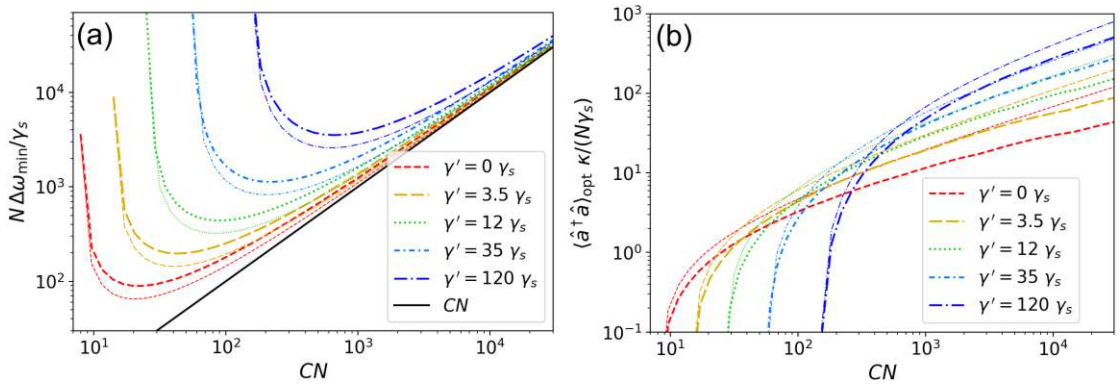

Figure 4.3: Dependency of minimum attainable linewidth $\Delta\omega_{\min}$ in units of γ_s/N (a), and the respective intracavity photon number $\langle\hat{a}^\dagger\hat{a}\rangle_{\rm opt}$ multiplied by $\kappa/(N\gamma_s)$ (b) on the parameter CN for a system with inhomogeneous cosine-modulated coupling (thick curves) system for different values of atomic dephasing rate ν at $N = 10^5$, $\mathcal{F} = 10^5$. The cavity length is $l_{\rm cav} = 10$ cm. Thin curves represent the linewidths and the intracavity photon numbers calculated according to the homogeneous model, the same colour and style corresponds to the same value of ν.

rates $R_{\rm opt}$ that minimize the linewidth. The atoms were grouped into $M = 21$ clusters, each containing an equal number of atoms. The coupling strengthes g_j for the jth cluster were chosen to be proportional to $\cos\left(\frac{\pi(j-0.5)}{2M}\right)$; all other parameters were kept the same across clusters, and $\Delta_j = \delta_c = \xi = 0$. The single-atom cooperativity C is redefined according to

$$CN = \sum_j \frac{4g_j^2}{\kappa\gamma_s}. \tag{4.24}$$

For comparison, we present the dependencies of $\Delta_{\min}$ and $\langle\hat{a}^\dagger\hat{a}\rangle_{\rm opt}$ calculated using the homogeneous model. It can be observed that the homogeneous model slightly underestimates the attainable linewidth and overestimates the intracavity photon number, both by a factor of approximately 1.4 near the optimally chosen CN. Specifically, at $\nu = 12\gamma_s$, the minimum linewidth is $\Delta\omega \approx 4.3 \times 10^2\gamma_s/N$ for inhomogeneous coupling, whereas it is $\Delta\omega \approx 3.1 \times 10^2\gamma_s/N$ for homogeneous coupling.

Figure 4.4 illustrates the minimized linewidth $\Delta_{\min}$ for a system where both the coupling of the atoms to the cavity mode is inhomogeneous, and the lasing transitions in different atoms experience different shifts Δ_j. These shifts can arise from variations in environmental parameters across the atomic ensemble. In this scenario, we considered the simplest case where the atomic detunings Δ_j are uniformly distributed over 11 clusters within $\pm\Delta_0$, and the couplings are distributed over 7 clusters, resulting in a total of 77 clusters. At $\nu = \Delta_0 = 12\gamma_s$, the minimum attainable linewidth is $\Delta\omega_{\min} \approx 7 \times 10^2\ \gamma_s/N$, whereas increasing Δ_0 to 120 γ_s raises the linewidth to approximately $\Delta\omega_{\min} \approx 4.65 \times 10^3\ \gamma_s/N$.

Finally, it is useful to consider the dependence of the linewidth $\Delta\omega_{\rm opt}$, which is doubly minimized with respect to both R and CN, on the dephasing rate ν and the inhomogeneous

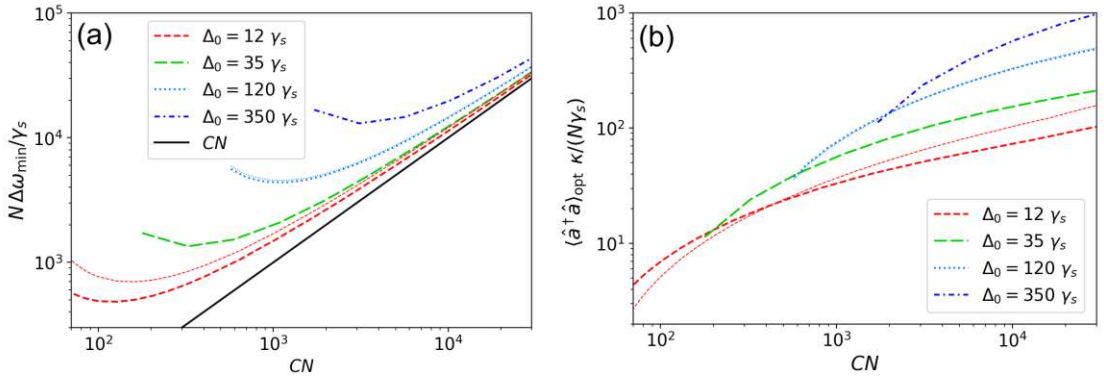

Figure 4.4: Dependency of minimum attainable linewidth $\Delta\omega_{\min}$ in units of γ_s/N (a), and the respective intracavity photon number $\langle\hat{a}^\dagger\hat{a}\rangle_{\rm opt}$ multiplied by $\kappa/(N\gamma_s)$ (b) on the parameter CN for a system with inhomogeneous cosine-modulated coupling for different values of broadening Δ_0 at $N = 10^5$, $\mathcal{F} = 10^5$. The atomic dephasing rate is $\nu = 0$ (thick curves), and $\nu = 12\gamma_s$ (thin curves; only for $\Delta_0 = 12\gamma_s$ and $\Delta_0 = 120\gamma_s$, the same color-style encoding corresponds to the same values of Δ_0). The cavity length is $l_{\rm cav} = 10$ cm.

broadening Δ_0. By fitting the results of the simulations, we obtain the estimated linewidth in the following form:

$$\Delta\omega_{\rm opt} \approx (90\gamma_s + 30\nu + 35\Delta_0)/N. \tag{4.25}$$

Expressing the linewidth via the more useful dispersion of the shifts $\Delta_0' = \Delta_0/\sqrt{3}$ for the flat distribution assumed in the simulations, gives approximately

$$\Delta\omega_{\rm opt} \approx (90\gamma_s + 30\nu + 60\Delta_0')/N \tag{4.26}$$

Similarly, one can find approximate expressions for the optimal pumping rate R_{opt}, for the collective cooperativity CN_{opt}, and for the intracavity photon number, where the smallest linewidth Δ_{opt} is achieved:

$$R_{opt} \approx 5\gamma_s + 1.13\nu + 1.5\Delta_0' \tag{4.27}$$

$$CN_{opt} \approx 25 + 5.5\frac{\nu}{\gamma_s} + 20\frac{\Delta_0'}{\gamma_s} \tag{4.28}$$

$$\langle\hat{a}^\dagger\hat{a}\rangle_{opt} \approx \frac{N}{\kappa}\,(0.9\gamma_s + 0.25\nu + 1.45\Delta_0') \tag{4.29}$$

4.2 Active optical frequency standard and its stability

The spectral characteristics of the output field E of a bad cavity laser can be described by its power spectral density $S_E(f)$. This can be derived from the two-time correlation function $\langle\hat{a}^\dagger(t_0+\tau)\hat{a}(t_0)\rangle$ using the Wiener-Khintchine theorem, see equation (3.14), and [24, 25]. To a first approximation, $\langle\hat{a}^\dagger(t_0+\tau)\hat{a}(t_0)\rangle$ can be represented by an exponentially

decaying function, which corresponds to a Lorentzian lineshape for $S_E(f)$ centered at the ordinary frequency $f_0 = \omega_0/(2\pi)$ with a half-width of $\Delta f = \Delta\omega/(2\pi)$. This type of signal exhibits white frequency noise, with a single-sided spectral power density $S_y(f)$ of fractional frequency fluctuations $y = \Delta\omega/\omega_0$, given by

$$S_y(f) = \frac{\Delta f}{\pi f_0^2} = \frac{2\Delta\omega}{\omega_0^2}, \tag{4.30}$$

corresponding to a spectral power density $S_\phi(f)$ of phase fluctuations

$$S_\phi(f) = \frac{\Delta f}{\pi f^2} = 2\Delta\omega f^2, \tag{4.31}$$

and Allan deviation

$$\sigma_y'(\tau) = \sqrt{\frac{\Delta\omega}{\omega_0^2\tau}}. \tag{4.32}$$

Furthermore, due to the finite rate of emitted photons, the field with power P exhibits quantum fluctuations, which result in a limited signal-to-noise ratio (SNR) given by the ratio of signal power to the noise power per unit bandwidth, expressed as $\mathrm{SNR} = P/(\hbar\omega_0)$ [38]. These fluctuations manifest as white amplitude and phase noise in the signal. When the active-laser output is heterodyned with an ideal, powerful, and perfectly stable continuous-wave (cw) laser, the amplitude noise generally does not significantly affect frequency stability. In this case, the power spectral density of the white phase noise S_ϕ is given by

$$S_\phi(f) = \mathrm{SNR}^{-1} = \frac{\hbar\omega_0}{P}, \tag{4.33}$$

with the corresponding Allan deviation [39, 40]

$$\sigma_y''(\tau) = \frac{1}{\tau}\sqrt{\frac{3\hbar f_h}{\omega_0 P}}. \tag{4.34}$$

As the Allan deviation would diverge for white phase noise with unlimited bandwidth, the noise is set to zero for frequencies above a cut-off frequency f_h (in ordinary frequency units) to obtain a finite value. In practice, this low-pass behavior can appear from the bandwidth of a phase-locked loop using the heterodyne signal.

To avoid the dependence on the arbitrary cut-off frequency, in this case, the modified Allan deviation is often used:

$$\mathrm{mod}\,\sigma_y''(\tau) = \frac{1}{\tau^{3/2}}\sqrt{\frac{3\hbar}{2\omega_0 P}}. \tag{4.35}$$

Adding the random walk noise of the phase associated with damping of the two-time correlation of the cavity field and the white phase noise associated with shot noise in the number of emitted photons results in the overall Allan deviation

$$\sigma_y(\tau) = \sqrt{(\sigma_y'(\tau))^2 + (\sigma_y''(\tau))^2} = \sqrt{\frac{\Delta\omega}{\omega_0^2\tau} + \frac{3\hbar f_h}{\omega_0 P\tau^2}}. \tag{4.36}$$

and the overall modified Allan deviation

$$\operatorname{mod}\sigma_y(\tau) = \sqrt{\operatorname{mod}\sigma'_y(\tau)^2 + \operatorname{mod}\sigma''_y(\tau)^2} = \sqrt{\frac{\Delta\omega}{2\omega_0^2\tau} + \frac{3\hbar}{2\omega_0 P\tau^3}}. \tag{4.37}$$

At short averaging times τ it is determined by the bad-cavity laser's output power P and at long times by its linewidth $\Delta\omega$.

The contribution $\sigma''_y(\tau)$ (4.34) to the total instability $\sigma_y(\tau)$ is associated with photon shot noise. Its impact depends on the bandwidth of the feedback loop used to phase-lock a secondary laser with good short-term stability to the bad cavity laser (see the discussion in section 4.3). On the other hand, the contribution $\sigma'_y(\tau)$ (4.32) is more fundamental, as it does not depend on the characteristics of the secondary laser and determines the stability limit over longer timescales.

4.3 Estimation of attainable stability

To perform quantitative estimations, we need to consider realistic parameters of the atomic ensemble. The double forbidden ${}^1S_0 \leftrightarrow {}^3P_0$ transition (clock transition) in fermionic isotopes of alkaline-earth-like atoms (Be, Mg, Ca, Sr, Zn, Cd, Hg, and Yb) seems to be a good choice for optical clocks with neutral atoms. This transition is totally forbidden in bosonic isotopes and becomes slightly allowed in fermionic isotopes due to hyperfine mixing. These atoms can be trapped in a magic-wavelength optical lattice potential and pumped into the upper ${}^3P_0$ lasing state.

In an active optical clock, the clock transition should be coupled to a high-finesse cavity in the strong cooperative coupling regime, which is problematic for wavelengths around 458 nm (corresponding to the clock transition in Mg) and shorter. Therefore, Ca, Sr, and Yb, with clock transition wavelengths λ of 660, 698, and 578 nm, respectively, are the most feasible candidates for the role of gain atoms in active optical clocks.

We will primarily perform our estimations for the ^{87}Sr isotope because, first, this element is the most used one in modern optical clocks with neutral atoms, and its relevant characteristics are the most studied among all the alkaline-earth-like atoms. Secondly, the natural linewidth of the clock transition in ^{87}Sr ($\gamma_s = 8.48\times10^{-3}$ s^{-1} [41]) lies between the linewidths of ^{43}Ca (2.2×10^{-3} s^{-1}) and Yb (43.5×10^{-3} s^{-1} and 38.5×10^{-3} s^{-1} for ^{171}Yb and ^{173}Yb, respectively) [42].

The finesse $\mathcal{F}$ of the best cavities at a wavelength of 698 nm can reach values of up to 10^6. However, it is quite difficult to build such a cavity. More feasible finesse values would range from tens to hundreds of thousands. For the sake of definiteness, we take $\mathcal{F} = 10^5$ as a typical parameter.

The coupling strengths g_j between the lasing transition in the jth atom and the cavity field can be estimated as

$$g_j \approx \frac{1}{w_c}\sqrt{\frac{6c^3\gamma_s}{l_{\text{cav}}\omega_0^2}}\cos(k_0 z_j), \tag{4.38}$$

where $k_0 = \omega_0/c$ is the wave number of the cavity mode, w_c is the cavity waist radius, and z_j is the z-coordinate of the jth atom along the cavity axis [43]. For the sake of simplicity, here we neglect the dependency of the coupling strength g on the distance from the atom to the cavity axis, which is proportional to $\exp(-(x_j^2 + y_j^2)/w_c^2)$ (this dependency can be relevant for atoms trapped in 2D or 3D optical lattices as well as for relatively hot atomic ensembles in a shallow 1D optical lattice).

Note that the cooperativity $C = 4\sum_j g_j^2/(N\kappa\gamma_s)$ does not depend on the length of the cavity l_{cav} but only on the cavity finesse $\mathcal{F}$ and the cavity mode waist w_c, because both g_j^2 and κ are inversely proportional to l_{cav}. Therefore, the cavity length l_{cav} is not a very important parameter, as long as the energy decay rate $\kappa = \pi c/(l_{\text{cav}}\mathcal{F})$ of the cavity mode is much larger than the linewidth of the laser gain. For the calculations performed in section 4.1.3, we take $l_{\text{cav}} = 10$ cm, which corresponds to a decay rate $\kappa = 9.42 \times 10^4$ s$^{-1} \approx 2\pi \times 15$ Hz at $\mathcal{F} = 10^5$.

Let us first compare the ultimate stability of an incoherently pumped active optical frequency standard with the stability of a quantum projection noise (QPN) limited passive frequency standard, assuming the same number of trapped atoms in both standards and no inhomogeneous broadening or decoherence. The fundamental limit of the superradiant laser linewidth is then $\Delta\omega \approx 90\,\gamma_s/N$, as follows from expression (4.26). This corresponds to a short-term stability

$$\sigma_{y,\text{lim}}(\tau) \approx \frac{1}{\omega}\sqrt{\frac{90\gamma_s}{N\tau}} \approx \frac{9.5}{\omega}\sqrt{\frac{\gamma_s}{N\tau}}. \tag{4.39}$$

For passive optical clocks, the quantum projection noise limited stability $\sigma_{y,\text{QPN,Rams}}$ and $\sigma_{y,\text{QPN,Rabi}}$ for Ramsey and Rabi interrogation schemes respectively can be estimated as [3, 44]

$$\sigma_{y,\text{QPN,Rams}}(\tau) = \frac{1}{\omega\sqrt{NT_p\tau}}, \tag{4.40}$$

$$\sigma_{y,\text{QPN,Rabi}}(\tau) \approx \frac{1.69}{\omega\sqrt{NT_p\tau}}, \tag{4.41}$$

If the total Rabi or Ramsey interrogation time T_p is much longer than all the other durations required for state preparation and measurement, and if it is much shorter than the excited state lifetime $1/\gamma_s$, then comparing equations (4.39) with (4.40) and (4.41), one can see that the ultimate stability (4.39) attainable with an active optical clock with incoherent pumping can be matched by the QPN limited stability of a passive clock, at interrogation times of $T_p = 1/(90\,\gamma_s) \approx 0.011/\gamma_s$ for Ramsey, and at $T_p = 1.69^2/(90\,\gamma_s) \approx 0.032/\gamma_s$ for Rabi interrogation. For clocks using ^{87}Sr, these times are $T_p = 1.31$ s for Ramsey, and $T_p = 3.74$ s for Rabi interrogation. For the $^1S_0 \leftrightarrow {}^3P_0$ transition in ^{173}Yb, the corresponding times are 0.25 s and 0.72 s respectively, and for ^{43}Ca 5.05 s and 14.4 s.

A more realistic comparison between the achievable stability of active and passive optical frequency standards must additionally account for the dephasing of the atomic transition,

as well as imperfections of the local oscillator in a passive clock. The transverse dephasing rate $\nu = 2/T_2$ of the atomic transition is limited by Raman scattering of photons from the optical lattice potential [45] and by site-to-site tunneling of the atoms [46].

In a shallow cubic 3D optical lattice with ^{87}Sr [47], an optimized coherence time $T_2 \approx 10$ s was achieved, corresponding to $\nu \approx 0.2$ s^{-1}. This decoherence time may be further reduced using more technically challenging setups, such as optical lattices with increased lattice constants formed by interfering laser beams at different angles or by optical tweezer arrays [47].

Moreover, collisions with residual background gas also destroy the coherence and reduce the trap lifetime. From this point of view, $\nu = 0.2$ s^{-1} seems to be a good estimate for the minimum atomic decoherence rate that can be achieved without extraordinary efforts. Assuming an inhomogeneous broadening Δ_0 of the atomic ensemble of $\Delta_0 \approx 2\pi \times 15$ mHz ≈ 0.09 s^{-1}, one can estimate the optimized linewidth $\Delta\omega_{\text{opt}}$ of the superradiance laser as $\Delta\omega_{\text{opt}} \approx \frac{10}{N}$ s^{-1}, corresponding to a stability of a ^{87}Sr active clock.

$$\sigma_y'(\tau) = \frac{1}{\omega}\sqrt{\frac{\Delta\omega}{\tau}} \approx \frac{1.17 \times 10^{-15}}{\sqrt{N\,\tau}}. \tag{4.42}$$

For $N = 10^4$ it results in an instability of 10^{-17} at 1 s of averaging, and of 10^{-18} after 100 seconds, whereas a bad-cavity laser with $N = 10^5$ atoms would provide an instability of $\sigma_y'(\tau) \approx 3.7 \times 10^{-18}/\sqrt{\tau[\text{s}]}$.

Let us now compare this stability with the one that can be attained in a passive clock with the same number of atoms. An ideal quantum projection noise-limited, zero dead time, passive ^{87}Sr optical clock can attain such stability at interrogation times of $T_p = 0.1$ s for Ramsey, and $T_p = 0.29$ s for Rabi interrogation, as follows from equations (4.40) and (4.41). These interrogation times are short compared to the inverse inhomogeneous broadening and to the decoherence time of the atomic ensemble as estimated above, thus, these effects would not yet limit the passive clock. However, in a passive optical clock based on the sequential discontinuous interrogation of the clock transition in single atomic ensembles, the frequency fluctuations of the local oscillator contribute substantially to the instability due to the Dick effect [8].

For example, in [3] the contribution to instability $\sigma_{y,\text{Dick}}$ from the Dick effect was on the level of $\sigma_{y,\text{Dick}} \approx 3.8 \times 10^{-17}/\sqrt{\tau[\text{s}]}$ (see Fig. 4.5). Such a level of stability has been obtained with a local oscillator laser pre-stabilized to an elaborate 21 cm cryogenic silicon resonator at 124 K. The bad cavity laser can provide similar stability at a linewidth $\Delta\omega \approx 0.01$ s^{-1}, that can be attained with $N = 10^4$ atoms and a dephasing rate $\nu \approx 1.5$ s^{-1}, or with $N = 10^5$, $\nu \approx 5$ s^{-1} ($T_2 = 2/\nu = 0.4$ s), if the inhomogeneous broadening Δ_0' is much less than the dephasing rate. Therefore, the short-term stability of an active optical frequency standard may match and even significantly exceed the stability of passive clocks limited to the noise of the local oscillator via the Dick effect. On the other hand, the quantum projection noise-limited stability of a passive clock based on a similar atomic ensemble can still be better than the one of the passive standard.

We should note that the Dick effect in passive optical clocks can be avoided (or at least significantly suppressed down to contributions of finite-length $\pi/2$ pulses) by an interleaved, zero dead time operation of two clocks [48]. When comparing two clocks using the same atomic transition, the Dick effect can also be eliminated, and the interrogation time extended beyond the coherence time of the laser by using synchronous interrogation [3, 48, 49] of the two atomic ensembles. In the extreme case, comparing different parts of the same cloud, a fractional instability of $\sigma_y \approx 4 \times 10^{-18}/\sqrt{\tau[\mathrm{s}]}$ could be achieved [50]. Similarly, comparing clocks operating on different atomic transitions, differential spectroscopy [51] or dynamical decoupling methods [52] can be employed.

At the optimum stability, the output power P of the bad cavity laser amounts to a photon flux of $P/\hbar\omega_0 = \eta\kappa\langle\hat{a}^\dagger\hat{a}\rangle \approx \eta N(0.9\gamma_s + 0.25\nu + 1.45\Delta_0')$, see expressions (4.8) and (4.29). Taking $\eta = 0.5$ and parameters of the atomic ensemble listed above ($\gamma_s = 8.48 \times 10^{-3}\ s^{=1}$, $\nu = 0.2\ s^{=1}$ and $\Delta_0' = \Delta_0/\sqrt{3} \approx 0.054\ \mathrm{s}^{-1}$), the photon flux at the optimized cooperativity and pumping rate will be about 680 s^{-1} for $N = 10^4$ and 6800 s^{-1} for $N = 10^5$.

The output power of the active clock is usually too small for practical application, thus a suitable secondary laser needs to be phase-locked to the weak output to boost the available power. The bandwidth of this phase-lock depends on the stability of the (shot noise limited) active clock and the stability of the free-running secondary laser.

The Allan deviations for the superradiant laser output are shown in Fig. 4.5. Including the phase-locked laser would only cap the strong increase in stability towards short averaging times and limit the instability to values of 10^{-15} below 0.1 s.

Besides the fundamental limit to the stability from the superradiant laser's linewidth, the stability of the active clock may also degrade due to drifts or fluctuations in environmental parameters, such as the bias magnetic field. For example, the Zeeman shift of the π-transition $|^3P_0, m\rangle \rightarrow |^1S_0, m\rangle$ in ^{87}Sr amounts to about $\Delta\omega/B = 2\pi \cdot 1.10\ \mathrm{Hz}/\mu\mathrm{T} \cdot m_F$ [53], resulting in a shift of about $2\pi \times 4.95\ \mathrm{Hz}/\mu\mathrm{T}$ for the transition between the two stretched states $|^3P_0, m = 9/2\rangle$ and $|^1S_0, m = 9/2\rangle$. To attain a 10^{-18} level of relative uncertainty of the clock transition frequency, one must reduce the uncertainty of the bias magnetic field to below 87 pT.

In passive clocks, the linear Zeeman effect is typically canceled by averaging Zeeman transitions with opposite shifts, alternating from one interrogation cycle to the next. This method eliminates drifts and slow fluctuations of the bias magnetic field but cannot cancel fluctuations on timescales shorter than the duration of a single interrogation cycle. In contrast, active clocks can operate on two Zeeman transitions simultaneously, generating two-frequency laser radiation from both π-transitions between pairs of stretched states $|^3P_0, m = 9/2\rangle \rightarrow |^1S_0, m = 9/2\rangle$ and $|^3P_0, m = -9/2\rangle \rightarrow |^1S_0, m = -9/2\rangle$. The arithmetic mean of both these frequencies will be robust to fluctuations of the first-order Zeeman shift, as well as to vector light shifts from the lattice field. Both transitions can independently contribute to lasing if they interact with the same mode of the cavity and are detuned from each other far enough so that they neither synchronize nor significantly affect each other. This condition can be easily met under realistic conditions: for

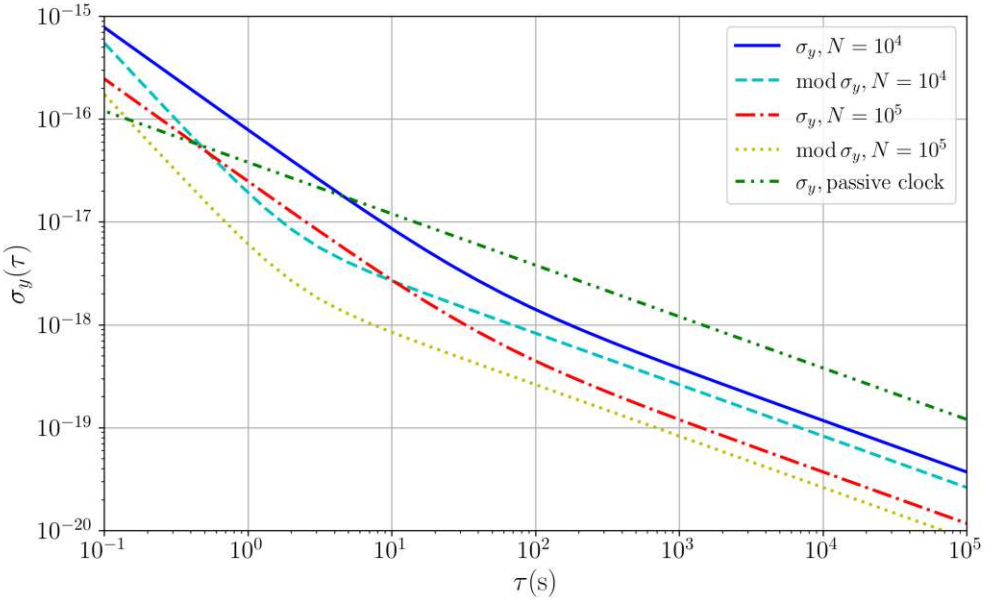

Figure 4.5: Stability of the ^{87}Sr active clock output expressed as Allan deviation σ_y with $f_h = 10$ Hz for $N = 10^4$ (blue solid line) and $N = 10^5$ (red dash-dotteded line). The corresponding modified Allan deviation mod σ_y is shown by the cyan dotted line and the yellow dotted line. The different slopes are due to contributions from photon shot noise and atomic phase diffusion. For comparison, the stability of a Dick effect limited passive clock, as discussed in the text, is shown as a green dash-dot-dot line.

instance, a bias magnetic field $B = 1$ G $= 0.1$ mT splits these two transitions by about $2\pi \times 1$ kHz. This splitting is less than the linewidth κ of the cavity (estimated above as $\kappa \approx 2\pi \times 15$ kHz at $l_{\text{cav}} = 10$ cm and $\mathcal{F} = 10^5$), but much larger than the optimized pumping rate $R_{\text{opt}} \approx 0.35$ s^{-1} [37, 54], as estimated from equation (4.27).

This concludes our study of the ultimate frequency stability that can be obtained with active optical frequency standards. We have demonstrated that these standards can outperform traditional passive optical frequency standards in terms of stability. Additionally, active optical frequency standards may serve as local oscillators in future passive optical clocks. Even if their short-term stability is slightly poorer than the quantum projection noise-limited stability of a passive optical clock with a similar number of clock atoms, the stability of active optical frequency standards can still be significantly better than that of a good-cavity laser pre-stabilized to an ultra-stable cavity, as used in modern passive optical clocks.

In the next chapter, we will discuss the superradiant laser setup at the University of Amsterdam-mHz machine, which has the potential to be used as an active optical frequency standard.

CHAPTER 5

Modeling towards continuous loading in optical conveyor

The bulk of this chapter has been submitted to Physical Review Research [55]

As mentioned in the previous chapter, superradiant lasing on an extremely narrow optical clock transition in neutral atoms has been proposed as a promising candidate to increase the short-term stability of state-of-the-art atomic clocks [9, 56]. The first steps towards this goal have already been taken, with pulsed superradiant lasing utilizing the $^1S_0 \rightarrow {}^3P_0$ transition observed in ^{87}Sr atoms [57, 58] and quasi-continuous operation on the $^1S_0 \rightarrow {}^3P_1$ transition in ^{88}Sr [59, 60].

With the pulsed operation, the linewidth of the superradiant emission is Fourier-limited. To overcome this limit and achieve the superradiant emission with a linewidth at the level of or below the natural linewidth of the lasing transition, we must have a truly continuous operation, where the active atoms leaving the cavity will be replenished by the fresh ones and the inversion will be maintained. This can be achieved with the help of a continuous delivery of the atoms into the cavity, either prepared in the excited state before entering the cavity or pumped in the cavity.

In this chapter, we discuss the simulations of the continuous loading of ^{88}Sr atoms into a ring cavity, the pumping process into the upper lasing state to create a continuous inverted gain medium. All the simulation parameters are based on the apparatus constructed at the University of Amsterdam, which is based on their previously built quantum hardware to generate a high flux of ultra-cold Sr atoms[61, 62].

In section 5.1, we discuss the motivation behind the development of the Amsterdam machine and the reasons for using ^{88}Sr. section 5.2 covers the architecture and key parameters of the machine. In section 5.3, we focus on the simulation and optimization

of the transport and cooling processes of ^{88}Sr atoms into the science chamber, followed by their loading into a moving optical lattice. In section 5.4, we propose a scheme for incoherently pumping these loaded atoms into the upper lasing clock state and perform simulations to optimize the relevant parameters.

5.1 Bad cavity laser on optical conveyor: basic ideas

Strontium is an alkaline earth element with 2 valence electrons whose spins can be either parallel (triplet states, $S = 1$) or antiparallel (singlet states, $S = 0$). Its levels relevant for cooling and pumping are presented in figure 5.1. The lower singlet state is the ground state which in the Russel-Saunders notation ($^{2S+1}L_J$, where S is spin, L is orbital quantum number in the spectroscopic notation, and J is the total angular momentum quantum number) is written as ^{1}S$_0$. The second singlet state, ^{1}D$_2$ state (not shown in figure 5.1), lies about 2.5 eV above. However, this state is very weakly coupled to the ground state, because the transition is forbidden in dipole approximation, in contrast to the next state, the ^{1}P$_1$ state with energy of about 2.69 eV above the ground state. The ^{1}P$_1 \rightarrow ^1$ S$_0$ "blue" transition with $\lambda \approx 461$ nm is quite strong, with natural linewidth $\gamma_{^1\mathrm{P}_1 \rightarrow ^1\mathrm{S}_0} \approx 2\pi \times 30$ MHz, what corresponds to the Doppler limit for laser cooling $T_{\mathrm{Doppler}} = \hbar\gamma_{^1\mathrm{P}_1 \rightarrow ^1\mathrm{S}_0}/k_B \approx 0.73$ mK. This transition is suitable for deceleration of hot Sr beams in Zeeman slowers, and for preliminary cooling in magneto-optical traps (MOT). The lowest triplet states are ^{3}P$_\mathrm{J}$ states with $J = 0, 1$ and 2. The 698 nm ^{1}S$_0 \rightarrow ^3$P$_0$ "clock" transition, totally forbidden in bosonic but slightly allowed in fermionic isotopes, is quite robust to fluctuations of external magnetic field and polarization of the auxiliary laser fields, because the electrons in this state has zero total angular moment. This is why this transition is used as clock transition in optical frequency standards. The 689 nm ^{1}S$_0 \rightarrow ^3$ P$_1$ "red" transition with natural linewidth of about $2\pi \times 7.4$ kHz, what

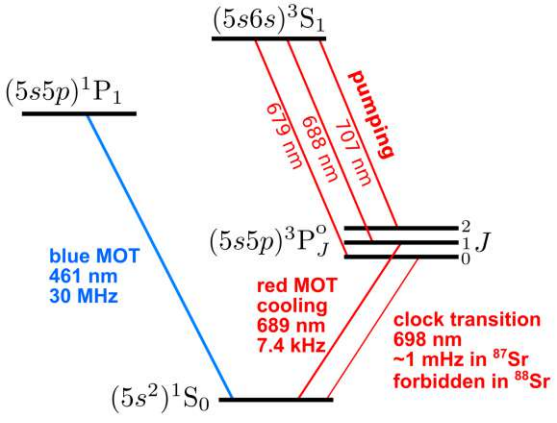

Figure 5.1: Levels of neutral strontium atom relevant for trapping, cooling, pumping and lasing.

corresponds to $T_{\text{Doppler}} \approx 0.18\ \mu$K is well suitable for the second stage of cooling of cold strontium atoms pre-cooled in the "blue" MOT. Also, we should mention the $^3S_1$ state with energy of about 3.6 eV above the ground state. This state together with $^3P_1$ state can be used for pumping the atoms into the $^3P_0$ state, in order to create inversion. We should note that other alkaline-earth elements, such as Be, Mg, Ca, as well as some other "alkaline-earth-like" elements (Yb, Hg, Cd and Zn), have similar structures of levels.

Continuous operation of the superradiant laser requires continuous replenishing of the atoms and maintatining the population inversion. It can be realized with the help of a magic-wavelength moving optical lattice, or the *optical conveyor*, which confines the atoms and drags them controllably through the active zone, where the atoms will be coupled to the superradiant cavity mode. Practical implementation of this scheme becomes possible with the creation of a continuous source of guided ultracold Sr atoms.

Such a source, able to deliver several tens of millions of ^{88}Sr, or several millions of ^{87}Sr atoms per second, was created in the University of Amsterdam [61, 62].

The second crucial point of the design is the choice of the way how the optical conveyor drags the atoms through the cavity. First, the atoms should be pulled through the cavity relatively slowly, to have enough time for coherent interaction with the cavity mode. Second, the density of the atoms should not be too high, to avoid undesirable collisional effects, although the overall number of the atoms must be high enough to initiate the lasing. And, third, the atoms should be delivered fast enough from the source into the cavity, not to get lost due to collisions with each other and with the backgound gas on the way to the cavity, as well as due to off-resonance scattering of the far-detuned light of the optical conveyor. A possible and very promising scheme is based on a ring-cavity playing the role of the superradiant cavity, where also the magic-wavelength optical conveyor is created by injection of two counter-propagating magic-wavelength laser modes with slightly different frequencies. similar design was proposed [63] and used [64, 65] in Thompson group for active optical clocks, as well as in Katori group for passive continuously-operating optical clock with Ramsey interrogation scheme [66, 67]. They demonstrated continuous transfer of atomic fluxes at the level of 10^7 from the Red MOT into a moving optical lattice within a ring cavity.

5.1.1 Lasing transistion

The transition we want to use for our superradiant laser is $^1S_0 \rightarrow {}^3P_0$ transition in a bosonic isotope of Sr, namely, ^{88}Sr. This isotoipe is the most abundant (83%, more than 10 times the abundance of ^{87}Sr), and it has zero nuclear magnetic momentum and no hyperfine structure, therefore, one can use more simple laser systems for cooling and pumping of the atoms. However, the $^3P_0 \rightarrow {}^1S_0$ transition in the bosonic isotopes is completely forbidden in free space. To make it slightly allowed, one can apply a DC magnetic field mixing the $^3P_0$ and $^3P_1, m = 0$ states [68].

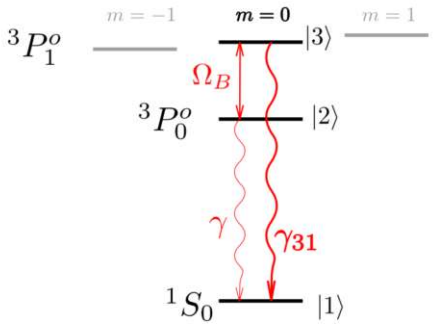

Figure 5.2: Partial level scheme of ^{88}Sr relevant for magnetic-induced $^1\mathrm{S}_0 \to {}^3\mathrm{P}_0$ transition.

Consider an atom of ^{88}Sr placed in external DC magnetic field B. We can restrict our consideration to 3 states $|1\rangle = |^1\mathrm{S}_0\rangle$, $|2\rangle = |^3\mathrm{P}_0\rangle$ and $|3\rangle = |^3\mathrm{P}_1, m = 0\rangle$, see figure 5.2. The Hamiltonian corresponding to these states can be written as

$$\hat{\mathcal{H}} = \hbar \left[\omega_2 |2\rangle \langle 2| + \omega_3 |3\rangle \langle 3| + \Omega_B(|3\rangle \langle 2| + |2\rangle \langle 3|)\right], \tag{5.1}$$

where we took the energy of the state $|1\rangle$ as zero level. Let us take the z-axis along the magnetic field. Then the z-projection of the atomic magnetic moment operator can be written as $\hat{\mu}_z = -\mu_B(2\hat{S}_z + \hat{L}_z)$, where μ_B is the Bohr magneton, S_z and L_z are the z-projections of spin and orbital angular momenta of the atomic electrons respectively. Then we can write the matrix element Ω_B as

$$\Omega_B = -\frac{1}{\hbar} \langle 2| B \cdot \hat{\mu}_z |3\rangle = \frac{\mu_B B}{\hbar} \langle 2| 2\hat{S}_z + \hat{L}_z |3\rangle . \tag{5.2}$$

To find its value, we can expand the states $|2\rangle$ and $|3\rangle$ with defined J and m quantum numbers corresponding to total angular momentum and its projection respectively via the states with defined S_z and L_z quantum numbers as

$$\begin{aligned} |2\rangle &= |L = 1, S = 1, J = 0, m = 0\rangle \\ &= \sum_q C(1,1,0;q,-q,0)\, |L = 1, S = 1, m_l = q, m_s = -q\rangle , \\ |3\rangle &= |L = 1, S = 1, J = 1, m = 0\rangle \\ &= \sum_m C(1,1,1;m,-m,0)\, |L = 1, S = 1, m_s = m, m_l = -m\rangle , \end{aligned} \tag{5.3}$$

where $C(1,1,J;m,-m,0)$ are the Clebsch-Gordan coefficients. Using the values of the Clebsch-Gordan coefficients, we can find

$$\Omega_B = -\frac{|B|\mu_B}{\hbar}\sqrt{\frac{2}{3}}. \tag{5.4}$$

Diagonalizing the Hamiltonian at $\Omega_B \ll \Delta_{32}$ we find the eigenstate $|2'\rangle$ and the associated eigenvalue are

$$|2'\rangle = |2\rangle - \frac{\Omega_B}{\Delta_{32}}|3\rangle\,; \quad \omega_2' = \omega_2 - \frac{\Omega_B^2}{\Delta_{32}}. \tag{5.5}$$

State $|2'\rangle$ is a ${}^3P_0$ state dressed by the magnetic field B. Presence of the pure state $|3\rangle$ in $|2'\rangle$ allows the spontaneous decay of $|2'\rangle$ into the state $|1\rangle = |{}^1S_0\rangle$. The rate γ_t of this decay and the frequency shift Δ_2 is given by

$$\gamma_t = \gamma_{31}\frac{\Omega_B^2}{\Delta_{32}^2}, \quad \Delta_2 = \frac{\Omega_B^2}{\Delta_{32}}. \tag{5.6}$$

Taking the values of $\gamma_{31} = 4.69 \times 10^4 \mathrm{s}^{-1}$, and $\Delta_{32} = 2\pi \times 5.6 \times 10^{12}$ Hz [69], we can express γ_t and Δ_2 via magnetic fields as

$$\gamma_t \approx 1.95 \times 10^{-9}\ \mathrm{s}^{-1} \times \left(\frac{B}{1\ \mathrm{G}}\right)^2, \quad \Delta_2 \approx -1.465\ \mathrm{s}^{-1} \times \left(\frac{B}{1\ \mathrm{G}}\right)^2, \tag{5.7}$$

which gives the following relation between the shift and the magnetic-induced spontaneous decay rate:

$$\left|\frac{\Delta_2}{\gamma_t}\right| = \frac{\Delta_{32}}{\gamma_{31}} \approx 7.5 \times 10^8. \tag{5.8}$$

5.2 Design of the setup

The experimental setup is based on a steady-state narrow-line magneto-optical trap (MOT) operating on the ${}^1\mathrm{S}_0 \rightarrow {}^3\mathrm{P}_1$ transition to create a continuous μK-temperature source of strontium. In this design the cooling and trapping stages are separated in space rather than in time in order to provide continuous operation. For different steps the setup has different chambers.

First, hot strontium atoms exiting the oven are slowed by a Zeeman slower resonant with the 460 nm ${}^1\mathrm{S}_0 \rightarrow {}^1\mathrm{P}_1$ "blue" transition, see figure 5.3. Then they are trapped by a 2D "blue" magneto-optical trap (MOT) operating on the same transition, where they are cooled down to millikelvin temperatures. The lack of confinement in vertical direction of the 2D Blue MOT allows the atoms to drop down into a second chamber, where they are trapped in a narrow-line "red" MOT operating on the 689 nm ${}^1\mathrm{S}_0 \rightarrow {}^3\mathrm{P}_1$ transition, where they are cooled to a microkelvin temperatures. Then the atoms must be guided into the so-called "science chamber", where they get loaded into the optical conveyor, pumped and dragged through the superradiant laser cavity.

To realize a continuous laser operation, we use a high-finesse ring cavity in bow-tie configuration, where not only the superradiant laser mode is excited, but also the magic-wavelength optical conveyor dragging the atoms along the cavity is created, see Fig 5.4. This conveyor supports the atoms against gravity and pulls them through the pumping zone, where they are pumped, through the emission zone, where they contribute to the cavity field, towards the ejection zone, where they are ejected from the conveyor by a dedicated "blue" push beam, in order to prevent coating of the cavity mirrors.

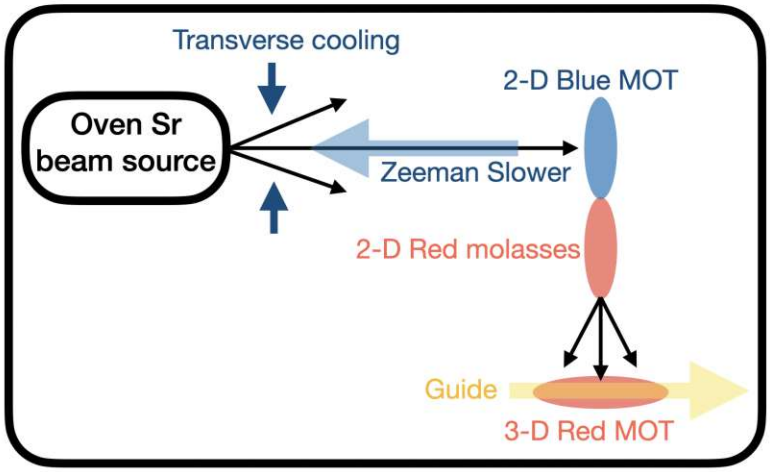

Figure 5.3: The schematic diagram of Guided Strontium atomic beam source.

The ring cavity in bow-tie configuration is housed in a separate science chamber. This chamber is isolated from stray optical and magnetic fields originated from the Zeeman slower, blue- and Red MOTs, as well as from the outside. The 20 cm length differential pumping tube, which connects the MOT and the science chamber with each other, ensures optical isolation from stray 461 nm and 689 nm photons, and the magnetic shielding of the science chamber provide magnetic isolation .

The atoms will be transported between the Red MOT and the science chamber using a combination of a dipole guide beam and a Bloch accelerator. The Bloch accelerator [70, 71], created by a shallow angle lattice [72] overlapped with the Red MOT chamber, as it is shown in figure 5.4, is designed to accelerate the atoms to a speed of up to 50 cm/s. Then the atoms will be guided and held against gravity by a 200 W, 150 μm waist dipole guide, created by 1070 nm single mode laser. As the atoms arrive in the science chamber, they will be decelerated with the first molasses beam and cooled into a dipole trap reservoir overlapping with the cavity mode using two extra red molasses beams.

The dipole guide and the reservoir beams induce an AC differential light shift for the $^1S_0 \rightarrow {}^3P_0$ transition, which is enough to decouple the atoms in the reservoir from resonance with the atoms in the emission zone, thus reducing the influence on the lasing process.

The atoms collected in the reservoir will then be loaded into a vertical, magic-wavelength moving optical lattice created inside the same bow-tie cavity, which pulls the atoms upward through the pumping, emission, and ejection zones. The lattice is sufficiently deep to confine the atoms even if they are heated during the pumping. Because the atoms are distributed along the cavity mode, we can store large amount of atoms at relatively low density.

The number of atoms simultaneously coupled to the cavity mode and the time of interaction can also be adjusted by tuning the speed of the magic moving lattice.

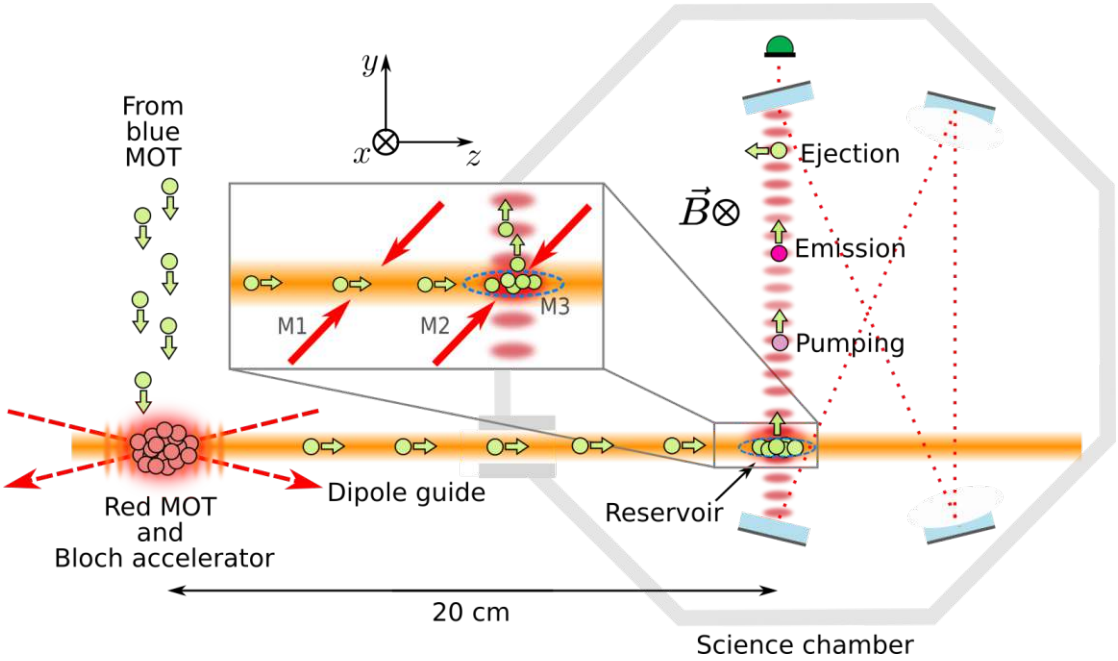

Figure 5.4: Schematics of the science chamber. Atoms falling down from a 2D Blue MOT (not shown here, see figure 5.3) are continuously collected and cooled in a Red MOT. From there, they are loaded into a dipole guide beam formed by a single-pass 1070-nm beam. The guide beam is overlapped with a shallow-angle lattice, which can be used as a Bloch accelerator. The atoms are transported over 20 cm from the Red MOT chamber to the science chamber. In the science chamber, the atoms are collected in the reservoir (denoted by blue dashed oval, formed by crossing of the guide beam with an extra 1070-nm beam propagating into the (x, z)-plane and tilted by 5° with respect to the z-axis), and loaded into the magic wavelength optical conveyor lattice. The optical conveyor moves upwards through a pumping zone, where atoms are pumped to the excited $^3P_0$ state. After that, they are drawn through a well-controlled emission zone, where superradiant emission into the cavity mode can occur. After the emission zone, atoms are ejected by a push beam to avoid coating the surface of the cavity mirrors. The atoms are decelerated with the first set of red molasses beams (M1) and then further cooled into the reservoir dipole trap by the second (M2) and third (M3) set of red molasses beams. (M3) is orthogonal to the (y, z)-plane.

The dimensions of the compact bowtie cavity are 50 x 13 mm. It is comprised of two flat mirrors and two curved mirrors coated for both the clock transition and magic wavelengths. The total roundtrip length l_{cav} along the cavity is about 20 cm, what corresponds to a free spectral range of about 1.5 GHz.

The cavity is designed to have a finesse of about 50 000 at 698 nm and 2000 at 813 nm. In the emission zone of the moving lattice, the minimum waist of the 698 nm cavity mode will be around 130 μm. The round-trip length of the cavity is finely tuneable using a piezo stack attached to one of the flat mirrors in order to create a resonant cavity mode

with the $^1S_0 \rightarrow {}^3P_0$ transition.

Because of the shielded science chamber our apparatus can accommodate experiments with both ^{87}Sr and ^{88}Sr. In order to open the completely forbidden clock transition in the bosonic isotope and benefit from the high natural abundance and relatively simple level structure, we need to apply a relatively strong bias magnetic field (few hundred Gauss), as it has been described in section 5.1.1. On the top of this, the magnetic field must be highly homogeneous in the emission zone in order to minimize position dependence of the second-order Zeeman shift.

Table 5.1: Parameters for different beams.

Beam Type	Dipole guide	Reservoir	Lattice
Polarization	along x-y	π	along x-z
$U_0(^1S_0),\ \mu K$	-166	-50	-32
$U_0(^3P_1, m=0),\ \mu k$	-60	-14.6	-10.6
Waist, μm	$(200, 200)$	$(400, 100)$	140
Wavelength, nm	1070	1070	813
Propagation along	z-axis	x-y plane 5° from z	y-axis

This concludes our discussion of the design of the science chamber, in the subsequent section we will discuss the simulation associated with the transport and cooling of the atoms.

5.3 Transport and cooling of atoms

The atoms in the Red MOT are pushed by the Bloch accelerator [71], [73] via the dipole guide beam towards the science chamber, where they are stopped, cooled down and loaded into the moving optical lattice. In this section we consider these processes in more details.

5.3.1 Deceleration of atoms

The guided atoms leaving the Bloch accelerator overlapped with the Red MOT can have the speed up to 50 cm/s towards the science chamber, where we must slow them down. We can't use just a Bloch decelerator because it will not cool the atoms. Initially we considered pumping atom to $^3P_0$, slowing them using a potential hill for the $^3P_0$ state and transferring them to $^1S_0$ at the hill's peak, but our simulations indicated issues with non-uniform potential effects due to the possible hill's alignment could leading to a broad velocity spread and hinder effective trapping.

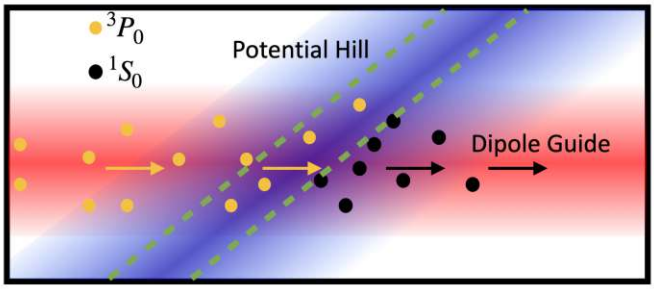

Figure 5.5: Schemetic digram of potential hill.

Another method for cooling of atoms that we have considered is SWAP. The main mechanism for momentum removal in SWAP cooling is the coherent transfer of a particle toward zero momentum via adiabatic passage. Momentum is removed by time ordered stimulated absorption and emission of photons caused by interaction with a standing wave formed by counter propagating laser beams similar to Bloch accelerator.

To achieve SWAP cooling without heating the system we have to staisfy the following conditions as given in [70]-

- Low probability of Spontaneous emmision when atom in excited state.

$$\tau_e = \frac{2kv - 4\omega_r}{\alpha} + \frac{2\Omega_0}{\alpha} \ll \frac{1}{\Gamma} \tag{5.9}$$

- High velocity regieme that is two resonant phenoemna must be seperated

$$\tau_{\text{res}} > \tau_{jump} = |kv - 2\omega_r| > \Omega_0 \tag{5.10}$$

- Adiabaticity condition that is to have a substantial probability for an adiabatic transition at each resonance

$$\Omega_0^2 > \alpha \tag{5.11}$$

- Sweep range should be large enough to have both lasers in resonance.

$$\Delta_s > |4kv| \tag{5.12}$$

To model this for our system we define 3 numbers a_1, a_2, a_3 associated with relvent paramters described in terms of recoil frequency $\omega_r = \frac{\hbar k^2}{2m}$

$$\Omega_0 = a_1\omega_r, \quad \alpha = (a_2\omega_r)^2, \quad T_s = a_3/\omega_r, \tag{5.13}$$

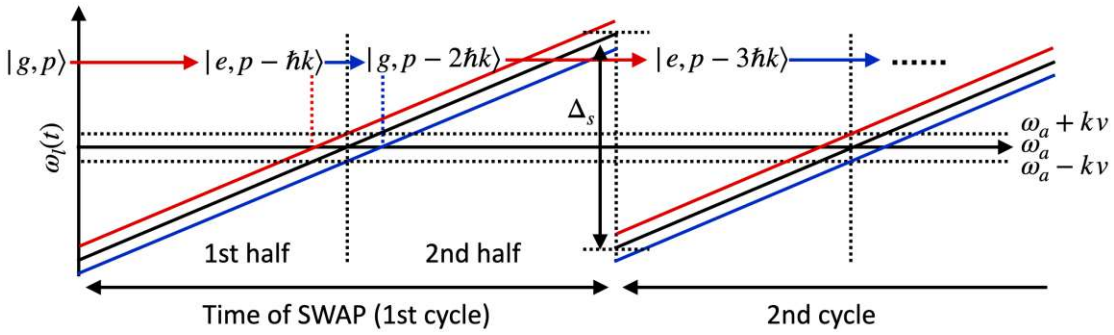

Figure 5.6: Schemetic digram of SWAP cycle.

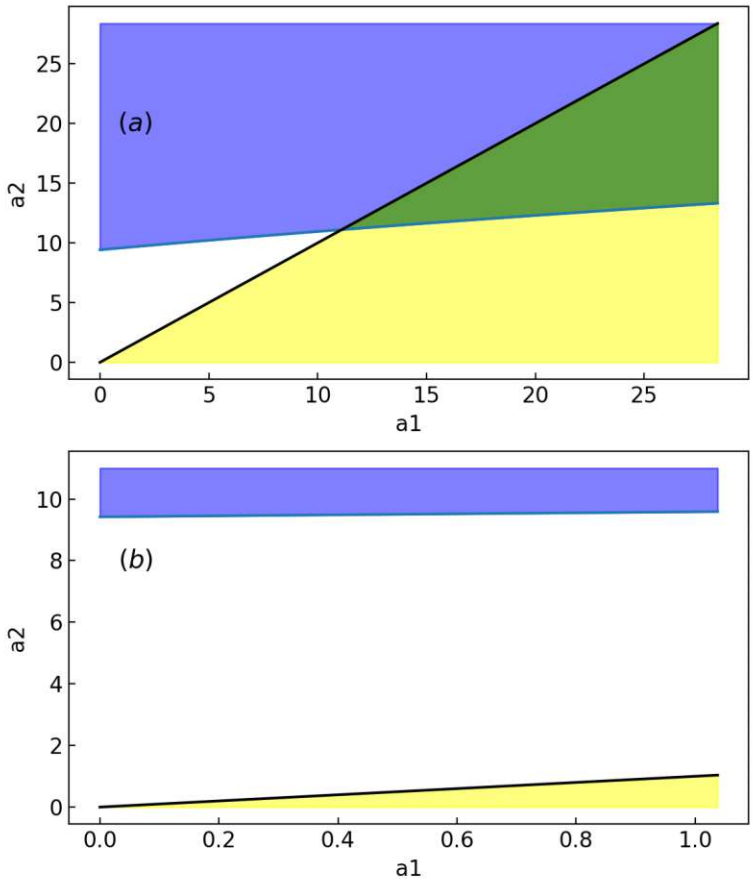

Figure 5.7: Blue part shows the region of parameter a1 and a2 satisfying 1st condition and yellow part shows the region with the 3rd condition and the overlap shown by green represents parameter with both conditions satisfied. In plot(a) we see that the allowed set of parameters for atoms coming out with 50cm/s velocity can be cooled to 10cm/s but in plot (b) we don't see any overlap for 10cm/s incoming velocity.

and translate the above conditions in terms of a_1, a_2, a_3

$$\left(\frac{2kv_i}{\omega_r} - 4 + 2a_1\right) \ll \frac{a_2^2\omega_r}{\Gamma},$$
$$a_1 < \left|\frac{kv_0}{\omega_r} - 2\right|, \quad a_1 > a_2, \quad a_2^2 a_3 > |\frac{4kv_i}{\omega_r}| \tag{5.14}$$

For our system we need to slow the atoms to 1cm/s or lower, and for that we were not able to find a good set of parameters that satisfied all the above conditions as shown in figure 5.7 Finally, another method that we have considered is simply using the molasses beams and scanning the frequency over a large set of capture velocity. In the next section we discussed this in detail.

5.3.2 Molasses beam

As described in figure 5.4, before the loading of atoms into the moving optical lattice, we implement 3 molasses beams, 2 of them running on ${}^1S_0 \rightarrow {}^3P_1, m = 0$ transition and the third one running on ${}^1S_0 \rightarrow {}^3P_1, m = 1$ transition. The first molasses beam is used to cool atoms coming with high velocities accelerated by a Bloch accelerator before they enter the reservoir, while the other two beams are positioned close to the loading point inside the reservoir, aiming to lower the temperature of the atoms sufficiently, to prepare them for transfer onto the moving optical conveyor.

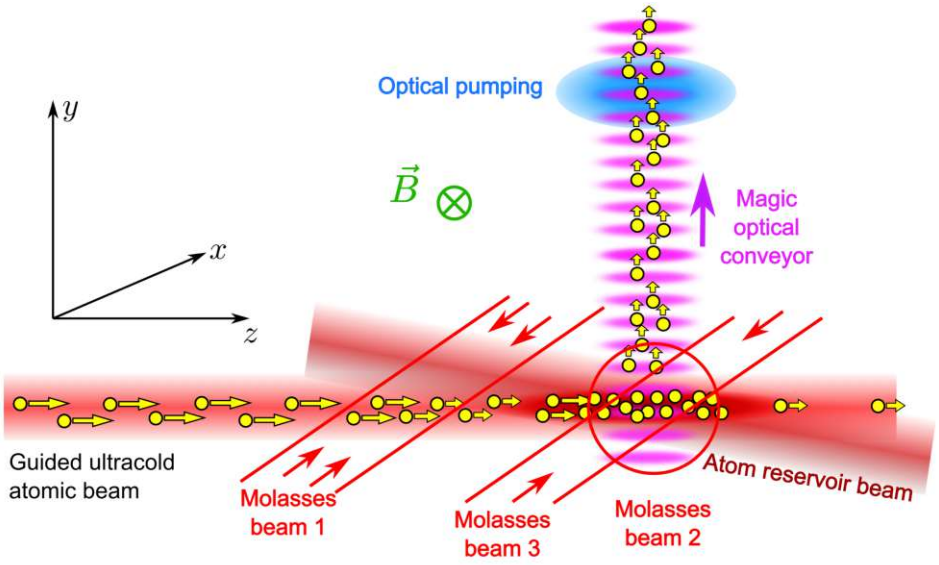

Figure 5.8: The first molasses beam is outside the science chamber, and the second and third molasses beam are centered at the loading point. All the molasses beams contain multiple frequencies to have large capture velocities.

As the dipole potentials of the guide beam, reservoir, and the optical lattice for ${}^1S_0$, ${}^3P_1, m = 0$ states are different, there will be significant position-dependent light shifts on

the cooling transitions. We calculate these shifts using the expression for polarizability given in chapter 2, section 2.1.4, and we used the data presented in [74].

5.3.3 Simulation of cooling of atoms

For simulation of the molasses, it's important to know how many photons are scattered per atom to predict the average energy of an atomic cloud; using the dipole force, we will not get that information, and applying MCWF is not feasible, so instead, we employ the SCMC method as described in 2, section 2.3.3.2 but now in 3 dimensions. We suppose that the atom will not change significantly its position during the typical evolution time of its internal state. Further, instead of modulating frequency in time, we take into account multiple frequencies simultaneously.

We start our discussion with the Hamiltonian

$$\hat{\mathcal{H}} = -\hbar \sum_{i=1}^{3} \delta_i \hat{\sigma}_{ii} + \sum_{ik} \frac{\Omega_{ik}}{2} (\hat{\sigma}_{i0} + \hat{\sigma}_{0i}) \tag{5.15}$$

where i represents the substates $^3P_1, m = \{-1, 0, 1\}$ corrsponding to $i = \{1, 2, 3\}$ respectively and k is associated with different frequencies consecutively, the Bloch equations look like

$$\begin{aligned}
\frac{d\rho_{ii}}{dt} &= -\sum_{k} \frac{i\Omega_{ik}}{2} (\rho_{0i} - \rho_{eg}) - \gamma_s \rho_{ii} \\
\frac{d\rho_{0i}}{dt} &= -i\delta_i \rho_{0i} + \sum_{k} \frac{i\Omega_{ik}}{2} (\rho_{00} - \rho_{ii}) - \frac{\gamma_s}{2} \rho_{0i} - \sum_{i \neq j,k} \frac{i\Omega_{jk}}{2} \rho_{ji} \\
\frac{d\rho_{ji}}{dt} &= i(\delta_j - \delta - i)\rho_{0i} + \sum_{k} \frac{i\Omega_{ik}}{2} \rho_{j0} - \sum_{k} \frac{i\Omega_{jk}}{2} \rho_{0i} - \gamma_s \rho_{ji}
\end{aligned} \tag{5.16}$$

For ^{88}Sr in relatively strong magnetic field $\rho_{ij} \xrightarrow{i \neq j} 0$

$$\rho_{00} = \left(1 + \sum_{ik} \frac{s_{ik}}{2 + s_{ik}}\right)^{-1}, \quad \rho_{ii} = \sum_{k} \frac{s_{ik}}{2 + s_{ik}} \rho_{00} \tag{5.17}$$

$$s_{ik} = s^0_{ik} \left(1 + 4\frac{\delta^2_{ik}}{\gamma^2_s}\right)^{-1}, \quad s^0_{ik} = \frac{2\Omega^2_{ik}}{\gamma^2_s} \tag{5.18}$$

$$\Omega_{ik} = \sqrt{\frac{I^i_k(r)}{2I^i_{\text{sat}}}} \gamma_s. \tag{5.19}$$

where the s_{ik} is the saturation parameter associated with ith transition and kth frequency as defined by 5.19. In terms of individual intensities of lasers, the saturation rate and

the detuning looks like

$$
\begin{aligned}
s_{ik}(r,v) &= \frac{I_k^i(r)}{I_{\text{sat}}^i}\left(1+\left(\frac{2\delta_{ik}(r,v)}{\gamma_s}\right)^2\right)^{-1} \\
\delta_{ik}(r,v) &= \delta'_{ik} - \Delta_i^D(r) - \Delta_i^{(R)}(r) + \vec{k}_{ik}\cdot\vec{v} \quad , \quad I_{\text{sat}} = \frac{2\pi^2\hbar c\gamma_s}{3\lambda^3} \\
\delta'_{ik} &= \frac{\Delta_{\text{band}}(2k-N_f-1)}{2(N_f-1)} + \delta_i^c
\end{aligned}
\tag{5.20}
$$

Δ_{band} is the bandwidth, δ_i^c is the the central frequency and N_f is the total number of frequency. For ith transition the differential light shifts associated with dipole beam (Δ^D), and reservoir (Δ^R) are given by

$$
\Delta_i^{\{D,R\}}(r) = -\frac{1}{\hbar}\left(\frac{\alpha_{^1S_0} - \alpha_i}{\alpha_{^1S_0}}\right)U_{\{D,R\}}^{^1S_0}(r) \tag{5.21}
$$

Resulting in a scattering rate

$$
\Gamma_i(r,v) = \sum_k \left(\frac{\gamma_s s_{ik}(r,v)}{2+s_{ik}(r,v)}\right)\left(1+\sum_{i,j}\frac{s_{i,j}(r,v)}{2+s_{i,j}(r,v)}\right)^{-1} \tag{5.22}
$$

We use this position-dependent scattering rate to generate random numbers, and accordingly, we artificially model the absorption and emission of photons by evolving the scattering rate (5.22) along the trajectory of atoms. We have performed the simulation by following the steps mentioned below-

- Starting with an initial state $(\vec{x}_j, \vec{p}_j)$ at time t_j we evolve the equation of motion $(\dot{\vec{x}}_j, \dot{\vec{p}}_j)$ and the scattering rate $\Gamma_m(x,v)$ till $t_{i+1} = t_j + dt$.
- Generate a vector $\vec{v}_s = (\sin\theta\cos\phi, \sin\theta\sin\phi, \cos\theta)$ with θ and ϕ randomly generated numbers and a random number r_1 in the interval $[0,\pi]$, $[0,2\pi]$ and $[0,1]$ respectively.
- If $r_1 > e^{-\int_{t_j}^{t_{i+1}}\Gamma_m(\vec{x}_j,\vec{v}_j)dt}$ set $\vec{p}_{i+1} = \vec{p}_j - \hbar\vec{k} + \vec{v}_s\hbar k$ and regenerate $\{r_1,\theta,\phi\}$ or else without changing anything take another step.
- Repeat the above three steps until we reach the desired evolution time.

In our system, we utilize a broad spectrum of frequencies to accommodate a wide range of capture velocities. The maximum scattering rate is significantly lower than the spontaneous emission rate, allowing us to assume that an atom instantaneously emits a photon after absorbing it.

As mentioned before, the role of the first molasses beam is to cool down atoms that are coming with a high velocity from the Bloch accelerator along the dipole beam in the

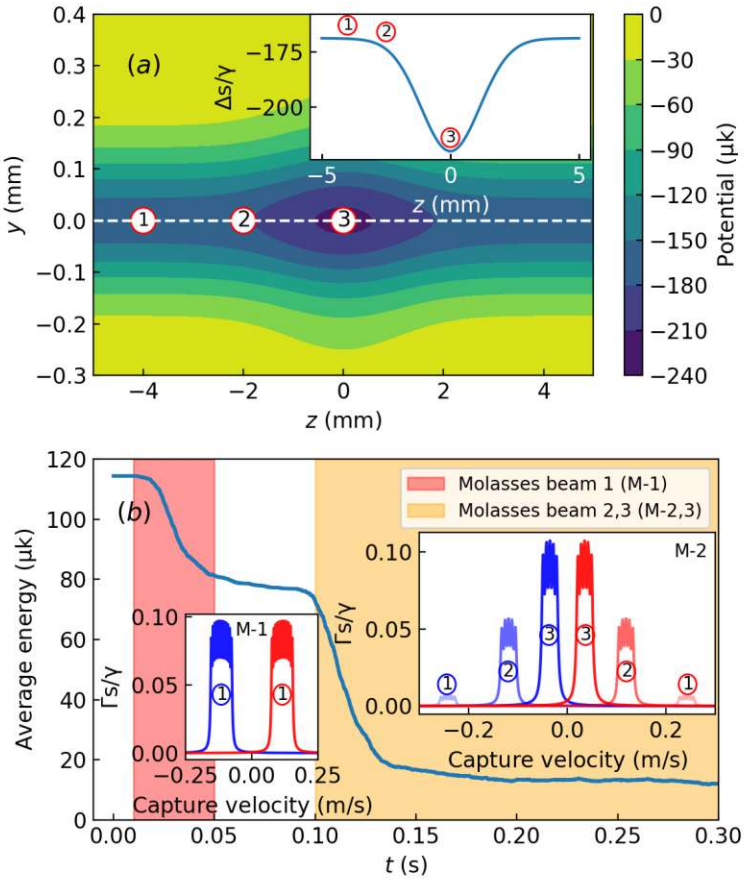

Figure 5.9: (a) Potential of reservoir and dipole guide in (y, z)-plane. The inset shows the differential light shift in the reservoir, along the z-axis, for the ${}^1S_0 - {}^3P_1$ molasses cooling transition. (b) Cooling dynamics of atoms with an incoming velocity of 10 cm/s, where the time that atoms interact with a specific molasses beam is marked by the red or orange shading. The first molasses beam (M1, red shading), slows atoms to 1 cm/s. Shortly afterwards, the atoms enter the reservoir region, where further molassess beams (M2 & M3, orange shading) slow and trap them inside the reservoir, and finally cool them to μK-temperatures. The inset shows how the capture velocity changes with position. To avoid heating the frequencies of M2 and M3 are chosen such that there is no interaction before the atoms reach the center of the reservoir.

z direction. For this beam, the potential gradient only affects the (x, y)-plane, as the light shift is essentially constant along the z-axis. If we choose the frequencies of the first molasses beam matching the maximal light shift, the atoms close to the center will consistently achieve resonance and scatter photons.

However, as the atoms approach the reservoir, the change in light shift along the $\hat{z}$ direction becomes significant, as the reservoir beam propagates 5° from the $\hat{z}$-direction in the (x, z)-plane. This makes the capture velocity position dependent also along $\hat{z}$, as shown in Fig. 5.9. This dependence must be considered when choosing the frequencies of

Table 5.2: Parameters of molasses beams

Molasses Beam	M1	M2	M3
Intensity (total)	$2\,I_{\text{sat}}$	I_{sat}	I_{sat}
Δ_{band}	$0.01(2\pi)\mu\text{s}^{-1}$	$0.01(2\pi)\mu\text{s}^{-1}$	$0.01(2\pi)\mu\text{s}^{-1}$
N_f	12	4	5
δ_i^c	$-45\frac{\Gamma}{2}+\Delta_{\text{D}}^{\max}$	$-15\frac{\Gamma}{2}+\Delta_{\text{D+R}}^{\max}$	$-15\frac{\Gamma}{2}+\Delta_{\text{D+R}}^{\max}$
Waist, μm	(200,200)	(200,200)	(200,200)
λ, nm	689	689	689
center, (mm)	(0,0, -5)	$(0,0,0)$	$(0,0,0)$
Polarization	in (y,z)-plane	along x	in (y,z)-plane
Propagation	in (y,z)-plane, 7° from z	along x	in (y,z)-plane, 7° from z

the second and third optical molasses beams, as they interact with atoms in the reservoir. There is no overlap between red and blue scattering rate before $z=0$ (otherwise the system will heat), we can trap large number of atoms in the reservoir.

For different set of incoming velocities if we choose the frequencies correctly, the energy distribution of atoms post-reservoir remains relatively consistent. Without the optical lattice within the reservoir, the thermal equilibrium average energy achievable is approximatly $12\mu k$. However, as we shall explore in the subsequent section, In presence of moving optical lattice this scenario poses a challenge when atoms approach the proximity of the optical lattice.

5.3.4 Loading into moving Optical lattice

To simulate loading into the moving optical lattice, we must also consider the differential light shift caused by the substantial depth of the lattice resulting in a significant change in the capture velocities we previously calculated. Because we are using a *moving* optical lattice, the capture velocity range for the second and third optical molasses beams will oscillate with the motion of the optical lattice. Consequently, scattering events will decrease as atoms move toward the optical lattice since the laser frequencies align only around the maximum value of the light shift.(Figure 5.10). Again using SCMC, but now including the time-dependent optical lattice light shift, the scattering rate is explicitly time-dependent, given by-

$$\Gamma_i(r,v)=\sum_l\left(\frac{\gamma_s s_{ik}(r,v,t)}{2+s_{ik}(r,v,t)}\right)\left(1+\sum_{i,j}\frac{s_{i,j}(r,v,t)}{2+s_{i,j}(r,v,t)}\right)^{-1} \tag{5.23}$$

where the saturation parameter $s(r,v,t)$ is

$$s_{ik}(r,v)=\frac{I(r)}{I_{\text{sat}}}\left(1+\left(2\frac{\delta_{ik}-\Delta_i^{(D)}(r)-\Delta_i^{(R)}(r)-\Delta_i^{(ol)}(r,t)+\vec{k}_{ik}\cdot\vec{v}}{\gamma_s}\right)^2\right)^{-1} \tag{5.24}$$

and the light shifts Δ_{ol} being

$$\Delta_i^{(ol)}(r,t) = -\frac{1}{\hbar}\left(\frac{\alpha_{^1S_0} - \alpha_i}{\alpha_{^1S_0}}\right) U_0^{^1S_0} \cos(k(y - v_{ol}t)) \exp\left(-2\frac{(x^2+y^2)}{w_0^2}\right) \tag{5.25}$$

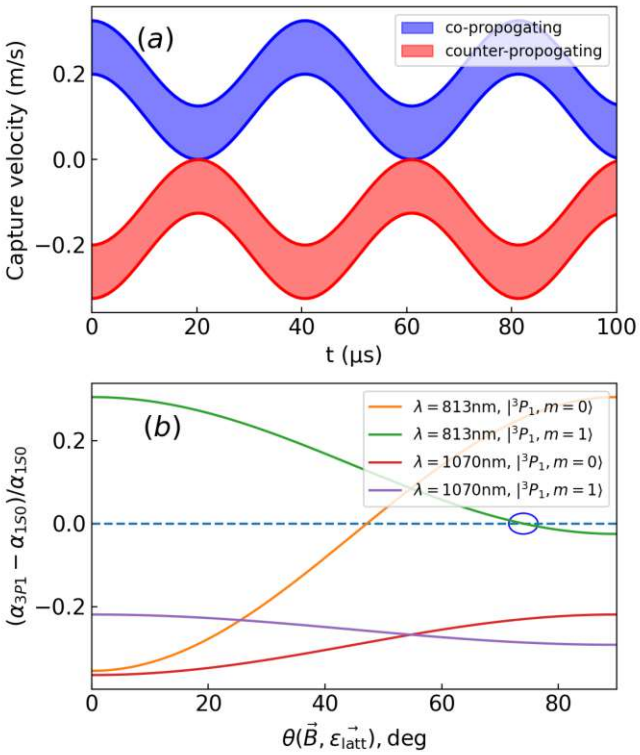

Figure 5.10: (a) The time-dependent oscillation of the capture velocity range as seen by atoms at a fixed position ($z = 10\mu m$) because of the optical lattice moving with a velocity of 1 cm/s.(b) Polarizability of the atoms as a function of the angle between the bias magnetic field $\vec{B}$ and the optical lattice polarization. At an angle of $\approx 74°$ between the optical lattice polarization, the ${}^3P_1, m = 0 \rightarrow {}^1S_0$-transition becomes magic due to the tuned tensor polarizability term.

Upon entering the radially symmetric optical lattice potential, atoms must scatter photons from the second and third molasses beams to stay trapped. Due to the oscillation of the capture velocity range caused by the moving lattice, there is an increase in the average energy distribution of the atoms, which reaches a value of approximately 20 μK. To avoid this and to achieve a low mean energy we can tune the Tensor polarizability term of the the transition (${}^1S_0 \rightarrow {}^3P_1, m = 1$) to a magic polarization(Figure 5.10, which minimizes the increase in the average energy of the atomic sample.

We find that efficient loading into the optical conveyor moving with a speed of $\approx$1 cm/s is possible. This is illustrated by the simulated trajectories shown in Figure 5.11(a). However, as we increase the velocity of the conveyor, the average energy of the trapped cloud increases and the percentage of trapped atoms decreases, as shown in Figure 5.11b.

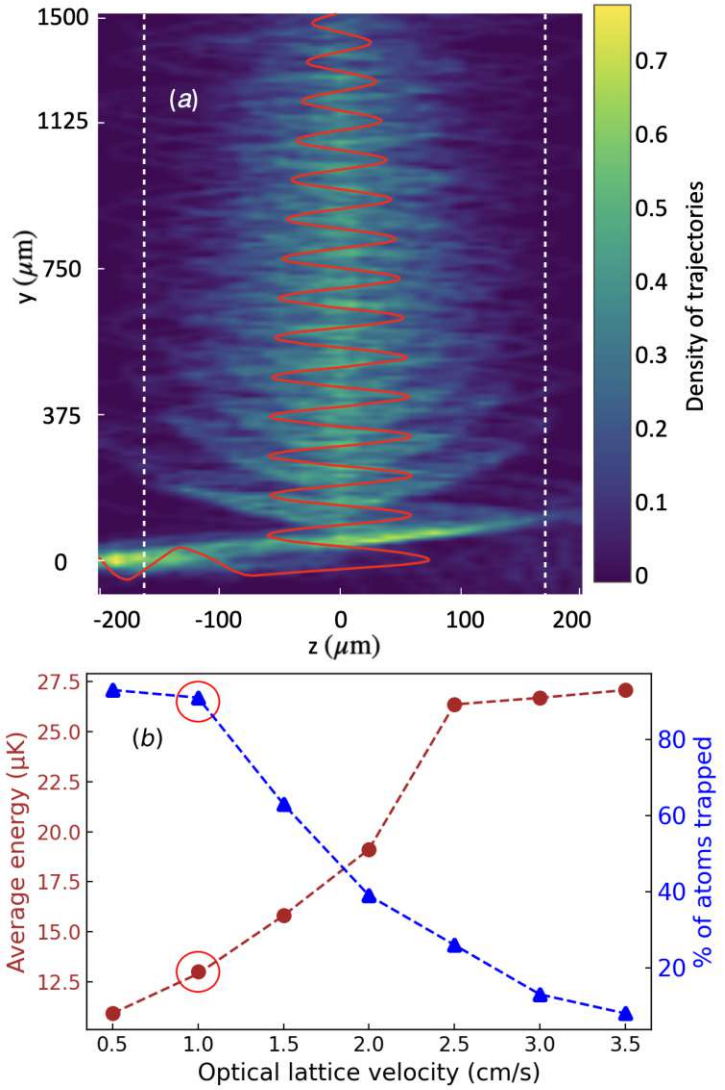

Figure 5.11: (a) Density of 100 trajectories of atoms as they travel along the moving optical lattice (velocity of optical lattice = 1 cm/s and potential depth = 32 μK). A typical trajectory is shown by the red trace. The outline of the optical lattice is indicated by the white dashed lines. (b) Average energy in μK (brown circles) and percentage of atoms trapped (blue triangles) as a function of the optical lattice velocity are represented. The blue and brown lines connecting the points are added to guide the eye.

The advantage of this design is that the atom number in the cavity mode is adjustable by tuning the speed of the magic moving lattice. By slowing the speed, the superradiant lasing threshold and a detectable signal can be reached with loading fluxes approaching two orders of magnitude smaller than the design values. Decreasing lattice speeds can compensate for other potential construction defects, such as low cavity finesse. Similarly, increasing the conveyor speed or moving the ejection beam lower to reduce the active

cavity length can reduce the cavity atom number and eliminate pulsing, while at the same time, it will increase the capture velocity oscillation, leading to less scattering and higher energies of loaded atoms. This flexibility is critical to cope with the enormous unknowns in achieving our goal.

5.4 Pumping inside moving optical lattice

After loading atoms into the optical lattice, we must pump them into the $^3P_0$-state. Figure 5.12 shows a possible pumping scheme [35] that is compatible with our experiment.

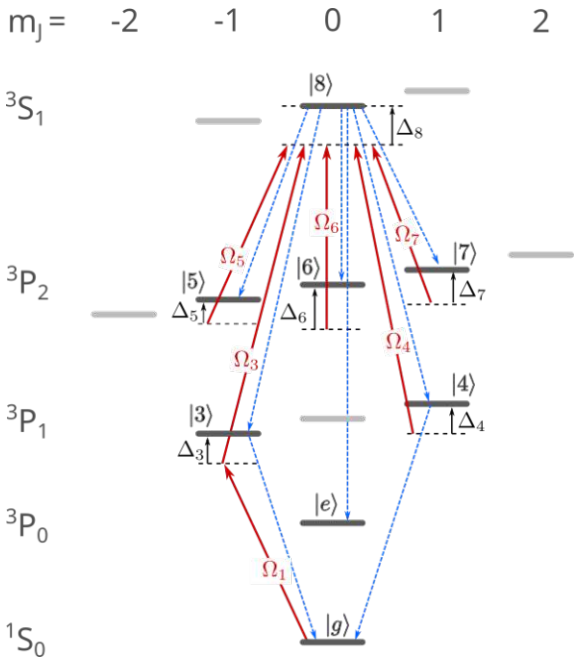

Figure 5.12: Possible pumping scheme with relevant matrix elements Ω_j and frequency detunings Δ_j. Laser-induced transitions are shown by solid red, and spontaneous decays by dashed blue arrows. The levels which do not participate in the repumping process are shown by pale gray. . Note that transition $^3\mathrm{S}_1, m = 0 \rightarrow {}^3\mathrm{P}_1, m = 0$ is forbidden in E1 approximation.

In the presence of the strong magnetic field required to open the clock transition in ^{88}Sr, the Zeeman sublevels of the excited states will split, allowing them to be independently addressed. To substantially populate $^3\mathrm{P}_0$, we first pump atoms to the $^3\mathrm{S}_1$ state. From there, atoms can decay to $^3\mathrm{P}_0$, but most likely will decay to the unwanted states, $^3\mathrm{P}_1$, $m_J = \pm 1$ and $^3\mathrm{P}_2$, $m_J = -1, 0, 1$ (but not into $^3\mathrm{P}_1, m_J = 0$ as this decay is prohibited by angular moment selection rules). We must repump atoms out of these unwanted states, particularly the $^3\mathrm{P}_2$-states, as they do not quickly decay to the ground state (lifetime of ≈110 min, compared to 22 μs for the $^3\mathrm{P}_1$-states) [75]. The pumping

beam has a waist of 250 μm and is aligned along the z-axis, with its center positioned 2 mm away from the reservoir along the y-axis. With $v_{\text{conv}} = 1\,\text{cm/s}$, we have an interaction time of about 5 ms. In order to decrease the heating all the pumping lasers are applied from both the opposite directions.

To find out realistic parameters for our multilevel pumping scheme and we solve the time dependent master equation for our scheme. Here we neglect all the collision-induced processes, because the pumping occurs in a very narrow zone with 250 nm waist, and these process does not affect significantly the internal state of the atoms. Therefore, we consider isolated atom interacting with pumping fields. The multilevel pumping scheme is presented in Figure 5.12.

$$\frac{\hat{\mathcal{H}}^0}{\hbar} = \sum_{j=g}^{8} \omega_j \hat{\sigma}_{jj} + \Omega_1 \left[\hat{\sigma}_{g3} e^{i(\omega_{3g}^L t+\phi_1)} + \hat{\sigma}_{3g} e^{-i(\omega_{3g}^L t+\phi_1)}\right] + \sum_{j=3}^{7} \Omega_j \left[\hat{\sigma}_{j8} e^{i(\omega_{8j}^L t+\phi_j)} + \hat{\sigma}_{8j} e^{-i(\omega_{8j}^L t+\phi_j)}\right], \quad (5.26)$$

Here $\hat{\sigma}_{ij} = |i\rangle\langle j|$, Ω_j are transition matrix elements which can be expressed via intensities I_j of the respective laser fields as seen by atoms, saturation intensities I_{sat}^j and the respective spontaneous transition rates Γ_{kj} as

$$\Omega_j = \sqrt{\frac{I_j}{8I_{\text{sat}}^j}}\Gamma_{kj}. \quad (5.27)$$

In turn, ω_{ij}^L is the frequency of the laser acting on the $|j\rangle \to |i\rangle$-transition, and ϕ_i is the time-dependent random phase of a laser applied to $|g\rangle \to |3\rangle$ transition at $i = 1$, and to $|i\rangle \to |8\rangle$ transition at $i = 3$ to 7. Here we suppose that all the lasers are independent, and their fluctuations corresponds to a white frequency noise, namely

$$\langle \dot{\phi}_i(t)\dot{\phi}_j(t')\rangle = \Gamma_i^L \delta_{ij}\delta(t-t'), \quad (5.28)$$

where Γ_i^L is the linewidth of the laser acting on $|i\rangle \to |j\rangle$-transition. As a next step we, following the approach used in [76], switch into the instantaneous rotating frame with the unitary transformation

$$\begin{aligned}\hat{U} = \exp\Big[-i\Big(&\hat{\sigma}_{gg}\,\omega_g t + \hat{\sigma}_{ee}\,\omega_e t + \hat{\sigma}_{33}\,[(\omega_g + \omega_{3g}^L)t + \phi_1] \\ &+\hat{\sigma}_{88}[(\omega_g + \omega_{3g}^L + \omega_{83}^L)t + \phi_{13} + \phi_3] \\ &+\sum_{i=4}^{7} \hat{\sigma}_{ii}[(\omega_1 + \omega_{31}^L + \omega_{83}^L - \omega_{84}^L)t + \phi_1 + \phi_3 - \phi_i]\Big)\Big].\end{aligned} \quad (5.29)$$

It is convenient to introduce "new" fluctuating phases

$$\begin{aligned}&\varphi_1 = -\phi_1, \quad \varphi_3 = -\phi_3 \\ &\varphi_j = \phi_j, \quad j \in \{4,5,6,7\},\end{aligned} \quad (5.30)$$

whose fluctuations also corresponds the white frequency noise (5.28). Then the new Hamiltonian

$$\hat{\mathcal{H}} = \hat{U}^\dagger \hat{\mathcal{H}}^0 \hat{U} - i\hbar \hat{U}^\dagger \frac{\partial \hat{U}}{\partial t} = \hat{\mathcal{H}}^D + \sum_j \hat{\mathcal{H}}^S_j \dot{\varphi}_j \tag{5.31}$$

can be represented as a sum of deterministic part $\hat{\mathcal{H}}^D$ and a series of stochastic parts $\hat{\mathcal{H}}^S_i \dot{\varphi}_i$. The deterministic part can be written as

$$\frac{\hat{\mathcal{H}}^D}{\hbar} = \sum_{j=3}^{8} \Delta_j \hat{\sigma}_{jj} + \Omega_1(\hat{\sigma}_{g3} + \hat{\sigma}_{3g}) + \sum_{j=3}^{7} \Omega_j(\hat{\sigma}_{j8} + \hat{\sigma}_{8j}), \tag{5.32}$$

where

$$\begin{aligned}
\Delta_3 &= \omega_3 - \omega_g - \omega^L_{3g}, \\
\Delta_4 &= \omega_4 - \omega_g - \omega^L_{3g} - \omega^L_{83} + \omega^L_{84}, \\
\Delta_5 &= \omega_5 - \omega_g - \omega^L_{3g} - \omega^L_{83} + \omega^L_{85}, \\
\Delta_6 &= \omega_5 - \omega_g - \omega^L_{3g} - \omega^L_{83} + \omega^L_{86}, \\
\Delta_7 &= \omega_5 - \omega_g - \omega^L_{3g} - \omega^L_{83} + \omega^L_{87}, \\
\Delta_8 &= \omega_8 - \omega_g - \omega^L_{3g} - \omega^L_{83}.
\end{aligned} \tag{5.33}$$

In turn, stochastic parts has the form

$$\begin{aligned}
\frac{\hat{\mathcal{H}}^S_1}{\hbar} &= \sum_{j=3}^{8} \hat{\sigma}_{jj}, \quad \frac{\hat{\mathcal{H}}^S_3}{\hbar} = \sum_{j=4}^{8} \hat{\sigma}_{jj}, \\
\frac{\hat{\mathcal{H}}^S_4}{\hbar} &= \hat{\sigma}_{44}, \quad \frac{\hat{\mathcal{H}}^S_5}{\hbar} = \hat{\sigma}_{55}, \\
\frac{\hat{\mathcal{H}}^S_6}{\hbar} &= \hat{\sigma}_{66}, \quad \frac{\hat{\mathcal{H}}^S_7}{\hbar} = \hat{\sigma}_{77}.
\end{aligned} \tag{5.34}$$

Evolution of some system operator $\hat{O}$ follows the Langevin-Heisenberg equation

$$(\mathrm{S})\frac{d\hat{O}}{dt} = \frac{i}{\hbar}\left[\hat{\mathcal{H}}^D, \hat{O}\right] + \hat{\hat{\mathcal{L}}}_{\mathrm{dec}}\hat{O} + \sum_{k,l} \hat{F}_{\mathrm{dec},kl} + \sum_j \frac{i}{\hbar}\left[\hat{\mathcal{H}}^S_j, \hat{O}\right]\dot{\varphi}_j, \tag{5.35}$$

which needs to be interpreted as a Stratonovic stochastic differential equation (indicated by (S)). Here $\hat{\hat{\mathcal{L}}}_{\mathrm{dec}}\hat{O}$ is a Liouvillian term describing spontaneous transitions between atomic levels

$$\hat{\hat{\mathcal{L}}}_{\mathrm{dec}}\hat{O} = \sum_{k,l} \frac{\Gamma_{kl}}{2}\left(2\hat{\sigma}_{kl}\hat{O}\hat{\sigma}_{lk} - \hat{\sigma}_{kk}\hat{O} - \hat{O}\hat{\sigma}_{kk}\right) = \sum_{k,l} \Gamma_{kl}\hat{\hat{\mathfrak{D}}}[\hat{\sigma}_{lk}]\hat{O}, \tag{5.36}$$

where Γ_{kl} is the rate of spontaneous transition $|k\rangle \to |l\rangle$, and $\hat{F}_{\mathrm{dec},kl}$ is the Langevin force associated with this transition.

To derive the Itô equation corresponding to the Stratonovic equation (5.35), consider the contribution into the differential $d\hat{O}$ of some operator $\hat{O}$, corresponding to fluctuation of the phase φ_j:

$$
\begin{aligned}
(\mathrm{S})\frac{i}{\hbar}\left[\hat{\mathcal{H}}_j^S,\hat{O}\right]\dot{\varphi}_j dt &\equiv \frac{i}{\hbar}\left[\hat{\mathcal{H}}_j^S,\hat{O}(t+0.5dt)\right]\dot{\varphi}_j\,dt \\
&= \frac{i}{\hbar}\left[\hat{\mathcal{H}}_j^S,\hat{O}(t)+0.5\left(\hat{\hat{\mathcal{L}}}_{\mathrm{reg}}\hat{O}(t)+0.5\sum_{k,l}\hat{F}_{\mathrm{dec},kl}\right)dt+\sum_k\frac{i}{\hbar}\left[\hat{\mathcal{H}}_k^S,\hat{O}\right]d\varphi_k\right]d\varphi_j \\
&\approx \frac{i}{\hbar}\left[\hat{\mathcal{H}}_j^S,\hat{O}(t)+0.5\frac{i}{\hbar}\left[\hat{\mathcal{H}}_j^S,\hat{O}\right]d\varphi_j\right]d\varphi_j \\
&\approx \frac{i}{\hbar}\left[\hat{\mathcal{H}}_j^S,\hat{O}(t)\right]d\varphi_j-\frac{\Gamma_j^L}{2\hbar^2}\left[\hat{\mathcal{H}}_j^S,\left[\hat{\mathcal{H}}_j^S,\hat{O}(t)\right]\right]dt, \qquad (5.37)
\end{aligned}
$$

where we neglected high-order terms proportional to $d\varphi_j dt$, dt^2 etc., replaced $d\varphi_j d\varphi_k$ by $\delta_{jk}\Gamma_j^L dt$ according to the Itô rule [77], and used the fact that the Langevin forces $\hat{F}_{\mathrm{dec},kl}$ associated with spontaneous decays are not correlated with fluctuations of the phases. So, we can transform the equation (5.35) into Itô form as

$$
\begin{aligned}
(\mathrm{I})\frac{d\hat{O}}{dt} =& \frac{i}{\hbar}\left[\hat{\mathcal{H}}^D,\hat{O}\right]+\hat{\hat{\mathcal{L}}}_{\mathrm{dec}}\hat{O}+\sum_{k,l}\hat{F}_{\mathrm{dec},kl} \\
&+\sum_j\frac{i}{\hbar}\left[\hat{\mathcal{H}}_j^S,\hat{O}\right]\dot{\phi}_j+\sum_j\frac{\Gamma_j^L}{2\hbar^2}\left(2\hat{\mathcal{H}}_j^S\hat{O}\hat{\mathcal{H}}_j^S-\hbar\hat{\mathcal{H}}_j^S\hat{O}-\hbar\hat{O}\hat{\mathcal{H}}_j^S\right), \qquad (5.38)
\end{aligned}
$$

similar to how it has been done in [76]. Here we supposed that the temperature is low (i.e., that the bath modes resonant to the frequencies of spontaneous transitions are not occupied), and used $\hat{\mathcal{H}}_j^{S\dagger}=\hat{\mathcal{H}}_j^S=\hat{\mathcal{H}}_j^{S\,2}/\hbar$. By averaging this equation the stochastic part vanishes, and we get

$$
\frac{d}{dt}\langle\hat{O}\rangle=\frac{i}{\hbar}\left\langle\left[\hat{\mathcal{H}}^D,\hat{O}\right]\right\rangle+\langle\hat{\hat{\mathcal{L}}}\hat{O}\rangle. \qquad (5.39)
$$

The dissipative processes are described by the Liouvillian part

$$
\hat{\hat{\mathcal{L}}}\hat{O}=\hat{\hat{\mathcal{L}}}_{\mathrm{dec}}\hat{O}+\sum_j\frac{\Gamma_j^L}{2\hbar^2}\left(2\hat{\mathcal{H}}_j^S\hat{O}\hat{\mathcal{H}}_j^S-\hat{\mathcal{H}}_j^S\hat{O}-\hat{O}\hat{\mathcal{H}}_j^S\right) \qquad (5.40)
$$

which can be represented as

$$
\hat{\hat{\mathcal{L}}}\hat{O}=\sum_j\frac{R_j}{2}\left(2\hat{J}_j^\dagger\hat{O}\hat{J}_j-\hat{J}_j^\dagger\hat{J}_j\hat{O}-\hat{O}\hat{J}_j^\dagger\hat{J}_j\right)=\sum_j R_j\hat{\hat{\mathfrak{D}}}[\hat{J}_j]\hat{O}, \qquad (5.41)
$$

where $\hat{J}_j$ are the jump operatos with corresponding rates R_j, see section 2.3.1. The list of jump operators and rates for the full 8-level system is presented in Table 5.3. In figure 5.13 and 5.14, we have presented how the population densities of different states changes during the pumping cycle for different sets of parameters.

Table 5.3: Dissipative processes in the 8-level pumping scheme. Decay rates were calculated as $\Gamma_{|n'L'J'm'\rangle\to|nLJm\rangle} = \Gamma_{|n'L'J'\rangle\to|nLJ\rangle} C(J,1,J';m,m'-m,m')^2$, where the decay rates $\Gamma_{|n'L'J'\rangle\to|nLJ\rangle}$ between fine-structure levels $|n'L'J'\rangle$ and $|nLJ\rangle$ were taken from [69], $C(J,1,J';m,m'-m,m')^2$ are the Clebsch-Gordan coefficients, and J', m' (J,m) are the angular moment and its projection associated with the upper (lower) state.

j	$\hat{J}_j$	R_j	value (order of magnitude)	description
1	$\hat{\sigma}_{58}$	Γ_{85}	$1.26\times10^7\,\mathrm{s}^{-1}$	decay from $\|8\rangle$ to $\|5\rangle$
2	$\hat{\sigma}_{68}$	Γ_{86}	$1.68\times10^7\,\mathrm{s}^{-1}$	decay from $\|8\rangle$ to $\|6\rangle$
3	$\hat{\sigma}_{68}$	Γ_{87}	$1.26\times10^7\,\mathrm{s}^{-1}$	decay from $\|8\rangle$ to $\|6\rangle$
4	$\hat{\sigma}_{48}$	Γ_{84}	$1.35\times10^7\,\mathrm{s}^{-1}$	decay from $\|8\rangle$ to $\|4\rangle$
5	$\hat{\sigma}_{38}$	Γ_{83}	$1.35\times10^7\,\mathrm{s}^{-1}$	decay from $\|8\rangle$ to $\|3\rangle$
6	$\hat{\sigma}_{e8}$	Γ_{8e}	$8.9\times10^6\,\mathrm{s}^{-1}$	decay from $\|8\rangle$ to $\|e\rangle$
7	$\hat{\sigma}_{g4}$	Γ_{4g}	$4.69\times10^7\,\mathrm{s}^{-1}$	decay from $\|4\rangle$ to $\|g\rangle$
8	$\hat{\sigma}_{g3}$	Γ_{3g}	$4.69\times10^7\,\mathrm{s}^{-1}$	decay from $\|3\rangle$ to $\|g\rangle$
9	$\hat{\sigma}_{ge}$	Γ_{eg}	γ	decay from $\|e\rangle$ to $\|g\rangle$
10	$\sum_{k=3}^{8}\hat{\sigma}_{kk}$	Γ_1^L	about kHz	Fluctuations of laser acting on $\|g\rangle\to\|3\rangle$
11	$\sum_{k=4}^{8}\hat{\sigma}_{kk}$	Γ_3^L	about MHz	Fluctuations of laser acting on $\|3\rangle\to\|8\rangle$
12	$\hat{\sigma}_{44}$	Γ_4^L	about MHz	Fluctuations of laser acting on $\|4\rangle\to\|8\rangle$
13	$\hat{\sigma}_{55}$	Γ_5^L	about MHz	Fluctuations of laser acting on $\|5\rangle\to\|8\rangle$
14	$\hat{\sigma}_{66}$	Γ_6^L	about MHz	Fluctuations of laser acting on $\|6\rangle\to\|8\rangle$
15	$\hat{\sigma}_{77}$	Γ_7^L	about MHz	Fluctuations of laser acting on $\|7\rangle\to\|8\rangle$

We identified a set of detunings where the trapping of population into the dark states doesn't play a significant role. Leveraging this carefully selected set of parameters, as described in 5.4, we found that the population densities of atoms in states $^3P_1$, $^3P_2$, and $^3S_1$ remain low. The intensity of the laser for the transition $|3\rangle\to|8\rangle$ is chosen such that $\Gamma_{38}^P \gg \Gamma_{31}^{\mathrm{decay}}$, thereby preventing excessive scattered photons from the $|1\rangle\leftrightarrow|3\rangle$ transition, which would otherwise cause heating, see figure 5.14.

Under conditions of far-detuned lasers, the intensities given in 5.4, and the fact that the motion of these atoms does not significantly change during the pumping cycle, we can assume that only the effect of individual lasers acting on two levels at a time needs to be considered. To estimate the pumping efficiency and the heating of atoms within the moving optical lattice, we apply the SCMC method described earlier.

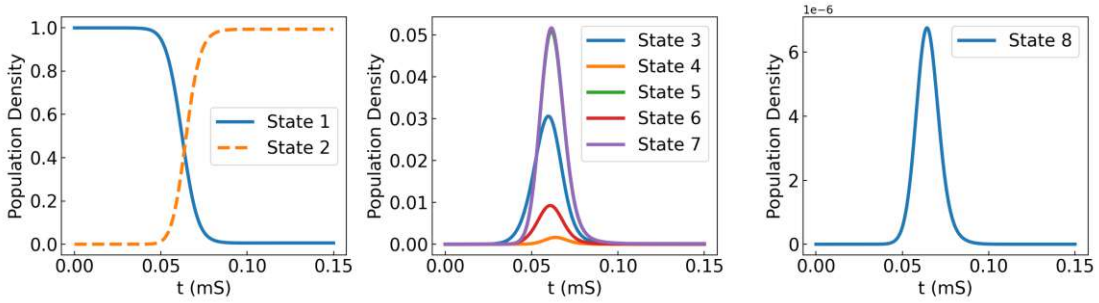

Figure 5.13: Population density profile for parameters given in table 5.4 except with $I_{38} = 0.02 I_{\text{sat}}$. Here we can see that at the end of the pumping cycle all the population ends up in the state $|2\rangle$ but the total number of scattered photons is approximatly 39.37 with total photons emitted from state $|8\rangle$ is 8.699 and from the cycle $|1\rangle \leftrightarrow |3\rangle$ transition is 29.401. To accomodate this large number of photons we need too deep optical lattice and this will cause huge heating in our system.

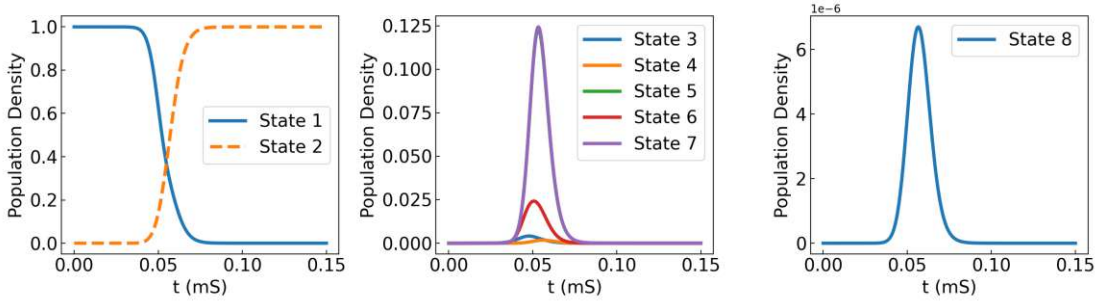

Figure 5.14: Population density profile for parameters given in table 5.4. To prevent excessive scattered photons from the $|1\rangle \leftrightarrow |3\rangle$ transition, the intensity of the laser for the transition $|3\rangle \rightarrow |8\rangle$ ($I_{38} = 0.5 I_{\text{sat}}$) is made stronger leading to total number of scattered photons to be 12.3, with 8.05 photons scatted from $|8\rangle$ and 2.16 from the cycle $|1\rangle \leftrightarrow |3\rangle$ transition

The pumping rate associated with each individual two-level system is calculated using:

$$\Gamma^{p}_{mj}(\vec{r},\vec{v}) = \sum_{l} \left(\frac{\gamma_{mj} s^{p}_{mj}(\vec{r},\vec{v})}{2 + s^{p}_{mj}(\vec{r},\vec{v})} \right) \left(1 + \frac{s^{p}_{mj}(\vec{r},\vec{v})}{2 + s^{p}_{mj}(\vec{r},\vec{v})} \right)^{-1}, \tag{5.42}$$

where

$$s^{p}_{mj}(\vec{r},\vec{v}) = \frac{I(r)}{I_{\text{sat}}} \left(1 + 2 \left(\frac{\delta_{mj}(\vec{r},\vec{v})}{\Gamma_{mj}} \right)^{2} \right)^{-1} \tag{5.43}$$

The spontaneous decay from ${}^3S_1$ is modeled by generating a random number based on the relative decay rates for different transitions. Momentum kicks are applied similarly to the molasses simulation, as the decay rate from ${}^3S_1$ is 100 times higher than any other process. For the ${}^3P_1$, $\quad m = -1$ state, which has a smaller decay rate, the momentum kicks are modeled using Einstein's rate equation. Three Random numbers are generated in the

Table 5.4: Parameters of pumping beams. Here P-1 acts on the $|^1S_0\rangle \rightarrow |^3P_1, m=-1\rangle$ transition. Similarly, P-2 and P-3 acts on the $|^1S_0\rangle \rightarrow |^3P_1, m=\pm 1\rangle$ transitions, whereas P-4, P-5, and P-6 pump atoms from the $|^3P_2, m=-1\rangle$, $|^3P_2, m=0\rangle$ and $|^3P_2, m=1\rangle$-states to the $|^3S_1, m=0\rangle$-state, respectively. The partial deacay rates Γ associated with the corresponding transitions are Γ_{total} for P-1, $0.5\,\Gamma_{total}$ for P-2,3, $0.3\,\Gamma_{total}$ for P-4,6, and $0.4\,\Gamma_{total}$ for P-5 respectively. The Intensities mentioned in the table corresponds to the circular polarized field component.

Pumping Beam	P-1	P-{2,3}	P-{4,5,6}
Intensity	$0.32\,I_{\text{sat}}$	$\{0.5, 0.02\}\,I_{\text{sat}}$	$0.02\,I_{\text{sat}}$
Γ_{total}, μs^{-1}	4.69×10^{-2}	27.0	42.0
Waist, μm	(250,250)	(250,250)	(250,250)
λ, nm	689	688	707
center, mm	(0,2,0)	(0,2,0)	(0,2,0)
Polarization	along x-axis	along x-axis	along {x,z,x}-axis
Propagation	along z-axis	along z-axis	along z-axis
$\Delta/(2\pi)$	-1 kHz	$\{0, -2\}$ MHz	$\{-19.9, 0.1, 20.1\}$ MHz

interval $[0, 1]$ and compared with the probabilities associated with different channels. Pumping from all other $^3P_2$ states is considered as individual 2 level systems.

- Starting with an initial state $(\vec{x}_i, \vec{p}_i)$ and state $|1\rangle$ at time t_i we evolve the equation of motion $(\dot{\vec{x}}_i, \dot{\vec{p}}_i)$ and all the scattering rate associated with pumping.
- Generate a vector $\vec{v}_s = (\sin\theta\cos\phi, \sin\theta\sin\phi, \cos\theta)$ to model spontaneous emmision kicks with θ and ϕ randomly generated numbers and nine random number $\{r_i, i \in 1 \text{ to } 9\}$ in the interval $[0, \pi]$, $[0, 2\pi]$ and $[0, 1]$ respectively.
- If the system is in state $|1\rangle$ and $r_1 > e^{-\int_{t_i}^{t_{i+1}} \Gamma^p_{13}(x,v)dt}$, the state is set to $|3\rangle$.
- Then, depending on whether $r_2 > e^{-\int_{t_i}^{t_{i+1}} \Gamma^p_{38}(x,v)dt}$ or $r_3 > e^{-\int_{t_i}^{t_{i+1}} \Gamma^{decay}_{31}dt}$, the state is either changed to $|8\rangle$ or returned to $|1\rangle$, with corresponding momentum kicks applied and we reset all the random numbers. Otherwise without changing anything we take another step.
- if the state is $|8\rangle$, the spontaneous decay from $^3S_1$ is modeled by generating a random number r_s based on the relative decay rates for different transitions and accordingly the state is set to $|j\rangle$ where j belongs to $\{2, 3, 4, 5, 6, 7\}$.
- Now if the the state $|j\rangle$ for j in $\{5, 6, 7\}$ the atoms are pumped back to $|8\rangle$ depending on the condition $r_j > e^{-\int_{t_i}^{t_{i+1}} \Gamma^p_j(x,v)dt}$ if the state is $|3\rangle$ or $|4\rangle$ we repeat the step 4. Otherwise without changing anything take another step
- Repeat the above steps until we reach the desired evolution time that is atoms are no longer in pumping region.

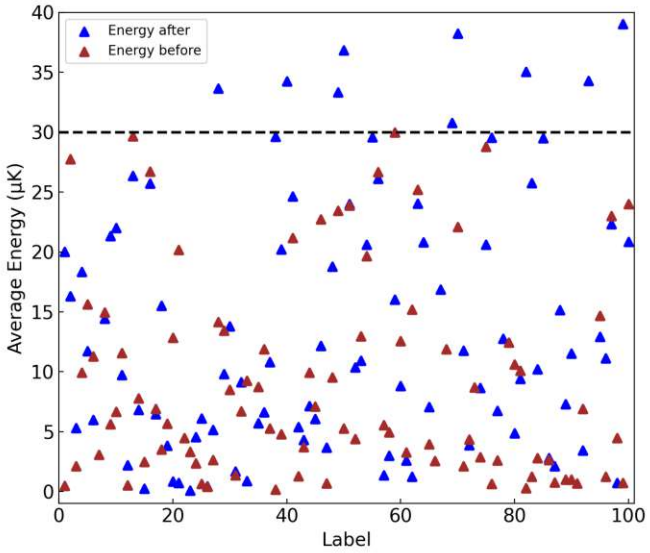

Figure 5.15: The change in the individual energy of the atoms before and after pumping. Before pumping the average energy of trapped atoms was around $12.32\mu k$ after pumping around 8% of the atoms are lost and the average energy of the trapped atoms goes to $16.11\mu k$.

Atoms will undergo an average of 12 photon recoils throughout the pumping process, leading to heating. To keep the atoms in the optical lattice, its depth must account for this heating as shown in 5.15. Too shallow a lattice could lead to atoms getting lost before they can contribute to superradiant emission.

An optical lattice depth of 32 μK will be sufficient, as the average energy of the pumped atoms is approximately 16 μK for an optical lattice velocity of 1 cm/s, see figure 5.16. Elastic collisions, which could create higher energy atoms, are negligible under our conditions. Using this scheme, a pumping efficiency of 83% can be achieved.

This concludes our discussion on the design of a continuously-operating superradiant laser on the $^1S_0 \rightarrow {}^3P_0$ transition in ^{88}Sr. We discussed the mechanism by which we will continuously load atoms from the dipole trap into a magic wavelength optical conveyor lattice generated inside a bow-tie cavity. This bow-tie cavity creates the strong collective coupling between atoms that should enable superradiant emission which we will discuss in the next chapter.

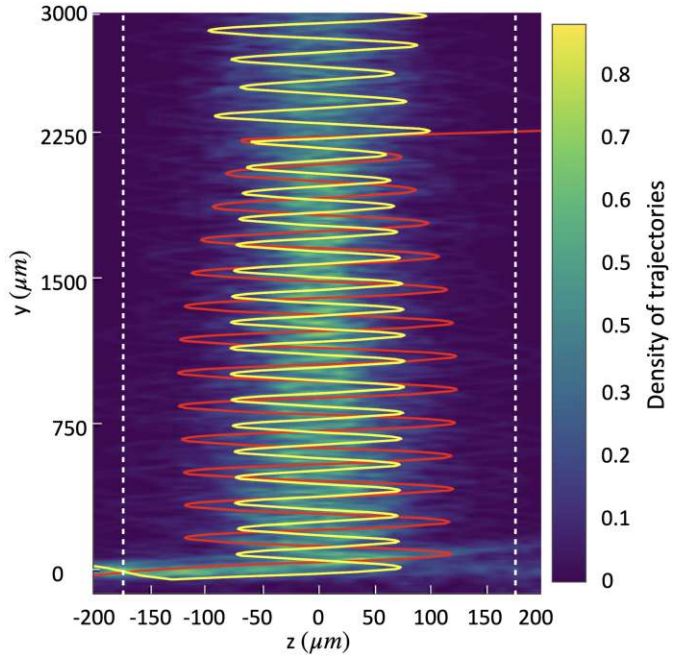

Figure 5.16: The marked yellow trajectory shows the atom which after pumping escaped the optical lattice while the yellow one shows an atom which stayed trapped in the optical lattice

CHAPTER 6

Simulation of the optical conveyor laser

The bulk of this chapter has been submitted to Physical Review Research [55]

The design of the mHz setup as well as the simulation of cooling and pumping processes have been presented in chapter 5. In this chapter we present the results of simulation of the superradiant laser output which can be achieved in such a machine.

In section 6.1 we discuss the position-dependent shift caused by inhomogenity of the magnetic field. In section 6.2 we reduce the real pumping scheme discussed in section 5.4 to an equivalent two-level one using the method derived in [35]. In sections 6.3 and 6.3.1, we construct the mean-field model which includes collisional effects and perform simulations and analyses for various sets of parameters. In this model the elastic collisions between the atoms in the ground state leads to dephasing, according to [78]. In section 6.4, we modify this model in order to improve estimations by taking into account the possible dephasing due to elastic collisions in the excited state.

6.1 Magnetic-induced shifts

As mentioned in chapter 5, single-photon $^3\mathrm{P}_0 \rightarrow {}^1\mathrm{S}_0$ transitions in isolated bosonic strontium are forbidden to all orders of multipole expansion. This transition might be made slightly allowed in the presence of an external field, for example, a static magnetic field B [68], mixing the $|^3\mathrm{P}_0\rangle$ and $|^3\mathrm{P}_1, m = 0\rangle$ states. Such a field not only opens this transition but also shifts the position of the dressed $^3\mathrm{P}_0$ state by a second-order Zeeman shift $\delta\omega_{3\mathrm{P0}-1\mathrm{S0}}$ related to the induced E1 transition rate $\gamma_s = \gamma_{3\mathrm{P0}-1\mathrm{S0}}$ as

$$\delta\omega_{3\mathrm{P0}-1\mathrm{S0}} = \Delta_0 + \Delta_{\mathrm{mg}} = \gamma_s \frac{\omega_{3\mathrm{P1}-3\mathrm{P0}}}{\gamma_{3\mathrm{P1}\rightarrow 1\mathrm{S0}}} = \beta B^2 \tag{6.1}$$

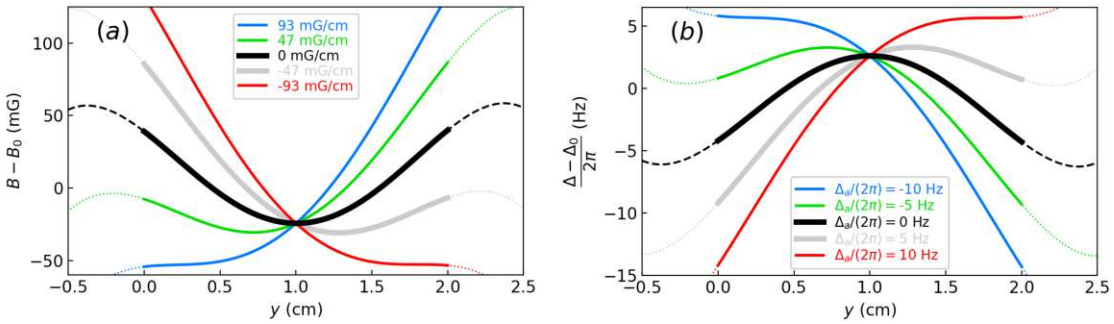

Figure 6.1: Spatial inhomogeneity of magnetic field and the resulting clock transition frequency change. (a) Magnetic field magnitude B along the direction of the optical conveyor and (b) corresponding second-order Zeeman shift, referenced to their values for the offset field $B_0 = 230$ G, which corresponds to a frequency shift $\Delta_0 \approx -2\pi \times 12.3\ kHz$. The curves are rendered solid in the emission zone. The black curve corresponds to the simulated magnetic field of the Helmholtz coil pair. The colored curves correspond to the presence of an additional magnetic field gradient. The resulting position-dependent frequency shift is shown in (b) with the same color encoding (see legend in (b) for the values).

where $\beta \approx -1.465\ \mathrm{s}^{-1}/\mathrm{G}^2 \approx -2\pi \times 23.3\ \mathrm{MHz}/\mathrm{T}^2$, see expressions (5.7) in section 5.1.1. The sensitivity of this narrow transition frequency to variations δB in the bias field B thus scales as B. This leads to considerable sensitivity in the narrow transition to magnetic field fluctuations for practical bias field strengths. For an external bias field $B = 200$ G corresponding to a transition linewidth $\gamma_s \approx 2\pi \times 12\ \mu$Hz, the second order differential Zeeman shift $\Delta_{\mathrm{mg}} \approx \Delta_0 - 2\pi \times 93\ \mathrm{mHz/mG} \times (B - B_0)$ where $\Delta_0 = \beta B_0 \approx -2\pi \times 9.33$ kHz. The superradiance chamber of our setup is isolated by magnetic shielding. In order to allow the ${}^1S_0 \leftrightarrow {}^3P_0$ transition, we apply a fairly strong and homogeneous bias magnetic field $B \approx B_0 = 200\ G$ created by a set of Helmholtz coils. This magnetic field is orthogonal to the axis of the optical conveyor as well as the axis of the transfer beam, and the superradiance mode is polarized along its direction, see figure 5.4.

In order to evaluate the dependence of the second-order Zeeman shift Δ_{mg} on the position along the conveyor, the distribution of the magnetic field strength B was calculated in University of Amsterdam with COMSOL. the results are shown by the black curve in Figure 6.1.

Another issue is related to the density. The identical bosons interact with each other via s-wave collisions. This leads to potentially large shifts and decoherences.

The bias magnetic field inhomogeneity in the centre of the emission zone is mostly due to the incompletely closed magnetic shielding, where the holes are required for optical access and connection to the rest of the vacuum system. Because of spatial constraints, we have not considered placing curvature coils in the science chamber to compensate this inhomogeneity's. The simulated imperfections will lead to a position-dependent shift $\Delta_{\mathrm{mg}}(y)$, and this frequency shift only becomes more significant, if the field strength is increased further. To counteract this problem, we consider the possibility of adding an

extra gradient G_B to the bias field B, which will add an additional position-dependent shift $\Delta_a(2y/\ell_{\text{conv}} - 1)$. Therefore, the overall position-dependent shift caused by magnetic field has the form

$$\Delta(y) = \Delta_{\text{mg}}(y) + \Delta_a(2y/\ell_{\text{conv}} - 1). \tag{6.2}$$

In this expression, the amplitude Δ_a of the extra position-dependent shift can be calculated from the magnetic field gradient G_B as

$$\Delta_a = \beta B_0 G_B \ell_{\text{conv}}.. \tag{6.3}$$

This position-dependent shift can help us partially compensate irregularities in Δ_{mg} in parts of the emission region. Interestingly, it also allows to compensate the collisional shifts (6.20), which depend on the densities of the atoms in the ground and the excited states. The total shift varies as the atoms move along the conveyor, as shown in Figure 6.3 (g).

6.2 Reduction of multilevel pumping scheme to an equivalent 2-level scheme

The atoms are loaded into the optical conveyor from the dipole guide in the $^1S_0$ state, and they get pumped into the upper lasing state about 2 mm after the point where they are loaded. Therefore, the atoms during the pumping process are coupled to the cavity field. This pumping can lead to dephasing and cause light shifts on the atomic transition, and may affect the frequency of the superradiant laser output. In order to include these pumping-induced effects into the model without adding all the equations for complete set of the atomic levels participating in the repumping process and coherences between these levels, we can map the real multilevel systems into an equivalent 2-level one with incoherent pumping, using the method developed in [35]. This section is dedicated to such a mapping.

We neglect here all the collision-induced processes, because the pumping occurs in a very narrow zone (250 μm waist), and these process will not significantly affect the internal state of the atoms during the repumping process. Therefore, we consider isolated atoms interacting with the pumping fields. The 8-level realistic pumping scheme is presented in Figure 5.12.

The evolution of some deterministic part $\hat{\mathcal{H}}^D$ of the Hamiltonian describing this system is given by equations (5.38) – (5.41), corresponing to the master equation

$$\frac{d\hat{\rho}}{dt} = -\frac{i}{\hbar}\left[\hat{\mathcal{H}}^D, \hat{\rho}\right] + \sum_j \hat{\hat{\mathfrak{D}}}'[J_j]\hat{\rho}, \tag{6.4}$$

where the (deterministic) Hamiltonian $\hat{\mathcal{H}}^D$ is given by equation 5.32:

$$\frac{\hat{\mathcal{H}}^D}{\hbar} = \sum_{j=3}^{8} \Delta_j \hat{\sigma}_{jj} + \Omega_1(\hat{\sigma}_{g3} + \hat{\sigma}_{3g}) + \sum_{j=3}^{7} \Omega_j(\hat{\sigma}_{j8} + \hat{\sigma}_{8j}), \tag{6.5}$$

and the rates R_j and the jump operators $\hat{J}_j$ corresponding to various dissipative processes are listed in table 5.3.

Table 6.1: Dissipative processes in the equivalent 2-level scheme with incoherent pumping.

j	$\hat{J}_j$	R_j	description
1	$\hat{\sigma}_{ge}$	γ_s	decay from $\|e\rangle$ to $\|g\rangle$
2	$\hat{\sigma}_{eg}$	w	incoherent pumping from $\|g\rangle$ to $\|e\rangle$
3	$\hat{\sigma}_{gg}$	ν_g	dephasing on $\|g\rangle$
4	$\hat{\sigma}_{ee}$	ν_e	dephasing on $\|e\rangle$

We want to map this multilevel scheme to an equivalent 2-level one, where the density matrix describing the states $|g\rangle$ and $|e\rangle$ follows the master equation with an effective 2-level Hamiltonian

$$\hat{\mathcal{H}}^D_{2-\text{level}} = \hbar(\delta_g \hat{\sigma}_{gg} + \delta_e \hat{\sigma}_{ee}), \tag{6.6}$$

and the dissipative processes are listed in Table 6.1.

The procedure of mapping of multilevel pumping scheme to an equivalent 2-level scheme with incoherent pumping is described in detail in [35]. In brief, as a first step one has to find the steady-state values of ρ_{ee} and ρ_{gg}, solving the master equation (6.4). Then the equivalent incoherent pumping rate is

$$w = \Gamma_{eg} \frac{\rho_{ee}}{\rho_{gg}}. \tag{6.7}$$

Second, one has to diagonalise the effective non-hermitian Hamiltonian which is expressed here:

$$\hat{\mathcal{H}}^{\text{nh}}_{\text{eff}} = \hat{\mathcal{H}}^D - \frac{i\hbar}{2} \sum_j R_j \hat{J}_j^+ \hat{J}_j \tag{6.8}$$

to get the complex eigenvalues E_g and E_e, corresponding to the eigenstates with the highest overlap with the unperturbed "clock" states $|g\rangle$ and $|e\rangle$. Then one can extract the effective frequency shifts

$$\delta_{e,g} = \text{Re}(E_{e,g}) \tag{6.9}$$

and dephasing rates

$$\nu_g = -2\text{Im}(E_g) - \Gamma_{eg}; \quad \nu_e = -2\text{Im}(E_e) - w. \tag{6.10}$$

In the Table 6.2 we present four examples of mapping the realistic 8-level pumping scheme into the effective 2-level scheme using incoherent pumping. For all 4 sets of parameters we have taken: $I = 0.32 I_{\text{sat}}$ is the laser acting on $|g\rangle \to |3\rangle$ transition that gives $\Omega_1 = 9.38 \times 10^3\ \text{s}^{-1}$), $I = 0.5 I_{\text{sat}}$ for laser acting on $|3\rangle \to |8\rangle$ transition, what gives $\Omega_3 = 3.375 \times 10^6\,\text{s}^{-1}$ and $I = 0.02 I_{\text{sat}}$ for all other lasers, that gives $\Omega_3 = \Omega_4 = 6.75 \times 10^5\ \text{s}^{-1}$, $\Omega_5 = \Omega_7 = 6.3 \times 10^5\ \text{s}^{-1}$, $\Omega_6 = 8.4 \times 10^5\ \text{s}^{-1}$, according to expression (5.19).

Table 6.2: Examples of correspondence between pumping parameters of the realistic 8-level scheme and equivalent 2-level scheme. Here we introduced $\Delta\omega_{kl} = \omega_{kl}^L - \omega_k + \omega_l$ and supposed that all the lasers except the one acting on $|g\rangle \to |e\rangle$ transition have the same linewidth. Here $\nu = \nu_g + \nu_e$, and $\delta_p = \delta_e - \delta_g$. Intensities of the pumping lasers are specified in the text.

	Parameters	1st Set	2nd Set	3rd Set	4th Set
8-level scheme	$\Delta\omega_{3g}/(2\pi)$	20 Hz	-100 Hz	50 Hz	500 Hz
	$\Delta\omega_{83}/(2\pi)$	-1 MHz	-2.0 MHz	0	0
	$\Delta\omega_{84}/(2\pi)$	1 MHz	0	2 MHz	2 MHz
	$\Delta\omega_{85}/(2\pi)$	-20 MHz	-19.9 MHz	-20 MHz	-17 MHz
	$\Delta\omega_{86}/(2\pi)$	0	-100 kHz	0	-3 MHz
	$\Delta\omega_{87}/(2\pi)$	20 MHz	20.1 MHz	20 MHz	-23 MHz
	$\Gamma_1^L/(2\pi)$	1 kHz	1 kHz	1 kHz	2 kHz
	$\Gamma_j^L/(2\pi),\ j = 3$ to 8	3 MHz	3 MHz	1 MHz	1 MHz
2-level	w	272.6 s^{-1}	272.8 s^{-1}	248.0 s^{-1}	246 s^{-1}
	$\nu = \nu_g + \nu_e$	401 s^{-1}	404 s^{-1}	346 s^{-1}	341 s^{-1}
	$\delta_p/(2\pi)$	6.26 Hz	12.4 Hz	0.02 Hz	0.42 Hz

6.3 Mean-field model of the optical conveyor laser

In this section we construct the model of the superradiant laser on the optical conveyor schematically presented in figure 6.2. We use mean-field equations, in which we neglect quantum correlations between different atoms, and where we suppose that each atom interacts with the cavity field created by all the atoms. This model allows us to analyse the impact of systematic effect, particularly collisional decoherences, losses and shifts, as well as inhomogeneity of the external magnetic field. We consider the ring cavity in bow-tie configuration with total length $l_{\text{cav}} = 20$ cm. We suppose that the atoms interact only with the running-wave cavity mode co-propagating (or counter-propagating) with the optical conveyor, which is resonant with the atomic transition in the rest frame of the conveyor: this is because the other running-wave mode, counter-propagating (or co-propagating) with the optical conveyor will be detuned by $\Delta_{\text{Doppler}} = 2\omega v_{\text{conv}}/c \approx 2\pi \times 28.6$ kHz at $v_{\text{conv}} = 1$ cm/s, and the atoms which are synchronized with, say, the co-propagating mode can not collectively interact with the counter-propagating one due to the mismatch of the relative phases.

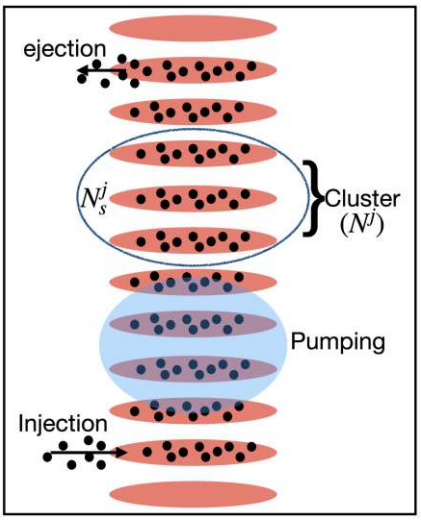

Figure 6.2: Scheme of the optical conveyor carrying the atoms along the superradiance cavity.

To include the collisional effetcs, consider first the the atoms inside the single lattice site.

The periods of the atom radial and axial motion in a single lattice site (of order of 0.01 s and 10^{-5} s, respectively) are much shorter than the interaction time between the atom and the field (around 1 s). Therefore, we can average the position-dependent effects as well as the spatial distribution of the atoms over the single lattice site. To perform this averaging, we use a harmonic oscillator approximation for the dipole potential of the lattice site and a Maxwell-Boltzmann spatial distribution of the atoms:

$$p(x', y', z') = \frac{2^{3/2}}{\pi^{3/2} W_r^2 W_y} \exp\left(-2\frac{x'^2 + z'^2}{W_r^2} - 2\frac{y'^2}{W_y^2}\right), \tag{6.11}$$

where x', y' and z' are the distances from the center of the lattice site. The $1/e^2$ radii W_r and W_y of the atomic cloud in the radial and axial directions are calculated as

$$W_r = W_{\text{conv}}\sqrt{T/U_{\text{conv}}}, \tag{6.12}$$

$$W_y = \frac{1}{k}\sqrt{2\frac{(T^\theta + (U_{\text{conv}}E_R)^{\theta/2})^{1/\theta}}{U_{\text{conv}}}}, \tag{6.13}$$

where T is the temperature of the atomic ensemble which is set to $T = 10$ μK. Next, $U_{\text{conv}} = 30$ μK is the depth, and $E_R = k^2\hbar^2/(2\text{m}_{\text{Sr}}k_B) \approx 0.165$ μK is the recoil energy of the moving optical lattice potential in units of temperature. The phenomenological parameter $\theta = 2.5$ is chosen such that eq. (6.11) well reproduces the probability density of the atom in the harmonic potential in the cross-over between the "classical thermal limit" ($k_BT \gg \hbar\omega_y = 2\sqrt{E_R U_{\text{conv}}}$) and the "frozen quantum" limit ($k_BT \ll \hbar\omega_y$). Here we consider the possibility that higher vibrational states along the y-axis can be occupied.

The number density n_j averaged over the atomic motion can be represented as

$$n_j = N\int p^2(x', y', z')dx'dy'dz' = \frac{N_{\text{lc}}}{V_{\text{eff}}}, \tag{6.14}$$

where $N_{\text{lc}} = N^j\lambda_{\text{conv}}/(2\ell_c)$ is the number of atoms in a single lattice site and

$$V_{\text{eff}} = W_r^2 W_y \pi^{3/2} \tag{6.15}$$

is the effective volume of a single lattice site.

The atom-cavity coupling strength is then can be calculated as

$$g = \frac{\exp\left(\frac{-k^2W_y^2}{8}\right)}{1 + \frac{W_r^2}{2W_0^2}}\sqrt{\frac{3c^3\gamma_s}{l_{\text{cav}}\omega^2 W_0^2}}, \tag{6.16}$$

where the prefactor before the square root describes the averaging over the spatial distribution of the atoms over one lattice site, and $k = 2\pi/\lambda_{\text{conv}}$ is the wave number of the conveyor lattice.

The mean-field equations for the cavity field $\langle\hat{a}\rangle$ looks like

$$\frac{d\langle\hat{a}\rangle}{dt} = -\left[\frac{\kappa}{2} + i\delta_a\right]\langle\hat{a}\rangle - i\sum_j g(y_j)\langle\hat{\sigma}^j_{ge}\rangle \tag{6.17}$$

where $\delta_a = \delta_c - k_0/v_{\text{conv}}$, δ_c is the detuning of the cavity field from the rotating frame where we consider the system, v_{conv} is the speed of conveyor, and k_0 is the wave number of the cavity mode. The sum is taken only over the atoms within the optical conveyor. Because the conditions (3.31) is satisfied, the field $\langle\hat{a}\rangle$ gets fast into equilibrium with atomic degrees of freedom and can be adiabatically eliminated:

$$\langle\hat{a}\rangle = \frac{-2i}{\kappa + 2i\delta_a}\sum_j g(y_j)\langle\hat{\sigma}^j_{ge}\rangle N^j \tag{6.18}$$

To reduce the computational cost we, similar to how it has been done in chapter 4, group the atoms into M clusters distributed along the optical conveyor, with all the atoms of the same cluster having the same internal states as suggested in section 4.1.1. Each cluster occupies a segment of length $\ell_c = \ell_{\text{conv}}/(M-1)$ centered at position y_j along the conveyor. In order to simulate smooth introduction and removal of the atoms, the clusters are initialized at position $y_{j,0} = -\ell_c/2$, and the atoms get removed only when they reach the position $y_{j,f} = \ell_{\text{conv}} + \ell_c/2$. When $-\ell_c/2 < y_j < \ell_c/2$ or $\ell_{\text{conv}} - \ell_c/2 < y_j < \ell_{\text{conv}} + \ell_c/2$, the coupling strength g between the atoms and the cavity field is multiplied by the fraction of atoms in the cluster inside the active part of the conveyor. The number N^j of the atoms in jth cluster is randomly distributed around $\Phi\ell_c/v_{\text{conv}}$ where we used Poissonian distribution.

In turn, the equations for atomic coherence $\langle\sigma^j_{ab}\rangle = |a^j\rangle\langle b^j|$ of individual atoms are

$$\begin{aligned}
\frac{d\langle\hat{\sigma}^j_{ge}\rangle}{dt} &= -\left[\frac{\gamma_s+\gamma_e+\gamma_g+w(y_j)}{2} + \gamma_R + \nu_p(y_j) + \Gamma^j_{\text{coll}} + i\left(\Delta(y_j) + \Delta^j_{\text{coll}} + \delta_p(y_j)\right)\right]\langle\hat{\sigma}^j_{ge}\rangle \\
&\quad + ig(y_j)\langle\hat{a}\rangle(\langle\hat{\sigma}^j_{ee}\rangle - \langle\hat{\sigma}^j_{gg}\rangle), \\
\frac{d\langle\hat{\sigma}^j_{ee}\rangle}{dt} &= ig(y_j)\left[\langle\hat{a}^\dagger\rangle\langle\hat{\sigma}^j_{ge}\rangle - \langle\hat{a}\rangle\langle\hat{\sigma}^j_{eg}\rangle\right] - (\gamma_e+\gamma_s)\langle\hat{\sigma}^j_{ee}\rangle + n_j(\gamma_{ee}\langle\hat{\sigma}^j_{ee}\rangle + \gamma_{eg}\langle\hat{\sigma}^j_{gg}\rangle)\langle\hat{\sigma}^j_{ee}\rangle \\
&\quad + w(y_j)\langle\hat{\sigma}^j_{gg}\rangle, \\
\frac{d\langle\hat{\sigma}^j_{gg}\rangle}{dt} &= -ig(y_j)\left[\langle\hat{a}^\dagger\rangle\langle\hat{\sigma}^j_{ge}\rangle - \langle\hat{a}\rangle\langle\hat{\sigma}^j_{eg}\rangle\right] + \gamma_s\langle\hat{\sigma}^j_{gg}\rangle - \left[\gamma_g + w(y_j) + n_j\gamma_{ge}\langle\hat{\sigma}^j_{ee}\rangle\right]\langle\hat{\sigma}^j_{gg}\rangle
\end{aligned} \tag{6.19}$$

where $\Delta(y)$ is the position-dependent magnetic shift (6.2), γ_s is the spontaneous transition rate ($\gamma_s = 7.8\times10^{-5}$ s^{-1} at $B_0 = 230$ G), γ_e and γ_g are density-independent inverse lattice lifetimes for the ground and the excited states. Here, we take $\gamma_e = \gamma_g = 0.33$ s^{-1} as a conservative estimation, which corresponds to 3 s of lattice lifetime. The effective position-dependent pumping rate is denoted by $w(y)$, and the shift and dephasing rates in the pumping zone by $\delta_p(y)$ and $\nu_p(y)$, respectively

The extra density-independent dephasing rate caused by elastic collisions with a background gas and Raman scattering of photons from the optical lattice potential is denoted by γ_R [79]. We have taken $\gamma_R = 0.3\ \mathrm{s}^{-1}$ and define the total rate of collision decoherence as

$$\Gamma^j_{\mathrm{coll}} = n_j \left[\frac{\langle\hat{\sigma}^j_{ee}\rangle\gamma_{ee} + [\langle\hat{\sigma}^j_{gg}\rangle + \langle\hat{\sigma}^j_{ee}\rangle]\gamma_{ge}}{2} + \gamma_{\mathrm{dep}}\langle\hat{\sigma}^j_{gg}\rangle \right] \tag{6.20}$$

and the collisional shift as

$$\Delta^j_{\mathrm{coll}} = n_j[\mu(\langle\hat{\sigma}^j_{ee}\rangle + \langle\hat{\sigma}^j_{gg}\rangle) + \epsilon(\langle\hat{\sigma}^j_{ee}\rangle - \langle\hat{\sigma}^j_{gg}\rangle)] \tag{6.21}$$

Here, we define the loss, dephasing, and shift coefficients as follows: $\gamma_{ee} = (4 \pm 2.5) \times 10^{-12}\ \mathrm{cm}^3/\mathrm{s}$, $\gamma_{ge} = (5.3 \pm 1.9) \times 10^{-13}\ \mathrm{cm}^3/\mathrm{s}$, $\gamma_{\mathrm{dep}} = (3.2 \pm 1.0) \times 10^{-10}\ \mathrm{cm}^3/\mathrm{s}$, $\mu = 2\pi \times 8.2 \cdot 10^{-11}\ \mathrm{cm}^3 \cdot \mathrm{Hz}$, and $\epsilon = 0.33\mu$ [78]. The coefficients μ and ϵ were extracted from [78], where the collisional shift coefficient was measured as $(7.2 \pm 2.0) \times 10^{-17}\ \mathrm{Hz} \times \mathrm{m}^3$ for 35% of excited atom *in the end of* the Rabi pulse, what corresponds to about 31.75% of excited atoms *in average over the pulse*. Also, it was observed a relative influence of about $(2.9 \pm 4.5) \times 10^{-3}$ per percent excitation probability, i.e., per percent of excited atoms after the pulse.

6.3.1 Results of the simulation for the "basic" model

In this section, we present the results of numerical simulations of the superradiant laser output using the semiclassical model described above and with the collisional dephasing rate given by Eq. (6.20) for mHz machine where atoms are traveling in an optical conveyor along a running-wave optical cavity. We assume a total roundtrip length $l_{\mathrm{cav}} = 20$ cm and cavity finesse $\mathcal{F} = 5 \times 10^4$, which gives the decay rate κ of the cavity field energy equal to

$$\kappa = \frac{2\pi c}{\mathcal{F} l_{\mathrm{cav}}} \approx 1.88 \times 10^5\ \mathrm{s}^{-1} \tag{6.22}$$

The output laser power per single intracavity photon can be estimated as $\kappa\hbar\omega\eta \approx 1.34 \times 10^{-14}$ W, where $\omega \approx 2\pi \times 429$ THz is the frequency of the $^1\mathrm{S}_0 \to {}^3\mathrm{P}_0$ transition and η is the fraction of output power emitted through the outcoupling mirror. We assume all four mirrors have equal transparency, which leads to $\eta = 0.25$. The waist W_0 of the superradiant cavity mode is taken as

$$W_0 = W_{\mathrm{conv}}\sqrt{\frac{\lambda}{\lambda_{\mathrm{conv}}}} \approx 130\ \mu\mathrm{m}, \tag{6.23}$$

where $W_{\mathrm{conv}} = 140\ \mu$m is the waist of the moving optical lattice, $\lambda_{\mathrm{conv}} = 813$ nm is the magic wavelength, and $\lambda = 698$ nm is the wavelength of the superradiant mode. The coupling strength g between the atomic transition and the running-wave cavity mode is calculated according to (6.16). With conservative estimation $T = 10\ \mu$K of the temperature of the atomic ensemble, and taking the depth U_{conv} of the optical lattice as

$U_{\mathrm{conv}} = 32\ \mu$K and the spontaneous transition rate $\gamma_s = 7.8 \times 10^{-5}\ \mathrm{s}^{-1}$ corresponding to $B_0 = 230$ G (the value of averaged magnetic field which we have taken for simulation presented in this section), we estimate $g = 0.443\ \mathrm{s}^{-1}$.

The atoms are loaded into the conveyor in the $^1\mathrm{S}_0$ state and get pumped into the upper lasing state, as described in section 5.4. The pumping process was simulated using the following position-dependent incoherent pumping rate $w(y) = w_0 p(y)$, as well as pumping-related dephasing rate $\nu(y) = \nu_0 p(y)$ and light shift $\delta_p(y) = \delta_p^0 p(y)$, where

$$p(y) = \exp\left(-\frac{2(y-y_p)^2}{W_p^2}\right), \tag{6.24}$$

$y_p = 2$ mm, and $W_p = 250\ \mu$m. We take $w_0 = 270\ \mathrm{s}^{-1}$ and $\nu_0 = 400\ \mathrm{s}^{-1}$ as a typical values, see Table in section 6.2. At this point, we set the pumping-induced light shift, $\delta_p^0 = 0$. Later, however, we check that reasonable values of pumping-induced light shift will have only a minor influence on the amplitude and frequency of the output laser field. Using these parameters, we perform a series of simulations of the superradiant laser output for different atomic fluxes Φ. Note that the mean-field equations (6.19) are invariant to a common phase shift of atomic coherence $\sigma_{ge}^j = \langle \hat{\sigma}_{ge}^j \rangle$ and cavity field $a = \langle \hat{a} \rangle$. To break this phase symmetry and initiate the lasing process, we assume that, at the beginning of the simulation, the atomic ensembles in the cavity have some small "seed" coherence: $\sigma_{ee}^j = (1 - \cos(\theta_0))/2$, $\sigma_{gg}^j = (1 + \cos(\theta_0))/2$, $\sigma_{ge}^j = \sin(\theta_0)\exp(i\phi_0^j)$, where $\theta_0 = 0.07$ rad and ϕ_0^j are randomly distributed between 0 and 2π. Here and below we, for the sake of brevity, introduce the short notation $o = \langle \hat{O} \rangle$ for mean values of operators. All the atomic ensembles loaded into the conveyor after that are fully in the upper lasing state, without any "seed" coherence.

In Figure 6.3 (a,b) we present results of simulations of the intracavity photon number n in steady-state and the shift Δ_{out} of the output radiation frequency (with respect to the frequency of $^1\mathrm{S}_0 \to {}^3\mathrm{P}_0$ transition at $B = B_0$) for different values of the atomic flux Φ and magnetic field gradient G_B, see section 6.1, expression (6.3). For the calculations, we vary the atomic flux Φ and the magnetic field gradient G_B. We choose Φ in the range $2.4 \times 10^5\ \mathrm{s}^{-1} \leq \Phi \leq 8 \times 10^6\ \mathrm{s}^{-1}$, which corresponds to the values of parameter $\mathcal{A}$ defined in Appendix A, equation (A.18) in the range $0.173 < \mathcal{A} < 1$ and should produce stable nonzero solutions. We fixed the number of clusters $M = 51$.

The full simulated time is 40 s, but we truncate the first 20 s and use the last 20 s to calculate the characteristics of the signal once stabilized. Only stable solutions, where the variations of the amplitude of the intracavity field over the last half of the simulation period were less than 10 % of the mean, are presented in Fig. 6.3. We can see that for some combinations of (Φ, G_B), the solutions are unstable. Notably, we see no laser output for $\Phi < 2 \times 10^6\,\mathrm{s}^{-1}$, which corresponds to $A > 0.346$. Such an increase of the threshold atomic flux for superradiant emission in comparison with the idealized model is associated with atomic losses and dephasings, as well as position-dependent shifts, which hinder lasing.

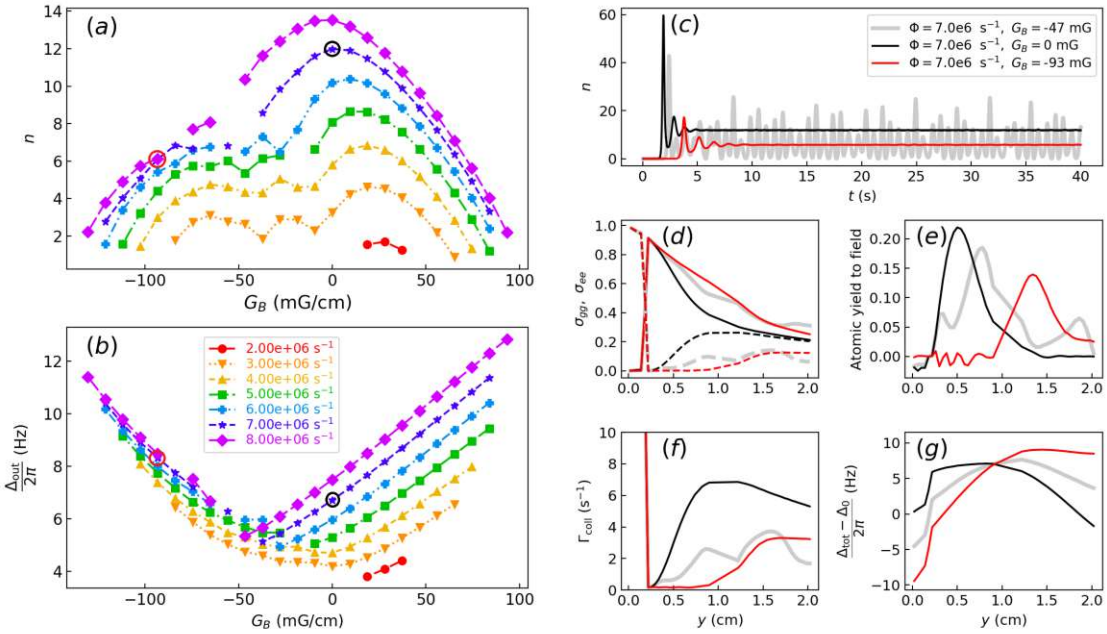

Figure 6.3: Results of superradiant lasing simulation. (a) Simulated intracavity photon numbers, (b) Frequency shifts of the output field, relative to the atomic transition, versus gradient G_B of the magnetic field for different atomic fluxes Φ (see legend; same color code for (a) and (b)). Here we use $B_0 = 230\,\mathrm{G}$ and $\mathcal{F} = 50000$. Circled points correspond to stable solutions investigated in detail in (c) – (g). (c) Examples of intracavity photon number over time for $\Phi = 7 \times 10^6\ \mathrm{s}^{-1}$ and three different values of the magnetic field gradient G_B. (d) Distributions of populations σ_{ee} (solid) and σ_{gg} (dashed) along the conveyor. (e) Distribution of atomic yield to the cavity field a defined as the imaginary part of $\sigma_{ge}\exp[-i\arg(a)]$. (f) Distribution of collision-induced dephasing. (g) Total (magnetic plus collision-induced) shift $\Delta_{\mathrm{tot}} = \Delta(y) + \Delta_{\mathrm{coll}}$ along the conveyor. The color code for (c) – (g) is shown in (c).

To further investigate the lasing process, we perform simulations for $\Phi = 7 \times 10^6\ \mathrm{s}^{-1}$ at three different values of magnetic field gradient: $G_B = -47$ mG, -93 mG, and 0 mG. The simulated time-dependent intracavity photon numbers for these cases are shown in Figure 6.3(c). It is evident that the solutions are stable for $G_B = 0$ mG and -93 mG, while for $G_B = -47$ mG, the intracavity field becomes unstable, exhibiting irregular superradiant pulsations. In Figure 6.3(d), we present the spatial distribution of the ground state (σ^j_{gg}) and excited state (σ^j_{ee}) populations in the emission region at the end of the simulation ($t = 40$ s) for the same parameters. Note that $\sigma_{ee} + \sigma_{gg} < 1$ due to atom loss from the conveyor, as described by equations (6.19). The results indicate that for $G_B = 0$ mG/cm (black curves), atoms return to the ground state more quickly than for $G_B = -47$ mG/cm and $G_B = -93$ mG/cm (gray and red curves, respectively).

This is because, for $G_B = 0$ mG/cm, the atoms are coherently coupled to the cavity field primarily in the first half of the optical conveyor, whereas for $G_B = -93$ mG/cm, they couple in the second half. This behavior aligns with the atomic contribution to the

intracavity field shown in Fig. 6.3(e). In the case of $G_B = -47$ mG/cm (unstable regime), we observe oscillations between the ground and excited states, along with corresponding oscillations in the intracavity field. At the end of the emission zone, it is also evident that σ_{ee} remains larger than σ_{gg} for all three cases, indicating that less than half of the energy stored in the $^1\mathrm{S}_0 \rightarrow {}^3\mathrm{P}_0$ transition is converted into the cavity field's energy.

We define the contribution of single-atom coherence to the intracavity field as $\mathrm{Im}(\sigma_{ge} \exp(-i \arg(a)))$, consistent with Eq. (6.18). Upon closer inspection of the position dependence of this quantity in Fig. 6.3(e), we observe that it aligns with regions where the variation in the overall shift (magnetic plus collision) is minimal. For instance, when $G_B = 0$ mG/cm, the main contribution to the intracavity field comes from atoms in the first half of the emission zone, corresponding to a plateau in the overall shift shown in Fig. 6.3(g). Similarly, for $G_B = -93$ mG/cm, the primary contribution arises from the second half of the emission zone, but since a significant fraction of the atoms have been lost from the conveyor by this point, the signal's amplitude is reduced. In the unstable regime, where $G_B = -47$ mG/cm, we observe random absorption and emission events between the atoms and the cavity field. These energy oscillations lead to chaotic behavior in the out-coupled laser field.

In Fig. 6.3(f,g), we present the position-dependent collisional dephasing rates Γ_{coll} and the total frequency shifts (magnetic and collision-induced) along the length of the optical conveyor. For all three values of G_B, the collisional dephasing rate is highest at the beginning of the emission zone, when the atoms are still in the ground state, but it sharply decreases at $y = 0.2$ cm, as the atoms are pumped into the $^3P_0$ state. The dephasing rate then increases again as the atoms emit and transfered from the excited state back to the ground state. This behavior is consistent with our model, where the dominant source of dephasing is ground state collisions (6.20). Eventually, the dephasing decreases again as the total atomic density decreases due to losses.

Finally, we compare the total position-dependent shift shown in Fig. 6.3(g) with the magnetic shift presented in Fig. 6.1(b) for the same magnetic field gradient to assess the impact of the collision shift on the total shift. The variation of the collision shift along the emission zone is dynamic: it decreases as atoms are lost from the optical conveyor but increases as atoms transition from the excited state back to the ground state. A qualitative comparison of the two plots indicates that the magnetic shift dominates throughout the emission zone, and the variation in collision shift has a minimal effect on the total shift.

We can now estimate the fraction of atoms contributing to the intracavity field and the expected output lasing power for such an experiment. With a flux of 7×10^6 s^{-1}, the maximum power that could, in principle, be emitted into the cavity mode is $\hbar\omega\Phi \approx 2$ pW. We calculate the actual power emitted into the cavity field as $P_{\mathrm{field}} = \hbar\omega\kappa n$. For $G_B = 0$ and $n \approx 11.9$, this results in $P_{\mathrm{field}} = 0.64$ pW. Thus, approximately 32% of the atoms pumped to the excited state contribute to the intracavity field. This can be attributed to the loss of excited-state atoms from the optical conveyor and partial transfers between

the excited and ground states. Consequently, the expected output lasing power on the clock transition under optimal conditions is $P_{\text{out}} = \eta P_{\text{field}} = 0.16$ pW, assuming $\eta = 0.25$.

To assess the sensitivity of the laser output to the pumping-induced light shift δ_p, we conduct additional simulations for $\delta_p^0 = 2\pi \times 25$ Hz, which is a typical estimate of the effective light shift, and $\delta_p^0 = 2\pi \times 500$ Hz, representing a more conservative upper bound. These simulations correspond to the marked points in Fig. 6.3(a,b) (Table 6.2). We find that the stability of solutions with the same Φ and G_B is independent of δ_p^0. For stable regimes, the difference in the amplitude of the intracavity field between solutions with identical Φ and G_B but varying δ_p^0 is less than a few percent. Additionally, the frequency shift of the output field varies by less than 50 mHz when δ_p^0 changes from 0 to 500 Hz, which is near the Fourier-limited resolution of our simulation. This robustness can be attributed to the fact that atoms do not contribute significantly to the intracavity field while being affected by the pumping-induced light shift δ_p, as the pumping zone is approximately 20 times smaller than the emission zone. Moreover, the large dephasing associated with this pumping further mitigates its impact on the output of the superradiant laser.

The quantum noise-limited linewidth of the superradiant output can be estimated using the second-order cumulant expansion [11, 36]. This approach involves clustering the atomic ensemble based on their positions in the optical conveyor and treating the collision-induced shifts, along with loss and dephasing rates, as external parameters. These parameters are pre-calculated using the semiclassical model described earlier. For a flux of $\Phi = 7 \times 10^6$ atoms/s, the quantum noise-limited linewidths are approximately 5 μHz for $G_B = 0$ and 7 μHz for $G_B = -93$ mG/cm. It is important to note that this sub-natural linewidth is achievable only due to the collective superradiant nature of the system and persists despite the inhomogeneous broadening on the Hz level, as shown in Fig. 6.3(g). This noise suppression, on the order of one million, can only be realized in a truly continuous system without any Fourier limitations.

Examining the sensitivity of the output frequency to variations in atomic flux Φ in Fig. 6.3(b), we observe that this sensitivity is minimized for negative values of G_B between -120 mG/cm and -90 mG/cm. Within this range, the shift sensitivity is approximately $2\pi \times 0.3$ Hz per 10^6 atoms/s. Consequently, a mean atomic flux of $\Phi = 7 \times 10^6$ s^{-1} with a 5% fluctuation in atom number would result in an output frequency linewidth broadened by about 100 μHz. These fluctuations appear to be the primary factor limiting the short-term frequency stability of the output laser signal.

6.4 Simulation with full dephasing

Our simulations thus far are based on the model presented in [78], where it is assumed that the primary source of dephasing is elastic collisions with atoms in the $^1S_0$ ground state. According to this model, the ground state dephasing coefficient due to elastic collisions, γ_{dep}, is significantly larger than the loss coefficients associated with inelastic collisions between atoms in the excited state (γ_{ee}) and between ground and excited state

atoms (γ_{ge}), by factors of approximately 100 and 1000, respectively (see section 6.3). Consequently, the impact of dephasing due to elastic collisions with excited state atoms has not been taken into account.

Strictly speaking, such an approximation is acceptable in situation considered in [78], where the fraction of the atoms in the excited state never exceed one third of the total amount of the atoms. However, in our case the atomic sample is fully inverted after the pumping zone, and in the emission zone the fraction of inverted atoms is almost always larger than the fraction of atoms atoms in the ground state, as illustrated in Figure 6.3(d). Therefore, dephasing due to elastic collisions in the excited state cannot be overlooked in our case. In this section, we explore the feasibility of the bad cavity laser using an "extended" dephasing model that includes dephasing due to elastic collisions in the excited state. In the absence of experimental data, we set the dephasing coefficient for the excited state, $\gamma_{\text{dep}} = 3.2 \times 10^{-10}$ cm^3/s, equal to the dephasing coefficient in the ground state. Accurate determination of this coefficient will be in the focus of future experimental studies. It should be noted that dephasing due to elastic collisions between excited and ground-state atoms is still not considered in this model.

To now account for the additional two-body collision dephasing effects, we, instead of (6.20), use the following expression for the collisional dephasing rate:

$$\Gamma^j_{\text{coll}} = n_j \left[\frac{\langle \hat{\sigma}^j_{ee} \rangle \gamma_{ee} + [\langle \hat{\sigma}^j_{gg} \rangle + \langle \hat{\sigma}^j_{ee} \rangle] \gamma_{ge}}{2} + \gamma_{\text{dep}} (\langle \hat{\sigma}^j_{gg} \rangle + \langle \hat{\sigma}^j_{ee} \rangle) \right]. \tag{6.25}$$

With this new dephasing rate, we find that we must increase the bias magnetic field in order to achieve a larger atom-field coupling to obtain steady-state superradiant emission. Here, we choose $B_0 = 574$ G, which is 2.5 times stronger than before. Calculations with COMSOL show almost perfectly proportional scaling of magnetic field deviations $B(y) - B_0$, within 1%. This field corresponds to $\gamma_{^3P_0 \to {}^1S_0} = 6.43 \times 10^{-4}$ s^{-1} $= 2\pi \times 102$ μHz, what, in turn, gives the coupling strength $g = 1.1$ s^{-1} between the atomic transition and the cavity field.

The dependencies of the intracavity photon number and the shift of the output radiation on G_B for stable solutions are shown in Figure 6.4(a,b). In contrast to the dependence depicted in Figure 6.3(a), the intracavity photon number as a function of G_B exhibits two maxima and a broad dip in the range $-180 < G_B < 50$. This behavior is attributed to the proportionally stronger variation in the magnetic shift along the optical conveyor. In Figure 6.4(c-g), we present results of simulations for $\Phi = 4 \times 10^6$ s^{-1} and three different values of the magnetic field gradient, similar to the method used for Figure 6.3. We use a smaller atomic flux than was used in the basic dephasing model, since no stable solutions are obtained for higher values of flux with the extended model. Again, we present two stable (violet and light blue curves) solutions and one unstable (yellow curve) solution. The variation of the position-dependent shift presented in Figure 6.4(g) is much larger than in Figure 6.3(d) due to the proportionally larger inhomogeneity of the magnetic field along the optical conveyor. The maximum steady-state intracavity photon number is $n \approx 6.62$ in Figure 6.4(c), which is 45% lower than the value presented in Figure 6.3(c).

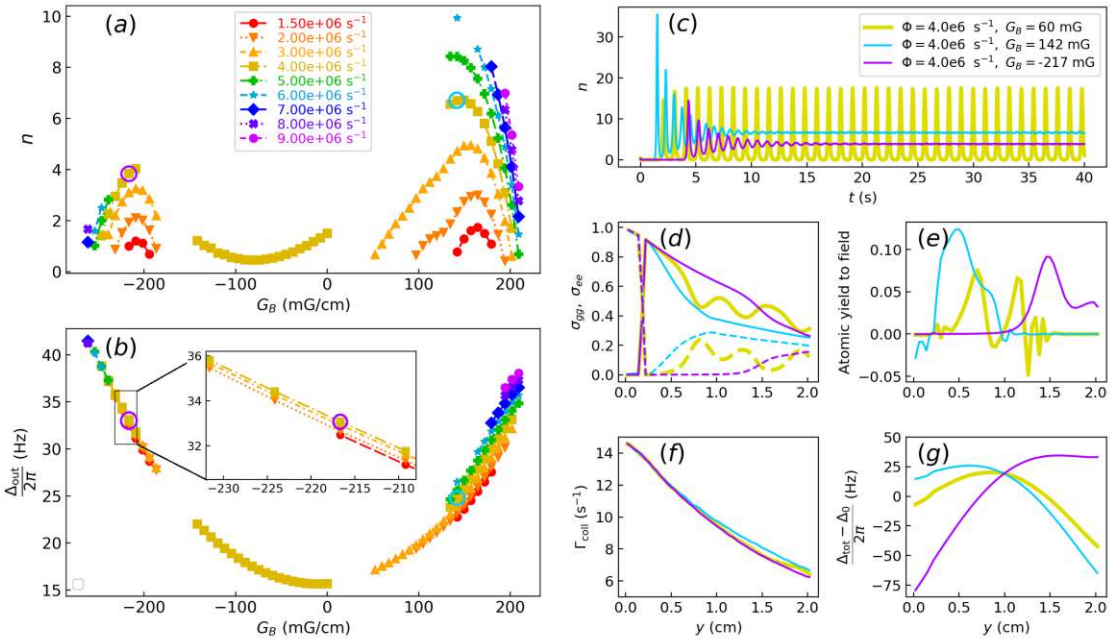

Figure 6.4: Simulation for the full dephasing model. (a) Intracavity photon numbers and (b) frequency shifts of the output field (relative to the atomic transition) depending on magnetic field gradient G_B and atomic flux Φ (see legend). Inset: magnetic field gradient range in which output frequency is least sensitive to flux. Circled points correspond to stable solutions investigated in detail in (c) – (g). (c) Examples of intracavity photon number over time for $\Phi = 4 \times 10^6$ s^{-1} and three different values of the magnetic field gradient G_B. (d) Distributions of populations σ_{ee} (solid) and σ_{gg} (dashed) along the conveyor. (e) Atomic yield to the cavity field a defined as the imaginary part of $\sigma_{ge} \exp[-i\arg(a)]$. (f) Distribution of collision-induced dephasing. (g) Total (magnetic plus collision-induced) shift $\Delta_{\text{tot}} = \Delta(y) + \Delta_{\text{coll}}$ along the conveyor. The color code for (c) – (g) is shown in (c). The magnetic field $B_0 = 574$ G and all other parameters are the same as in Figure (6.3)

This reduction can be partially explained by the 40% lower atomic flux. For such a flux, the maximum power that can be emitted into the cavity mode is $\hbar\omega\Phi \approx 1.14$ pW, whereas the power transferred into the cavity field is about $P_{\text{field}} = 350$ fW for $G_B = 142$ mG/cm, corresponding to a 31% transfer efficiency. As a result, the output laser power $P_{\text{out}} = \eta P_{\text{field}}$ can be estimated as about 90 fW, assuming all mirrors of the cavity have the same reflectivity.

In contrast to the situation presented in Figure 6.3(c), the unstable solution produces relatively regular pulses, rather than a chaotic regime. The dynamics of intracavity populations shown in Figure 6.4(d) demonstrate nearly the same population transfer efficiency for $\Phi = 4.0 \times 10^6$ s^{-1}, $G_B = 142$ mG/cm (light blue curves) as for $\Phi = 7.0 \times 10^6$ s^{-1}, $G_B = 0$ in the basic model (black curves in Figure 6.3(d)). The smaller atomic number density and relatively lower collision losses used in the extended dephasing model lead to the same transfer efficiency, even though the total shift in the emission

zone is larger. The atomic contribution to the intracavity field for the unstable solution (yellow curve in Figure 6.4(e)) shows two strong peaks corresponding to simultaneous lasing at two slightly different frequencies, resulting in pulses. The collision-induced dephasing rate presented in Figure 6.4(f) is nearly proportional to the total population change, whereas in the basic model it is primarily determined by the population of the ground state.

The simulations presented in Figure 6.4 were performed for a pumping-induced light shift δ_p of zero. To test the robustness of the output laser signal against a non-zero shift, we performed simulations for $\delta_p^0 = 2\pi \times 25$ Hz and $\delta_p^0 = 2\pi \times 500$ Hz. Using these two values for the pumping-induced light shift to simulate the generated field for the two marked solutions in Figure 6.4(c), we obtained a stable solution in all four cases. In these cases, the variation in the number n of intracavity photons was less than 1%, and the constant output frequency shift Δ_{out} was smaller than $2\pi \times 50$ mHz. This leads us to the assumption that the pumping zone has a very small influence on the performance of the superradiant laser.

The minimum achievable linewidth of the output radiation at two selected points corresponding to a stable solution for $\Phi = 4 \times 10^6$ s^{-1} and $G_B = 142$ mG/cm is on the order of $2\pi \times 120$ μHz, and for $\Phi = 4 \times 10^6$ s^{-1} and $G_B = -217$ mG/cm, it is on the order of $2\pi \times 50$ μHz. The larger linewidth values compared to those presented in the previous section are due to the greater variations in the position-dependent shift along the optical conveyor. In this case, the collective nature of superradiance again suppresses the inhomogeneous broadening effects in our system by approximately six orders of magnitude, resulting in a linewidth comparable to the natural linewidth, even at this level of inhomogeneity of the bias magnetic field B.

For G_B lying between approximately -230 mG/cm and -210 mG/cm, as shown in Figure 6.4(b), we observe that the output frequency is more robust against variations in the atomic flux Φ than in the case considered in section 6.3.1. Five percent fluctuations in the atom number around $\Phi = 4 \times 10^6$ s^{-1} result in a broadening of approximately 50 mHz, which corresponds to a broadening by a factor of about one thousand compared to the minimum achievable linewidth. From this, we can conclude that in our simulations, fluctuations in the atom number remain the main source of instability for the superradiant laser.

This concludes our discussion on the simulation of the superradiant signal for the mHz machine.

6.5 Outlook

In this chapter, we have focused on the ^{88}Sr isotope due to its high natural abundance and relatively simple internal structure. However, it requires a strong external magnetic field to partially enable the $^1S_0 \rightarrow {}^3P_0$ transition, which leads to unavoidable position-dependent shifts caused by imperfections in the applied magnetic field. Additionally,

significant dephasing and frequency shifts arise from strong s-wave collisions between bosonic atoms. As demonstrated, atom number fluctuations are the primary source of linewidth broadening in our system. Therefore, minimizing these fluctuations is the most straightforward approach to enhancing the frequency stability of the superradiant laser. Improved experimental measurements of dephasing and loss coefficients in both the ground and excited states, as well as collisional-induced shifts, could deepen our understanding and facilitate a more precise numerical optimization of parameters to minimize linewidth broadening effects. Furthermore, reducing magnetic field curvature by balancing opposing curvatures from two coil pairs can help lower the overall position-dependent shift.

Our simulations also suggest that light shifts associated with pumping have minimal impact on the output frequency, as strongly dephased atoms do not contribute to the cavity field during pumping. Therefore, adding an additional repumping zone within the optical conveyor to repopulate the excited state could potentially increase the emitted power.

Alternatively, we could investigate using fermionic ^{87}Sr on the $^1S_0, F = 9/2, m_F = \pm 9/2 \rightarrow {}^3P_0, F = 9/2, m_F = \pm 9/2$ transition in our system (see appendix B for details). Although the more complex internal structure, including hyperfine and Zeeman splitting, would require more sophisticated cooling and pumping schemes, the non-zero clock transition rate and stronger coupling to the cavity, even at zero magnetic field, would reduce the collective atomic number threshold for superradiant emission. Additionally, the suppression of s-wave collisions due to the Pauli exclusion principle could enhance the robustness of the output laser field against fluctuations in atomic flux. This direction remains promising for future theoretical and experimental investigations.

CHAPTER 7

Conclusion

In this thesis we performed a series of calculations towards practical implementation of continuously-operating superradiant laser on $^1S_0 \rightarrow {}^3P_0$ transition in neutral strontium. In the beginning we lay out the theoretical foundations necessary for description of open quantum systems, such as atoms interacting with cooling and pumping fields, atomic ensembles collectively coupled to bath modes, and lasers, particularly the bad-cavity lasers. We start from the description of electromagnetic field in the cavity and its quantization and interaction between the field and a 2-level atom. Then we consider spontaneous transition in the atom due to interaction with modes of thermal bath, as well as Dicke superradiance. The superradiant emission from the ensemble of atoms is faster than the emission of a single atom, because of constructive interference between decay channels of different atoms collectively coupled to the same bath modes. The idea of superradiant laser also can be described as a collective coupling of the atoms to a single mode with the help of the optical cavity. Next, we consider open quantum systems, and introduce the density matrix, master equation, Langevin-Heisenberg equations, as well as some calculation technics such as the Monte-Carlo wavefunction method and semiclassical Monte-Carlo method for simulation of cooling of the atoms.

Further we introduce the most important approximate numerical methods of simulation of the superradiant laser, namely the mean-field approach, the c-number Langevin equations, the cumulant expansion to the second order, and compare these methods with each other as well as with the "full" quantum solution, using quite a simple model of bad-cavity laser with incoherent pumping without inhomogeneous effects. Such a system allows the full quantum treatment for moderate number of atoms (of about 100). We calculated characteristics of the superradiant laser output using these methods, and we concluded that the mean-field approach is an effective approximate method for calculation of the atomic inversion and the intracavity photon number, whereas for calculation of the linewidth the second-order cumulant approach is the better option than c-number Langevin equations. The 2nd-order cumulant approach is more accurate than

the method based on c-number Langevin equations, and it does not require averaging over many trajectories obtained from numerical simulation of stochastic differential equations. However, for inhomogeneous systems divided into M clusters the number of equations is proportional to M^2 for the second-order cumulant approach, and to M in the c-number Langevin approach.

Then, using the 2nd-order cumulant approach we calculated ultimate frequency stability achievable with active optical frequency standards. We analyzed the dependence of the linewidth of a bad-cavity laser with incoherent pumping on its parameters and determined an estimated minimum linewidth and optimal operational parameters for different situations (homogeneous system, system with inhomogeneous atom-cavity coupling, and with inhomogeneous coupling and broadening). We demonstrated that the instability $\sigma_{y,\mathrm{Dick}} \approx 3.8 \times 10^{-17}/\sqrt{\tau[\mathrm{s}]}$ associated with the Dick effect in a passive optical frequency standard, which uses one of the best local oscillators pre-stabilized to a cryogenic Si cavity [3], can be matched by a bad-cavity laser with $N = 10^5$ ^{87}Sr atoms and a coherence time of $T_2 \approx 0.4$ s.

Further we discussed the design of a continuously operating superradiant laser on the $^1\mathrm{S}_0 \rightarrow {}^3\mathrm{P}_0$ transition in ^{88}Sr at the University of Amsterdam, which could serve as a future active optical frequency standard. We discussed the mechanism of continuously cooling, loading and pumping of atoms from a dipole trap into a moving magic wavelength optical conveyor lattice inside a bow-tie cavity, which establishes strong collective coupling between atoms and enables superradiant emission. Simulations indicated highly efficient atom loading for a moving optical lattice at a speed of a few cm per second, with up to 83% of atoms being trapped and pumped into the optical lattice with an average energy slightly above 16 μK.

We then numerically simulated the output of a continuous superradiant laser, considering factors like inhomogenity of magnetic field applied to open the $^1\mathrm{S}_0 \rightarrow {}^3\mathrm{P}_0$ transition in ^{88}Sr, collisional dephasing, shifts and losses, and pumping-induced effects. Two models for collisional decoherence were considered. In the first, based on [78], we assumed that ground state collisions were the primary source of decoherence. Under experimentally realistic conditions, we showed the feasibility of creation of the superradiant laser with an output power of approximately 160 fW and a quantum fluctuation-limited linewidth of a few μHz. The primary limitation on linewidth was broadening due to atomic flux fluctuations, influenced by the collisional shift and redistribution of atomic coherence across emission zones. A five percent fluctuation in atomic number would broaden the linewidth to about 100 mHz. The second model supposes that elastic collisions with the atoms in the excited state also contribute into the dephasing. We showed that stable superradiant lasing requires stronger magnetic field (574 G instead of 230 G), which leads to proportionally stronger variations of the magnetic field and, as a result, to stronger position-dependent shifts. These shifts can be partially mitigated with the help of an extra magnetic field gradient. Interestingly, light shift effects caused by pumping fields were found to be negligible due to strong dephasing of pumped atoms, which disrupts correlations between ground and excited states and shields the cavity field from

interacting with these atoms.

In conclusion, this study shows that creation of continuously-operating superradiant laser on $^1S_0 \rightarrow {}^3P_0$ transition in strontium is technically feasible, and that active optical frequency standard based on such laser could be competitive in short-term stability with current state-of-the-art passive frequency references.

APPENDIX A

Bad cavity laser on optical conveyor: a simple analytical model

Here we discuss a simple analytical model of the superradiant laser based on the optical conveyor. An extended version of this model, including stochastic terms (c-number Langevin equations) has been proposed in [80] for description of the "atomic beam laser", where the flying atoms prepumped into the upper lasing state crosses the cavity. Similar technics for related tasks was also used in earlier papers [81] and [26]. Although this method do not incorporate position-dependent shifts, collisional dephasing, losses and other important real-life effect, it can give us simple expressions for estimation of the atomic flux necessary to initiate the lasing.

First, we consider the atoms interacting with only one cavity mode (co- or counter-propagating with the direction where the atoms are drawn), and jth atom enters the cavity at time t_j in the upper lasing state, and leaves it after time τ. Then the Hamitonian describing such a system can be written, in the properly chosen rotating frame, as

$$\hat{\mathcal{H}} = \hbar \left\{ \Delta_a \sum_{j=1}^{N} \hat{\sigma}_{eg}\hat{\sigma}_{ge} + \delta_c \hat{a}^\dagger \hat{a} + g \sum_{j=1}^{N} \Gamma^j(t) \left(\hat{a}^\dagger \hat{\sigma}_{ge} + \hat{a}\hat{\sigma}_{eg} \right) \right\} \tag{A.1}$$

where g is the coupling strength between the cavity mode and the atomic transition, and the function $\Gamma^j(t)$ describes the introduction and ejection the atoms from the cavity

$$\Gamma^j(t) = \Theta(t - t_j) - \Theta(t - t_j - \tau). \tag{A.2}$$

Here τ is the total time the atom spends in the cavity. If we assume that the typical relaxation of the atom is much less than $1/\tau$, we can neglect these rates and only keep

the cavity field decay rate $\kappa/2$. Then the mean-field equations will take the following form:

$$\begin{aligned}\frac{d}{dt}\langle\hat{a}\rangle =& -\frac{1}{2}(\kappa+2i\delta_c)\langle\hat{a}\rangle - ig\sum_{j=1}^{N}\langle\hat{\sigma}_{ge}^{j}\rangle\Gamma^{j}(t)\\ \frac{d}{dt}\langle\hat{\sigma}_{ge}^{j}\rangle =& -i\Delta_a\langle\hat{\sigma}_{ge}^{j}\rangle + ig\langle\hat{a}\rangle\langle\hat{\sigma}_{ee}^{j}-\hat{\sigma}_{gg}^{j}\rangle\Gamma^{j}(t)\\ \frac{d}{dt}\langle\hat{\sigma}_{ge}^{j}\rangle =& ig(\langle\hat{a}^{\dagger}\rangle\langle\hat{\sigma}_{ge}^{j}\rangle - \langle\hat{a}\rangle\langle\hat{\sigma}_{eg}^{j}\rangle)\Gamma^{j}(t)\end{aligned} \tag{A.3}$$

Instead of treating atoms in the cavity individually, it would be better to introduce macroscopic variables, as we have assumed homogeneity throughout the cavity

$$\begin{aligned}\mathcal{E} &= \langle\hat{a}\rangle\\ \mathcal{M} &= -i\sum_{j}\Gamma_j(t)\langle\hat{\sigma}_{ge}^{j}(t)\rangle\\ \mathcal{N}_e &= \sum_{j}\Gamma_j(t)\langle\hat{\sigma}_{gg}^{j}(t)\rangle\\ \mathcal{N}_g &= \sum_{j}\Gamma_j(t)\langle\hat{\sigma}_{ee}^{j}(t)\rangle\end{aligned} \tag{A.4}$$

Then, using the expression (A.2) If the interval between times t_j of subsequent incomes of atoms is much less than the typical evolution time of the system. and supposing that the atoms enter the cavity in the upper lasing state, we can rewrite the equations (A.3) in terms of these macroscopic variables as

$$\begin{aligned}\frac{d\mathcal{E}}{dt} &= -(\kappa/2+i\delta_c)\,\mathcal{E} + g\mathcal{M}\\ \frac{d\mathcal{M}}{dt} &= i\sum_{j}\Delta(t-t_j-\tau)\langle\hat{\sigma}_{ge}^{j}(t_j+\tau)\rangle - i\Delta_a\mathcal{M} + g(\mathcal{N}_e-\mathcal{N}_g)\mathcal{E}\\ \frac{d\mathcal{N}_e}{dt} &= \sum_{j}\Delta(t-t_j) - \sum_{j}\Delta(t-t_j-\tau)\langle\hat{\sigma}_{ee}^{j}(t_j+\tau)\rangle - g(\mathcal{M}\mathcal{E}^{*}+\mathcal{M}^{*}\mathcal{E})\\ \frac{d\mathcal{N}_g}{dt} &= -\sum_{j}\Delta(t-t_j-\tau)\langle\hat{\sigma}_{gg}^{j}(t_j+\tau)\rangle + g(\mathcal{M}\mathcal{E}^{*}+\mathcal{M}^{*}\mathcal{E})\end{aligned} \tag{A.5}$$

Now, to find the **steady-state solution** for the constant flux Φ of the atoms, we will set $\mathcal{E}=$ constant, and assuming that the flux is constant and the intervals between times t_j of subsequent incomes of atoms is much less than τ. Then we can replace

$$\sum_{j}\Delta(t-t_j-\tau)\approx\sum_{j}\Delta(t-t_j)\approx\Phi. \tag{A.6}$$

Then the atoms will expect Rabi oscillations as shown in section 2.1.7, and their states after time τ in the cavity will look like

$$\begin{aligned}
\hat{\sigma}^j_{ee}(t_j+\tau) &\equiv A(\mathcal{E},\Delta_a) = \cos^2\frac{\Omega\tau}{2} + \frac{\Delta_a^2}{\Omega^2}\sin^2\frac{\Omega\tau}{2} \\
\hat{\sigma}^j_{gg}(t_j+\tau) &\equiv B(\mathcal{E},\Delta_a) = 1 - A(\mathcal{E},\Delta_a) = \frac{4g^2\mathcal{E}^2}{\Omega^2}\sin^2\frac{\Omega\tau}{2} \\
\hat{\sigma}^j_{ge}(t_j+\tau) &\equiv C(\mathcal{E},\Delta_a) = \frac{2g\mathcal{E}\Delta_a}{\Omega^2}\sin^2\frac{\Omega\tau}{2} + i\frac{2g\mathcal{E}}{\Omega}\sin\frac{\Omega\tau}{2}\cos\frac{\Omega\tau}{2}
\end{aligned} \tag{A.7}$$

where $\Omega = \sqrt{\Delta_a^2 + 4g^2\mathcal{E}^2}$. We suppose that $\mathcal{E}$ is real non-negative. Then the set equations (A.5) for the steady-state solution of the macroscopic variables can be rewritten as

$$\begin{aligned}
\frac{d\mathcal{E}}{dt} &= 0 = -(\kappa/2 + i\delta_c)\,\mathcal{E} + g\mathcal{M} \\
\frac{d\mathcal{M}}{dt} &= 0 = i\Phi C(\mathcal{E},\Delta_a) - i\Delta_a\mathcal{M} + g(\mathcal{N}_e - \mathcal{N}_g)\mathcal{E} \\
\frac{d\mathcal{N}_e}{dt} &= 0 = \Phi B(\mathcal{E},\Delta_a) - g(\mathcal{M}\mathcal{E}^* + \mathcal{M}^*\mathcal{E}) = -\frac{d\mathcal{N}_g}{dt}
\end{aligned} \tag{A.8}$$

From the first of equations (A.8) follows

$$\mathcal{M} = \frac{\kappa + 2i\delta_c}{2g}\mathcal{E} \quad \Rightarrow \quad \mathcal{M} + \mathcal{M}^* = \frac{\mathcal{E}\kappa}{g} \Rightarrow \Phi B = \mathcal{E}^2\kappa, \tag{A.9}$$

or

$$\frac{4\Phi g^2}{\Omega^2}\sin^2\frac{\Omega\tau}{2} = \kappa. \tag{A.10}$$

Introducing $\chi = \Omega\tau/2$, we obtain an equation

$$\sin^2\chi = \frac{\chi^2\kappa}{\Phi g^2\tau^2}, \quad \text{or} \quad \chi \pm \sqrt{\frac{\Phi g^2\tau^2}{\kappa}}\sin\chi = 0. \tag{A.11}$$

Equation (A.11) may have different number of solutions depending on $\Phi g^2\tau^2/\kappa$. Particularly, if $\Phi g^2\tau^2 < \kappa$, non-zero solutions do not exist. In turn, a single solution exists if

$$1 < \frac{\Phi g^2\tau^2}{\kappa} < 21.19072856... \tag{A.12}$$

To find Ω at given Φ, g and τ, one need to solve equation (A.11) numerically with respect to χ, and then calculate Ω as $2\chi/\tau$. Then it is straightforward to calculate A, B, and C.

To calculate $\mathcal{E}$, it is necessary to find also Δ_a, so we take the imaginary part of the 2nd equation from (A.8):

$$\Phi \cdot \mathrm{Im}(C) = \Delta_a \mathrm{Im}(\mathcal{M}) + g\mathcal{E}(\mathcal{N}_e - \mathcal{N}_g). \tag{A.13}$$

Then, using (A.9), we get, after some algebra

$$\Delta_a \delta_c = \Phi g^2 \left[\mathcal{N}_g - \mathcal{N}_e + \frac{\Phi}{\Omega} \sin(\Omega\tau) \right]. \tag{A.14}$$

For Rabi oscillations we have

$$\begin{aligned} \mathcal{N}_g - \mathcal{N}_e &= \Phi \int_0^\tau (2\hat{\sigma}_{gg}(t) - 1) dt \\ &= \Phi \int_0^\tau \left(\frac{8g^2\mathcal{E}^2}{\Omega^2} \sin^2 \frac{\Omega t}{2} - 1 \right) dt = -\Phi \left[\frac{\Delta_a^2 \tau}{\Omega^2} + \frac{4g^2\mathcal{E}^2}{\Omega^3} \sin(\Omega\tau) \right]. \end{aligned} \tag{A.15}$$

Then we express $\mathcal{N}_g - \mathcal{N}_e$ from (A.14), substitute it into (A.15). Then, using the definition of Ω we arrive, after some algebra, to the equation for δ_c:

$$\delta_c = \frac{g^2 \Phi \Delta_a}{\Omega^2} \left(\frac{\sin(\Omega\tau)}{\Omega} - \tau \right). \tag{A.16}$$

Introducing the detuning Δ_0 of the cavity from the atomic transition $\Delta_0 = \delta_c - \Delta_a$, we get

$$\Delta_a = -\frac{\Delta_0}{1 + \frac{g^2\Phi}{\Omega^2} \left(\tau - \frac{\sin(\Omega\tau)}{\Omega} \right)}. \tag{A.17}$$

Therefore, to find the steady-state cavity field, one need, first, find $\Omega = 2\chi/\tau$ from the equation (A.11), then find Δ_a using (A.17) and, finally, find the steady-state cavity field as $\mathcal{E} = \sqrt{\Omega^2 - \Delta_a^2}/(2g)$. If $|\Delta_a| \geq \Omega$, there are no non-zero steady-state solutions.

For convenient estimation of the number of possible steady-state solutions in the resonant or near-resonant case (i.e., when $|\Delta_a - \delta_c| \ll \kappa$), we define a parameter called $\mathcal{A}$ as

$$\mathcal{A} = \sqrt{\frac{\kappa}{\Phi g^2 \tau^2}} \tag{A.18}$$

One can easily see that the number of solutions of equation (A.11) is determined by the value of $\mathcal{A}$. Particularly, one can find that for

$$\begin{aligned} 1 < \mathcal{A} &: \text{ 0 solutions,} \\ 0.21723 < \mathcal{A} < 1 &: \text{ 1 solution,} \\ 0.12837 < \mathcal{A} < 0.21723 &: \text{ 2 solutions,} \\ 0.091325 < \mathcal{A} < 0.12837 &: \text{ 3 solutions,} \\ &\text{etc.} \end{aligned} \tag{A.19}$$

APPENDIX B

Mean-field model of optical conveyor laser on Sr-87

The bulk of this appendix has been presented as part of [32]

The nucleus of ^{87}Sr has a non-zero magnetic moment and a total spin $I = 9/2$. The hyperfine interaction between the nuclear and electronic moments leads to a mixing of the $^3P_0$ and $^3P_1$ states. Consequently, single-photon transitions are slightly allowed in fermionic ^{87}Sr, eliminating the need for a strong external magnetic field. A weak magnetic field of about 1 G is employed to lift the degeneracy, thereby preventing undesirable coherent effects between different Zeeman substates of the upper and lower lasing states.

The differential Zeeman shift between Zeeman sublevels of the $^3P_0$ and $^1S_0$ states with equal projection m of the total momentum onto the quantization axis is given by $2\pi \times 108.4$ Hz/G $\times\, m \times B$ [82]. The atoms can be pumped into the stretched states with $m = \pm 9/2$. The bad-cavity laser can operate simultaneously on both of these transitions.

The mean-field equation for the cavity field a (co-propagating with the optical conveyor) is

$$\frac{da}{dt} = -\left[\frac{\kappa}{2} + i\delta\right]a - ig\sum_j(\sigma_{ge}^{-,j} + \sigma_{ge}^{+,j}), \tag{B.1}$$

where δ is the detuning of the running-wave cavity mode from the resonance with (unperturbed) $^1S_0 \rightarrow {}^3P_0$ transition in ^{87}Sr atom (including the Doppler shift), and the sum is taken over all the atoms within the conveyor. We neglect the counter-propagating field because it will be out of resonance due to the first-order Doppler shift, and the atoms will get synchronized in favor of coherent interaction with the co-propagating mode. Additionally, we assume that the cavity field is linearly polarized and collinear with the external magnetic field (in π-polarization) and that there is no field with orthogonal

polarization. Such a field can be neglected if, for example, it is out of resonance due to the polarization-dependent effective cavity length.

This setup, combined with the preparation of the atoms initially in two stretched states $m_f = \pm 1/2$, allows us to reduce the effective model of the atom to four levels $|e^{\pm}\rangle$, $|g^{\pm}\rangle$ if spin-exchange processes are also neglected. We use the standard notation $\sigma^{\pm}_{xy} = |x^{\pm}\rangle\langle y^{\pm}|$.

Similiar to how it has been done in section 6.18, one can perform adiabatic elimination of the cavity field

$$a = \frac{-2ig}{\kappa + 2i\delta} \sum_j (\sigma^{-,j}_{ge} + \sigma^{+,j}_{ge}) N^j \tag{B.2}$$

Where N^j is a number of the atoms in the jth cluster. Equations for coherences $\sigma^{\pm,j}_{xy} = \langle \sigma^{\pm,j}_{xy} \rangle$ of individual atoms are

$$\begin{aligned}
\frac{d\sigma^{\pm,j}_{ge}}{dt} &= -\left[\frac{R + \gamma_s + \Gamma_e + \Gamma_g + \Gamma^{\pm,j}_{e,scat}}{2} + \gamma_R + i\Delta^{\pm,j}\right]\sigma^{\pm,j}_{ge} \\
&\quad + iga\left(\sigma^{\pm,j}_{ee} - \sigma^{\pm,j}_{gg}\right) \\
\frac{d\sigma^{\pm,j}_{ee}}{dt} &= -ig\left[a\sigma^{\pm,j}_{eg} - a^*\sigma^{\pm,j}_{ge}\right] - (\gamma_e + \Gamma^{\pm,j}_{e,scat} + \gamma_s)\sigma^{\pm,j}_{ee}, \\
\frac{d\sigma^{\pm,j}_{gg}}{dt} &= ig\left[a\sigma^{\pm,j}_{eg} - a^*\sigma^{\pm,j}_{ge}\right] + \gamma_s\sigma^{\pm,j}_{ee} - \Gamma_g\sigma^{\pm,j}_{gg}
\end{aligned} \tag{B.3}$$

Collisional shifts $\Delta^{\pm,j}$ and decay rates $\Gamma^{j,\pm}_e$ have been extracted from [83–85]

$$\begin{aligned}
\Delta^{\pm,j} &= \Delta^{\pm,j}_{\text{scat}} \pm 2\pi \cdot \frac{9}{2} \cdot 108.4\,\text{Hz} \cdot B[\text{G}]; \\
\Delta^{\pm,j}_{\text{scat}} &= (\overline{C}(\sigma^{j,\pm}_{ee} + \sigma^{j,\pm}_{gg}) + \overline{\chi}(\sigma^{j,\pm}_{ee} - \sigma^{j,\pm}_{gg}) \\
&\quad + \overline{\Lambda}\sigma^{j,\mp}_{gg} + \overline{M}\sigma^{j,\mp}_{ee})\frac{N^j}{N^j_s}
\end{aligned} \tag{B.4}$$

where N^j is the number of atoms in jth group, N^j_s is the number of optical lattice antinodes in this group (number of sites), and coefficients

$$\begin{aligned}
\overline{C} &= \frac{b^3_{ee} - b^3_{gg}}{2}\langle P\rangle, \quad \overline{\chi} = \frac{b^3_{ee} + b^3_{gg} - 2{b^+_{eg}}^3}{2}\langle P\rangle, \\
\overline{\Lambda} &= \frac{a^+_{eg} + a^-_{eg} - 2a_{gg}}{4}\langle S\rangle + \frac{{b^+_{eg}}^3 + {b^-_{eg}}^3 - 2{b_{gg}}^3}{4}\langle P\rangle, \\
\overline{M} &= \frac{2a_{ee} - a^+_{eg} - a^-_{eg}}{4}\langle S\rangle + \frac{2{b_{ee}}^3 - {b^+_{eg}}^3 + {b^-_{eg}}^3}{4}\langle P\rangle.
\end{aligned} \tag{B.5}$$

Here a is s-scattering length; b^3 is p-scattering volume, coefficients $\langle S\rangle$ and $\langle P\rangle$ are $s-$ and p-wave matrix elements averaged over thermal distribution. We have recalculated

these dependencies on temperature and parameters of the lattice potential from [83], supposing that the atoms are in the lowest vibrational state in the axial direction:

$$\begin{aligned} a_0^3\langle P\rangle &= 3.35\times 10^7\,\mathrm{s}^{-1}\left(\frac{\omega_R}{2\pi\times 600\,\mathrm{Hz}}\right)^2\sqrt{\frac{\omega_z}{2\pi\times 8\times 10^4\,\mathrm{Hz}}},\\ a_0^3\langle S\rangle &= 0.08\frac{s^{-1}}{T[\mu\mathrm{K}]}\left(\frac{\omega_R}{2\pi\times 600\,\mathrm{Hz}}\right)^2\sqrt{\frac{\omega_z}{2\pi\times 8\times 10^4\,\mathrm{Hz}}}. \end{aligned} \tag{B.6}$$

Here ω_R and ω_z are radial and axial oscillation frequencies of the Sr atom in the trap site, and a_0 is the Bohr radius.

Also, we extracted collision-induced loss rate from [86]

$$\Gamma_{e,\mathrm{scat}}^{\pm,j} = \frac{N^j}{V_{\mathrm{eff}}N_s^j}\left(\gamma_{ee}\sigma_{ee}^{\pm,j} + K_{ee}\sigma_{ee}^{\mp,j}\right), \tag{B.7}$$

where the effective volume V_{eff} can be calculated using (6.15).

It is important to note that atoms can occupy higher-lying vibrational states. Our model considers only averaged shifts, whereas, in reality, different atoms will experience different collisional shifts depending on their oscillatory states; see more details in [83, 84]. However, since these shifts are relatively small compared to the lifetime of the atoms in the trap, it is expected that this inhomogeneous broadening will not significantly affect the lasing process, and only the averaged shift may play a role.

This model is instrumental in understanding the macroscopic properties of the atomic ensemble and serves as a foundational tool for further theoretical and experimental investigations into superradiant systems with ^{87}Sr.

APPENDIX C

Experimental update

Currently, our collaborators at university of Amsterdam have assembled the whole setup of mHz machine and they have succesfully demonstrated a flux of approximatly 10^8 atoms in the 3-D Red MOT and they are planning to implement the bloch accelerator for the transport of atoms to the Science Chamber. Next step is to setup the molasses beams for cooling. Below I present some of there results

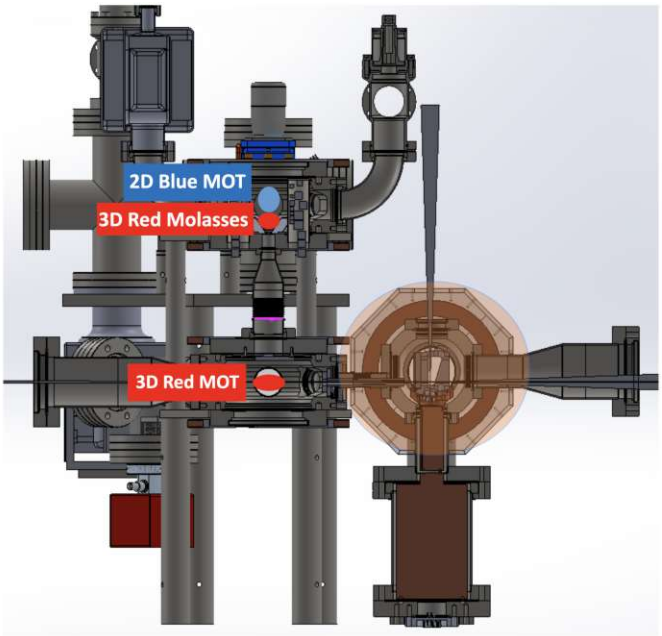

Figure C.1: The architecture of the apparatus. In the Red MOT chamber, the atoms falling down from Blue MOT are continuously collected and cooled. From there, they are loaded into a dipole guide beam formed by a single pass 1070 nm beam.

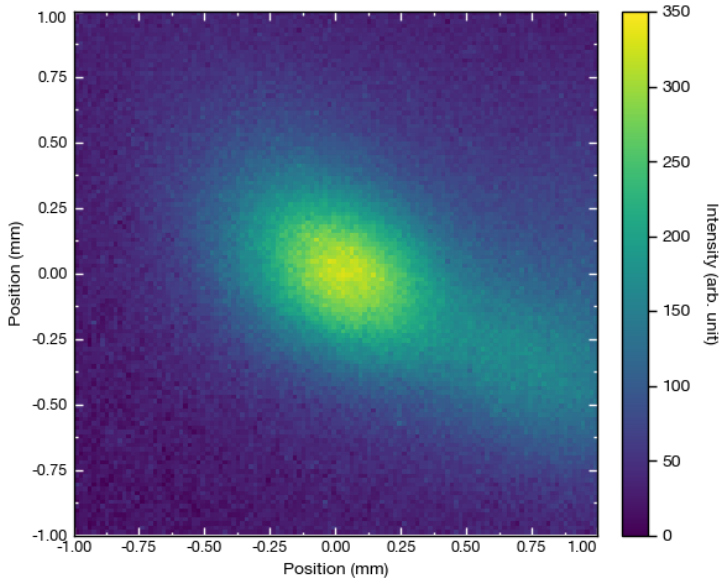

Figure C.2: Trapped cloud in 2-D Blue MOT.

Absorption pictures are taken by switching off the trap rapidly and let the cloud fall under the influence of gravity at different t from this the change in width is extracted. Value of temperature is extracted via

$$\sigma(t) = \sqrt{\sigma_0^2 + k_B T t^2/m} \tag{C.1}$$

Where σ is the phase space density, for details of 2-D Blue MOT see[87] and [88] .

For the 3-D Red MOT we have a double Red MOT with a single frequency Red MOT (700 KHz 700 KHz red detuned to the spectrum.) above the broad modulated multi frequency (modulated for all the beams with 0.9-2.5 MHz red detuned, modulation 50kHz) one constructed with two set of retro reflected beams in the horizontal direction and one beam shooting upwards against gravity. Because of the detuning of the frequency Red MOT, the atoms balance at different location, where the light-induced force equals with gravity. The location depends on resonance with the vertical Red MOT beam and the position of the zero position of the quadrupole field.

MOT loading time is given by

$$N_{MOT}(t) = (1 - e^{-t/\tau})L\tau \tag{C.2}$$

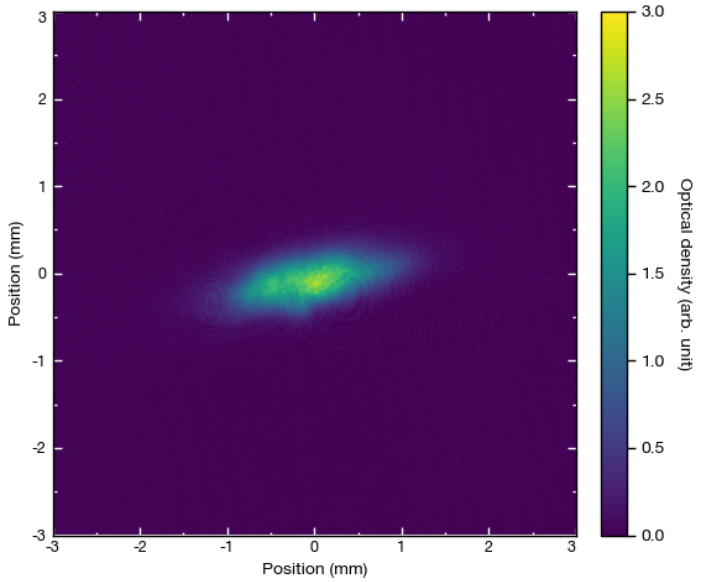

Figure C.3: Pulsed 3-D single frequency Red MOT.

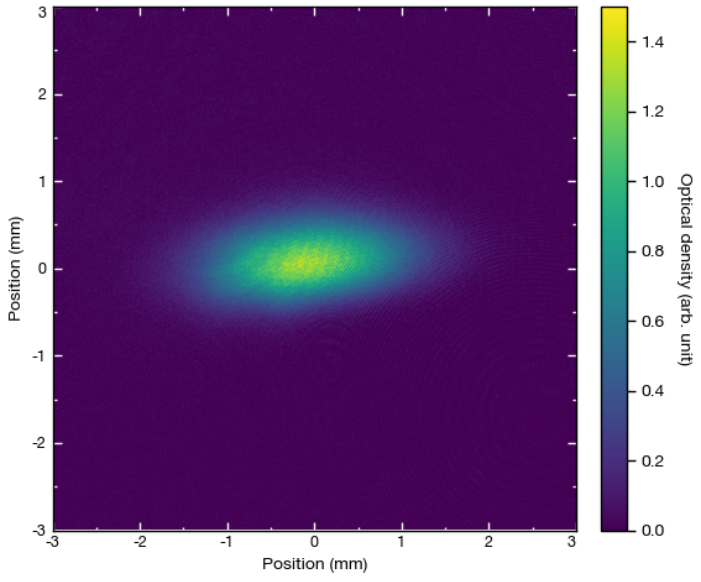

Figure C.4: Trapped cloud in continuous 3-D broadband Red MOT.

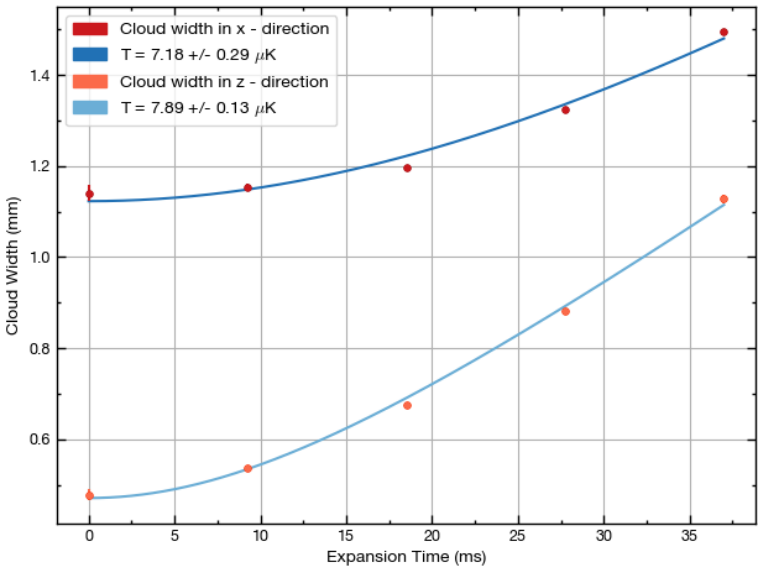

Figure C.5: Characterization of broadband Red MOT.

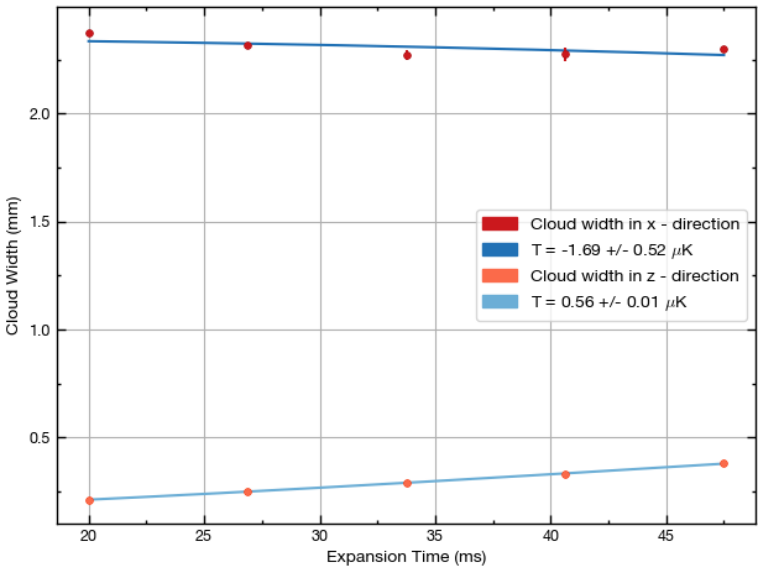

Figure C.6: Characterization of single frequency Red MOT

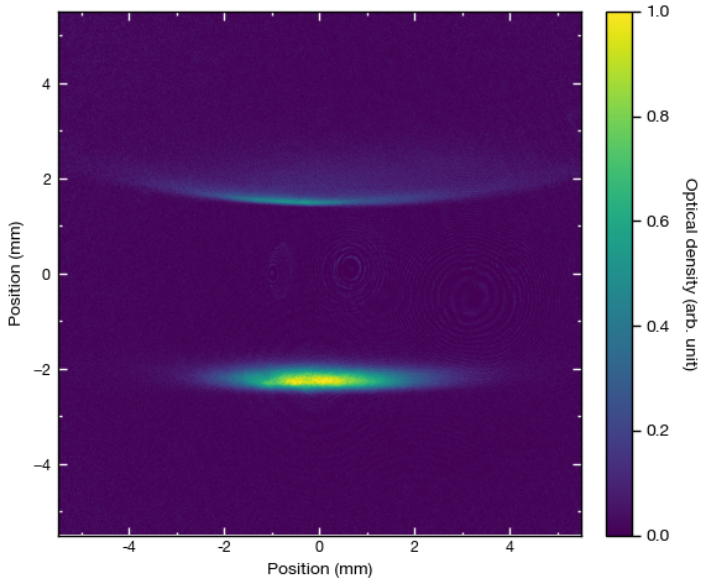

Figure C.7: Single and broadband MOT at the same time but spaced apart

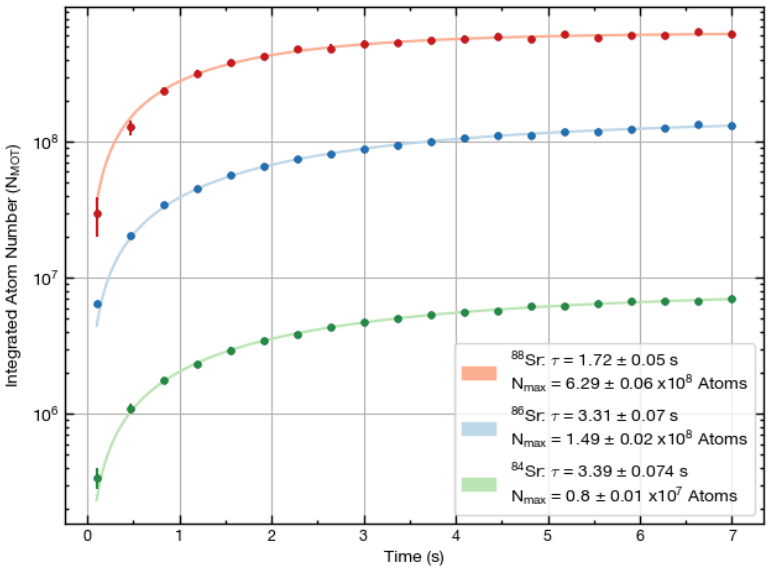

Figure C.8: MOT loading time for different isotopes.

Bibliography

[1] Norman F. Ramsey. „History of atomic clocks“. In: *Journal of Research of the National Bureau of Standards* 88 (1983), p. 301.

[2] Louis Essen and J. V. L. Parry. „The caesium resonator as a standard of frequency and time“. In: *Philosophical Transactions of the Royal Society of London A: Mathematical, Physical and Engineering Sciences* 250.973 (1957), pp. 45–69. DOI: 10.1098/rsta.1957.0009.

[3] Eric Oelker, R. Hutson, C. Kennedy, et al. „Demonstration of 4.8×10^{-17} stability at 1 s for two independent optical clocks“. In: *Nature Photonics* 13 (Oct. 2019). DOI: 10.1038/s41566-019-0493-4.

[4] Barry C. Barish and Rainer Weiss. „LIGO and the detection of gravitational waves“. In: *Physics Today* 52 (1999), pp. 44–50.

[5] S. Blatt, A. D. Ludlow, G. K. Campbell, et al. „New Limits on Coupling of Fundamental Constants to Gravity Using ^{87}Sr Optical Lattice Clocks“. In: *Phys. Rev. Lett.* 100 (14 Apr. 2008), p. 140801. DOI: 10.1103/PhysRevLett.100.140801.

[6] Dhruv Kedar, Jialiang Yu, Eric Oelker, et al. „Frequency stability of cryogenic silicon cavities with semiconductor crystalline coatings“. en. In: *Optica* 10.4 (Apr. 2023), p. 464. DOI: 10.1364/OPTICA.479462.

[7] Jialiang Yu, Sebastian Häfner, Thomas Legero, et al. „Excess Noise and Photoinduced Effects in Highly Reflective Crystalline Mirror Coatings“. en. In: *Physical Review X* 13.4 (Oct. 2023), p. 041002. DOI: 10.1103/PhysRevX.13.041002.

[8] G. John Dick. „Local oscillator induced instabilities in trapped ion frequency standards“. In: *Proceedings of* 19^{th} *Annu. Precise Time and Time Interval Meeting, Redendo Beach, 1987*. Washington, DC: U.S. Naval Observatory, 1988, pp. 133–147.

[9] D. Meiser, Jun Ye, D. R. Carlson, et al. „Prospects for a Millihertz-Linewidth Laser“. In: *Phys. Rev. Lett.* 102 (16 Apr. 2009), p. 163601. DOI: 10.1103/PhysRevLett.102.163601.

[10] JingBiao Chen. „Active optical clock“. In: *Chinese Science Bulletin* 54.3 (Feb. 2009), pp. 348–352. DOI: 10.1007/s11434-009-0073-y.

[11] Georgy A. Kazakov, Swadheen Dubey, Anna Bychek, et al. „Ultimate stability of active optical frequency standards“. In: *Phys. Rev. A* 106 (5 Nov. 2022), p. 053114. DOI: 10.1103/PhysRevA.106.053114.

[12] Walter R. Johnson. *Atomic Structure Theory: Lectures on Atomic Physics*. Springer, 2007.

[13] David J. Griffiths. *Introduction to Electrodynamics*. 3rd. Upper Saddle River, NJ: Prentice Hall, 1999.

[14] Thanu Padmanabhan. *Quantum Field Theory: The Why, What and How*. 1st ed. Graduate Texts in Physics. New York: Springer International Publishing, 2016.

[15] J.J. Sakurai and Jim Napolitano. *Modern Quantum Mechanics*. Revised edition. Addison-Wesley, 1994.

[16] R. H. Dicke. „Coherence in Spontaneous Radiation Processes“. In: *Phys. Rev.* 93 (1 Jan. 1954), pp. 99–110. DOI: 10.1103/PhysRev.93.99.

[17] Heinz-Peter Breuer and Francesco Petruccione. *The Theory of Open Quantum Systems*. Oxford University Press, Jan. 2007. DOI: 10.1093/acprof:oso/9780199213900.001.0001.

[18] R. Dum, P. Zoller, and H. Ritsch. „Monte Carlo simulation of the atomic master equation for spontaneous emission“. In: *Phys. Rev. A* 45 (7 Apr. 1992), pp. 4879–4887. DOI: 10.1103/PhysRevA.45.4879.

[19] Klaus Mølmer, Yvan Castin, and Jean Dalibard. „Monte Carlo wave-function method in quantum optics“. In: *J. Opt. Soc. Am. B* 10.3 (Mar. 1993), pp. 524–538. DOI: 10.1364/JOSAB.10.000524.

[20] *Documentation of QuantumOptics.jl*. https://docs.qojulia.org/. Accessed: March 1, 2024.

[21] Crispin Gardiner and Peter Zoller. *The Quantum World of Ultra-Cold Atoms and Light Book II: The Physics of Quantum-Optical Devices*. IMPERIAL COLLEGE PRESS, 2015. DOI: 10.1142/p983. eprint: https://worldscientific.com/doi/pdf/10.1142/p983.

[22] M.O. Scully and M.S. Zubairy. *Quantum optics*. Cambridge University Press, 1997.

[23] C. W. Gardiner and M. J. Collett. „Input and output in damped quantum systems: Quantum stochastic differential equations and the master equation“. In: *Phys. Rev. A* 31 (6 June 1985), pp. 3761–3774. DOI: 10.1103/PhysRevA.31.3761.

[24] Kamanasish Debnath, Yuan Zhang, and Klaus Mølmer. „Lasing in the superradiant crossover regime“. In: *Phys. Rev. A* 98 (6 Dec. 2018), p. 063837. DOI: 10.1103/PhysRevA.98.063837.

[25] F. Riehle. *Frequency Standards: Basics and Applications*. Wiley, 2006.

[26] Claus Benkert, M. O. Scully, J. Bergou, et al. „Role of pumping statistics in laser dynamics: Quantum Langevin approach“. In: *Phys. Rev. A* 41 (5 Mar. 1990), pp. 2756–2765. DOI: 10.1103/PhysRevA.41.2756.

[27] G. A. Kazakov and T. Schumm. „Active optical frequency standard using sequential coupling of atomic ensembles“. In: *Phys. Rev. A* 87 (1 Jan. 2013), p. 013821. DOI: 10.1103/PhysRevA.87.013821.

[28] D. A. Tieri, Minghui Xu, D. Meiser, et al. *Theory of the crossover from lasing to steady state superradiance*. 2017. eprint: arXiv:1702.04830.

[29] David Tieri. „Open Quantum Systems with Applications to Precision Measurements“. PhD thesis. University of Colorado: Department of Physics, 2015.

[30] Ryōgo Kubo. „Generalized cumulant expansion method“. In: *Journal of the Physical Society of Japan* 17 (1962), pp. 1100–1120.

[31] David Plankensteiner, Christoph Hotter, and Helmut Ritsch. „QuantumCumulants.jl: A Julia framework for generalized mean-field equations in open quantum systems“. In: *Quantum* 6 (Jan. 2022), p. 617. DOI: 10.22331/q-2022-01-04-617.

[32] G. Kazakov, A. Bychek, Chr. Hotter, et al. *iqClock project. Deliverable D6.5: Summary report on quantitative computational models*. "https://cordis.europa.eu/project/id/820404/results". 2022.

[33] Stephan Hartmann. *Generalized Dicke States*. 2012. arXiv: 1201.1732 [quant-ph].

[34] G. A. Kazakov and T. Schumm. „Active optical frequency standards using cold atoms: Perspectives and challenges“. In: *2014 European Frequency and Time Forum (EFTF)*. 2014, pp. 411–414. DOI: 10.1109/EFTF.2014.7331523.

[35] Christoph Hotter, David Plankensteiner, Georgy Kazakov, et al. „Continuous multi-step pumping of the optical clock transition in alkaline-earth atoms with minimal perturbation“. In: *Opt. Express* 30.4 (Feb. 2022), pp. 5553–5568. DOI: 10.1364/OE.445976.

[36] A Bychek, C Hotter, D Plankensteiner, et al. „Superradiant lasing in inhomogeneously broadened ensembles with spatially varying coupling“. In: *Open Research Europe* 1.73 (2021). DOI: 10.12688/openreseurope.13781.2.

[37] G. A. Kazakov and T. Schumm. „Stability analysis for bad cavity lasers using inhomogeneously broadened spin-1/2 atoms as a gain medium“. In: *Phys. Rev. A* 95 (2 Feb. 2017), p. 023839. DOI: 10.1103/PhysRevA.95.023839.

[38] M. C. Teich and R. Y. Yen. „On the Signal-to-Noise Ratio for Optical Heterodyne Detection“. In: *J. Appl. Phys.* 43.5 (1972), pp. 2480–2481. DOI: 10.1063/1.1661538.

[39] Enrico Rubiola. „On the measurement of frequency and of its sample variance with high-resolution counters“. In: *Rev. Sci. Instrum.* 76 (2005), p. 054703. DOI: 10.1063/1.1898203.

[40] Samuel T. Dawkins, John J. McFerran, and André N. Luiten. „Considerations on the measurement of the stability of oscillators with frequency counters“. In: *IEEE Trans. Ultrason. Ferroelectr. Freq. Control* 54 (2007), pp. 918–925. DOI: 10.1109/TUFFC.2007.337.

[41] Juan A. Muniz, Dylan J. Young, Julia R. K. Cline, et al. *Cavity-QED determination of the natural linewidth of the ^{87}Sr millihertz clock transition with 30 μHz resolution*. 2020. arXiv: 2007.07855 [physics.atom-ph].

[42] Sergey G. Porsev and Andrei Derevianko. „Hyperfine quenching of the metastable $^3P_{0,2}$ states in divalent atoms“. In: *Phys. Rev. A* 69 (4 Apr. 2004), p. 042506. DOI: 10.1103/PhysRevA.69.042506.

[43] A. Gogyan, G. Kazakov, M. Bober, et al. „Characterisation and feasibility study for superradiant lasing in 40Ca atoms“. In: *Opt. Express* 28.5 (Mar. 2020), pp. 6881–6892. DOI: 10.1364/OE.381991.

[44] Andrew D Ludlow, Martin M Boyd, Jun Ye, et al. „Optical atomic clocks“. In: *Reviews of Modern Physics* 87.2 (2015), p. 637.

[45] Sören Dörscher, Roman Schwarz, Ali Al-Masoudi, et al. „Lattice-induced photon scattering in an optical lattice clock“. In: *Phys. Rev. A* 97 (Feb. 2018), p. 063419. DOI: 10.1103/PhysRevA.97.063419.

[46] Pierre Lemonde and Peter Wolf. „Optical lattice clock with atoms confined in a shallow trap“. In: *Phys. Rev. A* 72 (3 Sept. 2005), p. 033409. DOI: 10.1103/PhysRevA.72.033409.

[47] Ross B. Hutson, Akihisa Goban, G. Edward Marti, et al. „Engineering Quantum States of Matter for Atomic Clocks in Shallow Optical Lattices“. In: *Phys. Rev. Lett.* 123 (12 Sept. 2019), p. 123401. DOI: 10.1103/PhysRevLett.123.123401.

[48] M. Schioppo, R. C. Brown, W. F. McGrew, et al. „Ultra-stable optical clock with two cold-atom ensembles“. In: *Nature Photonics* 11 (2017), pp. 48–52. DOI: 10.1038/nphoton.2016.231.

[49] Tetsushi Takano, Masao Takamoto, Ichiro Ushijima, et al. „Geopotential measurements with synchronously linked optical lattice clocks“. In: *Nature Photonics* 10 (2016), pp. 662–666. DOI: 10.1038/nphoton.2016.159.

[50] Tobias Bothwell, Colin J. Kennedy, Alexander Aeppli, et al. „Resolving the gravitational redshift across a millimetre-scale atomic sample“. In: *Nature* 602.7897 (2022), pp. 420–424. DOI: 10.1038/s41586-021-04349-7.

[51] May E. Kim, William F. McGrew, Nicholas V. Nardelli, et al. *Optical coherence between atomic species at the second scale: improved clock comparisons via differential spectroscopy.* arXiv:2109.09540 [physics.atom-ph]. Sept. 2021. DOI: 10.48550/arXiv.2109.09540.

[52] Sören Dörscher, Ali Al-Masoudi, Marcin Bober, et al. „Dynamic decoupling of laser phase noise in compound atomic clocks“. In: *Commun. Phys.* 3 (2020), p. 185. DOI: 10.1038/s42005-020-00452-9.

[53] Martin M. Boyd, Tanya Zelevinsky, Andrew D. Ludlow, et al. „Nuclear Spin Effects in Optical Lattice Clocks“. In: *Phys. Rev. A* 76 (2007), p. 022510. DOI: 10.1103/PhysRevA.76.022510.

[54] Minghui Xu, D. A. Tieri, E. C. Fine, et al. „Synchronization of Two Ensembles of Atoms“. In: *Phys. Rev. Lett.* 113 (15 Oct. 2014), p. 154101. DOI: 10.1103/PhysRevLett.113.154101.

[55] Swadheen Dubey, Georgy A. Kazakov, Benedikt Heizenreder, et al. *Modeling of a continuous superradiant laser on the sub-mHz $^1S_0 \rightarrow {}^3P_0$ transition in neutral strontium-88*. 2024. arXiv: 2409.06575 [physics.atom-ph].

[56] JingBiao Chen. „Active optical clock“. In: *Chinese Science Bulletin* 54.3 (Jan. 2009), pp. 348–352. DOI: 10.1007/s11434-009-0073-y.

[57] Matthew A. Norcia, Matthew N. Winchester, Julia R. K. Cline, et al. „Superradiance on the millihertz linewidth strontium clock transition“. In: *Science Advances* 2.10 (2016). DOI: 10.1126/sciadv.1601231. eprint: https://advances.sciencemag.org/content/2/10/e1601231.full.pdf.

[58] Matthew A Norcia. „New tools for precision measurement and quantum science with narrow linewidth optical transitions“. PhD thesis. University of Colorado: Department of Physics, 2018.

[59] Eliot A. Bohr, Sofus L. Kristensen, Christoph Hotter, et al. „Collectively enhanced Ramsey readout by cavity sub- to superradiant transition“. en. In: *Nature Communications* 15.1 (Feb. 2024), p. 1084. DOI: 10.1038/s41467-024-45420-x.

[60] Sofus Laguna Kristensen, Eliot Bohr, Julian Robinson-Tait, et al. „Subnatural Linewidth Superradiant Lasing with Cold Sr 88 Atoms“. en. In: *Physical Review Letters* 130.22 (May 2023), p. 223402. DOI: 10.1103/PhysRevLett.130.223402.

[61] Chun-Chia Chen, Shayne Bennetts, Rodrigo González Escudero, et al. „Continuous Guided Strontium Beam with High Phase-Space Density“. In: *Phys. Rev. Applied* 12 (4 Oct. 2019), p. 044014. DOI: 10.1103/PhysRevApplied.12.044014.

[62] Chun-Chia Chen, Rodrigo González Escudero, Jivrí Minávr, et al. „Continuous Bose–Einstein condensation“. In: *Nature* 606.7915 (June 2022), pp. 683–687. DOI: 10.1038/s41586-022-04731-z.

[63] J.R. Cline, D. Young, V. M. Schäfer, et al. „Continuous loading and transport of strontium atoms in a ring cavity“. In: *52nd Annual Meeting of the APS Division of Atomic, Molecular and Optical Physics, online*. 2021.

[64] Julia R. K. Cline, Vera M. Schäfer, Zhijing Niu, et al. *Continuous collective strong coupling between atoms and a high finesse optical cavity*. 2022. arXiv: 2211.00158 [physics.atom-ph].

[65] V. M. Schäfer, Z. Niu, J. R. K. Cline, et al. *Continuous momentum state lasing and cavity frequency-pinning with laser-cooled strontium atoms*. 2024. arXiv: 2405.20952 [quant-ph].

[66] Ryoto Takeuchi, Hayaki Chiba, Shoichi Okaba, et al. „Continuous outcoupling of ultracold strontium atoms combining three different traps“. In: *Applied Physics Express* 16.4 (Apr. 2023), p. 042003. DOI: 10.35848/1882-0786/accb3c.

[67] Shoichi Okaba, Ryoto Takeuchi, Shigenori Tsuji, et al. „Continuous generation of an ultracold atomic beam using crossed moving optical lattices“. In: *Phys. Rev. Appl.* 21 (3 Mar. 2024), p. 034006. DOI: 10.1103/PhysRevApplied.21.034006.

[68] A. V. Taichenachev, V. I. Yudin, C. W. Oates, et al. „Magnetic Field-Induced Spectroscopy of Forbidden Optical Transitions with Application to Lattice-Based Optical Atomic Clocks“. In: *Phys. Rev. Lett.* 96 (8 Mar. 2006), p. 083001. DOI: 10.1103/PhysRevLett.96.083001.

[69] A. Kramida, Yu. Ralchenko, J. Reader, et al. *NIST Atomic Spectra Database (version 5.11), [Online]*. https://physics.nist.gov/asd [Accessed May 19, 2024]. DOI: https://doi.org/10.18434/T4W30F.

[70] John P. Bartolotta and Murray J. Holland. „Sawtooth-wave adiabatic passage in a magneto-optical trap“. In: *Phys. Rev. A* 101 (5 May 2020), p. 053434. DOI: 10.1103/PhysRevA.101.053434.

[71] E. Peik, M. Ben Dahan, I. Bouchoule, et al. „Bloch oscillations and an accelerator for cold atoms“. en. In: *Applied Physics B: Lasers and Optics* 65.6 (Dec. 1997), pp. 685–692.

[72] T. C. Li, H. Kelkar, D. Medellin, et al. „Real-time control of the periodicity of a standing wave: an optical accordion“. en. In: *Optics Express* 16.8 (Apr. 2008), p. 5465. DOI: 10.1364/OE.16.005465.

[73] Pierre Cladé et al. „Bloch Oscillations in Atom Interferometry“. In: *Physical Review Letters* 102.24 (2009), p. 240402. DOI: 10.1103/PhysRevLett.102.240402.

[74] Xiaoji Zhou, Xia Xu, Xuzong Chen, et al. „Magic wavelengths for terahertz clock transitions“. In: *Phys. Rev. A* 81 (1 Jan. 2010), p. 012115. DOI: 10.1103/PhysRevA.81.012115.

[75] V. Klüsener, S. Pucher, D. Yankelev, et al. *Coherent excitation of a μHz scale optical magnetic quadrupole transition*. 2024. arXiv: 2401.03934 [physics.atom-ph].

[76] Christoph Hotter, David Plankensteiner, and Helmut Ritsch. „Continuous narrow-band lasing with coherently driven V-level atoms“. In: *New Journal of Physics* 22.11 (Nov. 2020), p. 113021. DOI: 10.1088/1367-2630/abc70c.

[77] C. Gardiner. *Stochastic Methods: A Handbook for the Natural and Social Sciences*. Springer-Verlag, 2009.

[78] Ch. Lisdat, J. S. R. Vellore Winfred, T. Middelmann, et al. „Collisional Losses, Decoherence, and Frequency Shifts in Optical Lattice Clocks with Bosons“. In: *Phys. Rev. Lett.* 103 (9 Aug. 2009), p. 090801. DOI: 10.1103/PhysRevLett.103.090801.

[79] Sören Dörscher, Roman Schwarz, Ali Al-Masoudi, et al. „Lattice-induced photon scattering in an optical lattice clock“. In: *Phys. Rev. A* 97 (6 June 2018), p. 063419. DOI: 10.1103/PhysRevA.97.063419.

[80] Deshui Yu and Jingbiao Chen. „Laser theory with finite atom-field interacting time“. In: *Phys. Rev. A* 78 (1 July 2008), p. 013846. DOI: 10.1103/PhysRevA.78.013846.

[81] M. I. Kolobov, L. Davidovich, E. Giacobino, et al. „Role of pumping statistics and dynamics of atomic polarization in quantum fluctuations of laser sources“. In: *Phys. Rev. A* 47 (2 Feb. 1993), pp. 1431–1446. DOI: 10.1103/PhysRevA.47.1431.

[82] Martin M. Boyd. „High Precision Spectroscopy of Strontium in an Optical Lattice: Towards a New Standard for Frequency and Time“. PhD thesis. University of Colorado: Department of Physics, 2007.

[83] X. Zhang, M. Bishof, S. L. Bromley, et al. „Spectroscopic observation of SU(N)-symmetric interactions in Sr orbital magnetism“. In: *Science* 345.6203 (2014), pp. 1467–1473. DOI: 10.1126/science.1254978. eprint: https://science.sciencemag.org/content/345/6203/1467.full.pdf.

[84] M. J. Martin, M. Bishof, M. D. Swallows, et al. „A Quantum Many-Body Spin System in an Optical Lattice Clock“. In: *Science* 341.6146 (2013), pp. 632–636. DOI: 10.1126/science.1236929. eprint: https://science.sciencemag.org/content/341/6146/632.full.pdf.

[85] Michael J. Martin. „Quantum Metrology and Many-Body Physics: Pushing the Frontier of the Optical Lattice Clock“. PhD thesis. University of Colorado: Department of Physics, 2013.

[86] M. Bishof, M. J. Martin, M. D. Swallows, et al. „Inelastic collisions and density-dependent excitation suppression in a ^{87}Sr optical lattice clock“. In: *Phys. Rev. A* 84 (5 Nov. 2011), p. 052716. DOI: 10.1103/PhysRevA.84.052716.

[87] Aden Zhenhao Lam, Claire Warner, Niccolò Bigagli, et al. *Compact Two-Dimensional Magneto-Optical Trap for Ultracold Atom Setups*. 2021. arXiv: 2012.06688 [physics.atom-ph].

[88] R. Hobson, W. Bowden, A. Vianello, et al. „Midinfrared magneto-optical trap of metastable strontium for an optical lattice clock“. In: *Phys. Rev. A* 101 (1 Jan. 2020), p. 013420. DOI: 10.1103/PhysRevA.101.013420.

Acknowledgements

The work was supported by the European Union Horizon 2020 research and innovation programme, project No 860579 “MoSaiQC” and “Thorium nuclear clock”. The computational results presented have been achieved in part using the Vienna Scientific Cluster (VSC).

The completion of this thesis would not have been possible without the support and encouragement of the people around me in my personal and professional life. I apologize to anyone whose name I could not include here.

First and foremost, I express my most profound appreciation and gratitude to my supervisor, Dr. Georgy Kazakov. This thesis would not have gotten any results if it hadn’t been your ideas and inspirations. The support you have provided me from day one is inexpressible. Understanding the details of the superradiant laser experiment, the simulations. Thank you so much for being immensely responsive whenever I had doubts about anything and also for proofreading my thesis, your support really helped me dive into this new territory.

Using this opportunity, I would also like to thank my MoSaiQC colleagues. I am utterly grateful to our collaborators at University of Amsterdam for hosting me and constantly supporting me to understand the superradiant mHz machine. I really enjoyed all the MoSaiQcC events, all the scientific non-scientific discussions and conference dinners from Japan to Birmingham with Benedict, Abhilash, Balsant, Eliot, Julian, Anna. Specifically I’m greatful to Benedict for clearing all the doubts that I ever had related to the experiment. Producing the final results would not have been possible without your help.

Without the support of the Quantum Gas team at UvA, I would not have been able to understand the intricacies of the process and solve the problems I had dealt with during the modeling. Thank you for the detailed discussions we had during the tuesday meetings, which helped clear a lot of air and triggered new ideas as well. I am also grateful to Prof. Florian Schrek for the amazing lectures on bose and fermi gasses, which helped me understood a lot of theoretical concepts.

The Atominstitut is an exceptional place to work, particularly with its Wednesday events and the BBQs after the VCQ talks. Despite not being as involved due to my secondments and the lockdown, I had a wonderful experience with my colleagues. I am deeply grateful

to Prof. Thorsten Schumm for his patience and unwavering support throughout my time there.

I arrived in Vienna just as the COVID pandemic began. Initially, everything was in lockdown, but as things improved, I hoped to make new friends. Now, I realize I've found a family. I want to take this opportunity to thank Dr. Diksha and her fiancé, Dr. Mateusz, Disha, Shivam, Rishabh, Astha, Sampriti, and her fiancé Daniel for all the wonderful indian meals and the guidance you've provided along the way.

Sourav, Arushi and Marcel, spending time with you guys and chatting about random things helped me to relieve all my stress. Our weekly meetups were incredibly precious to me. You truly made my time in Vienna as amazing as it was. Particularly, I am deeply grateful to Dr. Shubham Gupta, a friend I made during my time in Vienna, with whom I explored everything from Corsica to Iceland, from discussing the philosophy of time to watching India's Got Latent, we had a blast. I can truly say I found a brother in arms, and all I can hope is that Tarang bani rehni chahiye!

A special thanks to Shashank, Priyasha, Dr. Adarsh and Dr. Navdeep for all their support throughout my journey, from my bachelor's degree to my PhD. I can hardly believe how quickly these 10 years have flown by.

Finally, my deepest gratitude goes to my brother, Raghav, and to my entire family, both on my mother's and father's side. A special thanks to my parents, Mrs. Abha Dubey and Er. Narendra Kumar Dubey, for their unwavering support and for embracing all of my decisions, whether in my studies, career, or even the impulsive adventures I only shared after the fact. Your faith in me and constant presence by my side have meant the world to me. To my beloved grandfather, R.K. Dubey, whom I lost along the way—I know you would have been proud. This accomplishment is dedicated equally to all of you.